Nonlinear refraction and absorption: mechanisms and magnitudes

Demetrios N. Christodoulides,[1] Iam Choon Khoo,[2] Gregory J. Salamo,[3] George I. Stegeman,[1,*] and Eric W. Van Stryland[1]

[1]College of Optics and Photonics, Center for Research in Optics and Lasers, University of Central Florida, 4000 Central Florida Boulevard, Orlando, Florida 32816, USA

[2]Department of Electrical Engineering, 121 Electrical Engineering East, Pennsylvania State University, University Park, Pennsylvania 16802, USA

[3]Department of Physics, University of Arkansas, 226 Physics Building, 825 West Dickson Street, Fayetteville, Arkansas 72701, USA

*Corresponding author: george@creol.ucf.edu

Received August 6, 2009; revised October 27, 2009; accepted October 27, 2009; published January 26, 2010 (Doc. ID 115416)

We provide an in-depth treatment of the various mechanisms by which an incident light beam can produce an intensity- or flux-dependent change in the refractive index and absorption coefficient of different materials. Whenever possible, the mechanisms are initially traced to single-atom and -molecule effects in order to provide physical understanding. Representative values are given for the various mechanisms. Nine different mechanisms are discussed, starting with the Kerr effect due to atoms and/or molecules with discrete states, including organic materials such as molecules and conjugated polymers. Simplified two and/or three-level models provide useful information, and these are summarized. The nonlinear optics of semiconductors is reviewed for both bulk and quantum-confined semiconductors, focusing on the most common types II–VI and III–V. Also discussed in some detail are the different nonlinear mechanisms that occur in liquid crystals and photorefractive media. Additional nonlinear material systems and mechanisms such as glasses, molecular reorientation of single molecules, the electrostrictive effect, the nuclear effect (vibrational contributions), cascading, and the ever-present thermal effects are quantified, and representative tables of values are given.

OCIS codes: 190.4720, 160.4330.

Nonlinear refraction and absorption: mechanisms and magnitudes

Demetrios N. Christodoulides, Iam Choon Khoo, Gregory J. Salamo, George I. Stegeman, and Eric W. Van Stryland

1. Introduction

Nonlinear processes occur in abundance in nature. Optics is of course no exception, and nonlinearities are inevitable. At high input optical intensities, there is an intensity-dependent change in a material's refractive index, frequently linked to an intensity-dependent absorption change. (Note that here we adopt the more commonly used term "intensity" rather than "irradiance" to describe light in units of power/area.) Nonlinear index and absorption changes play the key role in many important nonlinear phenomenon such as all-optical switching or soliton generation; they may be harmless artifacts, for example, in degenerate four-wave mixing, or they may be deleterious, for example, in second-harmonic generation or parametric mixing. Nonlinear absorption is the key phenomenon in nonlinear spectroscopy. It is surprising that, given the important role of such nonlinear effects, the relevant information is scattered throughout the scientific literature and there is no review of the different physical phenomena responsible for these effects.

The intensity-dependent refractive index $n_2(I)$, where I is the intensity, is defined by $\Delta n = n_2(I)I$. Historically $n_2(I)$ was first defined for the Kerr effect in terms of the sum of the real part of the third-order electronic susceptibilities $\chi^{(3)}(-\omega : -\omega, \omega, \omega) + \chi^{(3)}(-\omega : \omega, -\omega, \omega) + \chi^{(3)}(-\omega : \omega, \omega, -\omega)$. In this case, the index change is local and effectively instantaneous so that $\Delta n = n_2 I$. This *electronic* nonlinearity has proved very useful for probing different nonlinear interactions, since many problems can be solved analytically with this particular form for the index change. However, in addition to the Kerr effect there is a myriad of additional physical mechanisms that also lead to an intensity-dependent refractive index change. Many of them depend on the state of the matter that is being probed optically, e.g., polymer, semiconductor, liquid crystal, or glass. In this tutorial review we discuss the physics of these mechanisms and derive, where possible, formulas that link index change to intensity, and we provide typical values for the intensity-dependent refractive index coefficients and the characteristic times that it takes to produce the index change when an optical field is turned on and the decay time when the field is turned off. In order to achieve these goals, it proved useful in this review to first describe the pertinent physics of some of the unique states of matter such as conjugated polymers, semiconductors, liquid crystals, and photorefractive (PR) materials.

Although a principal goal of this paper is to discuss the relevant physical mechanisms that give rise to an intensity-dependent refractive index and absorption, in

the final analysis it is necessary to evaluate these pertinent nonlinear coefficients experimentally. First, the very parameters that enter into expressions for the nonlinearity require experimental determination. Second, although many nonlinear mechanisms can be described on a single-molecule level, the transition to the condensed matter phase is not very precise because of intermolecular interactions, collisions, local field effects, etc. Therefore, although many of the gross features, such as location of maxima, symmetry relations, and a first-order estimate of dispersion with frequency, can be obtained successfully from single-molecule theories, ultimately experimental measurements of nonlinear coefficients, most specifically in this case the nonlinear refractive index, are needed in order to interpret data and accurately predict phenomena. Nonlinear optics is primarily an experimental discipline!

The nonlinear mechanisms to be discussed in this review are listed below:

1. Nonlinearities involving transitions between discrete molecular states
2. "Glass" nonlinearities
3. Semiconductor nonlinearities
4. Nuclear (vibrational) contributions to n_2.
5. Molecules with anisotropic polarizabilities
   (a) Molecular reorientation
   (b) Liquid crystals
6. Photorefractive effects
7. Electrostriction
8. Thermal nonlinearities
9. Cascading of second-order nonlinearities

This list is arranged to be approximately in order of increasing time constants, except for cascading, which is a special case. Note that some of the mechanisms occur in all materials, and others are material specific.

In Section 2, nonlinear refraction and absorption due to transitions between discrete states in matter, principally dielectric and organic media, are explored. Since the general case is very complicated, the formulas are reduced, assuming a two-level system, to analytical formulas for the nonlinearity near and on the one- and two-photon resonances; off resonance, in which case the damping term in the resonance denominators is set to zero; and finally in the nonresonant limit, in which the photon frequency is ignored relative to the resonance frequencies associated with the transitions. Insights into some general properties of nonlinearities gained from applying a two-level model are summarized. In addition, since organic molecules are classical systems with discrete energy levels, the physics and magnitudes of their nonlinearities are reviewed. Included are polyenes and their polymerized counterparts, i.e., conjugated polymers, a variety of symmetric and asymmetric charge transfer molecules, and the special cases of dendrimers. Finally, the phenomena of excited state and reverse saturable absorption (RSA) are discussed with illustrative examples.

In Section 3 the nonlinearities of glasses are briefly discussed. They are basically discrete energy level systems broadened to overlap between states by the random, amorphous, disordered nature of a glass. Although the focus is primarily on fused silica, for which the dispersion in n_2 is well known and highly relevant to communications fibers, the effect on the nonlinearities of adding various oxides is summarized. To date, the largest nonlinearities have been obtained in chalcogenide glasses whose absorption edge is in the near infrared.

Section 4 deals with semiconductors, which exhibit the largest and best understood range of physical phenomena responsible for different nonlinearities. The largest nonlinearities arise from the absorption of light with the consequent transfer of an electron from the valence to conduction bands. Even larger nonlinearities, but over a narrow spectral range, occur as a result of bleaching of exciton states located in the bandgap below the conduction band. The effects of applying active pumping of electrons from the valence band to conduction bands followed by stimulated emission reverses the sign of the nonlinearities and leads to nonlinear gain rather than loss. The different effects that lead to nonlinearities for photon energies below the bandgap are summarized next. The analytical formulas derived in this spectral region are shown to be in excellent agreement with experiment. Finally, the results for nonlinearities of the confinement of electrons to two (quantum wells), one (quantum wires) and zero (quantum dots, QDs) dimensions are reviewed. Evidence is presented for modest enhancements in quantum wells (factor of 2–3). However, it is clear that in most QD systems studied to date there is no clear measurable enhancement except perhaps for GaAs in one case, in which an order of magnitude enhancement has been reported.

Section 5 reviews the nonlinearity obtained from coupling to vibrational modes in matter. The contributions are of the order of a few tens of percent in glasses.

Section 6 deals with the reorientation of anisotropic molecules, individually or collectively, and the resulting contributions to nonlinear phenomena. For single molecules, the dipoles induced by an optical field tend to align the large molecule polarizability axis with the field, creating a refractive index anisotropy in the liquid state. In liquid crystals, intermolecular forces lead to collective behavior. This results in a spectrum of nonlinearites due to absorption and resulting temperature changes, which reduce the size of the aligned regions and hence the induced index change. If the liquid crystal molecules are anchored at the sample surfaces, the application of electric fields results in molecular reorientation with distance into the sample or a field-dependent threshold for decoupling from the surface anchoring. Both cases lead to an intensity-dependent refractive index. Finally, doping a liquid crystal with dye molecules that undergo structural changes (trans-cis isomerization) on light absorption can disrupt collective orientation in liquid crystals, resulting in huge nonlinearities. All of these effects are discussed in Section 6.

Photorefractive media, explored in Section 7, are another source of very large (and usually very slow) nonlinearities. Their physics involves absorption that raises an electron from a donor state to the conduction band, the motion of that electron either due to diffusion or applied fields, and then retrapping in an acceptor state some distance from the initial absorption. This process introduces nonlocality and electric fields due to the charge separation, which, via the electro-optic effect, yield index changes. The nonlocality is responsible for a number of different phenomena such as beam fanning and two-beam coupling. These processes are quantified, and typical numbers are given.

Section 8 contains information on the electrostrictive effect, which always compresses a material along the field direction. This effect, although relatively slow and small, leads to acoustic wave generation, which, depending on sample geometry, can cause spurious effects on the light beam.

The thermo-optic effect (described in Section 9) arises because of beam absorption, followed by changes in sample temperature and hence index changes. Depending on the time scale of measurements of the nonlinearity and the magni-

tude of the material absorption coefficient, this can be the dominant nonlinear effect. The decay time scale of the index change is slow and depends on beam geometry and the material's thermal properties.

The last contribution to nonlinear effects that mimic nonlinear absorption and changes in index proportional to intensity occurs owing to the cascading of second-order nonlinearities. This can occur at the molecular level (local cascading) or on propagation coincident with the generation of new frequencies (nonlocal cascading). The latter can lead to large effects, especially if the second-order process is near a phase-match condition, for example, in second-harmonic generation. These effects are described in Section 10.

Some concluding remarks are given in Section 11.

2. Nonlinearities Involving Transitions between Discrete Molecular States

The physical origin of nonlinearities involving transitions between discrete molecular states is the electric dipole interaction between the electrons in atoms and molecules and an electromagnetic field (see standard textbooks such as [1,2] for detailed discussions). Electrons are excited from the ground state to excited states via the product of three or more electric fields, which can be either the same or different electric fields. This changes the electron distribution in the atom or molecule, and hence the polarization induced by the field has a nonlinear component that is proportional to the product of three fields. The proportionality is calculated from first-order perturbation theory and described in the single-isolated-molecule limit by the sum of three different third-order susceptibilities $\bar{\gamma}^{(3)}_{ijkl}$, which are functions of the electric dipole transition elements between electronic states and the permanent dipole moments in the ground and excited states. In the condensed matter limit pertinent to nonlinear optics, the interactions are described by the sum of three different third-order susceptibilities $\chi^{(3)}_{ijkl}$ derived from the molecular susceptibilities.

The starting point for a calculation of $\chi^{(3)}_{ijkl}$ is the isolated-single-molecule third-order susceptibility $\bar{\gamma}^{(3)}_{ijkl}$. For detailed discussions see [1]. (In this tutorial review, parameters associated with single isolated molecules are identified with an overbar.) From a combination of repeated applications of first-order perturbation theory, the method of averages approach to deal with divergences, limiting the light–matter interaction to electric dipole coupling, assuming that the molecule's electrons are initially in the ground state, and limiting the interaction to a single electron excitation per molecule, the third-order molecular susceptibility $\bar{\gamma}^{(3)}_{ijkl}$ for arbitrary input frequencies ω_p, ω_q, and ω_r is given below by Eq. (2.1). For details see the classic paper by Orr and Ward [3]. Here both summations, each over all of the molecular *excited* states v, m, and n [see Fig. 1(a)] specifically exclude the ground state g (as indicated by the superscript $'$); i.e., they are taken over the excited states only. Furthermore, the energy separation between states, for example m and n, is written as $\bar{E}_m - \bar{E}_n = \hbar\bar{\omega}_{mn}$, and the transition dipole moment between these states is given by $\vec{\bar{\mu}}_{mn}$. The permanent dipole moment in state m is written as $\vec{\bar{\mu}}_{mm}$. Usually finite excited state lifetimes for the excited state to the ground state are added phenomenologically by making $\bar{\omega}_{mn}$ complex for the ex-

Figure 1

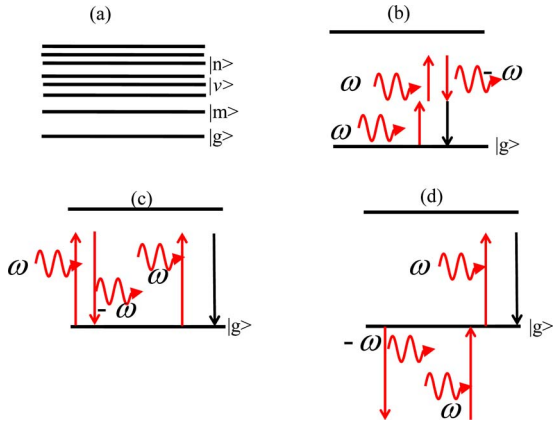

(a) Schematic of the electronic energy levels for a molecule; g is the ground state and m, v, and n are arbitrary excited states. Transition diagrams for (b) $\chi^{(3)}\times(-\omega;\omega,\omega,-\omega)$, (c) $\chi^{(3)}(-\omega;\omega,-\omega,\omega)$, and (d) $\chi^{(3)}(-\omega;-\omega,\omega,\omega)$.

cited states, i.e., $\bar{\omega}_{ng}\rightarrow\bar{\omega}_{ng}-i\bar{\Gamma}_{ng}$. Note that *subsequent to* Eq. (2.1) $\bar{\omega}_{ng}$ is a real quantity:

$$
\begin{aligned}
&\bar{\gamma}^{(3)}_{ijkl}(-[\omega_p+\omega_q+\omega_r];\omega_p,\omega_q,\omega_r)\\
&=\frac{1}{\varepsilon_0\hbar^3}\sum_{v,n,m}{}'\left\{\frac{\bar{\mu}_{gv,i}(\bar{\mu}_{vn,l}-\bar{\mu}_{gg,l})(\bar{\mu}_{nm,k}-\bar{\mu}_{gg,k})\bar{\mu}_{mg,j}}{(\bar{\omega}_{vg}-\omega_p-\omega_q-\omega_r)(\bar{\omega}_{ng}-\omega_q-\omega_p)(\bar{\omega}_{mg}-\omega_p)}\right.\\
&\quad+\frac{\bar{\mu}_{gv,j}(\bar{\mu}_{vn,k}-\bar{\mu}_{gg,k})(\bar{\mu}_{nm,i}-\bar{\mu}_{gg,i})\bar{\mu}_{mg,l}}{(\bar{\omega}^*_{vg}+\omega_p)(\bar{\omega}^*_{ng}+\omega_q+\omega_p)(\bar{\omega}_{mg}-\omega_r)}\\
&\quad+\frac{\bar{\mu}_{gv,l}(\bar{\mu}_{vn,i}-\bar{\mu}_{gg,i})(\bar{\mu}_{nm,k}-\bar{\mu}_{gg,k})\bar{\mu}_{mg,j}}{(\bar{\omega}^*_{vg}+\omega_r)(\bar{\omega}_{ng}-\omega_q-\omega_p)(\bar{\omega}_{mg}-\omega_p)}\\
&\quad\left.+\frac{\bar{\mu}_{gv,j}(\bar{\mu}_{vn,k}-\bar{\mu}_{gg,k})(\bar{\mu}_{nm,l}-\bar{\mu}_{gg,l})\bar{\mu}_{mg,i}}{(\bar{\omega}^*_{vg}+\omega_p)(\bar{\omega}^*_{ng}+\omega_q+\omega_p)(\bar{\omega}^*_{mg}+\omega_p+\omega_q+\omega_r)}\right\}\\
&\quad-\frac{1}{\varepsilon_0\hbar^3}\sum_{n,m}{}'\left\{\frac{\bar{\mu}_{gn,i}\bar{\mu}_{ng,l}\bar{\mu}_{gm,k}\bar{\mu}_{mg,j}}{(\bar{\omega}_{ng}-\omega_p-\omega_q-\omega_r)(\bar{\omega}_{ng}-\omega_r)(\bar{\omega}_{mg}-\omega_p)}\right.\\
&\quad+\frac{\bar{\mu}_{gn,i}\bar{\mu}_{ng,l}\bar{\mu}_{gm,k}\bar{\mu}_{mg,j}}{(\bar{\omega}^*_{mg}+\omega_q)(\bar{\omega}_{ng}-\omega_r)(\bar{\omega}_{mg}-\omega_p)}\\
&\quad+\frac{\bar{\mu}_{gn,l}\bar{\mu}_{ng,i}\bar{\mu}_{gm,j}\bar{\mu}_{mg,k}}{(\bar{\omega}^*_{ng}+\omega_r)(\bar{\omega}^*_{mg}+\omega_p)(\bar{\omega}_{mg}-\omega_q)}\\
&\quad\left.+\frac{\bar{\mu}_{gn,l}\bar{\mu}_{ng,i}\bar{\mu}_{gm,j}\bar{\mu}_{mg,k}}{(\bar{\omega}^*_{ng}+\omega_r)(\bar{\omega}^*_{mg}+\omega_p)(\bar{\omega}^*_{ng}+\omega_p+\omega_q+\omega_r)}\right\}.
\end{aligned}
\tag{2.1}
$$

This is called the "sum over states" equation, typically abbreviated S.O.S. The

usual notation is used in which the frequency of the field affected by the nonlinear interaction $[\omega_p+\omega_q+\omega_r]$ appears as the first argument in $\gamma^{(3)}_{ijkl}(-[\omega_p+\omega_q+\omega_r];\omega_p,\omega_q,\omega_r)$ and the input interacting fields have frequency components ω_p, ω_q, and ω_r. Note that in this notation all of the fields can be $\pm$ with the negative frequency components corresponding to the complex conjugate of the fields, which are written as

$$E_{j,\mathrm{inc}}(\vec{r},t)=\frac{1}{2}\mathrm{E}_j(\omega)e^{-i\omega t}+\mathrm{c.c.}=\frac{1}{2}\mathcal{E}_j(\omega)e^{i(\vec{k}\cdot\vec{r}-\omega t)}+\mathrm{c.c.} \tag{2.2}$$

If the medium of interest is a dilute gas of molecules so that molecules can still be considered isolated, the macroscopic third-order susceptibility $\chi^{(3)}_{ijkl}(-[\omega_p+\omega_q+\omega_r];\omega_p,\omega_q,\omega_r)$ is given by

$$\chi^{(3)}_{ijkl}(-[\omega_p+\omega_q+\omega_r];\omega_p,\omega_q,\omega_r)=N\bar{\gamma}^{(3)}_{ijkl}(-[\omega_p+\omega_q+\omega_r];\omega_p,\omega_q,\omega_r), \tag{2.3}$$

in which N is the number of molecules per unit volume. However, the principal interest in $n_{2,\mathrm{el}}$ is for condensed matter in which both intermolecular interactions and the electromagnetic fields generated by the dipoles induced at the site of a specific molecule by neighboring molecules are important. (See standard textbooks such as [1,2] for detailed discussions.) The former can lead to changes in the resonances and the lifetimes of the electrons in excited states, whereas the latter results in the local field at a molecule being different from those fields obtained from Maxwell's equations. (Solving the standard boundary conditions for input beams at a sample's interfaces yields the Maxwell fields in the medium of interest.) Unfortunately, there is no truly satisfactory way for calculating the local field correction to the Maxwell fields. One usually resorts to the approximate Lorenz–Lorenz relation in which each of the incident (Maxwell) fields associated with ω_p, ω_q, and ω_r, i.e., $\mathrm{E}_j(\omega_p)$, $\mathrm{E}_k(\omega_q)$, and $\mathrm{E}_l(\omega_r)$ is multiplied by $[\varepsilon^r_j(\omega_p)+2]/3$, $[\varepsilon^r_k(\omega_q)+2]/3$, and $[\varepsilon^r_l(\omega_r)+2]/3$, respectively, to approximate the local field. Here $\varepsilon^r_j(\omega_p)=n^2_j(\omega_p)$ is the relative dielectric constant for light polarized along the j axis, x in the current case. Thus, in condensed matter,

$$\chi^{(3)}_{ijkl}(-[\omega_p+\omega_q+\omega_r];\omega_p,\omega_q,\omega_r)=Nf^{(3)}\bar{\gamma}^{(3)}_{ijkl}(-[\omega_p+\omega_q+\omega_r];\omega_p,\omega_q,\omega_r),$$

$$f^{(3)}=\left[\frac{\varepsilon^r_i(\omega_p+\omega_q+\omega_r)+2}{3}\right]\left[\frac{\varepsilon^r_j(\omega_p)+2}{3}\right]\left[\frac{\varepsilon^r_k(\omega_q)+2}{3}\right]\left[\frac{\varepsilon^r_l(\omega_r)+2}{3}\right]. \tag{2.4}$$

Focusing the discussion to a single input field of frequency ω with polarization along the x axis of the material, there are three separate pathways to $n_{2,\mathrm{el}}$, illustrated in Figs. 1(b)–1(d), that affect the field at this frequency. Thus there will be three different susceptibilities $\chi^{(3)}_{xxxx}$ and a total of 24 separate terms needed to describe the nonlinear interaction for each summation over the excited states. The electronic nonlinear refractive index coefficient $n_{2,\mathrm{el}}$ is then defined in terms of the these susceptibilities by

$$n_{2,\mathrm{el}} = \frac{1}{4n_x^2\varepsilon_0 c}\{\chi^{(3)}_{\Re,xxxx}(-\omega;\omega,-\omega,\omega) + \chi^{(3)}_{\Re,xxxx}(-\omega;\omega,\omega,-\omega) + \chi^{(3)}_{\Re,xxxx}(-\omega;-\omega,\omega,\omega)\} = \frac{3}{4n_x^2\varepsilon_0 c}\tilde{\chi}^{(3)}_{\Re,xxxx}(-\omega;\omega,-\omega,\omega), \quad (2.5a)$$

where

$$\begin{aligned}\tilde{\chi}^{(3)}_{\Re,xxxx}(-\omega;\omega,-\omega,\omega) &= \frac{1}{3}\{\chi^{(3)}_{\Re,xxxx}(-\omega;\omega,-\omega,\omega) + \chi^{(3)}_{\Re,xxxx}(-\omega;\omega,\omega,-\omega) \\ &\quad + \chi^{(3)}_{\Re,xxxx}(-\omega;-\omega,\omega,\omega)\} \xrightarrow{\text{nonresonant},\omega\to 0} \\ &= \chi^{(3)}_{\Re,xxxx}(-\omega;\omega,-\omega,\omega) = \chi^{(3)}_{\Re,xxxx}(-\omega;\omega,\omega,-\omega) \\ &= \chi^{(3)}_{\Re,xxxx}(-\omega;-\omega,\omega,\omega), \end{aligned} \quad (2.5b)$$

where the subscripts $\Re$ and $\Im$ refer to the real and imaginary parts of $\chi^{(3)}$, respectively. This index change is accompanied by an intensity-dependent change in the absorption defined by $\Delta\alpha = \alpha_2(I)I$ with

$$\alpha_{2,\mathrm{el}} = \frac{\omega}{2n_x^2\varepsilon_0 c^2}\{\chi^{(3)}_{\Im,xxxx}(-\omega;\omega,-\omega,\omega) + \chi^{(3)}_{\Im,xxxx}(-\omega;\omega,\omega,-\omega) + \chi^{(3)}_{\Im,xxxx}(-\omega;-\omega,\omega,\omega)\}. \quad (2.5c)$$

The spectral breadth of an optical spectrum, for example, the absorption spectrum, is related to just the *radiative* lifetime of the excited state only in special circumstances [1,2]. In the formulas above it has been assumed that the decay is due to coupling to the ground state, which results in homogeneous broadening of the susceptibilities. However, there are other possible contributions to the state lifetime, especially in dense gases or condensed matter. These typically lead to inhomogeneous broadening of spectral lines and a variety of line shapes different from those given above. Examples are intermolecular forces, collisions in dense gases, and additional decay channels involving virtual states. It is primarily when a multiple of the incident photon energies approximately equals the energy difference between the ground and an excited state that the response takes on the simple form used above. Because of the multiple decay mechanisms possible, the results of the S.O.S. approach, which considers only a single, frequency-independent lifetime, cannot in principle be used in the so-called the zero-frequency limit, although it is frequently used successfully in *comparing* the magnitude of nonlinearities in families of molecules in the field of theoretical chemistry [4].

2.1. Two-Level Model in Isotropic Media

Even without the above considerations on excited state lifetimes, the above formulas for the general third-order susceptibility are quite complicated, since they involve multiple summations over all of the excited states. However, a great deal of physical insight can be obtained from a simple two-level model with one resonant frequency $\bar{\omega}_{10}$ for a single input beam (x polarized for example) in three common limits. In fact, a single dominant one-photon transition is a very useful approximation in many molecules for the interaction of radiation with that molecule.

Of the 24 terms that need to be evaluated in the general case, only 2 contain two-photon terms of the form $[(\bar{\omega}_{10}\pm 2\omega)^2+(\bar{\Gamma}_{10}/2)^2]$ due to $|\bar{\mu}_{10}|^2|\bar{\mu}_{11}-\bar{\mu}_{00}|^2$, and clearly only the resonance at $\bar{\omega}_{10}\approx 2\omega$ gives rise to an enhanced two-photon nonlinearity. That is, a molecule must have a nonzero difference in its permanent dipole moments, which rules out two-photon effects in symmetric molecules in the two-level approximation. (Two-photon effects solely due to dipole active transition moments between states occur in a three-level model of molecules of arbitrary symmetry!)

The remaining 22 terms contain terms of the form $[(\bar{\omega}_{10}\pm\omega)^2+(\bar{\Gamma}_{10}/2)^2]^m$ in their denominator with $m=1,2,3$. These terms arise owing to both $|\bar{\mu}_{10}|^2|\bar{\mu}_{11}-\bar{\mu}_{00}|^2$ and $|\bar{\mu}_{10}|^4$ interactions. Clearly in those cases enhancement only occurs when $\bar{\omega}_{10}\approx\omega$.

All of the terms were evaluated numerically for $\bar{\omega}_{10}\approx\omega$ and $\bar{\omega}_{10}\approx 2\omega$, and the results are summarized in Figs. 2 and 3.

Figure 2

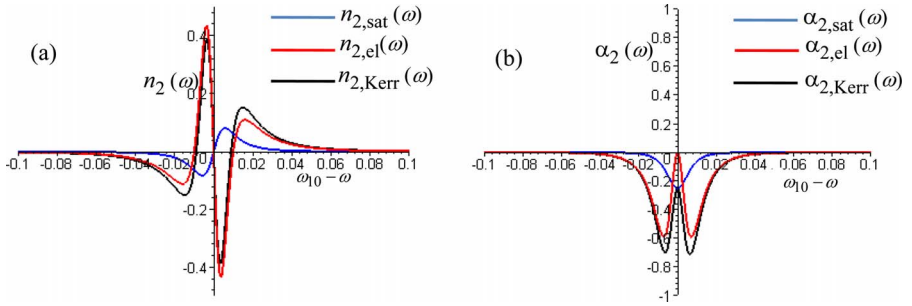

Frequency dispersion in the normalized (multiplied by $[\bar{\Gamma}_{10}/2]^3$) (a) $n_2(\omega)$ and (b) $\alpha_2(\omega)$ for the contributions due to $|\bar{\mu}_{10}|^4$ for $\omega\approx\bar{\omega}_{10}$. Here $\bar{\omega}_{10}=1$, $\bar{\Gamma}_{10}/2=0.01$. The exact and approximate (formulas in text) curves for $n_{2,\mathrm{el}}(\omega)$ and $\alpha_{2,\mathrm{el}}(\omega)$ coincide.

Figure 3

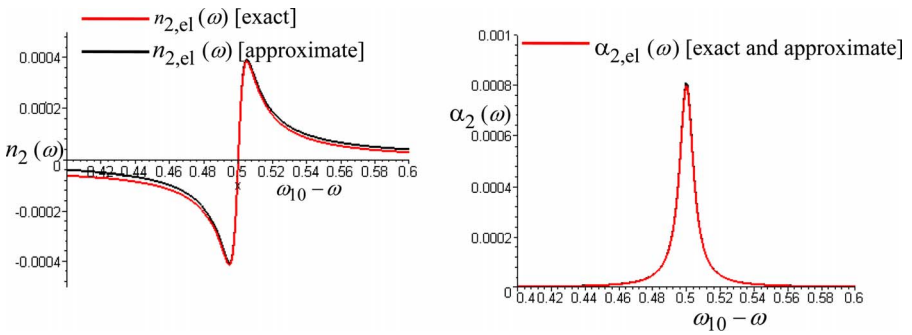

Frequency dispersion in the normalized (multiplied by $[\bar{\Gamma}_{10}/2]^3$) $n_2(\omega)$ and $\alpha_2(\omega)$ for the contributions due to $|\bar{\mu}_{10}|^2|\bar{\mu}_{11}-\bar{\mu}_{00}|^2$ for $2\omega\cong\bar{\omega}_{10}$. Here, $\bar{\omega}_{10}=1$ and $\bar{\Gamma}_{10}/2=0.01$.

Here, only the frequency dispersion terms are given and these have been multiplied in the numerator by $[\bar{\Gamma}_{10}/2]^3$ to produce dominant terms of order unity for the one-photon resonance case. In the curves labeled "exact" all of the terms were included, and it was assumed for simplicity that $|\bar{\mu}_{10}|^2|\bar{\mu}_{11}-\bar{\mu}_{00}|^2=|\bar{\mu}_{10}|^4$. In brief summary, near the one-photon resonances almost complete cancellation occurred ($\bar{\omega}_{10} \approx \omega$), although the individual contributions to the $|\bar{\mu}_{10}|^2|\bar{\mu}_{11}-\bar{\mu}_{00}|^2$ terms were large, and the net results were 4–5 orders of magnitude smaller than the leading $|\bar{\mu}_{10}|^4$ term, i.e., negligible unless $|\bar{\mu}_{11}-\bar{\mu}_{00}|$ is of the order of 25 or greater. And in all cases it was the triple resonance, $m=3$, term associated with $\chi^{(3)}(-\omega;\omega,-\omega,\omega)$ [Fig. 1(b)] that dominated the response. Based on these numerical results, approximate formulas were obtained for $n_{2,\mathrm{el}}$ and $\alpha_{2,\mathrm{el}}$ and are given below:

On and near resonance ($\bar{\omega}_{10} \gg \bar{\Gamma}_{10}$)

One-photon resonance: ($\sim |\omega-\bar{\omega}_{10}| \leq 5\bar{\Gamma}_{10}$):

$$n_{2,\mathrm{el}} \cong -\frac{1}{4n_x^2\varepsilon_0 c}\frac{N}{\varepsilon_0\hbar^3}f^{(3)}|\bar{\mu}_{10}|^4\frac{2(\bar{\omega}_{10}-\omega)\left[(\bar{\omega}_{10}-\omega)^2-\dfrac{\bar{\Gamma}_{10}^2}{4}\right]}{\left[(\bar{\omega}_{10}-\omega)^2+\dfrac{\bar{\Gamma}_{10}^2}{4}\right]^3}, \quad (2.6a)$$

$$\alpha_{2,\mathrm{el}} \cong -\frac{\omega}{2n_x^2\varepsilon_0 c^2}\frac{N}{\varepsilon_0\hbar^3}f^{(3)}|\bar{\mu}_{10}|^4\frac{\bar{\Gamma}_{10}(\bar{\omega}_{10}-\omega)\left[2\bar{\omega}_{10}(\bar{\omega}_{10}-\omega)+\dfrac{\bar{\Gamma}_{10}^2}{4}\right]}{\bar{\omega}_{10}\left[(\bar{\omega}_{10}-\omega)^2+\dfrac{\bar{\Gamma}_{10}^2}{4}\right]^3}. \quad (2.6b)$$

However, off resonance, for which the contribution of $\bar{\Gamma}_{10}$ in the denominators can be neglected, the contributions of all 24 different terms become comparable, and exactly equal in the $\omega \to 0$ limit. Exact formulas appropriate to these cases are given below.

Off-resonance ($\sim |\omega-\bar{\omega}_{10} \gg \bar{\Gamma}_{10}$):

$$n_{2,\mathrm{el}} = \frac{Nf^{(3)}}{4n_x^2\varepsilon_0^2 c\hbar^3}\left\{\frac{|\bar{\mu}_{10}|^2(\bar{\mu}_{11}-\bar{\mu}_{00})^2 12\bar{\omega}_{10}}{(\bar{\omega}_{10}^2-\omega^2)(\bar{\omega}_{10}^2-4\omega^2)}-\frac{|\bar{\mu}_{10}|^4 4\bar{\omega}_{10}}{(\bar{\omega}_{10}^2-\omega^2)^3}(3\bar{\omega}_{10}^2+\omega^2)\right\}, \quad (2.7a)$$

$$\alpha_{2,\mathrm{el}} = \frac{N}{2n_x^2\varepsilon_0 c^2\hbar^3}\frac{\omega^2\bar{\Gamma}_{10}\bar{\omega}_{10}}{(\bar{\omega}_{10}^2-\omega^2)^3}f^{(3)}\left\{|\bar{\mu}_{10}|^2(\bar{\mu}_{11}-\bar{\mu}_{00})^2\frac{104\omega^4-25\bar{\omega}_{10}^2\omega^2-7\bar{\omega}_{10}^4}{(\bar{\omega}_{10}^2-4\omega^2)^2}\right.$$
$$\left.+|\bar{\mu}_{10}|^4\frac{4(3\omega^2-\bar{\omega}_{10}^2)}{(\bar{\omega}_{10}^2-\omega^2)}\right\}. \quad (2.7b)$$

Nonresonant (limit $\omega \to 0$, i.e., $\bar{\omega}_{10} \gg 2\omega$):

$$n_{2,\mathrm{el}} = 3\frac{Nf^{(3)}}{n_x^2\varepsilon_0^2 c\hbar^3\bar{\omega}_{10}^3}\{|\bar{\mu}_{10}|^2(\bar{\mu}_{11}-\bar{\mu}_{00})^2 - |\bar{\mu}_{10}|^4\}. \tag{2.7c}$$

Note the interference between the $|\bar{\mu}_{10}|^2(\bar{\mu}_{11}-\bar{\mu}_{00})^2$ and $|\bar{\mu}_{10}|^4$ terms.

Similar calculations were for the frequency region $\bar{\omega}_{10} \approx 2\omega$ with results summarized in Fig. 3. Here only the $|\bar{\mu}_{10}|^2|\bar{\mu}_{11}-\bar{\mu}_{00}|^2$ term has a resonance. Given below are approximate formulas for both for $n_{2,\mathrm{el}}$ and $\alpha_{2,\mathrm{el}}$.

Two-photon resonance ($\sim |\omega - \bar{\omega}_{10}/2| \le 5\bar{\Gamma}_{10}$):

$$n_{2,\mathrm{el}} \cong \frac{1}{4n_x^2\varepsilon_0 c}\frac{N}{\varepsilon_0\hbar^3}f^{(3)}|\bar{\mu}_{10}|^2(\bar{\mu}_{11}-\bar{\mu}_{00})^2\left[\frac{8\left[(\bar{\omega}_{10}-2\omega)-\left(\frac{\bar{\Gamma}_{10}^2}{2\bar{\omega}_{10}}\right)\right]}{\bar{\omega}_{10}^2\left[(\bar{\omega}_{10}-2\omega)^2+\left(\frac{\bar{\Gamma}_{10}}{2}\right)^2\right]}\right], \tag{2.8a}$$

$$\alpha_{2,\mathrm{el}} \cong \frac{\omega}{2n_x^2\varepsilon_0 c^2}\frac{N}{\varepsilon_0\hbar^3}f^{(3)}|\bar{\mu}_{10}|^2(\bar{\mu}_{11}-\bar{\mu}_{00})^2\left[\frac{4\bar{\Gamma}_{10}}{\bar{\omega}_{10}^2\left[(\bar{\omega}_{10}-2\omega)^2+\left(\frac{\bar{\Gamma}_{10}}{2}\right)^2\right]}\right]. \tag{2.8b}$$

The difference between the exact and the approximate curves for the dispersion in $n_{2,\mathrm{el}}$ shown in Fig. 3 results from the neglect of the term with the denominator $[(\bar{\omega}_{10}+2\omega)^2+(\bar{\Gamma}_{10}/2)^2]$ in the approximate formula.

The question of "nonresonant" susceptibilities merits further comment. The literature is replete with measurements of n_2 that are claimed to be "nonresonant." Such claims are frequently erroneous and most likely refer to off-resonance. The key consideration is usually whether both $|\bar{\omega}_{10}-\omega| \gg \bar{\Gamma}_{10}$ and $\bar{\omega}_{10} \gg \omega$ are satisfied for a measurement to be in the nonresonant regime.

Recall that light of a given frequency can propagate with a specific wave vector $\vec{k}$ for a given frequency and direction in one of two orthogonally polarized eigenmodes. The refractive index of one of these eigenmodes can be changed by its own high intensity as discussed above and/or by an intense beam of the same frequency but with orthogonal polarization. Furthermore, the index can also be changed by a beam at a different frequency of either polarization. And, unless the frequencies of interest are clearly in the nonresonant regime, each of these can have different numerical values and different dispersion with frequency, even in isotropic media.

For an *amorphous isotropic* material the symmetry relations for $\chi^{(3)}$ lead directly to $n_{2\perp,\mathrm{el}}(-\omega_a;\omega_a) = \frac{2}{3}n_{2\parallel,\mathrm{el}}(-\omega_a;\omega_a)$ at any frequency ω_a, where the polarization of the index change of interest is identified by $\parallel$ and the orthogonal one inducing the change by $\perp$. In the nonresonant regime (*only*), the nonlinear refractive index co-

efficient at ω_a by a copolarized beam of frequency ω_b is $n_{2\parallel,\mathrm{el}}(-\omega_a;\omega_b) = 2n_{2\parallel,\mathrm{el}}(-\omega_a;\omega_a)$ and by an orthogonally polarized beam is $n_{2\parallel,\mathrm{el}}(-\omega_a;\omega_b) = \frac{4}{3}n_{2\parallel,\mathrm{el}}(-\omega_a;\omega_a)$. Unfortunately, in the literature there is frequently no distinction drawn between these different coefficients and they are assumed to be equal.

For crystalline media, the relations can be much more complex. The pertinent nonzero $\chi^{(3)}$ coefficients for crystalline media can be found in textbooks (see standard textbooks such as [1,2]).

In this review we focus primarily on the frequency degenerate case $n_{2\parallel,\mathrm{el}}(-\omega_a;\omega_a)$, usually written as n_2 for convenience.

2.2. Onset of Saturation of Electronic Transitions

In the preceding section the results for $n_{2,\mathrm{el}}$ were based on the assumption that a negligible fraction of electrons were excited out of the ground state (subscript g) into the excited states N_m, implying that $N_\mathrm{g} \cong N$ in the ground state; i.e., N_g is effectively a constant. This is, however, an approximation, especially in spectral regions characterized by strong absorption, i.e., $\omega \approx \bar{\omega}_{m\mathrm{g}}$ for some state m where N_m can become nonnegligible. Since $\chi^{(p)} \propto (N_\mathrm{g} - N_m)$, where p is an integer, this leads to a decrease in the magnitude of $\chi^{(p)}$ from its value with negligible population in the excited states. More important, for $N_m \to N_\mathrm{g}/2$ it also leads to a saturation effect for the linear absorption at ω, which over some time scales mimics the Kerr $\chi^{(3)}$ and has sometimes been interpreted as $\chi^{(3)}, \chi^{(5)}, \chi^{(7)}$, etc. Here we discuss only effective α_2 due to saturation, $\alpha_{2,\mathrm{sat}}$, the contribution that is linear in the intensity.

Again we resort to the two-level model to quantify this effect in the simplest possible case. As stated previously, the two-level model can yield a very good approximation, since frequently the largest transition dipole moment occurs from the ground state to just a single excited state we have labeled m.

The linear susceptibility $\chi^{(1)}$ for electric-dipole transitions from the ground to the mth excited state is given by

$$\chi^{(1)}_{xx}(-\omega;\omega) = \frac{(N_\mathrm{g} - N_m)}{\hbar\varepsilon_0}|\bar{\mu}_{m\mathrm{g}}|^2 f^{(1)} \frac{\bar{\omega}_{m\mathrm{g}} - \omega + i\bar{\Gamma}_{m\mathrm{g}}/2}{(\bar{\omega}_{m\mathrm{g}} - \omega)^2 + \bar{\Gamma}^2_{m\mathrm{g}}/4}, \tag{2.9}$$

in which $f^{(1)} = [\varepsilon^r(\omega) + 2]/3$ is the local field correction. The excited state decays asymptotically to the ground state with relaxation time $\bar{\tau}_{m\mathrm{g}} = \bar{\Gamma}^{-1}_{m\mathrm{g}}$, and it is assumed that the decay to all other excited states occurs over much longer times. When a cw beam of intensity $I(\omega)$ illuminates the material, the time dynamics of the ground and dominant excited state, under the assumption that both are only weakly coupled to other states, is given by

$$\frac{d}{dt}N_m = \bar{B}(N_\mathrm{g} - N_m)[f^{(1)}]^2 I(\omega) - \frac{N_m}{\bar{\tau}_{m\mathrm{g}}},$$

$$\frac{d}{dt}N_\mathrm{g} = -\bar{B}(N_\mathrm{g} - N_m)[f^{(1)}]^2 I(\omega) + \frac{N_m}{\bar{\tau}_{m\mathrm{g}}}. \tag{2.10}$$

Here $\bar{B}$ is the Einstein coefficient. In the steady state, for small population of the excited state and $N = N_\mathrm{g} + N_m$, the leading term for the population difference is

$$N_g - N_m \cong \frac{N}{1 + I(\omega)/I_{sat}(\omega)}. \tag{2.11}$$

Since the first of Eqs. (2.10) can be rewritten in terms of the linear absorption coefficient, this saturation intensity $I_{sat}(\omega)$ is defined in terms of $\bar{B}$ by

$$\frac{1}{I_{sat}(\omega)} = \frac{\bar{B}[f^{(1)}]^2}{\bar{\Gamma}_{mg}}\alpha_1(\omega) = \frac{k_{vac}}{2\hbar\omega n_x \hbar\varepsilon_0}[f^{(1)}]^3|\bar{\mu}_{mg}|^2\frac{1}{(\bar{\omega}_{mg}-\omega)^2 + \bar{\Gamma}_{mg}^2/4}. \tag{2.12}$$

Therefore for small values of $I(\omega)/I_{sat}(\omega)$

$$\chi^{(1)}_{xx,eff}(-\omega;\omega) = \frac{N}{\hbar\varepsilon_0}f^{(1)}|\bar{\mu}_{mg}|^2\frac{\bar{\omega}_{mg}-\omega+i\bar{\Gamma}_{mg}/2}{(\bar{\omega}_{mg}-\omega)^2 + \bar{\Gamma}_{mg}^2/4}\{1 - I(\omega)/I_{sat}(\omega)\}, \tag{2.13}$$

which now contains an intensity-dependent contribution of a form similar to $\Delta n = n_{2,el} I$.

For input intensities approaching $I_{sat}(\omega)$, the linear susceptibility (and hence the contribution to the refractive index) is reduced, i.e., the oscillator strength of the transition is bleached out. The nonlinear term ($\propto I$) is written as $\chi^{(3)}_{sat}(-\omega;\omega,-\omega,\omega)$ with a real part $\chi^{(3)}_{\Re,sat}(-\omega;\omega,-\omega,\omega)$, which gives

$$n_{2,sat} = \frac{\chi^{(3)}_{\Re,eff}(-\omega;\omega,-\omega,\omega)}{4n_x^2\varepsilon_0 c} = -\frac{N}{16n_x^2\varepsilon_0^2 c\hbar^3}[f^{(1)}]^4|\bar{\mu}_{mg}|^4\frac{\bar{\omega}_{mg}-\omega}{[(\bar{\omega}_{mg}-\omega)^2 + \bar{\Gamma}_{mg}^2/4]^2}. \tag{2.14a}$$

And the corresponding contribution to the nonlinear absorption is

$$\alpha_{2,sat} = -\frac{Nk_{vac}}{8n_x^2\hbar^3\varepsilon_0^2 c}[f^{(1)}]^4|\bar{\mu}_{mg}|^4\frac{\bar{\Gamma}_{mg}}{[(\bar{\omega}_{mg}-\omega)^2 + \bar{\Gamma}_{mg}^2/4]^2} \tag{2.14b}$$

Thus the saturation effect always leads to absorption that decreases with increasing intensity. As a result, this effect is sometimes called "bleaching" of the state. For an example in which both $\alpha_{2,sat}$ and $\alpha_{2,el}$ occur, see [5]. This effective nonlinearity proportional to $|\bar{\mu}_{mg}|^4$ is sometimes (mistakenly) identified as the one-photon resonant component of the electronic nonlinearity given by Eq. (2.6a). In fact it is a component of the Kerr nonlinearity with $n_{2,Kerr} = n_{2,el} + n_{2,sat}$.

It is interesting to compare this contribution near resonance for a fictitious molecule with zero permanent dipole moments and only one dominant electric dipole transition. (This corresponds to a symmetric molecule for which a single, large electric dipole transition may not be realistic.) The result is shown in Fig. 2(a). Clearly $n_{2,sat}$ is an important ($\sim 25\%$) contribution to $n_{2,Kerr}$ near the one-photon resonance. Its relative contribution decreases with increasing frequency. Note that although it is not strictly valid to extend Eq. (2.14a) too far from resonance and certainly not to the zero-frequency limit, since other considerations about radiative loss from virtual states would have to be included, such an extrapolation shows a contribution of only $\cong 2\%$ in the nonresonant limit.

Figure 4

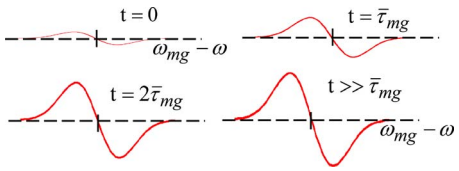

Recovery of the dispersion in the refractive index induced by the saturation effect after an optical field is turned off at $t=0$.

These contributions due to the terms $n_{2,\mathrm{el}}$ and $n_{2,\mathrm{sat}}$ can be differentiated from each other. The first way is by turning off the optical field abruptly (turn-off time $\Delta t \ll \bar{\tau}_{mg}$) and observing the return of the refractive index to its zero-intensity value. For the electronic case, the return is instantaneous for a detuning from resonance $\Delta\omega \gg \bar{\Gamma}_{mg}$, which involves virtual states, whereas the return due to the saturation effect takes place over the time scale of $\bar{\tau}_{mg}$, since it involves real population of the excited state, as shown in Fig. 4.

There are a variety of other examples similar to the one just discussed where index changes are produced by the redistribution of population densities via absorption, both linear and nonlinear absorption. The index changes occur both through the reduction of oscillator strength caused by saturation as discussed above, but also through the production of new absorbers. They will be discussed in Subsection 2.6 below. The signs of the respective refraction changes depend on the frequency position relative the absorption resonances.

2.3. Summary of the Two-Level Model

Although the above results are based on a simple two-level model and the assumption that there is only one contribution to the excited state lifetime that corresponds to homogeneous broadening, some useful conclusions can be made that are useful for more general cases.

1. Although there are resonant enhancements in the denominator of the expressions for n_2 and α_2 near the one- and two-photon (and multiphoton in the general case) resonances, this does not necessarily mean that enhancement actually occurs, because the numerators may vanish or be very small. For example, cancellation effects make the contributions of the $|\bar{\mu}_{10}|^2(\bar{\mu}_{11}-\bar{\mu}_{00})^2$ terms to $n_{2,\mathrm{el}}$ and $\alpha_{2,\mathrm{el}}$ negligible relative to the $|\bar{\mu}_{10}|^4$ term, which has a $[(\bar{\omega}_{10}-\omega)^2+(\bar{\Gamma}_{10}/2)^2]^{-3}$ term near the one-photon resonance.
2. An intensity-dependent change in the refractive index is always accompanied by a nonlinear change in the absorption.
3. The magnitude and dispersion of the one-photon resonant change in the index and absorption is negligible compared with the magnitude and dispersion in the linear refractive index and absorption, which occurs at exactly the same frequency and over the same spectral width. However, the 2PA occurs in a frequency region far from the dominant one-photon absorption (1PA) spectrum, it is resonantly enhanced and can be measured and used.
4. Intensity-induced population changes between the ground state and the excited state(s) produce significant contributions to the nonlinear index and ab-

sorption near the one-photon resonance. However, their relative contribution decreases with increasing $|\omega_{10}-\omega|$, and their contributions are negligible in the zero-frequency limit.

5. Off resonance the sign of the nonlinearity depends on the relative magnitudes of the contributions due to $|\bar{\mu}_{10}|^2(\bar{\mu}_{11}-\bar{\mu}_{00})^2$ and $|\bar{\mu}_{10}|^4$, and these contributions depend strongly on frequency. In contrast to the on-resonance case where one term dominates, the contributions of the different terms become comparable. If the molecule is symmetric (no permanent dipole moments), the nonlinearity is negative unless contributions from other states are included.

6. The nonlinear index coefficient approaches a constant value with decreasing frequency in the nonresonant limit, whereas the absorption change dies of as ω^2. Here all of the terms (except for the saturation) contribute equally to $n_{2,\mathrm{Kerr}}$.

Frequently third-harmonic generation, which depends on $|\chi^{(3)}(-3\omega;\omega,\omega,\omega)|^2$, is used to estimate the nonlinear refractive index coefficient given by Eq. (2.5a). In the *nonresonant limit* $\chi^{(3)}_{\Re,xxxx}(-3\omega;\omega,\omega,\omega)=\chi^{(3)}_{\Re,xxxx}(-\omega;\omega,-\omega,\omega)=\chi^{(3)}_{\Re,xxxx}\times(-\omega;\omega,\omega,-\omega)=\chi^{(3)}_{\Re,xxxx}(-\omega;-\omega,\omega,\omega)$, which makes this a valid procedure in that limit. However, in general for symmetric molecules

$$\chi^{(3)}_{xxxx}(-3\omega;\omega,\omega,\omega) = -\frac{N}{\varepsilon_0\hbar^3}f^{(3)}|\bar{\mu}_{10}|^4\left\{\frac{4\bar{\omega}_{10}+i\bar{\Gamma}_{10}\bar{\omega}_{10}/\omega}{[(|\bar{\omega}_{10}|^2-9\omega^2)-3i\omega\bar{\Gamma}_{10}][(|\bar{\omega}_{10}|^2-\omega^2)-i\omega\bar{\Gamma}_{10}]}\right\},$$

and it is clear that there is a different resonant structure for third-harmonic generation than for n_2 and α_2. Therefore in practice the input frequency must be chosen so that $3\omega\ll\omega_{10}$ for the two-level model, and in the more general case $3\omega\ll\omega_{\mathrm{mn}}$ for all transition frequencies ω_{mn}.

Listed in Table 1 are the measured n_2 and α_2 coefficients for a number of materials. Note that although the table contains the net n_2, which includes all of the contributions (some still to be discussed), these values (with the exception of nitrobenzene, which has a large rotational component) should be due mostly to the Kerr effect to within the accuracy of the measurements. There can be large differences ($\pm 50\%$) in reported values, depending on the measurement technique. The first comprehensive measurements for n_2 were reported by Adair *et al.* [6]. See Chase and Van Stryland [7] for extensive recent tabulations. Note that these values are either off-resonance or nonresonant, depending on the difference between the wavelengths of the absorption maxima and the measurement beams, and the spectral widths of the absorption features as discussed above. Furthermore, they may well contain small contributions from some of the other effects discussed here below.

From the simple two-level model results in Eqs. (2.6), (2.7a), (2.7b), (2.7c), (2.8), (2.10)–(2.13), (2.14a), and (2.14b), large n_2s can occur near one and two-photon resonances, i.e., when $\omega\cong\bar{\omega}_{10}$ or $2\omega\cong\bar{\omega}_{10}$, and when $|\bar{\mu}_{10}|^2$ is large and/or the difference between permanent dipole moments between the states, i.e., $(\bar{\mu}_{11}-\bar{\mu}_{00})^2$, is large, preferably both.

These conditions for large $\chi^{(3)}$ due to electronic transitions between *discrete* states are best satisfied in organic materials. To the nonchemist there seems to be a semi-infinite number of possible molecules for nonlinear optics. In fact, to date four special classes of organic materials were identified as promising and have received most of the attention: (1) linear or quasi-linear molecules and conjugated polymers with large π-electron delocalization lengths resulting in large

$|\bar{\mu}_{ng}|^2$ and/or $|\bar{\mu}_{mn}|^2$; (2) linear molecules with strong charge transfer groups, an electron donor at one end and an electron acceptor at the other end, with π-electron bridges between them, and hence large dipole moments and hyperpolarizabilities; (3) symmetric linear molecules with an electron acceptor group in the middle and an electron donor group at both ends, separated again by π-electron bridges, and (4) 3D molecules, with and without conjugation, such as porphyrines, phthalocyanines, and dendrimers. These properties can be molecularly engineered in many materials by judicious choices of chains of carbon bonds, which leads to electron delocalization along the chain. For detailed discussions, see *Nonlinear Optical Properties of Organic Molecules and Crystals*, volumes 1 and 2 [12]. Otherwise the values for n_2 in organic materials are typical of those found in Table 1.

2.4. Conjugated Molecules and Polymers

These systems are characterized by electron orbitals normally associated with the individual atoms becoming delocalized and extending over the whole molecule (polyenes) or even connected chains of molecules in the case of conjugated polymers. They were initially of interest in the field of electrical conductors, and much of the early development of these materials was focused on this application. Electrical conductivity rises by orders of magnitude when polyacetylenes are appropriately doped [13]. Interest in using such materials also for nonlinear optics was triggered by the seminal paper by Sauteret and co-workers [14] in which they reported large third-order nonlinearities from third-harmonic measurements at 1.89 and 2.62 μm in a number of conjugated polymers in their

Table 1. Representative Materials with Values of n_2 and α_2[a]

Material	E_g (eV)	$n_2 \times 10^{-15}$ (cm^2/W)				α^2 (cm/GW)		
		1064 nm	532 nm	355 nm	266 nm	532 nm	355 nm	266 nm
LiF	11.6	0.081	0.061	0.061	0.13	~0	~0	~0
MgF_2	11.3	0.057	0.057	0.066	0.15	~0	~0	~0
BaF_2	9.2	0.14	0.21	0.27	0.31	~0	~0	0.06
NaCl [6]	~8.7	1.8						
SiO_2	~7.8	0.21	0.22	0.24	0.78	~0	~0	0.05
MgO [6]	7.77	0.39						
Al_2O_3	7.3	0.31	0.33	0.37	0.60	~0	~0	0.09
BBO	6.2	0.29	0.55	0.36	0.003	~0	0.01	0.9
KBr	6.0	0.79	1.27			~0		
$CaCO_3$	5.9	0.29	0.29	0.37	1.2		0.018	0.8
$LiNbO_3$	3.9	0.91	8.3			0.38		
KTP	3.8	2.4	2.3			0.1		
ZnS [9]	3.66	6.3				3.4		
Te Glass	~3.6	1.7	9.0			0.62		
ZnSe [9]	2.67	29	−68			5.8		
ZnTe [10]	2.26	120				4.2		
CdTe [10]	1.44	−300				22		
GaAs [10]	1.42	−330				26		
RNglass [11]	~1.4	2.2						

[a]Ordered according to bandgap energy, E_g, or cutoff wavelength, taken from [8] except where noted. The values quoted were obtained by using multiple pulse widths in order to isolate the Kerr response. See the references for details. Blank cells indicate no measurement at this wavelength.

Figure 5

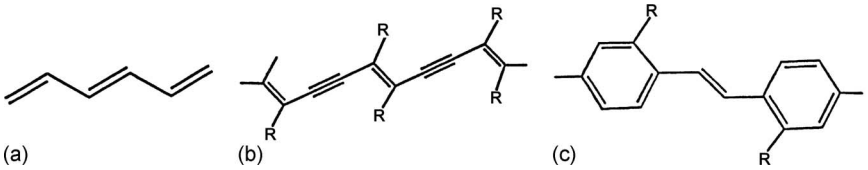

Structures of three generic types of conjugated polymers: (a) polyacetylene; (b) polydiacetylene, where R denotes PTS , 4BCMU, 3BCMU, etc; and (c) polyphenylvinelyne, where R denotes H, , alkyl, aryle, MEH etc.

resonant and near-resonant regimes. Specifically, for polydiacetylene [PTS, poly bis(*p*-toluene sulfonate) of they estimated $n_{2,\mathrm{Kerr}} = 1.8 \times 10^{-12}$ cm^2/W.

Based on carbon chemistry, there are three basic conjugated polymer types that are shown schematically in Fig. 5. In their pure form, they exhibit dominant absorption maxima (sometimes called exciton lines) in the 500–900 nm range with typically the longer the peak absorption wavelength, the more effective the conjugation. Of these three classes, namely, polyacetylenes, polydiacetylenes, and polyphenylvinylenes, in general it has not been possible to make optical-quality materials from their pure forms, and it has been necessary to add side groups to achieve solubility in solvents etc. In this way, polydiacetylenes and polyphenylvinylenes have been made suitable for optical applications. The backbone chains still dominate the molecular nonlinearity, which in the first approximation is independent of these side groups, although it does reduce the n_2 by the fractional extra volume due to the side groups; i.e., N is reduced.

Conjugated molecules are a result of the delocalization of the $2p_z$ orbitals associated with carbon atoms into π orbitals, which extend over the whole molecule as shown in Fig. 6 for the acetylene molecule. Consequently the electrons associated with the initial $2p_z$ orbitals can easily be displaced relatively large distances in the π orbitals, leading to enhanced polarizabilities along the carbon–carbon bonds. Furthermore, since the potential wells associated with these delocalized molecular orbitals are relatively shallow, they are strongly nonparabolic and are easily distorted by electric fields, leading to strong nonlinearities.

The prototypical molecules, which can be polymerized via heat or γ-ray illumination into conjugated polymer, are shown in Fig. 5 [15]. For acetylenes, R′—C═C—C═C—R, and diacetylenes,

$$\mathrm{R}' - \mathrm{C} = \mathrm{C} - \mathrm{C} \equiv \mathrm{C} - \mathrm{C} = \mathrm{C} - \mathrm{R},$$

the bonds shown as double and triple are the ones that delocalize; i.e., they share their bond character with the single bonds. R′ and R are end groups that terminate the molecule. In the liquid state, these quasi-linear molecules are randomly oriented, thus reducing the net nonlinearities to 1/5 of the value along the chain. These molecules can in some cases be polymerized to form amorphous media, in which case the orientations are essentially random, or thin films deposited on specially prepared surfaces for which some degree of alignment is also possible. Some molecules (unfortunately very few) can be polymerized into optical-quality single crystals so that the full nonlinearity can be obtained for one polarization. On polymerization, the bonds to the end groups are broken and multiple units are joined together, producing a polymer, an example of which (polydi-

Figure 6

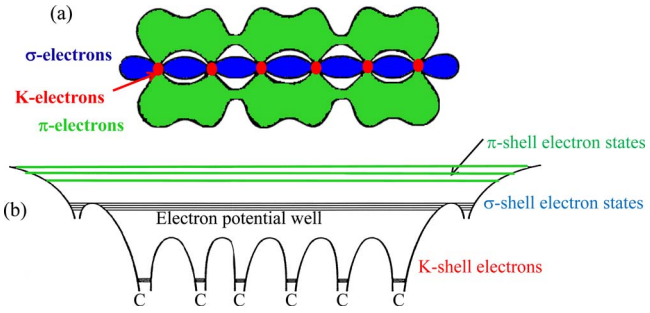

(a) Typical electron distribution in acetylene molecule. The π-shell electron states (originating from carbon atomic $p=2$ states), the σ-shell electron states originate from the carbon atomic $s=2$ states, and the tightly bound K electrons come from the atomic $s=1$ states. (b) Molecular potential well for the electrons.

acetylene PTS) is shown in Fig. 7. Note that the end groups R and R′ actually serve two functions, the coupling between the carbon–carbon chains in the crystal and also used to make the molecules soluble for crystallization from solution. Although the polymer chain may be hundreds or thousands of units long, in practice the electron coherence length (effective electron delocalization distance, important to nonlinear optics) is usually limited to at most a few tens of repeat units.

Pure *trans*-acetylene has been measured via third-harmonic generation to exhibit large third-order nonlinearities in the resonant and near resonant regimes [16,17]. However, it is not readily soluble and has not found application in nonlinear optics. Henceforth the polydiacetylenes (like PTS) and the polyphenylvinylenes [like MEH-PPV, (poly2-methoxy-5-(2′-ethylhexyloxy)-1,4- phenylenevinylene)] will be used as illustrative examples in the nonlinear optics domain.

The backbone chain (characterized by delocalized π electrons due to carbon–carbon bonds) responsible for the large nonlinearity has no permanent dipole moments in either its ground or excited states because of the linear symmetry. Furthermore, the linear symmetry means that the electronic states are either

Figure 7

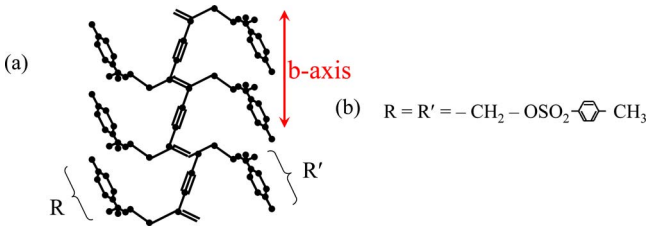

(a) Crystal structure of the polymer diacetylene PTS [poly bis(p-toluene sulfonate) of 2,4-hexadiyne-1,6-diol]. The large n_2 occurs along the b axis of the crystal. (b) End groups R and R′ (of the diacetylene molecule now link the adjacent polymer strands in the crystal lattice [22].

symmetric (gerade) or antisymmetric (ungerade). For allowed electric dipole transitions, the initial and final states must have different symmetries. It turns out that in this class of materials it is necessary for nonlinear optics to consider three states, two of which have even symmetry and one that has odd symmetry [18]. In both polydiacetylenes and polyphenylvinylenes, there are strong dipole allowed transitions from the even symmetry (gerade) ground state to the first odd symmetry (ungerade) excited state $1B_u$ (transition moment labeled $|\bar{\mu}_{10}|$), and from this excited state to a higher-lying even symmetry state mA_g ($|\bar{\mu}_{21}|$). For nondelocalized or only weakly localized molecules, the ordering of the electronic states in energy normally mirrors that of particles in a square well potential, alternating between gerade and ungerade. The electron correlation effects are sufficiently strong in these conjugated polymers that the first even symmetry ($1A_g$) excited state frequently lies below $1B_u$, but the dipole allowed transition moment between these two states is small and usually neglected [19,20]. The locations of the $1B_u$ and mA_g ($\equiv 3A_g$) states are measured from the linear and 2PA spectra. An example of each is shown in Figs. 8 and 9 for single-crystal polydiacetylene PTS [21,22]. Note that in both cases the existence of transitions within the vibrational subbands located to the high-energy side of the main peak arise because of the strong coupling to the vibrations of the main polymer chain [23,24]. The 1PA and 2PA spectra found in PPV-MEH also are broadened owing to vibrational subbands [24,25].

Based on the above discussion a minimum three-level model with $\bar{\mu}_{ii}=0$ (no permanent dipole moments in the three important states) is needed to describe the third-order nonlinearity in conjugated polymers. Furthermore, the decay from the even symmetry excited state mA_g is down to the $1B_u$ state, i.e., only $\bar{\tau}_{12}\neq 0$ and $\bar{\tau}_{10}\neq 0$. In the off-resonance regime

$$n_{2,\mathrm{Kerr}}=\frac{Nf^{(3)}|\bar{\mu}_{10}|^2}{n_x^2\varepsilon_0^2c\hbar^3(\bar{\omega}_{10}^2-\omega^2)^2}\left\{|\bar{\mu}_{21}|^2\left[\frac{\bar{\omega}_{20}(\bar{\omega}_{10}^2+\omega^2)+4\bar{\omega}_{10}\omega^2}{(\bar{\omega}_{20}^2-4\omega^2)}+2\frac{\bar{\omega}_{10}^2}{\bar{\omega}_{20}}\right]\right.$$
$$\left.-|\bar{\mu}_{10}|^2\left[\frac{\bar{\omega}_{10}}{(\bar{\omega}_{10}^2-\omega^2)}(3\bar{\omega}_{10}^2+\omega^2)+\frac{(\omega_{10}+\omega)^2}{16(\bar{\omega}_{10}-\omega)}\right]\right\}, \qquad (2.15a)$$

and for the nonresonant case

Figure 8

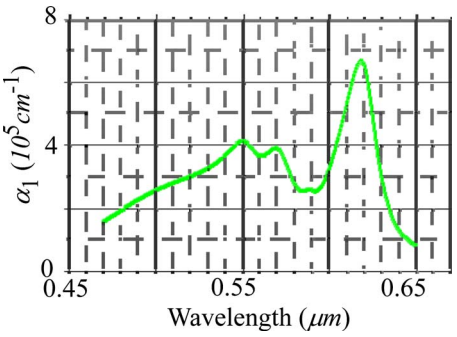

Linear absorption spectrum of the crystal polymer diacetylene PTS [22].

Figure 9

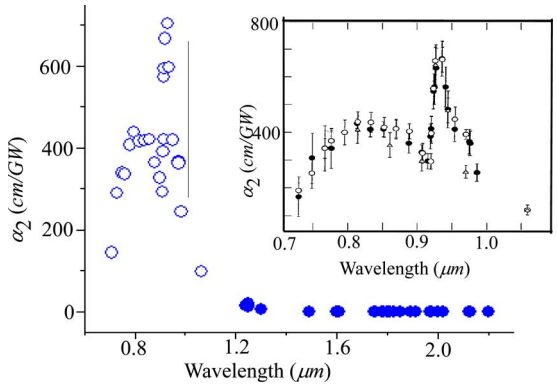

2PA spectrum (100 fs pulses) of the crystal polymer diacetylene PTS. Inset, details of the main two-photon spectrum measured with 100 fs, 2 ps, and 60 ps pulses [21,22].

$$n_{2,\mathrm{Kerr}} = 3\frac{Nf^{(3)}|\bar{\mu}_{10}|^2}{n_x^2\varepsilon_0^2 c\hbar^3\bar{\omega}_{10}^3}\left\{\frac{\bar{\omega}_{10}}{\bar{\omega}_{20}}|\bar{\mu}_{21}|^2 - \frac{49}{48}|\bar{\mu}_{10}|^2\right\}. \tag{2.15b}$$

Note that the interference between the ground to first excited state transition ($|\bar{\mu}_{10}|^2$) and the first antisymmetric to the higher-lying symmetric excited state transition ($|\bar{\mu}_{21}|^2$) in such conjugated systems can be actually detrimental to obtaining large nonresonant nonlinearities! Furthermore, since the two terms have both different signs and different frequency dispersion, the net sign of n_2 can depend strongly on frequency. This is illustrated in Fig. 10, which shows calculations of the frequency dispersion of n_2 typical of polydiacetylenes and squaraines (discussed below). As predicted by Eqs. (2.15a) and (2.15b), the sign of the nonlinearity can change with photon frequency depending on the relative magnitude of $|\bar{\mu}_{21}|^2/|\bar{\mu}_{10}|^2$.

Figure 10

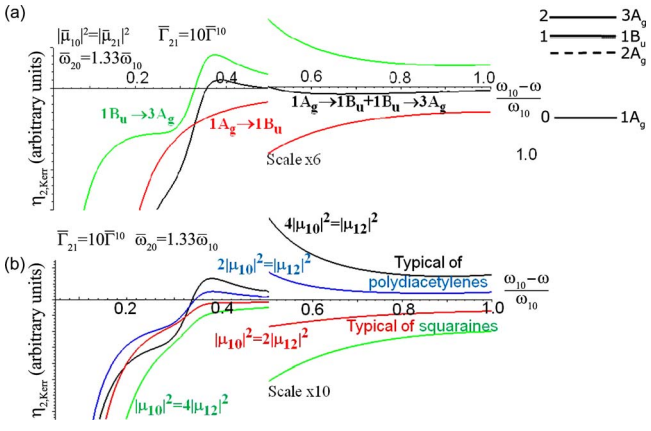

Frequency dispersion of $n_{2,\mathrm{Kerr}}$ for $\bar{\Gamma}_{21}=10\bar{\Gamma}_{10}$, $\omega_{20}=1.33\bar{\omega}_{10}$, and different relative values of $|\mu_{12}|^2/|\mu_{10}|^2$. (a) For $|\bar{\mu}_{10}|^2=|\bar{\mu}_{21}|^2$, the contributions due to $|\bar{\mu}_{10}|^2$ (red curve), $|\bar{\mu}_{21}|^2$ (green curve) and the sum of the two (black curve) are shown. (b) Sum of the contributions for different relative values of the transition dipole moments.

In polydiacetylenes the sign of n_2 is negative between the one- and two-photon resonances, becomes positive near the two-photon resonance, and generally remains positive all the way to zero frequency (nonresonant case). In contrast to this behavior, the nonlinearity in squaraines, which have weaker two-photon transition strength, remains negative over the full range $\bar{\omega}_{10} > \omega > 0$.

Many of the parameters such as $\bar{\omega}_{10}$, $\bar{\omega}_{20}$, $|\bar{\mu}_{10}|^2$, and $|\bar{\mu}_{21}|^2$, that are needed to evaluate n_2 depend on the lengths, distribution, and orientation of the conjugation chains, and these in turn depend weakly on the details of the R and R′ groups, but strongly on the preparation techniques, temperature, and density of defects. An example of the variation in the linear absorption spectrum and its effect on the nonlinearity is shown in Fig. 11 for PPV [26]. Another example is the polydiacetylene 4BCMU, which comes in blue, yellow, and red forms that are due to different molecular conformations possible with absorption maxima in the spectral regions for which they are named [27]. Dependences of the same factors on the even symmetry state properties are just not known. Furthermore, the propagation loss is known to be very sensitive to preparation technique, for example [28,29].

Figure 11

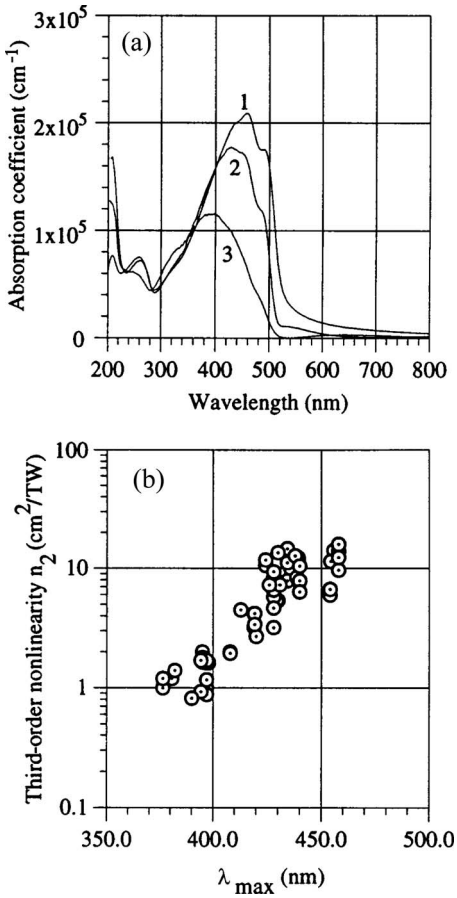

(a) Examples of absorption spectra for PPV prepared from precursors synthesized with sodium hydroxide base and water solvent (curve 1), organic base and 20% water, 80% methanol solvent (curve 2), and organic base and methanol solvent (curve 3). (b) Variation of the third-order nonlinearity of PPV as a function of the wavelength for maximum absorption λ_{max} [26].

Although in principle independent measurements of all of the above parameters are possible, there is an additional complication that is the main reason why a "near- and on-resonance" formula is not given here. In conjugated polymers, clearly a significant fraction of the oscillator strength occurs in transitions that occur at energies higher than the peak of the absorption involving the vibrational sidebands, and detailed theoretical treatments of such problems for calculating n_2 are not available.

Some of the best single-crystal polymers grown to date have been polydiacetylenes, of which PTS is the most thoroughly investigated [30]. The PTS crystal structure was shown in Fig. 7. It is characterized by large transition dipole moments, multiple debye, for the dominant transitions from the symmetric ground state to the first antisymmetric $(1A_g \rightarrow 1B_u)$ excited state and from this excited state to the second symmetric excited state $(1B_u \rightarrow 2A_g)$ [31]. The decay times from these excited states are in the few picosecond to ~100 fs range for $\bar{\tau}_{10}$ and $\bar{\tau}_{21}$, respectively [32].

There are too many reports of the nonlinearity in such polydiacetylene materials, primarily in the on- and near-resonant regime, to be summarized here: using a variety of techniques they collectively confirmed that the nonlinearities are indeed very large in the near-resonant and nonresonant regimes, where the 1PA and 2PA is also large. (Some examples are given in [33–36].) It is generally accepted that $n_2 < 0$ in the region between the 1PA and 2PA peaks, partially due to bleaching of the one-photon $(1A_g \rightarrow 1B_u)$ transition; see Fig. 12(a). This has been confirmed by both Z scan and the negative absorption change associated with bleaching of the 1PA there [5,21]. However, in the off-resonant regime, specifically at 1064 nm, some controversy exists about the sign of n_2, although the magnitude in the range $[5-10]\times 10^{-12}$ cm^2/W appears consistent [37,38]. This difference could be due to the different fabrication techniques used resulting in different values of dipole transition moments. In this region the nonlinear absorption change is positive. For example, see Fig. 13 [5]. The dispersion with increasing wavelength as shown in Fig. 12(b) indicates that indeed $\bar{\omega}_{10}|\bar{\mu}_{21}|^2 > \bar{\omega}_{20}|\bar{\mu}_{10}|^2$ and that the nonresonant value is positive (Fig. 11) at least for the sample studied, in agreement with calculations of transition dipole moments in polyenes [31].

Figure 12

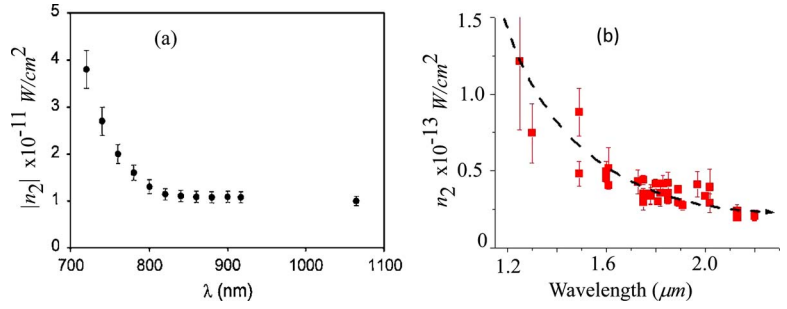

(a) Wavelength dispersion in $|n_2|$ over the range 0.72–1.06 μm measured by spectral broadening due to self-phase modulation in a sample made by the shear technique [22,36]. (b) Wavelength dispersion in n_2 over the range 1.2–2.2 μm measured by Z scan for hundreds of micrometers thick platelets of single-crystal polymer diacetylene PTS made by crystallization from solution. The dashed curve is a guide to the eye.

Figure 13

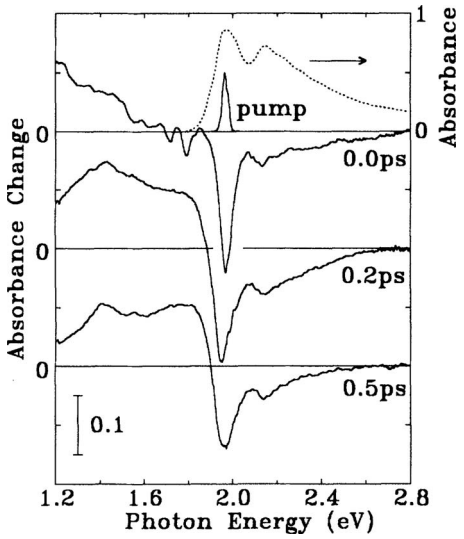

Absorption change induced by an intense pump pulse as measured in the polydiacetylene 3 BCMU by a probe pulse for three different delay times between the probe and the pump. The negative absorption change is due to the dominance of bleaching of the $1A_g \rightarrow 1B_u$ transition whose peak is located at 620 nm. At lower photon energies, interference with the two-photon transition $1A_g \rightarrow 2A_g$ with a peak located at 930 nm occurs, and after 660 nm the 2PA term dominates. These results also show that the decay time from $1B_u$ to the ground state is $\sim$1 ps [5].

In contrast to the conjugated polymers polyacetylene and polydiacetylene, which contain only carbon in their backbone chain, the main backbone chain of phenylenevinylene contains phenyl (benzene) rings as well as linear carbon–carbon bonds. Note that although the phenyls have double carbon bonds from which electrons can be delocalized, the benzene structure does not appear to lead to delocalization that is as effective as in the polyacetylenes and diacetyelenes. The PPV absorption maxima occur at shorter wavelengths than those of polydiacetylenes and polyacetylenes ($\cong$450 nm versus 620 and 650 nm, respectively). To improve the solubility and reduce the defects in PPV, side groups like MEH, i.e., to make MEH-PPV, are added. Thin film samples of both random and highly oriented forms have been fabricated and characterized for optical studies [39,40]. The details of the fabrication determine the optical losses that can be minimized to be as low as 0.1 dB/cm, orders of magnitude lower than in pristine PPV, as shown in Fig. 14.

There have been a number of nonlinear optical studies of PPVs. There is a strong 2PA maximum along with vibrational subbands for incident radiation at $\sim\bar{\omega}_{20}/2$ as shown in Fig. 15. Detailed measurements of n_2 have been reported around 800 nm by the Australian National University group for a number of PPV-related materials [41], and the wavelength dispersion at longer wavelengths of PPV-MEH by Chris Bubeck and collaborators at Max Planck Mainz [29]. Of particular interest is the dispersion (Fig. 15), which clearly shows a change of sign of the nonlinearity with increasing wavelength, as might be expected from Eqs. (2.15a) and (2.15b), similar to the results in polydiacetylene PTS.

Listed in Table 2 are values of n_2 and α_2 for a number of conjugated polymers

Figure 14

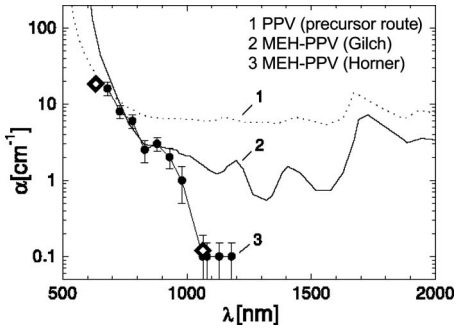

Comparison of residual absorption of PPV and MEH-PPV [29].

and the measurement technique used. The values are much larger than those found in normal dielectric media. More complete listings of n_2 at $\lambda = 0.8\ \mu$m can be found in [41]. Structures are shown in Fig.16.

The nonlinearity n_2 of 30–100 nm sized nanocrystallites of polydiacetylene in solution has been investigated by Nakanishi and co-workers [46]. The results were corrected for the random crystallite orientation and its concentration in solution. Although the magnitude and sign of n_2 was of the same order as that in bulk crystals, a number of quantum effects were clear in their measurements. Namely, the absorption peak was shifted to longer wavelengths, the spectrum of the vibronic sidebands on the low-wavelength side of the absorption peak changed in structure, and n_2 did depend on the crystal size.

The effect of metallic coating of polydiacetylene [with $R_1=(CH_2)_{11}CH_3$ and $R_2=(CH_2)_8COOH$] was evaluated in [47]. After polymerization via γ irradiation,

Figure 15

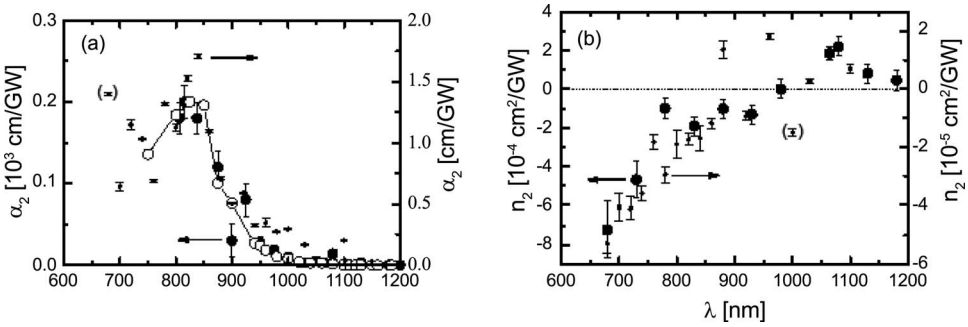

Nonlinear optical spectra of MEH-PPV measured at the laser wavelength λ. (a) Comparison of data of α_2 from nonlinear prism coupling (films, filled large dots, left-hand scale), from two-photon excitation spectra of fluorescence (solutions, open circles, arbitrary units scaled to the peak of film data, error bars are smaller than symbol size), and from Z scan (solution, small dots, right-hand scale). (b) Dispersion of n_2 from nonlinear prism coupling (films, filled large dots, left-hand scale), and Z scan (solution, small dots, right-hand scale). See [29] for details.

Table 2. Kerr and Nonlinear Absorption (Where Available) Coefficients for a Selection of Conjugated Polymers in Thin Film Form

Material	$n_2 \times 10^{-12}$ (cm^2/W)	α_2 (cm/GW)	λ (μm)	Measurement Technique
PPV [26]	$\lvert n_2 \rvert = 1-10$	[a]80	0.8	D4WM[b]
2,5-Dimethoxy *p*-PPV [42]	$\lvert n_2 \rvert = 4$		0.8	D4WM
2,5-Dimethoxy *p*-PPV [41]	$n_2 = -4$	25–80	0.8	Kerr gate
MEH-PPV [43]	$n_2 = -3$	180	0.5	Z scan
PPV-AC8H [41]	$n_2 = -1.1$	40	0.8	Z scan
DBSA-PANI [45]	$n_2 = -1.7$	42	1.054	Z scan
Polydiacetylene 4BCMU [44]	$n_2 = 0.05$	<0.25	1.31	Mach–Zehnder

[a]Measured by power-dependent transmission.
[b]Degenerate four-wave mixing.

the absorption spectrum resembled that of bulk polydiacetylenes. An enhancement due to the silver coating of $\sim \times 2$ was measured for n_2 at 532 nm.

2.5. Charge Transfer Molecules

The generic form for charge transfer molecules (also called chromophores) is shown in Fig. 17(a) [12]. For detailed discussion see, for example, [12]. As indicated in the cartoons in Fig. 17(b), the end groups have contrastingly different properties. The donor (D) groups, for example $N(CH_3)_2$, OCH_3, H_2N have loosely bound electrons. At the other end, there is an acceptor (A) group, for example NO_2, CN, etc., which easily accommodates additional electrons. The intermediate bridge group should facilitate the transfer of electrons between the two end groups. This is usually achieved by a structure for which $2p_z$ electrons are partially delocalized, such as a single or multiple benzene ring(s), or a sequence of single–double carbon bonds as discussed above. As indicated in Figs. 17(b) and 17(c), there is a partial transfer of charge from the donor to the acceptor groups, resulting in a permanent dipole moment in the ground (and excited)

Figure 16

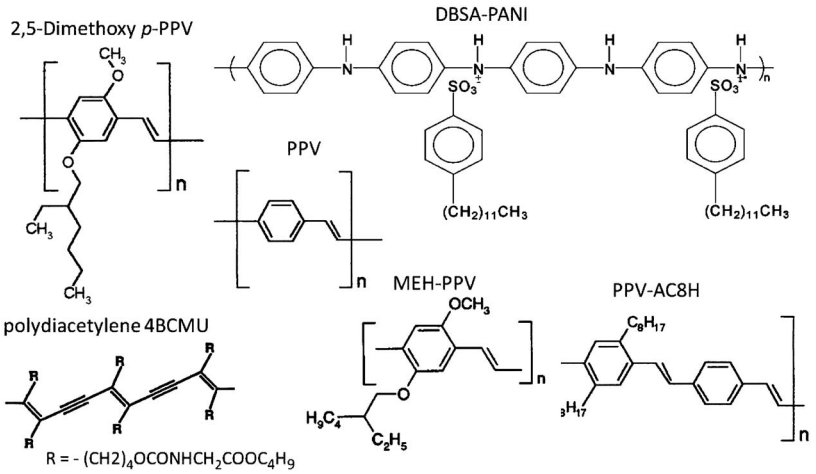

Structures for conjugated polymers of Table 2.

Figure 17

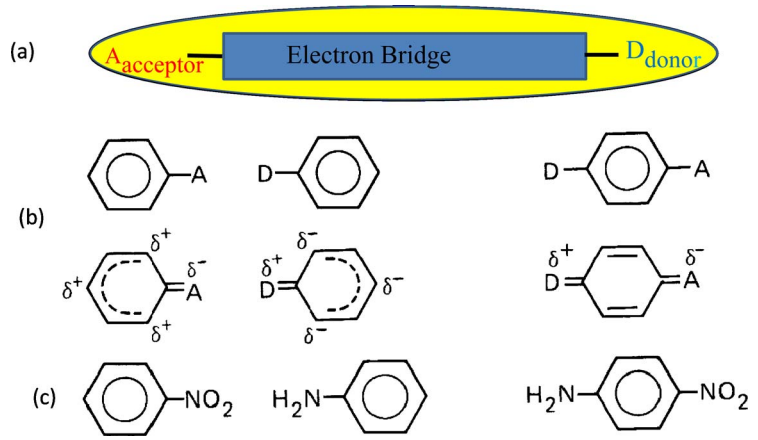

(a) Prototype charge transfer molecule with an electron acceptor group on one end, a donor group on the other end, separated by a bridge. (b) Change in charge distributions introduced by an electron acceptor group A, an electron donor group D, and both A and D. (c) The charge transfer molecule nitroaniline [12].

state(s). An example for which there are both large dipole moments as well as a reversal of their signs is shown in Fig. 18 [48]. In such molecules it is typical that their nonlinearity is dominated by the ground and first excited states; i.e., a two-level model is a reasonable approximation, i.e., in the nonresonant limit $n_{2,\mathrm{el}} \propto |\bar{\mu}_{10}|^2(\bar{\mu}_{11}-\bar{\mu}_{00})^2-|\bar{\mu}_{10}|^4$. The nonlinearity $n_{2,\mathrm{el}}$ can be dominated by the permanent dipole moments for large values of $(\bar{\mu}_{11}-\bar{\mu}_{00})^2$. An example is shown in Fig. 19 [49].

Typically, quantum chemical calculations (AM1, Austin Model 1) are needed to evaluate the molecular parameters as well as the molecular nonlinearities in such systems [50]. Such calculations have shown that the nonlinearity is linked to the degree of charge transfer from the donor to the acceptor, which is related to the

Figure 18

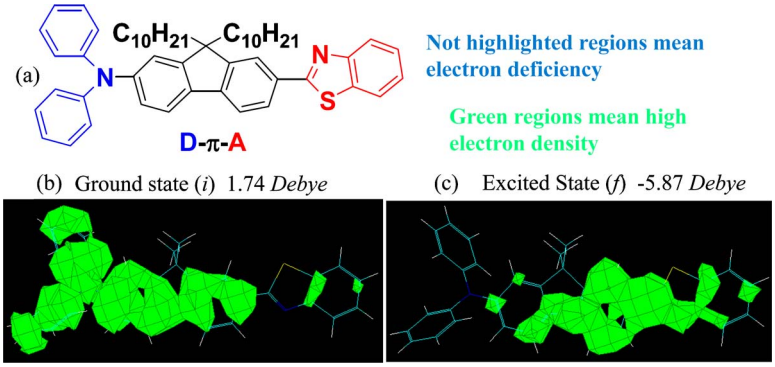

(a) Chromophore structure (KJS-1) with strong charge transfer properties. (b) Electron distribution in the ground state. (c) Electron distribution in the first excited state. Permanent dipole moments have different signs in the two states [48]!

Figure 19

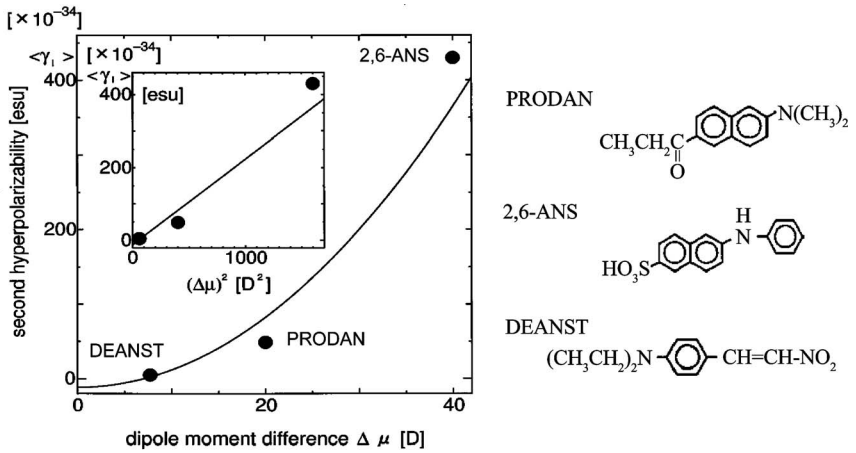

Plot of the molecular second hyperpolarizability $\langle \bar{\gamma}^{(3)} \rangle$ (averaged over all orientations) on permanent electric dipole-moment difference between excited and ground states $\Delta\mu$ for three charge transfer molecules [49]. DEANST, 4-(*N*,*N*-diethylamino)-β-nitrostyrene; 2,6-ANS, 2-anilinonaphthalene-6-sulfonic acid; PRODAN, 6-propionyl-2-dimethylamino naphthalene.

bond-length alternation (the average difference in length between single and double bonds in the molecule due to the charge transfer from the D to the A group). This led to a simple physical two-level model based on a linear combination of the two extreme (resonance) structures, the cyanine limit (called the valence bond configuration, VB) in which no electron transfer occurs and the zwitterionic limit (called the charge transfer configuration, CT) in which the maximum electron transfer occurs [51–53]. These limiting resonance structures have different single–double carbon bond linkage structures. Assuming a two-level model, which frequently is adequate for charge transfer molecules, the structure for a specific molecule is assumed to be a linear combination of the valence and charge transfer bond configurations. Writing Ψ_{VB} and Ψ_{CT} as the wave function of the two limiting configurations, the corresponding ground state energy levels as E_{VB} and E_{CT}, and $-t$ as the interaction between the donor and acceptor gives a molecule's Hamiltonian as

$$H_0 = \begin{pmatrix} 0 & -t \\ -t & V \end{pmatrix}, \quad V = E_{CT} - E_{VB}, \quad -t = \langle \Psi_{VB} | \mathcal{H} | \Psi_{CT} \rangle. \tag{2.16}$$

The Schrödinger wave equation is then solved for the ground state and excited state wave functions Ψ_{gr} and Ψ_{ex} and energies E_{gr} and E_{ex}, respectively of the coupled system in terms of the fraction f of the charge transfer configuration in the ground state, i.e., $\Psi_{gr} = \sqrt{1-f}\Psi_{VB} + \sqrt{f}\Psi_{CT}$ and

$$E_{gr} = \frac{1}{2}[V - \sqrt{V^2 + 4t^2}], \quad E_{ex} = \frac{1}{2}[V + \sqrt{V^2 + 4t^2}],$$

$$f = \frac{E_{gr}^2}{t^2 + E_{gr}^2} = \frac{1}{2} - \frac{V}{2\sqrt{V^2 + 4t^2}}. \tag{2.17}$$

The problem now requires finding the change in the carbon bonding distances in

terms of the above parameters. This change involves an additional elastic energy with force constant k associated with the optical phonon with displacements along the charge transfer axis. Noting that $E_{VB}=0.5k(q-q_{VB}^0)^2$ and $E_{CT}=V_0+0.5k(q-q_{CT}^0)^2$, where the decoupled state energy E_{VB} has been set to 0, V_0 is the adiabatic energy difference between the ground and excited states (i.e., at their minimum energy value), q is the molecule's bond length due to the charge transfer, and q_{CT}^0 and q_{VB}^0 are the equilibrium bond lengths in the decoupled valence and charge transfer bond configurations, the ground state energy is now given by

$$E_{gr}=\frac{1}{2}\left[V_0+\frac{1}{2}k\{(q-q_{VB}^0)^2+(q-q_{CT}^0)^2\}-\sqrt{V^2+4t^2}\right]. \tag{2.18}$$

The ground state corresponds to the minimum energy of $E_{gr}(q)$, i.e., $dE_{gr}(q)/dq=0$, which yields [51]

$$\rightarrow q_{opt}=\frac{1}{2}(q_{VB}^0+q_{CT}^0)+\frac{1}{2}(q_{VB}^0-q_{CT}^0)\frac{V}{\sqrt{V^2+4t^2}}\Rightarrow f=\frac{q_{VB}^0-q_{opt}}{q_{VB}^0-q_{CT}^0}. \tag{2.19}$$

Now an optical field is introduced in order to find the optical response. $\mu_{CT}=Q|e|L_{DA}$ is defined as the dipole moment created in the charge transfer state, where Q is the maximum charge transferred over a distance L_{DA} and the dipole moment of the coupled ground state is given by $f\mu_{CT}$. The application of an electric field $\mathcal{E}$ polarized along the charge transfer axis leads to a perturbation Hamiltonian added to the original Hamiltonian so that

$$H=\begin{pmatrix}E_{VB} & -t\\ -t & E_{CT}-\mu_{CT}\mathcal{E}\end{pmatrix}\rightarrow V_{\mathcal{E}}=E_{CT}-E_{VB}-\mu_{CT}\mathcal{E}\rightarrow\frac{df}{d\mathcal{E}}=\frac{df}{dV}\frac{dV_{\mathcal{E}}}{d\mathcal{E}}=\frac{2t^2\mu_{CT}}{E_{gr}^3}. \tag{2.20}$$

In the preceding formulation, V is now replaced by $V_{\mathcal{E}}$, and the polarization induced along the charge transfer axis by the application of the field is $p(\mathcal{E})=-dE_{gr}/d\mathcal{E}$, which contains all the contributions, linear, quadratic, cubic, etc., in the field $\mathcal{E}$. The nonlinear polarizability $\bar{\gamma}^{(3)}$ is now given by

$$\bar{\gamma}_{xxxx}^{(3)}=\frac{1}{6}\frac{d^3p_x}{d\mathcal{E}^3}\bigg|_{\mathcal{E}=0}=-\mu_{CT}^4\frac{d^3f}{dV_{\mathcal{E}}^3}\bigg|_{\mathcal{E}=0}=\frac{4t^2\mu_{CT}^4[V^2-t^2]}{E_{gr}^7}. \tag{2.21}$$

More detail can be found in [51–53].

The plot of $\bar{\gamma}^{(3)}$ versus the charge transfer fraction f in Fig. 20(a) shows how this approach can be used to optimize the third-order susceptibility in charge transfer molecules [53]. Clearly $f=0.5$ produces the largest nonlinearity $|\bar{\gamma}^{(3)}|$. This formulation has been verified experimentally as shown in Fig. 20(b) for a family of triene compounds by using solvents with different polarity (which contribute an additional field component) and donor-acceptor groups [53]. Therefore proper molecular design (molecular engineering) can lead to large values for $\bar{\gamma}^{(3)}$.

Such molecules can be used in any number of pure forms which, depending on the operating temperature, are single crystals or neat liquids. They have also been dissolved in appropriate solvents and, as shown in Fig. 21, in solid-state polymers. The chromophores can be included as "guests" dissolved uniformly in a host polymer and are not chemically attached to the polymer. Alternatively, the

Figure 20

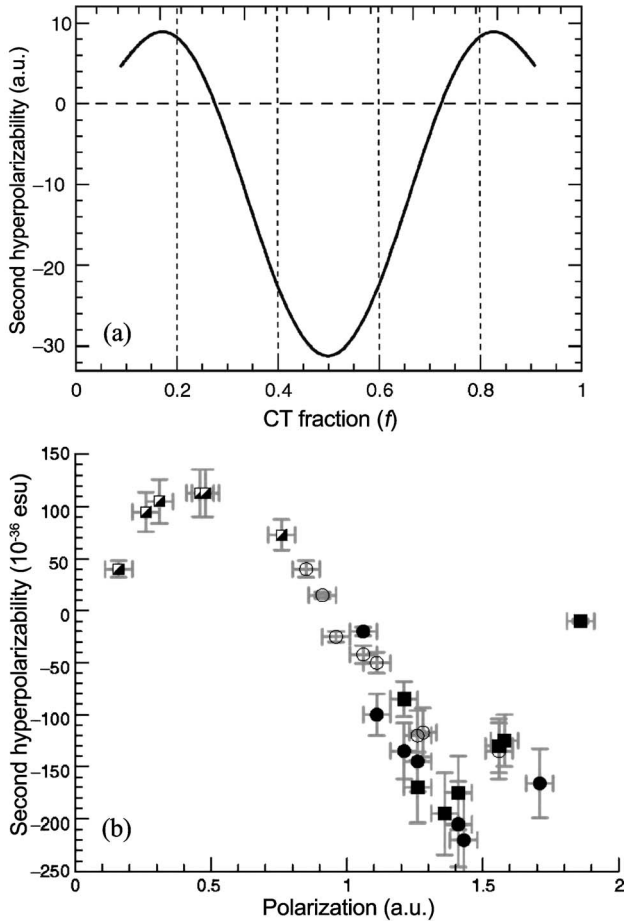

(a) Calculation of $\bar{\gamma}^{(3)}$ due to varying amounts of f, the fractional charge transfer from the donor D to the acceptor A. (b) Measurement of $\gamma^{(3)}$ by third-harmonic generation on the triene family of molecules in different solvents [53].

chromophores can be attached as pendants oriented more or less orthogonal to the main chain of the polymer by chemical bonding at one end of the molecule. It is also possible to bond (cross link) both ends of the chromophore to different or even the same polymer backbone chain (which can be folded) inside the polymer matrix. A fourth alternative is main chain attachment in which the chromophore is inserted (bonded) on both ends into the polymer backbone chain. The doping levels of the molecules into the polymers depend on the particular chromophore details, the host polymer and the form of attachment, increasing from 1%–30% for side-chain and guest–host systems to about in 50% doping in the main-chain and cross-linked cases. For random orientation of the molecules, the value of the *macroscopic* third-order susceptibility (and n_2) is reduced to about $1/5$ of the molecular value along the charge transfer axis. However, the technology for partially orienting the chromophores and forming the solid-state polymer solutions discussed here is very well developed because of the interest in using them for electro-optics applications [54,55]. Because the chromophores typically have large dipole moments in the ground state, electric field poling has been used to achieve some degree of alignment of the chromophores and hence

Figure 21

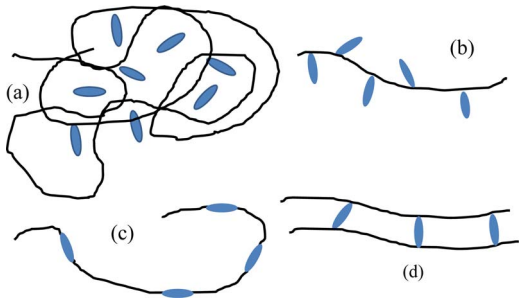

Different ways of including charge transfer molecules (chromophores) inside polymer matrices. (a) Guest–host system in which the molecules are dissolved in the polymer without bonding to it. (b) Chromophores bonded as pendants at one end to the polymer chain. (c) Charge transfer molecules bonded directly into the polymer chain. (d) Chromophores tethered at both ends either to the same polymer or to different polymers (case shown).

increase the net nonlinearity back toward its molecular value along the charge transfer axis.

Chromophore nonlinearities can also be accessed by dissolving them in compatible solvents, but of course with the 1/5 random orientation factor. Many of the suitable solvents tend to be polar, which can change the electron transfer characteristics of the chromophore dissolved in them and hence the nonlinearity. In fact, experimental verifications of the calculations shown in Fig. 20(b) were performed by using well-characterized solvents to change the electron transfer properties [53].

A word of caution is necessary when using bridge groups with double bonds such as carbon or nitrogen in the bridge group. Oxygen-induced photodegradation of the double bonds of the bridge when illuminated with light primarily in the visible or UV can lead to changes in chemical structure, drastically reducing the electron transfer properties of the bridge and hence the nonlinearity [56]. Pinhole-free encapsulation of the polymer is necessary for long-term stability.

Some representative values for large n_2 measured in polymers as well as in solution are given in Table 3. Structures are shown in Fig. 22. Clearly the values listed are higher than those in Table 1 for nonorganic dielectric media.

Table 3. Representative n_2 and α_2 (Where Available) Values for Some Randomly Oriented Charge Transfer Molecules

Material	$n_2\times10^{-14}$ (cm^2/W)	α_2 (cm/GW)	λ (μm)	Material	$n_2\times10^{-14}$ (cm^2/W)	α_2 (cm/GW)	λ (μm)
DANS[a][57]	+7	<1–2	1.06	DMSM[b][59]	16	<1	0.7
DAN2[a][57]	+20	<1–2	1.06	DEANST[c][59]	19	<1	0.7
MNA[d][58]	25		1.06				

[a] ~20% wt in PMMA.
[b] 20 wt. % in formamide.
[c] 30 wt. % in nitrobenzene.
[d] Extrapolated from measurements of 17% MNA in PMNMA.

Figure 22

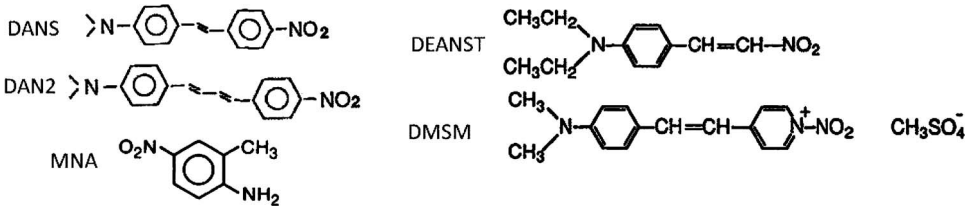

Structures for molecules in Table 3.

2.6. Miscellaneous Molecules

Symmetric squaraine dyes have exhibited large nonlinearities. They are essentially linear molecules that have identical donor groups at both ends of a D-A-D structure and hence have no permanent dipole moments. Their linear nature means that their ground and excited states have either even (A_g) or odd (B_u) symmetry, similar to that discussed previously for polyenes and conjugated polymers. Hence a three-level model of the type discussed previously for conjugated polymers is appropriate as a first approximation. Their absorption spectra, typically peaked in the 650–900 nm range, exhibit dipole transition moments >10 debye for the $1A_g \rightarrow 1B_u$ transition with very narrow linewidths and a transition dipole moment to the dominant two-photon state, i.e., $1B_u \rightarrow mA_g$, whose value is about one half of the $1A_g \rightarrow 1B_u$ value [60,61]. Equation (2.15a) and Fig. 10 predict a negative n_2 off-resonance and nonresonant value, and magnitudes in the $-5 \times 10^{-12} \rightarrow -10^{-14}$ cm^2/W range have been measured for 1500 nm > λ > 1064 nm [42,62–64]. Values for a few specific cases are given in Table 4. In most cases, significant 2PA was also found. Squaraine-based molecules have been successfully doped into polymer films and low-loss fibers [63].

Another family of molecules that have been of interest because of their large nonlinearities is the polymethines [65]. An example of the large nonlinearities available in the communications bands due to the electron delocalization along the acetylenelike bridging structure consisting of single and double carbon bonds is given in Table 4. Since the main absorption maxima occur around 1000 nm, the listed nonlinearities are off resonance, i.e., in the tails of the linear absorption spectra. Structures are shown in Fig. 23.

Table 4. Representative n_2 and α_2 (Where Available) Values for Miscellaneous Molecules[a]

Material	$n_2 \times 10^{-14}$ (cm^2/W)	λ (μm)	Material	$n_2 \times 10^{-14}$ (cm^2/W)	α_2 (cm/GW)	λ (μm)
(1 wt. %) ISQ	4.1 ($\lvert n_2 \rvert$) [63]	1.3	D-A-D squaraine	−80 [64]	46	1.3
([b]0.1 wt. %) ISQ	2.1($\lvert n_2 \rvert$) [62]	1.06	[c]Pyrole squaraine	−13 [140]		0.8
(1 wt. %) BSQ	8.8 ($\lvert n_2 \rvert$) [63]	1.3	Polymethine	−490 [65]	50	1.3
([b]2 wt. %) BSQ	20 ($\lvert n_2 \rvert$) [62]	1.06	Polymethine	−290 [65]		1.55
			[d](6.4 wt. %) SBAC	0.9 [59]	~0	0.8

[a]Random orientation of linear molecular axis.
[b]Percentage in PMMA fiber.
[c]Estimated from solution measurements in chloroform.
[d]SBAC dye in PMMA (a D-A-D structure) .

Finally, dendrimers have been of increasing interest for nonlinear optics [66]. They have proved useful as molecules for certain applications because of their ability to incorporate multiple functionalities needed, for example, for photorefractivity. For third-order nonlinear optics, specifically nonlinear absorption, they offer the possibility of broadband 2PA needed, for example, for optical limiting [67]. In fact limited cooperative effects have been observed in an experiment where the number of two-photon active species was doubled in a dendrimer, and a factor of 6 increase in the 2PA cross-section was measured [68]. Even though some large molecular nonlinearities $\sim\text{Real}\{\tilde{\gamma}^{(3)}\}$ have been reported, these dendrimers occupy much larger volumes than the molecules previously discussed here, and it is not clear whether the macroscopic $\chi^{(3)}$ will also be large. Goodson and colleagues have reported n_2 and α_2 measurements on the dendrimer CZD4NS2 (see Fig. 24) at a concentration of 3×10^{-3} mol/L in chloroform [69]. From their Z-scan data they calculated $n_2=-1.1\times10^{-13}$ cm^2/W and $\alpha_2=10^{-2}$ cm/GW at 800 nm. (The peak linear absorption occurs at 450 nm.) In addition they also observed higher-order nonlinear refraction effects. To check for cooperative effects potentially leading to an enhanced n_2 they measured the nonlinearities for both the nitroaminostilbene and carbazole functional groups (Fig. 24) alone. They found that the dendrimer nonlinearity was completely accounted for by the two nitroaminostilbene groups and that the carbazole had no effect on n_2. More experiments are clearly needed to truly assess the potential of dendrimers for enhanced n_2.

Here we have presented a very brief review of the origins and magnitude of n_2 in the two common organic material systems, namely, conjugated polymers and charge transfer molecules. More detailed information about the chemistry etc. can be found in review books containing many pertinent chapters such as [70,71] and discussions of the current status of materials for organic nonlinear optics in [52,53].

Figure 23

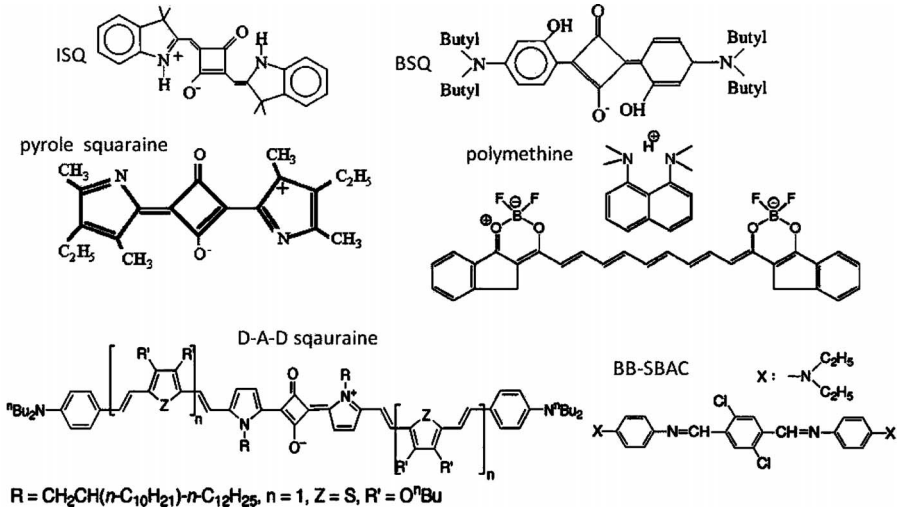

Structures for molecules in Table 4.

Figure 24

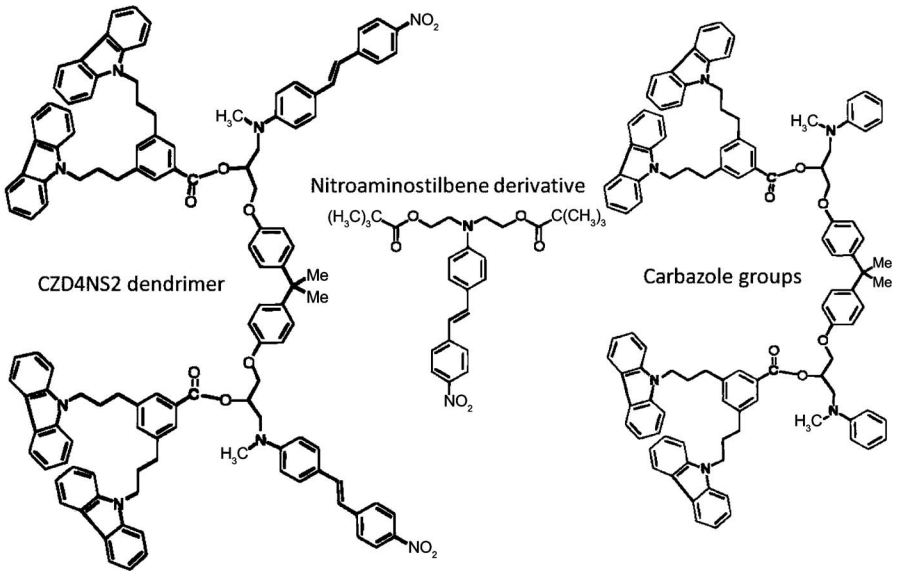

CZD4NS2 dendrimer structure and its constituents [69].

2.7. Excited-State Absorption and Reverse Saturable Absorption

There are a variety of examples such as the above where index changes are produced by the redistribution of population densities of two or more excited states via absorption, both via successive linear and nonlinear absorption processes [72,73]. The index changes occur through the reduction of oscillator strength due to saturation as discussed above, but also through the production of new absorbers as discussed in this subsection. The signs of the respective refraction changes depend on the frequency position relative to the absorption resonances.

Linear absorption can promote species to excited states that serve as the lower state of a second electric dipole allowed transition before the excited state electrons decay back to the ground state. Figure 25 shows a quasi-three-level system, described in more detail below, that is a good approximation for many organic dyes.

This process produces what is called excited state absorption (ESA). It is convenient to describe the second absorption process by an absorption cross section, σ_{21}, related to the dipole matrix element $|\mu_{21}|^2$, since the ESA coefficient is simply

$$\alpha_{21} = \sigma_{21} N_1, \tag{2.22}$$

where N_1 is the electron density of the first excited state, i.e.,

$$\frac{dN_1}{dt} = \frac{\alpha_{1g} I}{\hbar\omega}. \tag{2.23}$$

Here α_{1g} is the absorption coefficient from the ground state g (also described by a cross section σ_{1g} times the density of ground state absorbers N_g) and $\hbar\omega$ the photon energy—one excited state produced per photon absorbed.

Figure 25

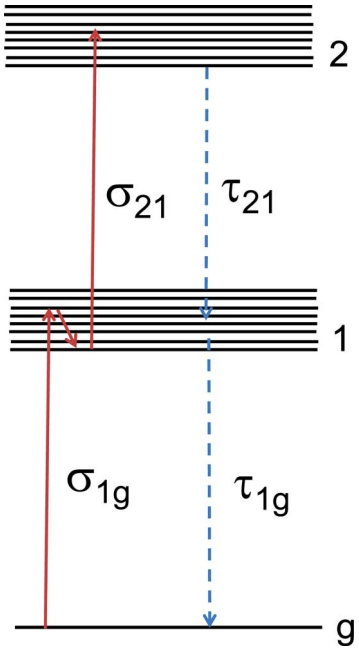

Level structure of a three-level system, showing the vibration-rotation manifold of the excited states, the absorption cross sections, and the relaxation routes.

Such equations can be integrated in time to see the effect of the ESA on the transmitted intensity. First, integrating Eq. (2.23) yields

$$N_1(t) = \frac{\alpha_{1g}}{\hbar\omega}\int_{-\infty}^{t} I(t')dt' \equiv \frac{\alpha_{1g}}{\hbar\omega}F(t), \tag{2.24}$$

where F is defined as the fluence, energy per unit area, which when plugged into the equation describing the intensity change,

$$\frac{dI}{dz} = -\sigma_{1g}N_g I - \sigma_{21}N_1 I, \tag{2.25}$$

gives

$$\frac{dF(t)}{dz} = -\sigma_{1g}N_g F(t) - N_g\frac{\sigma_{1g}\sigma_{21}}{2\hbar\omega}F^2(t). \tag{2.26}$$

A similar equation can be obtained for 2PA in which the fluence F (integrated energy of a pulse) is replaced by the intensity, and the product of density times cross sections divided by photon energy is replaced by a quantity called the 2PA coefficient, α_2. The process represented here is a pair of *sequential* linear absorption processes, as opposed to the usual nearly *instantaneous* 2PA, which is proportional to the product of the squares of the transition dipole moments $|\mu_{21}|^2|\mu_{g1}|^2$. Thus, Eq. (2.26) is a precursor to the results of perturbation theory for 2PA, and the transition from sequential 2PA [Eq. (2.26)] to instantaneous 2PA given by $dI(z) = -\alpha_2 I^2$ becomes apparent [74].

A realistic depiction of one-photon-absorption-induced ESA is shown by the three-level system with vibrational–rotational manifolds in the excited states in Fig. 25. Notice that, although many levels are shown, there are only two dominant transitions. For molecules with rotational and vibrational degrees of freedom coupled to the electronic transitions, excitation to higher-lying states in each manifold is rapidly followed by intrasystem relaxation to the bottom of the band. The ESA then proceeds from this relaxed excited state into a higher rotational–vibrational manifold. Rapid intersystem relaxation returns the electrons in the second excited state manifold to the bottom of the first excited band, where they can again absorb. Thus a single excited state absorber can efficiently absorb multiple times even for pulsed inputs.

If the ESA cross section is larger than that of the ground state, $\sigma_{21} > \sigma_{1g}$, where the absorption cross sections are now understood to be averages over the vibrational–rotation manifolds, then the absorption process is also referred to as reverse saturable absorption (RSA), and increasing input yields increasing loss [75]. This model is a useful model that can be used to describe ESA in many organic molecules, and as we will see in the discussion of semiconductors, can also describe some free-carrier absorption phenomena. Figure 26 shows Z-scan data on the organic dye chloro-aluminum phthalocyanine, CAP, showing the fluence dependence of both nonlinear absorption, following Eq. (2.26), and the nonlinear refraction following that discussed at the end of this Subsection [73]. In this figure, two sets of data are shown for the same energy but with pulse widths differing by a factor of 2. Thus the fluence used is identical, but the intensity differs by 2×. The fact that the nonlinearities are the same shows the fluence dependence. Table 4 gives parameters for a sampling of molecules showing RSA.

In cases where the input pulses deplete the population of the lower level and decay of the upper state is possible, the equations governing the process become more complicated [76]:

Figure 26

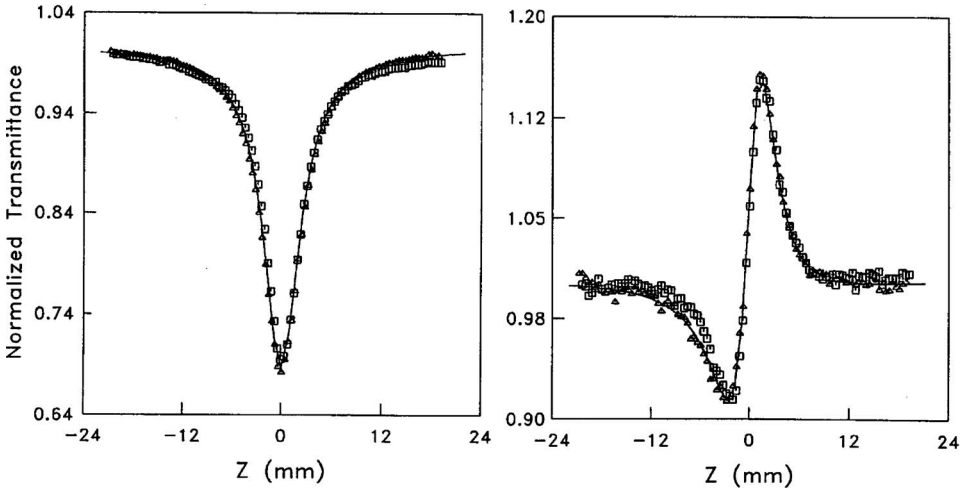

Open (left) and closed (right) aperture Z scans on chloro-aluminum phthalocyanine at 532 nm; triangles, using 30 ps pulses (FWHM); squares, 62 ps pulses (FWHM) [73].

$$\frac{dN_g}{dt} = -\frac{\sigma_{1g}N_g}{\hbar\omega}I + \frac{N_1}{\tau_{1g}}, \tag{2.27a}$$

$$\frac{dN_1}{dt} = \frac{\sigma_{1g}N_g}{\hbar\omega}I - \frac{N_1}{\tau_{1g}}, \tag{2.27b}$$

$$\frac{dI}{dz} = -\sigma_{1g}N_gI - \sigma_{21}N_1I. \tag{2.27c}$$

The refraction from these absorption processes is simply related to the redistribution of the population of levels when we are creating and/or removing absorbing species. Depending on which side of resonance, the index can be increased or lowered. For pulsed input, the index change follows the population in time. For pulses short compared with the population decay time, the index change follows the integrated energy, which has the shape of an error function.

In many situations involving organic molecules triplet states become involved, and the appropriate level structure is a five-level system [77]. Solutions of these equations show an increasing loss with increasing intensity that eventually turns into saturation for high inputs. More sophisticated approximations to Eq. (2.21) yield overall saturable absorption for $\sigma_{21} < \sigma_{1g}$, and RSA (i.e., increasing loss with increasing intensity) for $\sigma_{21} > \sigma_{1g}$, as seen in Fig. 27 [78]. References [79,80] give ESA including triplet states along with the dynamics.

We conclude this discussion of excited-state nonlinearities with the nonlinear refraction associated with the population redistribution. These refractive changes are a result of the changes in the linear absorption arising from creating excited states and removing population from the ground state. They were calculated from the Kramers–Kronig relations. The prediction is that there should be a decrease in index below resonance and an increase above resonance if the creation of the excited state absorbers dominates the absorption changes (as opposed to the loss of ground state absorbers). This should be the case where RSA dominates saturable absorption. As shown in Fig. 27 and listed in Table 5 (Fig. 28), the observed nonlinear refraction in CAP is positive, indicating above-resonance excitation. As for the absorption, defining a refractive cross section, σ_R, is more

Figure 27

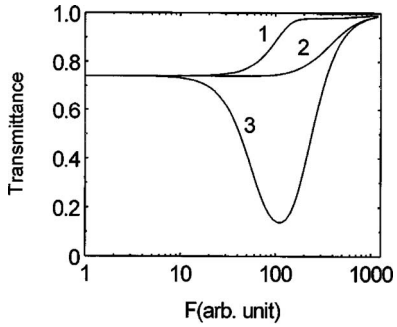

Transmittance versus input fluence for, curve 1, $\sigma_{21} < \sigma_{1g}$; 2, $\sigma_{21} = \sigma_{1g}$; 3, $\sigma_{21} > \sigma_{1g}$ [78].

Table 5. Parameters of RSA Dyes

Material/Solvent	σ_{1g}	σ_{21}	σ_{21}/σ_{1g}	σ_R	τ^a
Polymethine/ethanol [78]	0.7×10^{-17} cm^2	60×10^{-17} cm^2	81		0.3 ns
CAP/methanol [73]	2.2×10^{-18} cm^2	2.3×10^{-17} cm^2	10	1.8×10^{-17} cm^2	7.0 ns
SiNc/toluene [73]	2.8×10^{-18} cm^2	3.9×10^{-17} cm^2	14	4.7×10^{-18} cm^2	3.2 ns

[a]Here τ is the singlet state lifetime. In CAP and SiNc, much of the population goes to the triplet state in this time where it can strongly absorb as opposed to the ground state for the polymethine.

appropriate than using n_2. Values of σ_R for representative molecules are given in Table 5, using the following definition to give units of square centimeters for the cross section (another definition sometimes used is to drop the wave number k, yielding a cross section with units of cubic centimeters):

$$k_{vac}\Delta n = \sigma_R N_1. \tag{2.28}$$

It is interesting to note that if one calculated an $n_2$for CAP using, for example, the 30 ps data in Fig. 27, one would obtain a value of $n_2 = 1.2\times10^{-14}$ cm^2/W at a concentration of only 1.3 mM, i.e., a very large value if given a neat material. And, using the 62 ps data would yield a value for n_2 approximately twice as large, given that the intensity is only half as large.

3. Glass Nonlinearities

There are many definitions for a "glass." For example "any of a large class of materials with highly variable mechanical and optical properties that solidify from the molten state without crystallization. They are typically made by silicates fusing with boric oxide, aluminum oxide, or phosphorus pentoxide, are generally hard, brittle, and transparent or translucent, and are considered to be supercooled liquids rather than true solids" [81]. In optics, glass usually refers to silica, i.e., amorphous SiO_2 (silicon dioxide) doped with various atoms and/or molecules. Pure

Figure 28

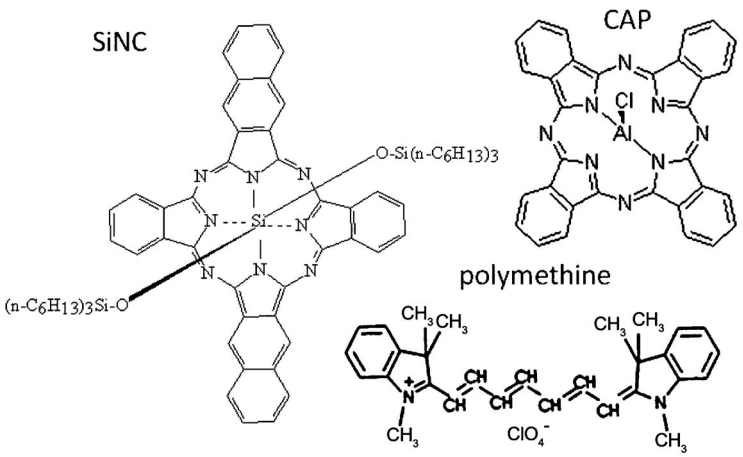

Structures of RSA dyes with parameters listed in Table 5.

silica, typically doped with Ge to increase its refractive index, is routinely used in fibers for transmission, and hence its linear and nonlinear optical properties have been studied extensively in optics, especially in the communications bands. On the one hand, a nonlinear refractive index is essential to soliton propagation, and on the other hand, it can produce detrimental crosstalk due to four-wave mixing etc. [82].

As stated in the above definition, the optical properties are not the same for every sample, as they would be, for example, in a single crystal of quartz. The reasons are primarily twofold. One, glass properties vary with the details of the preparation technique, which is usually proprietary to each commercial supplier. Different complexes can form on a local scale, especially for multicomponent glasses. Second, the optical properties depend on the purity of the starting materials, as well as upon small amounts of impurities added to the fabrication for stability, etc. In addition, the glass properties may depend on the location in the melt from which the sample was taken, the center, the edges, etc., although this aspect is probably less of an issue with glasses from commercial sources than with research grade samples made in small melts. Because of its importance in optics, n_2 has been measured in silica and lightly doped silica by many different techniques. Table 6 gives an indication of the variability in n_2 with supplier.

At 1.55 μm, which is far from all of the electronic resonances in the UV and hence is in the nonresonant regime, the recommended value is $n_2 = 2.5 \pm 0.1 \times 10^{-16}$ cm^2/W. This corresponds to one of the very few cases in nonlinear optics where such precision is possible, primarily due to the elaborate schemes for *in situ* measurements in fibers (see references cited in [83]). The dispersion with wavelength for fused silica is shown in Fig. 29. Note that the spread in values is the least at 1.55 μm because of the importance of this wavelength region. In the spectral regions where these glasses are used for nonlinear optics, the Kerr response is femtoseconds or less.

Over the past 10–20 years many new glasses, mostly heavy oxides and chalcogenides, have been synthesized with the goal of improving n_2 in glasses. The range of values along with the glass classification is documented in Fig. 30 [84]. However, the values for loss (α_1 in inverse centimeters) achieved to date in many of these materials have resulted in lower net figures of merit defined by n_2/α_1 than in fused silica. There are two principal reasons for this. In general, the larger the nonlinearity, the more the absorption edge due to electronic transitions is shifted to longer wavelengths, and hence the larger the residual absorption in the near infrared and 1–1.5 μm regions relative to fused silica. Second, fabrication techniques optimized for low loss have been pursued vigorously only for silica, Er-doped glasses, and some specialty glasses developed for applications other than nonlinear optics (with small to moderate n_2). Hence there is hope that scattering and other losses can be reduced in highly nonlinear glasses in the future.

A number of glasses in standard glass catalogs that were deemed promising for a

Table 6. Measured n_2 in Fused Silica at 800 nm from Various Suppliers [83]

Sample Source	$n_2 \times 10^{-16}$ cm^2/W
Suprasil	3.2
Schott SQ1	2.5
Heraeus	3.5
Herasil	3.3

Figure 29

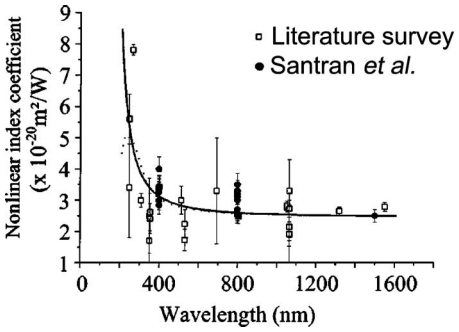

Dispersion in n_2 with wavelength for bulk fused silica as reported in Santran *et al.* [83].

combination of fiber processability and potentially high n_2 were investigated, primarily in the late 1980s and early 1990s. The range of values for n_2 was 10^{-15}–10^{-14}cm^2/W [11,85–88]. The inclusion of metal oxides in glasses for increasing the nonlinearity occupied members of the French glass community in the 1990s; the metal oxides included oxides of Te, Ti, Th, and Nb, which produced n_2 values in the range 10^{-15} to 6×10^{-14} cm^2/W [89–91].

The chalcogenide glass family has been of special interest because of its high nonlinearities in the near and mid-infrared. Values are typically in the 10^{-14} to 2×10^{-13} cm^2/W range as shown in Fig. 31. Many of these glasses have absorption cutoffs in the near infrared and are prone to optical damage for wavelengths that, depending on the specific glass composition, can extend to 1.3 μm [92–97].

In principle the S.O.S. Eqs. (2.1) and (2.3) can be used to calculate glass nonlinearities. In practice, the random, amorphous, disordered nature of a glass leads to broad distributions of resonant frequencies and decreased excited state lifetimes. The effect of this disorder on, for example, the linear spectrum of glasses

Figure 30

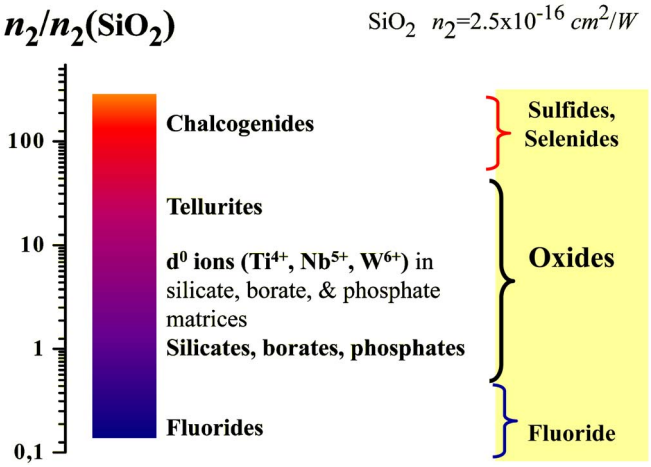

Summary of the trends in n_2 for different families of glasses [84].

Figure 31

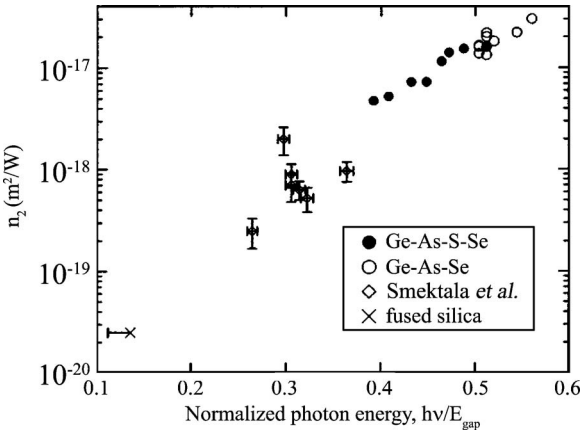

Variation of n_2 with normalized photon energy in chalcogenide systems with selenide, sulfoselenide, sulfide, and heavy-metal-doped oxides, all at 1.25 μm. Fused silica is also shown for comparison. The horizontal error bars account for absorption edge conventions different from that used in [96]. Smektala *et al.* refers to [95].

is dramatic. Although the absorption spectrum of silica still has structure that can be identified with the electronic transitions in the dominant glass constituent, gaseous SiO_2, the absorption spectrum is quasi continuous and not discrete. Furthermore, this corresponds to inhomogeneous broadening; so the inverse of the breadth of the spectrum does not yield the homogeneous relaxation times associated with S.O.S. Because of these complexities, there have been a number of approximate formulas proposed from which the n_2 of a multicomponent glass can be estimated based on the glass's linear optical properties. One such formulation that is widely used, and has been moderately successful provided that it is used in the off-resonant regime, is the BGO equation named after it's originators [98], namely,

$$n_2\ (\mathrm{cm}^2/\mathrm{W}) = \frac{0.29(n_d-1)(n_d^2+2)^2}{n(\lambda)v_d\sqrt{\dfrac{1.52+(n_d-1)(n_d^2+2)v_d}{6n_d}}} \times 10^{-13}, \qquad (3.1)$$

or in its simplified form

$$n_2 = \frac{1.64}{n}\frac{(n_d-1)}{[\sqrt[4]{v_d}]^5} \times 10^{-13}\ \mathrm{cm}^2/\mathrm{W}, \qquad (3.2)$$

where v_d is the Abbé number defined as $v_d=(n_d-1)/(n_F-n_c)$ and n_d, n_F, and n_c are the linear refractive indices at 0.48613, 0.58756, and 0.65627 μm, respectively. The Abbé number and (n_d-1) reflect the strength of the glass dispersion, and (n_d-1) as well as (n_d^2+2) the glass polarizability, both of which are in the S.O.S. expression. A comparison of the n_2 values measured at 1.55 μm and estimated from Eq. (3.2) is shown in Table 7. Although the agreement deteriorates when the glass's absorption edge approaches the refractive indices on which the Abbé number is based in multicomponent glasses, these formulas provide a useful estimation method.

Table 7. Comparison of Measured and Calculated n_2 Based on Eq. (3.2)

	Fused Silica	BK7	SF6
v_d	68	64	25
n_d	1.46	1.52	1.81
Theory n_2 (cm^2/W)	2.6×10^{-16}	3.0×10^{-16}	13×10^{-16}
Experiment n_2 (cm^2/W)	2.5×10^{-16}	3.4×10^{-16}	20×10^{-16}

4. Semiconductor Nonlinearities

Semiconductors are very important in optical technologies, since they emit and detect radiation efficiently and can be used to optically and electro-optically manipulate signals etc. As a result their optical properties are very well known, including their nonlinear optical properties [99].

There are multiple mechanisms that contribute to $\Delta n(I)$ in semiconductors. In some ways bulk semiconductors are more complex than molecules because they have multiple continuous bands and not discrete states. On the other hand, most semiconductor properties can often be well characterized by simply specifying the bandgap energy and wavelength of interest. The full spectrum of ultrafast nonlinearities can be predicted from a single material-related number to within factors of 2 or 3. This cannot be done for materials with discrete states where there are multiple two-photon (2PA) states and therefore knowledge of the full spectrum is required. In a semiconductor, a single measurement of the nonlinear optical response at a single wavelength, along with the bandgap energy, can give the full nonlinear spectrum [100]. Table 1 lists n_2 and α_2 for several representative semiconductors at different wavelengths.

Shown in Fig. 32 are the allowed electron states in an ideal semiconductor with a

Figure 32

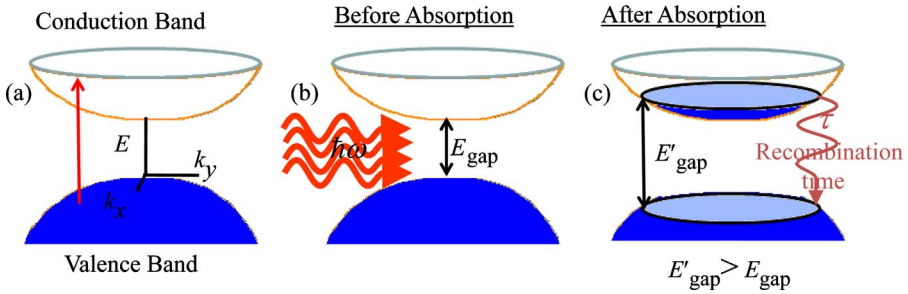

(a) Electron occupation (dark blue) of the valence and conduction bands in a two-band semiconductor at zero temperature as a function of electron energy E and wave vector $(k_x k_y)$. The red line indicates allowed transitions from the valence to the conduction band. (b) Incidence of optical field of photon energy $\hbar\omega > E_{gap}$. (c) Electron occupation of the bands subsequent to the optical field. $E'_{gap} > E_{gap}$ defines the resulting bandgap between the lowest energy unoccupied states in the conduction band and the highest energy occupied states in the valence band. τ is the spontaneous recombination time for a conduction band electron to return to the valence band.

single valence and conduction band [101]. The states lie on the surface of "bowls," upright for the conduction band and inverted for the valence band, and any electrons occupying the states at the top of the valence band and bottom of the conduction band have zero momentum (kinetic energy), i.e., away from this point $|\vec{k}| \neq 0$. In fact, a 4D representation of the densities of state in E–$\vec{k}$ space is necessary, since the electrons can move in all three spatial coordinates; i.e., Fig. 32 represents a cut in this space. At 0 K, all of the electrons exist in the valence band, none in the conduction band. At finite temperatures, the electrons pick up an additional energy $\propto k_B T$, and some electrons are excited into the lowest regions of the conduction band.

The largest changes in refractive index are associated with the absorption or emission of radiation that results in transfer of electrons to or from the conduction band, respectively [99]. Absorption of an incident beam of frequency $\omega > \omega_{gap} = E_{gap}/\hbar$ and intensity I leads in the steady state to a partial filling of the conduction band near its bottom and a lowering of the electron occupation level at the top of the valence band. This results in a change in the effective gap with $E_{gap}(I) > E_{gap}(0)$ and a change in the optical properties of the semiconductor called "band filling" or "band blocking," as indicated in Fig. 33.

Furthermore, when a negatively charged electron leaves the valence band it leaves behind a positively charged "hole." As a result of the coulomb interaction between the two, additional states called "excitons" are introduced into the bandgap near $\vec{k}=0$; see Fig. 34 [99]. Because of their close proximity to the bottom of the conduction band, these states can be easily bleached out, either by thermal fluctuations $\propto k_B T$ or by incident light, producing another change in the optical properties called "exciton bleaching."

The dimensionality of allowed electron motion (3D in bulk semiconductors) can be reduced to 2D in quantum wells and superlattices (k_x and k_y), to 1D in quantum wires (k_x) and 0D ($\vec{k}=0$, full confinement in all three directions) in QDs [102]. This reduction in dimensionality changes (1) the nature of the density of states in the valence and conduction bands, for example, from continuous in 3D to discrete states in 0D, as well as (2) the magnitude of electric dipole transition

Figure 33

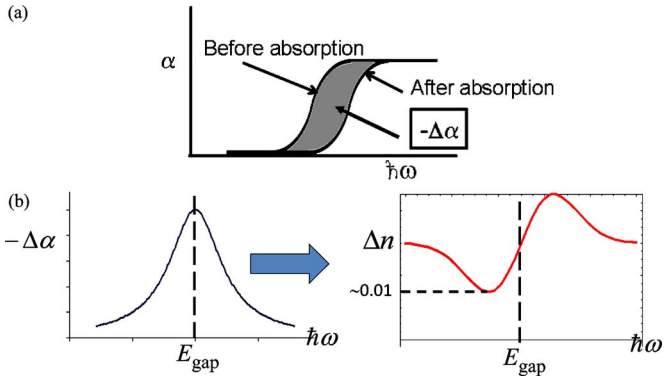

(a) Absorption spectrum and its change ($-\Delta\alpha$) before and after the passage of an optical field with $\hbar\omega > E_{gap}$ through the semiconductor. (b) Spectral dependence of the absorption and refractive index changes. The index change refers to GaAs.

Figure 34

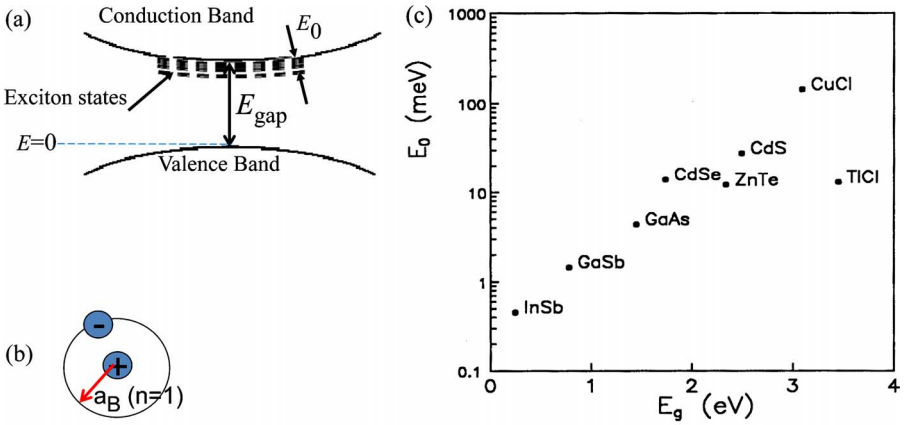

(a) Location of the exciton states relative to the conduction and valence bands. E_0 is the maximum binding energy. (b) Model for the electron–hole pair for exciton states. (c) Energy of the lowest-lying exciton state (E_0, n=1) versus the bandgap energy for a number of semiconductors [99].

elements due to changes in the overlap of the initial and final state electron wave functions. Hence n_2 also changes!

The nonlinearity is called "active" when a field is incident on a semiconductor in which the conduction band is initially occupied by pumping electrons from the valence band, either by electrical injection or by optical pumping so that for certain transition regions the occupation is higher in the conduction band than in the valence band and gain is achieved [103–106]. As shown in Fig. 35, similar

Figure 35

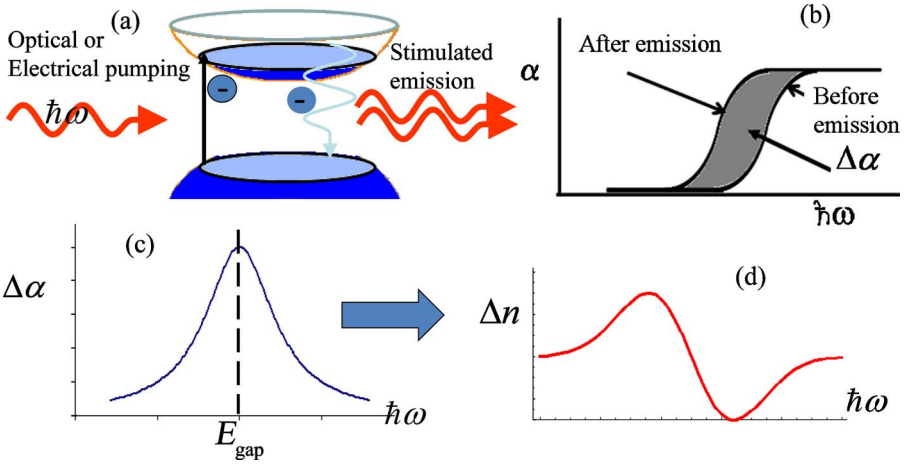

(a) Semiconductor with electrons in the conduction band resulting from optical (solid black arrow) or electrical pumping. An incident field stimulates an electron to drop down to the valence band, producing gain at the optical output. (b) and (c) Induced change in the absorption spectrum due to the stimulated emission. (d) Resultant change in the refractive index.

changes but opposite in sign occur in the refractive index, and the absorption is now negative; i.e., gain exists. Such semiconductor optical amplifiers are the most versatile all-optical signal processing elements available to date [105].

The characteristic time for both passive and active nonlinearities is the recombination time τ_r for electrons returning to the valence band from the conduction band, typically 10 ns for GaAs at room temperature. For example, for high input intensities the index change associated with the passive nonlinearity can be turned on in subpicosecond time scales but the turnoff time is dictated by the recombination time; i.e., the index change lingers for $\approx \tau_r$ as indicated previously in Fig. 4 , or by the time it takes to sweep out the electrons, for example, by an applied electric field [107]. There are also other mechanisms associated with electron dynamics in the conduction band that will be discussed with respect to semiconductor optical amplifiers and active nonlinearities [103–106].

In addition, there are other ultrafast nonlinearities like the usual Kerr effect, 2PA, and the Raman effect, which are relatively much weaker in spectral regions where there is significant linear absorption [100]. The quadratic (or ac) Stark effect (QSE), which is a significant contributor to the overall ultrafast nonlinear response below the band edge, is often referred to as "virtual saturation," since it becomes real saturation or band filling for input frequencies above the bandgap. For input frequencies lower than the bandgap region and Urbach tail, these ultrafast mechanisms dominate the nonlinear response of the semiconductor.

4.1. Carrier-Related Nonlinearities (Excitation and De-Excitation of Carriers)

4.1a. Bulk (3D) Semiconductors

At 0 K incident radiation of frequency $\omega_{\text{gap}}=E_{\text{gap}}/\hbar$ can be absorbed to move an electron from the top of the valence band to the bottom of the conduction band, and the absorption is zero for $\omega_{\text{gap}} > \omega$. For $\omega > \omega_{\text{gap}}$, absorption occurs via near vertical transitions [Fig. 32(a)] that conserve $\vec{k}$ with a maximum probability given by the product of the density of states in the valence band times the density of unoccupied states in the conduction band times the electric dipole transition matrix elements (which are a measure of the overlap of the spatial wave functions in the initial and final states) [99]. Thus the absorption spectrum rises smoothly from zero for $\omega > \omega_{\text{gap}}$. At finite temperatures, the electrons pick up an additional energy $\propto k_B T$, and the top and bottom of the bands are now blurred and extend into the gap over energies typically of order $k_B T$. In practice, defects also contribute to this additional region, which is called the Urbach tail. As a result, the absorption spectrum now decays smoothly to zero in the gap region even for $\omega_{\text{gap}} > \omega$. The more intense the incident light, the larger the change in the occupation of states in both bands with a resulting decrease of the absorption; see Fig. 33. The contribution to the refractive index is different for an electron in the valence versus the conduction bands, and hence the dispersion in the refractive index is also changed with increasing intensity (linked to the absorption change via the Kramers–Kronig relation). These nonlinearities are called "passive." Furthermore, since the density of states is high and the transition matrix elements large, the index change can be saturated at moderate intensities. For details, see [108].

Band filling (blocking): There are multiple theories of carrier nonlinearities in semiconductors; however, for most cases of interest they give comparable results. Here we follow the discussion of [100]. The theory of Banyai and Koch

[109], which includes the effects of electron–hole Coulomb interaction, plasma screening, and band filling, is perhaps the most general; however, in order to give a quantitative analysis, a knowledge of the value for the interband matrix element is required. This is often difficult to calculate from first principles, and the value is often approximately determined by comparing the computed and measured linear absorption spectrum. This theory is beyond the scope of this paper and luckily is often not needed, as the following theories give good agreement with experiments. The theories that we refer to as band-filling models are the model attributed to Aronov *et al.*, [110] and Austin *et al.*, [111] (BF1), and the dynamic Moss–Burstein model with Boltzmann statistics [112–114] (BF2). In both theories the refractive changes are attributed to carriers independent of the generation mechanism, for example by single-photon absorption or 2PA. In BF1 the nonlinear refraction from free carriers is calculated directly from the real part of the complex dielectric function. Creating a density ΔN_c of free electrons in the conduction band accompanied by the elimination of a density $-\Delta N_c$ of bound electrons in the valence band changes the index of refraction for off-resonance excitation ($\hbar\omega E_g$) by Δn [111],

$$\Delta n = -\frac{\Delta N_c e^2}{2\varepsilon_0 n_0 \omega^2 m_{cv}} \frac{E_g^2}{E_g^2 - (\hbar\omega)^2}, \tag{4.1}$$

where m_{cv} is the reduced effective mass of the electrons in the conduction band and the holes in the valence band. Hot-carrier effects are neglected in Eq. (4.1) for pulses longer than a few picoseconds, which is the time carriers take to reach the band edge (thermal equilibrium with the lattice discussed later in the context of active nonlinearities) for most semiconductors [111]. Shorter pulse excitation requires the more sophisticated analysis of Banyai and Koch [109]. The factor $E_g^2/(E_g^2 - \hbar^2\omega^2)$ can be thought of as an enhancement factor of the usual plasma index change. This simple theory explains most of the nonlinear refraction encountered for carrier nonlinearities where the carriers are generated by single- or multiple-photon absorption. We should also mention that the carrier nonlinear refraction is always negative, i.e., leads to self-defocusing nonlinearities. While the following heuristic is too simplistic to explain the details, if one thinks of creating zero-frequency oscillators, one is always above resonance so that the index change is negative.

A somewhat more sophisticated analysis is given in the BF2 model below. The excited carriers block the absorption at frequencies higher than the energy gap by filling the available states in the conduction band with electrons taken from the valence bands, Fig. 32. This model uses the Kramers–Kronig integral of the change in absorption to obtain the change in index. The total change in the index of refraction, including contributions from electrons, heavy holes, and light holes, is given by Wherrett *et al.* as [113]

$$\Delta n = -\frac{e^2}{2n_0\omega^2}\left\{\frac{\Delta N_c}{m_c}\left[1 + Z\left(\frac{m_{ck}}{m}J_{he} + \frac{m_{cl}}{m}J_{lc}\right)\right] + \frac{\Delta P_h}{m_h}\left(1 + Z\frac{m_{ch}}{m}J_{hh}\right) + \frac{\Delta P_l}{m_l}\left(1 + Z\frac{m_{cl}}{m}J_{ll}\right)\right\}, \tag{4.2}$$

where

$$Z = \frac{2}{3\sqrt{\pi}}\frac{E_p}{k_B T}\left(\frac{\hbar\omega}{E_g}\right)^2, \tag{4.3}$$

$$J_{ij} = \int_0^\infty \frac{x^2 e^{-x^2}}{x^2 + a_{ij}} dx, \tag{4.4}$$

$$a_{ij} = \frac{E_g - \hbar\omega}{k_B T} \frac{m_{ci}}{m_j}, \tag{4.5}$$

and where the photogenerated electron and hole densities are given by ΔN_c and ΔP_h. The subscripts c, h, and l represent the conduction, heavy hole, and light hole bands respectively. Similarly m is the free-electron mass, and the subscripts denote the bands as above. The electron charge is e, k_B the Boltzmann constant, T the temperature in kelvins, and E_p is the Kane momentum parameter, where E_P is ~21 eV for most semiconductors [115]. In Eqs. (4.4) and (4.5), i and j are dummy subscripts that represent c, h or l. ΔP_h and ΔP_l are determined from [113]:

$$\frac{\Delta N_c}{\Delta P_h} = 1 + \left(\frac{m_l}{m_h}\right)^{3/2}, \quad \frac{\Delta N_c}{\Delta P_l} = 1 + \left(\frac{m_h}{m_l}\right)^{3/2}. \tag{4.6}$$

Equations (4.2)–(4.5) are an approximation that is adequate for near-resonant excitation. Off resonance, as is the case for 2PA, J_{ij} should be replaced by F_{ij}, with F_{ij} defined by

$$F_{ij} = -2J\left(\frac{m_{ci}}{m_j}\frac{E_g}{k_B T}\right) + J\left(\frac{m_{ci}}{m_j}\frac{E_g - \hbar\omega}{k_B T}\right) + J\left(\frac{m_{ci}}{m_j}\frac{E_g + \hbar\omega}{k_B T}\right), \tag{4.7}$$

where the J defines the integral as in Eq. (4.4). For $\hbar\omega \sim E_g$ and $E_g \gg k_B T$, the second term on the right-hand side (RHS) of Eq. (4.7) is dominant, and F_{ij} reverts to J_{ij} as in Eq. (4.4) [101,103,104]. In 2PA experiments E_g-$\hbar\omega$ is comparable with E_g, and all three terms in Eq. (4.7) should be retained.

The contribution of the electrons to the index change, ΔN_c in Eq. (4.2) includes blocking due to electron transitions from the heavy-hole band and light-hole band in addition to the change in the electron population in the conduction band. ΔP_h and ΔP_l give the contributions of the holes from the respective transitions. In semiconductors like ZnSe, CdTe, and GaAs with two-photon excitation of carriers (thus using F_{ij} in Eq. (4.2) rather than Eq. (4.4) for J_{ij}) the change in index from transitions between the light-hole and the conduction band (electron blocking, light hole blocking, and free-light-hole generation) are nearly equal and contribute about one-third each to the total index change. This shows that for these semiconductors it should be a good approximation to use a two-band model. This is the case discussed in what follows. Examining J_{ij} in Eq. (4.4), we see for $a_{ij} \gg 1$ that $J_{ij} \approx \sqrt{\pi}/4a_{ij}$. Substituting this value for J_{ij} into Eq. (4.7), F_{ij} becomes proportional to $x^2/(1-x^2)$ with $x = \hbar\omega/E_g$. Assuming a two-band model and substituting F_{ij} for J_{ij} in Eq. (4.2) gives a change in index due to carrier transition blocking Δn_b as

$$\Delta n_b \propto \frac{(\hbar\omega)^2}{[E_g^2 - (\hbar\omega)^2]}. \tag{4.8}$$

The dominant frequency dependence here comes from the denominator and is the same as the enhancement factor in the theory of BF1 using a two-band model. This agreement is expected, since the same physical mechanism is used

in both calculations. Comparison of these theories for 2PA excitation in semiconductors like ZnSe, CdTe, and GaAs shows good agreement [10].

In this case we can write an equation for the nonlinear refraction by using a refractive cross section σ_R with units of square centimeters (as was used in Subsection 2.6 for molecules), using Eq. (4.2) to obtain a function of the ratio $\hbar\omega/E_g=x$ as

$$\Delta n = \frac{\sigma_R \Delta N}{k_{\text{vac}}} = \frac{\hbar^2 e^2}{2\varepsilon_0 n_0 m} \frac{E_p}{E_g^3} \frac{1}{x^2(x^2-1)} \Delta N_c, \tag{4.9}$$

where we replaced the effective mass with mE_g/E_p [100]. Often in the literature the k_{vac} is not used in the definition, leaving a cross section in cubic centimeters. Here we use k_{vac} so that we can compare these semiconductor free-carrier refractive cross sections with the molecular cross sections discussed in Subsection 2.6. There we saw values in the 0.5 to 2×10^{-17} cm^2 range, which as we will see is comparable with those for semiconductors; see Table 8 below. Since the hole densities are related by Eqs. (4.6) to the conduction band carrier density, the key parameter for describing the band filling effect is the electron density in the conduction band at energy E, $\Delta N_c(E)$. Assuming that the population of the conduction band can be neglected prior to the incidence of the optical beam, for a semiconductor with a single direct bandgap (two-band model),

$$\frac{d}{dt}\Delta N_c(E) = \alpha_1(I)\frac{I(t)}{\hbar\omega} - \frac{\Delta N_c(E)}{\tau_r}, \tag{4.10}$$

where α_1 is the intensity absorption coefficient and τ_r is the recombination time. In steady state,

$$\Delta N_c(E) = \alpha_1(I)\frac{I(t)}{\hbar\omega}\tau_r. \tag{4.11}$$

Defining σ_R as the cross section for the index change (from Eqs. (4.2)–(4.7) when a carrier is promoted from the valence to the conduction band and assuming minimal change in the absorption spectrum, the band-filling nonlinearity $n_{2,\text{scbf}}$ is deduced to be

Table 8. Parameters Needed for Carrier-Related Nonlinearities in Selected Semiconductors[a]

Parameter	InSb	GaAs	ZnSe	ZnS	CdS	ZnO	CdTe
E_g (eV)	0.18	1.42	2.67	3.66	2.42	3.2	1.44
σ (cm^2)	8×10^{-16} [116]		4.4×10^{-18} [9]	7×10^{-18} [9]	3×10^{-18} [117]	6.5×10^{-18} [118]	
σ_R (cm^2)	$2-4\times10^{-15}$ [119]	3.8×10^{-16} [10]	4.7×10^{-17} [10]		3.8×10^{-16} [117]	9×10^{-17} [118]	3.0×10^{-16} [10]
τ_r (ns)	50		1 [9]	~1 [9]	3.6 [117]	2.8 [118]	
λ	10 μm	1064 nm	1064 nm	1064 nm	532 nm	532 nm	1064 nm
n	4.0	3.43	2.7	2.4	2.6	1.9	2.7

[a]Defect-dependent and Auger (which dominate at high intensities) decay rates are not knowingly included.

$$\Delta n = \frac{\sigma_R \Delta N_c(E)}{k_{vac}} = \frac{\tau_r \alpha_1 \sigma_R}{k_{vac}\hbar\omega} I \rightarrow n_{2,scbf} = \frac{\tau_r \alpha_1 \sigma_R}{k_{vac}\hbar\omega}. \tag{4.12}$$

Note that saturation of the index change will occur when α_1 is reduced with increasing intensity. Furthermore, the electrons (and hence the index change) in the conduction band can diffuse over distances of a few micrometers so that the index change is not local. This nonlocality can be utilized to reduce the effective turnoff time in semiconductor waveguides with cross-sectional dimensions of a few wavelengths by applying an electric field to sweep out the carriers from the optical path [107].

In Table 8 are listed σ_R, τ_r, and E_{gap} for a number of common semiconductors. For GaAs, which exhibits an absorption maximum of $\sim 10^4$ cm^{-1}, this gives $n_{2,scbf} \sim 10^{-9}$ cm^2/W. Of course, the distance that the incident beam penetrates the semiconductor is only a few micrometers. Table 9 breaks down contributions to the refractive index change caused by plasma and blocking.

Frequently short pulses are used with pulse width $\Delta t \ll \tau_r$. In this case, subsequent to the passage of the pulse, the induced index change Δn_p is given as

$$\Delta n_p = \frac{\sigma_R N_c(E,t)}{k_{vac}} \xrightarrow{\tau_r \gg t > \Delta t} \frac{\alpha_1 \sigma_R}{k_{vac}\hbar\omega} \int_0^{t>\Delta t} I(t')dt' = \frac{\alpha_1 \sigma_R}{k_{vac}\hbar\omega} F, \tag{4.13}$$

where F is the fluence. This index change decays in time as

$$\Delta n_p(t) = \Delta n_p \exp[-t/\tau_r]. \tag{4.14}$$

More on free-carrier refraction and absorption: In Subsection 2.6 we discussed ESA and RSA in molecules. The absorption and refraction from excited states is analogous to that occurring in semiconductors that is due to photogenerated carriers (electrons and holes). Free-carrier absorption takes the role of ESA, and free-carrier refraction, as discussed above, takes the role of excited-state refraction. The discussion of nonlinear absorption is otherwise nearly identical to that of Subsection 2.6. The bands take on the role of the vibrational–rotational manifolds, and the equations describing the loss are the same with simple redefinitions of the quantities. For example, for linearly excited carriers in Eqs. (2.25) α_1 replaces the product of the ground state absorption cross section times the density, i.e., $N_g\sigma_{1g}$, where N_1 is the density of excited carriers (electrons and holes) and σ_{21} becomes the free-carrier absorption coefficient σ. Here the assumptions are that band filling can be ignored and that phonon relaxation to the bottom of the conduction band (top of the valence band) is rapid on the time scale of the pulse. The resulting nonlinear loss is then given by Eq. (2.26), reproduced here with the substitutions made for semiconductors:

Table 9. Contributions to Change in the Index of Refraction Caused by Plasma and Blocking

Semiconductor	Plasma Electron	Blocking Electron	Blocking Electron lh-c	Plasma h-hole	Blocking h-hole hh-c	Plasma l-hole	Blocking l-hole lh-c
ZnSe	20%	33%	23%	4%	16%	2%	2%
CdTe	27%	23%	21%	7%	15%	4%	3%
GaAs	34%	25%	24%	3%	10%	2%	2%

$$\frac{dF(t)}{dz} = -\alpha_1 F(t) - \frac{\alpha_1 \sigma}{2\hbar\omega} F^2(t). \tag{4.15}$$

Here the relaxation process within the band comes from phonon emission, and the free-carrier absorption takes the place of ESA. Of course, associated with each absorption process are the corresponding refractive changes described by a free-carrier refractive cross section, σ_R, as discussed in this section. Values for sample cross sections are given in Tables 8 and 10. While RSA is an important property for organic dyes, semiconductors cannot be diluted in solvents; so the linear absorption is usually too large to utilize this nonlinear response except perhaps in a few thin indirect bandgap materials [120]. However, free-carrier absorption and free-carrier refraction are independent of the method of photogeneration. Thus, for example, 2PA can create the excitation, resulting in further absorption from excited states in molecules or free carriers in semiconductors. These processes will appear as fifth-order nonlinearities, i.e., $\chi^{(3)}:\chi^{(1)}$ processes [10].

Exciton bleaching: As mentioned briefly before, exciton levels exist in the gap just below the conduction band in the vicinity of $\vec{k}=0$ [dashed curves in Fig. 34(a)] [99]. Since the hole–electron binding is weak, these are Wannier excitons, and their spectrum is hydrogenlike [Fig. 34(a)], with the levels becoming the continuum reaching the bottom of the conduction band, [99]

$$E_n = E_{\text{gap}} - E_0 \frac{1}{n^2} - \text{Coulomb correction}, \tag{4.16}$$

$$E_0 = \frac{\hbar^2}{2m_r a_B^2}, \quad a_B = \frac{\hbar^2 \varepsilon_0}{e^2 m_r}, \quad \frac{1}{m_r} = \frac{1}{m_e} + \frac{1}{m_h}. \tag{4.17}$$

Here E_n is exciton energy offset from the conduction band for states for $n = 1, 2, 3\ldots$, $a_B$is the Bohr exciton radius for the $n=1$ state, and m_r is the reduced exciton mass; see Fig. 34(b). Variation of the $n=1$ energy offset E_0 versus bandgap energy is shown in Fig. 34(c) for a selection of semiconductors and indicates an exponential relation between the two parameters.

In three dimensions well-defined exciton levels exist primarily at very low temperatures T, where $k_B T$ is smaller than the binding energy as shown in the calculations reproduced in Fig. 36 [99]. As the carrier excitation increases with increasing incident light intensity due to absorption, at low temperatures the exciton line is rapidly bleached out and becomes essentially indistinguishable

Table 10. Comparison of Experimental and Theoretical Values for the Index Change per Unit Carrier Density σ_R [10].

					σ_R (10^{-21} cm^3)		
Material	λ (nm)	E_g (eV)	m_c/m	m_v/m	Expt.	Theory (BF1)	Theory (BF2)
ZnSe	532	2.67	0.15	0.78	0.8	1.6	1.6
CdTe	1064	1.44	0.11	0.35	5.0	5.9	5.9
GaAs	1064	1.42	0.07	0.68	6.5	7.2	6.2
ZnTe	1064	2.26	0.12	0.60	0.75	2.4	2.2

Figure 36

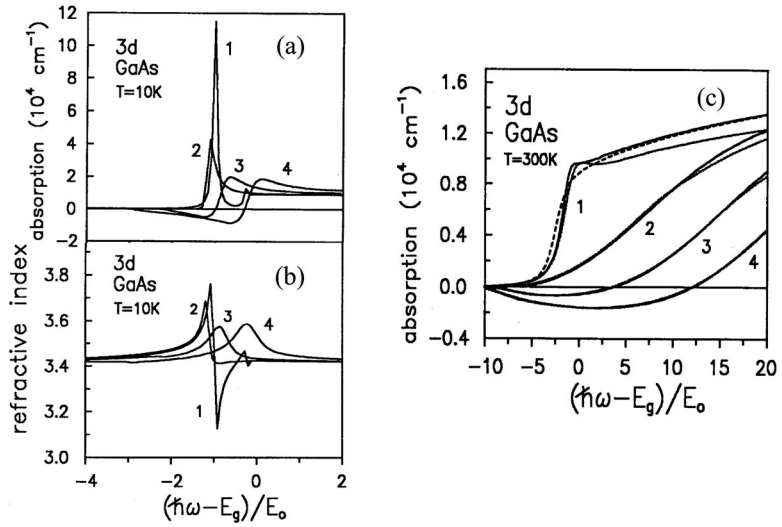

Theoretical (includes plasma screening and coulomb interactions) curves for the frequency dispersion of the (a) absorption and (b) refractive index at 10 K and (c) absorption at room temperature in GaAs for different electron densities N_e in the conduction band. For (a) and (b), curve1, $N_e=0$; 2, $N_e=5\times10^{15}$ cm^{-3}; 3, $N_e=3\times10^{16}$ cm^{-3}; 4, $N_e=8\times10^{16}$ cm^{-3}; and for (c), curve 1, $N_e=1\times10^{16}$ cm^{-3}; 2, $N_e=1\times10^{18}$ cm^{-3}; 3, $N_e=2\times10^{18}$ cm^{-3}; 4, $N_e=3\times10^{18}$ cm^{-3} [99]. Here $m_e=0.0665m_0$ $m_h=0.457m_0$, $a_B=12.5$ nm, and $E_0=4.2$ meV. Dashed curve, density of states.

from the absorption band edge, which moves to higher energies because of band blocking as discussed above. At room temperature in GaAs, the exciton peak is essentially bleached out owing to thermal excitation into the conduction band. Clearly at low temperatures the peak nonlinearity ($n_{2,\mathrm{exc}}\sim10^{-7}$ cm^2/W) associated with the exciton line can be much larger than that due to band renormalization but can also be much narrower in spectral width [99,121].

Figure 37 shows the measured absorption of GaAs and its refractive index calculated from the plasma model via the Kramers–Kronig relations for different cw input power levels at room temperature [108]. Initially, the index change is linear in the input power, showing that an effective n_2 provides a useful description for the nonlinearity. Note, however, that the saturation of the absorption and index change since the absorption change for $1\rightarrow3.2$ mW is comparable with the change for $20\rightarrow30$ mW.

4.1b. Active Nonlinearities (with Gain)

In this process an electron population inversion $[\Delta N_c(E_c)-\Delta P_v(E_v)>0]$ between the conduction and valence bands for some range of energy difference (E_c-E_v) must be created [103–106]. This population inversion is produced either by pumping optically (by absorption) electrons from the valence to the conduction band or by injecting these electrons via electrodes attached to the semiconductor. When a beam of frequency ω is incident inside the region of inversion, stimulated emission can occur, and the beam is amplified, accompa-

Figure 37

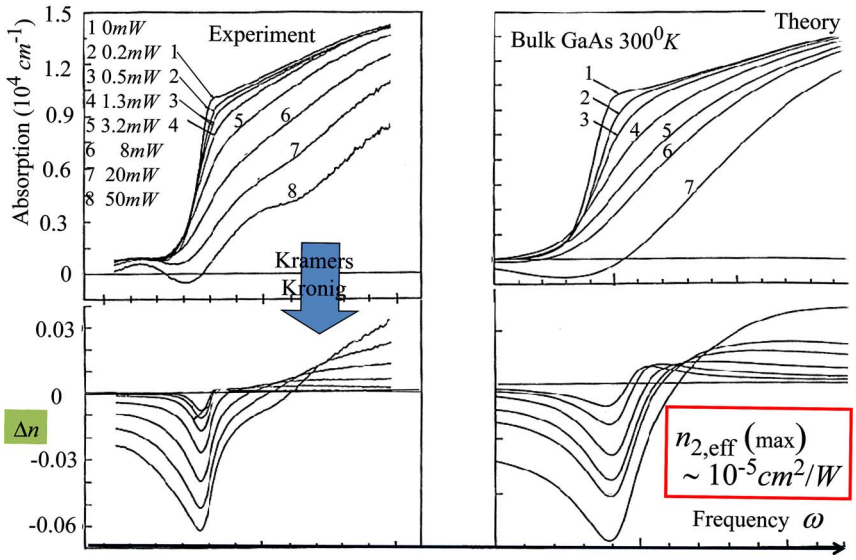

Experiment (left-hand side) and theory (right-hand side) of the frequency spectrum of the absorption and refractive index change in GaAs at different input powers. The experimental refractive index change was obtained by taking the Kramers–Kronig transform of the experimental absorption spectrum at different powers [108].

nied of course by electrons giving up energy by returning to the valence band. This amplification process is shown schematically in Fig. 35(a) and is described by

$$\frac{d}{dt}\Delta N_c(E) = -BI(t)[\Delta N_c(E) - \Delta P_{l,h}(E-\hbar\omega)] - \frac{\Delta N_c(E)}{\tau_r}. \qquad (4.18)$$

Typically optical pumping with radiation fields of frequency $\omega_{\text{pump}} > \omega_{\text{gap}}$ is used to achieve and maintain the population inversion, and very fast electron dynamics occurs in the conduction band when an optical pulse is applied to produce the steady-state Fermi electron distribution as shown in Fig. 38 [103,104]. The corresponding electron temperature T_c of this Fermi equilibrium distribution can be very high.

To understand the fast time dynamics, consider what occurs when a short pulse of frequency ω is incident [103,104]. As indicated in Fig. 38(b), stimulated emission occurs and the gain is reduced. This results in a hole in the electron distribution in the conduction band, Fig. 38(b), panel II. This process is called "spectral hole burning." This hole is filled in [Fig. 38(c), III] on a time scale of ~100 fs by electron scattering, and subsequently this distribution relaxes (carrier heating) on a picosecond time scale to a new Fermi equilibrium distribution [Fig. 38(c), IV] at a lower electron temperature (since the total number of conduction band electrons is reduced). Since pumping continues, eventually the conduction band electron distribution [Fig. 38(c), V] returns to that prior to the incidence of the pulse. This occurs on a time scale that depends directly on the pumping rate.

These dynamics have been probed experimentally and confirmed by modeling for very short pulses by passing an ultrashort probe beam through the sample

Figure 38

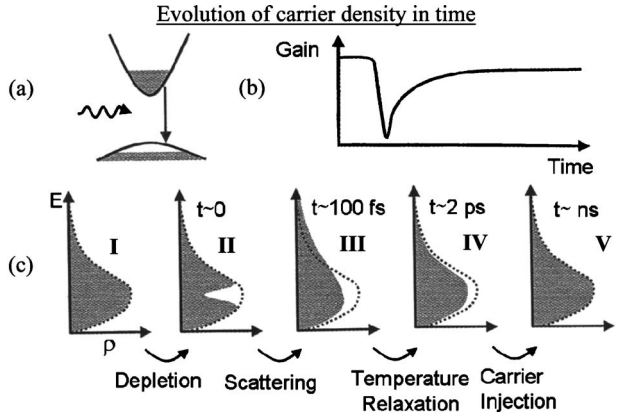

(a) Photon field incident on a semiconductor with conduction band partially populated. (b) Stimulated emission reduces the gain as the conduction band is depopulated. (c) I, Conduction Fermi band population distribution before optical field incidence. II, Hole produced in electron distribution due to stimulated emission. III, Relaxation to new electron distribution due to collisions. IV, Relaxation to new Fermi band distribution. V, Return to original (before field incidence) Fermi distribution by pumping (electrical or optical) [103,104].

and evaluating the nonlinear phase shift imparted on the probe as a function of time delay between pump and probe [106]. The calculated temporal evolution shown in Fig. 39 agreed well with experiment. The integrated conduction band electron density ΔN_c recovers on the time scale of nanoseconds in this example. The dominant effects are the Kerr effect, carrier heating, and partial depletion of the conduction band electron density. Note that an effective n_2 over the picosecond time scale is not a useful parameter for the active case. The off-resonance nonlinear response of these active devices can also be modeled by using Kramers–Kronig relations in a way similar to that done for the bound electronic response discussed in the next Subsection [122].

4.2. Ultrafast Passive Nonlinearities (Kerr Effect etc.)

Here we discuss the nonlinear refraction (along with the nonlinear absorption) associated with bound electrons in semiconductors and/or dielectrics. This nonlinear refraction is called the bound electronic Kerr effect. These nonlinearities are only dominant in the transparency range of the material where other nonlinear optical effects are negligible, as they are usually the smallest of the nonlinear responses discussed in this paper (but the fastest!). In the transparency range the nonlinear optical response is due to the anharmonic motion of bound valence electrons that have low mass and can respond at optical frequencies. Thus they are often referred to as "instantaneous" nonlinearities; however, because of the finite response time ($< 10^{-15}$ s) they still show dispersion, as we will see.

There are three nonlinear processes that need to be taken into account, 2PA, Raman absorption, and the so-called QSE, often referred to as the ac Stark effect or virtual band blocking; see Fig. 40. The nonlinear refraction can then be calculated by frequency nondegenerate Kramers–Kronig relations derived from cau-

Figure 39

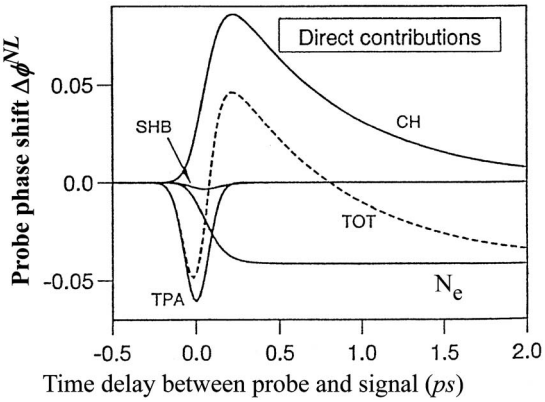

Theoretical modeling of the nonlinear phase shift (due to the index change) experienced by a probe beam as a function of delay time between an intense exciting beam and the probe beam. TPA, 2PA (Kerr effect); SHB, spectral hole burning; CH, carrier heating; TOT, total nonlinear phase shift; N_e, electron density in conduction band [106].

sality. The change in index at ω_1 due to the presence of a strong excitation beam at frequency ω_2 is related to an integral over all frequencies ω of the nondegenerate nonlinear absorption at frequency ω_2 that is due to the presence of the strong excitation light beam of frequency ω_2 by [123]:

$$n_2(\omega;\omega_2) = \frac{c}{\pi}\mathrm{P}\int_0^\infty \frac{\Delta\alpha(\omega_1;\omega_2)}{\omega_1^2-\omega^2}d\omega_1 \tag{4.19}$$

where P denotes the principal value of the integral, and

$$\Delta\alpha(\omega_1,\omega_2) = K\frac{\sqrt{E_p}}{n_{01}n_{02}E_g^3}F_2(x_1,x_2) \tag{4.20}$$

with x_1, x_2 given by $\hbar\omega_{1,2}/E_g$, is the nonlinear absorption with F_2 containing the spectral information as given in Table 11. K is a material-dependent constant given by

Figure 40

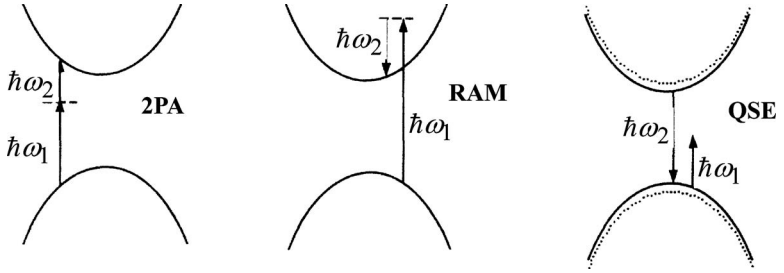

Principal ultrafast nondegenerate two-photon processes that dominate semiconductor nonlinearities below the bandgap [122].

Table 11. Components of Nonlinear Absorption Spectral Function $F_2(x_1, x_2)$

Process	$F_2(x_1,x_2)$
2PA $x_1+x_2>1$	$\frac{(x_1+x_2-1)^{3/2}}{2^7 x_1 x_2^2}\left(\frac{1}{x_1}+\frac{1}{x_2}\right)^2$
Raman $x_1-x_2>1$	$\frac{(x_1-x_2-1)^{3/2}}{2^7 x_1 x_2^2}\left(\frac{1}{x_1}-\frac{1}{x_2}\right)^2$
QSE $x_1>1$	$-\frac{1}{2^9 x_1 x_2^2 (x_1-1)^{1/2}}\left(\frac{x_1}{x_1^2-x_2^2}-\frac{2(x_1-1)(x_1^2+x_2^2)}{(x_1^2-x_2^2)^2}+\frac{8(x_1-1)^2}{x_2^2}\right)$

$$K=\frac{2^5}{5\pi}\frac{1}{\varepsilon_0{}^2}\frac{e^4}{\sqrt{m_0}c^2}, \tag{4.21}$$

and m_0 is the free-electron mass. The frequency degenerate $n_2=n_{2\text{scuf}}(-\omega;\omega)$ is given by setting $\omega=\omega_2$ after the integral has been performed.

The QSE functions in Table 11 are derived in [100] and come from a two-parabolic-band model of semiconductors, i.e., a single direct bandgap. Remarkably this simple theory gives excellent predictions for the magnitude and spectral dependence of the observed nonlinear absorption and refraction in semiconductors and even dielectrics. Refinements of this theory to include four bands (or even higher bands) have been performed [124] and can give even better descriptions of the nonlinear response to ultrashort pulses. This simple two-parabolic-band model gives the spectral dependence of degenerate 2PA as

$$F_2=\left(\frac{(2x-1)^{3/2}}{2^5x^5}\right), \tag{4.22}$$

where $x=\hbar\omega/E_g$, which is shown in Fig. 41. Also shown in Fig. 41 are 2PA measurements of several semiconductors with the data scaled according to

$$F_2\left(\frac{\hbar\omega}{E_g}\right)=\frac{1}{K\sqrt{E_p}}n^2E_g^3\alpha_2^{\text{exp}}, \tag{4.23}$$

where $K=3100$ cm GW^{-1} eV$^{5/2}$ (the experimental best fit) is used with E_p and E_g in electron volts. Values of the measured 2PA coefficients (α_2^{exp}) for representative semiconductors along with several dielectrics are shown in Table 1.

Plugging the F_2 components into Eq. (4.19), performing the integrals, and taking care to subtract divergences yields the nonlinear refractive index $n_{2,\text{scuf}}$:

$$n_{2,\text{scuf}}(\omega_1,\omega_2)=\frac{\hbar cK}{2}\frac{\sqrt{E_p}}{n_{01}n_{02}E_g^4}G_2(x_1,x_2), \tag{4.24}$$

where the dispersion function G_2 is given by

$$G_2(x_1,x_2)=\frac{2}{\pi}\int_0^\infty\frac{F_2(x';x_2)}{x'^2-x_1^2}dx'. \tag{4.25}$$

As pointed out in [125], this integral, when $\vec{E}\cdot\vec{r}$ Hamiltonians are used as opposed to $\vec{A}\cdot\vec{p}$, can prove to be difficult to perform, since it includes some diver-

Figure 41

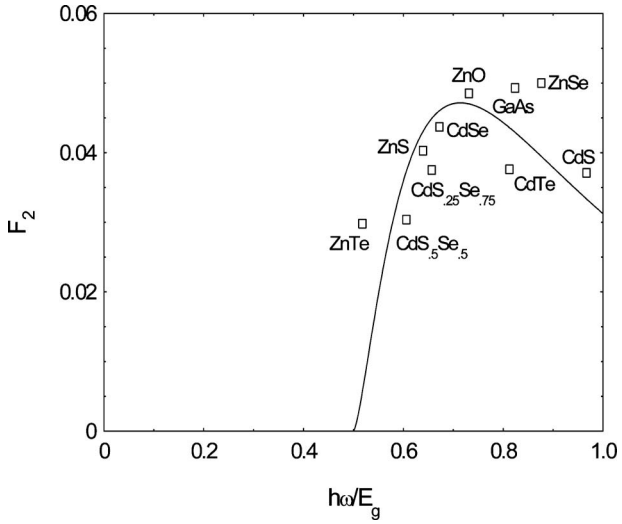

Function F_2 (for 2PA) of Eq. (4.22) plotted as a function of $\hbar\omega/E_g$ (solid curve) along with data scaled according to Eq. (4.23) [124].

gences that need to be subtracted out. However, this has been done with results that agree with experiments. The nonlinear absorption that goes into Eq. (4.19) is given in Table 11. The result is

$$n_{2,\mathrm{scuf}}(\omega) = \frac{A}{n_0^2 E_{\mathrm{g}}^4} G_2(\hbar\omega/E_{\mathrm{g}}), \tag{4.26}$$

where the spectral dependence is in the G_2 function as given in Table 12 and is quite complicated.

Table 12. Components of Dispersion of n_2 from Various Nonlinear Absorption Processes with $G_2(x_1;x_2) = G_2^{\mathrm{2PA}}(x_1;x_2) + G_2^{\mathrm{Raman}}(x_1;x_2) + G_2^{\mathrm{acStark}}(x_1;x_2)$

Process	$G_2(x_1;x_2)$
2PA	$H(x_1,x_2)+H(-x_1,x_2)$
Raman	$H(x_1,-x_2)+H(-x_1,-x_2)$
QSE $x_2 \neq x_2$	$\frac{1}{2^9 x_1^2 x_2^2}\left\{-\frac{1}{2}-\frac{4}{x_1^2}+\frac{4}{x_2^2}-\frac{x_2^2}{x_1}\frac{[(1-x_1)^{-1/2}-(1+x_1)^{-1/2}]}{x_1^2-x_2^2}\right.$ $+\frac{2x_1^2(3x_2^2-x_1^2)}{x_2^2(x_1^2-x_2^2)^2}[(1-x_2)^{1/2}+(1+x_2)^{1/2}]$ $\left.-\frac{2x_2^2(3x_1^2-x_2^2)}{x_1^2(x_1^2-x_2^2)^2}[(1-x_1)^{1/2}+(1+x_1)^{1/2}]\right\}$
$x_1=x_2$	$\frac{1}{2^9 x_1^4}\left[\frac{3}{4}\frac{(1-x_1)^{-1/2}-(1+x_1)^{-1/2}}{x_1}-\frac{(1-x_1)^{-3/2}+(1+x_1)^{-3/2}}{8}-\frac{1}{2}\right]$

Here

$$H(x_1,x_2)=\frac{1}{2^6x_1^4x_2^4}\left\{\frac{5}{16}x_2^3x_1^2+\frac{9}{8}x_2^2x_1^2-\frac{9}{4}x_2x_1^2-\frac{3}{4}x_2^3\right.$$
$$-\frac{1}{32}x_2^3x_1^2(1-x_1)^{-3/2}+\frac{1}{2}(x_2+x_1)^2$$
$$\times[(1-x_2-x_1)^{3/2}-(1-x_1)^{3/2}]$$
$$-\frac{3}{16}x_2^2x_1^2[(1-x_1)^{-1/2}+(1-x_2)^{-1/2}]$$
$$+\frac{3}{2}x_2x_1^2(1-x_2)^{1/2}+\frac{3}{2}x_2^2x_1(1-x_1)^{1/2}$$
$$+\frac{3}{4}x_2(x_2^2+x_1^2)(1-x_1)^{1/2}-\frac{3}{8}x_2^3x_1(1-x_1)^{-1/2}$$
$$\left.+\frac{1}{2}(x_2^2+x_1^2)[1-(1-x_2)^{3/2}].\right\} \tag{4.27}$$

The last term in Table 12 allows one to calculate the limit of the nondegenerate G_2 QSE. When the limit $x_1 \rightarrow x_2$ is taken, the contribution to the usual degenerate $n_{2,\text{scuf}}$ is obtained.

It is noteworthy that the bandgap scaling predicted can also be obtained by using a quasi-dimensional analysis. Such an analysis was used by Wherrett to obtain the bandgap energy scaling of $n_{2,\text{scuf}} \propto E_g^{-4}$ [126].

The different contributions are plotted in Fig. 42. In general, below the 2PA resonance, 2PA, and Raman effect contribute nearly equally to the small, positive, relatively dispersion free region of $n_{2,\text{scuf}}$, and then 2PA takes over around the 2PA resonance and begins to decrease n_2 to take it negative above the 2PA resonance. There the strong one-photon resonance negative contribution from the QSE kicks in as well to take n_2 very negative near the 1PA bandgap. This region of the spectrum where n_2 decreases rapidly for $\hbar\omega \rightarrow E_g$ is shown in Fig. 43 along with experimental data. This response evolves smoothly into the real band-blocking nonlinearity discussed in the paragraphs titled "4.1a Band filling (blocking)." Nonlinear refractive indices of several materials have been measured, covering a broad range of normalized frequency as shown in Fig. 44. Figure 45 shows the wavelength dispersion of $n_{2,\text{scuf}}$ in ZnS along with its 2PA spectrum [127]. In both cases, the agreement of theory with experiment is good.

The hidden E_g^{-4} scaling can be displayed more conveniently on a log/log plot of n_2 scaled by the dispersion function G_2 as in Fig. 46. Here it is seen that the nonlinear index at 1064 nm varies from -3.3×10^{-13} cm^2/W for GaAs, to $+3.1\times10^{-16}$ cm^2/W for Al_2O_3, to $+1.23\times10^{-13}$ cm^2/W for ZnTe. We also see that, for example, the measured values of n_2 for ZnSe at 1.06 and 0.532 μm, which have different signs, are consistent with the scaling law derived from a simple two-parabolic-band model. Again, several of the experimentally measured nonlinear parameters are shown in Table 1.

Figure 42

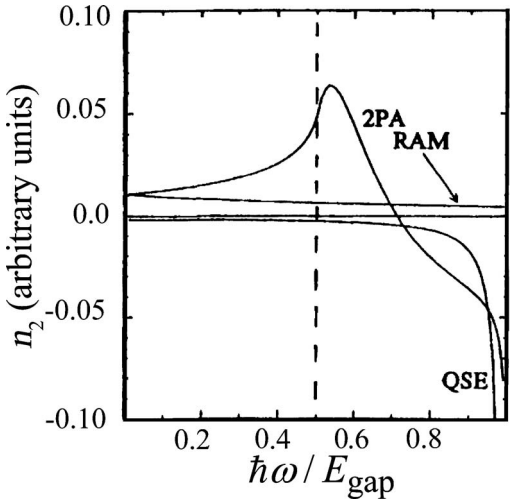

Spectral dependence of the different ultrafast contributions to the nonlinearity n_2 for $E_{gap} > \hbar\omega$. Here 2PA refers to the two-photon absorption mechanism (Kerr effect), RAM to the Raman effect, and QSE to the quadratic Stark effect [125].

4.3. Low-Dimensional Semiconductors

As we have seen in the previous discussion on semiconductor nonlinear optics, at telecommunications wavelengths of about $\lambda = 1.55\ \mu$m, typical bulk semiconductors have a nonlinear refractive index insufficient for many applications. For example, silicon has an $n_{2,el}$ of 0.5×10^{-13} cm^2/W, while GaAs is a bit larger at 1.5×10^{-13} cm^2/W [128,129]. Both, however, fall far short of the needed strong optical Kerr effect of an n_2 of about 10^{-10} cm^2/W to produce attractive index changes of the order of 10^{-2}–10^{-4} with MW/cm^2 intensities. Yet, since these semiconductor materials are exactly what is used in today's electronic platforms, optical devices made of compatible materials are needed if they are to be integrated as an active el-

Figure 43

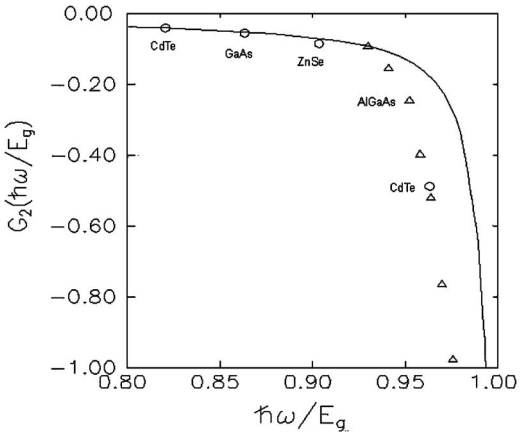

Spectral dependence of the function G_2 ($\propto n_2$) as $\hbar\omega \to E_{gap}$ along with data for a few measured semiconductors [125].

Figure 44

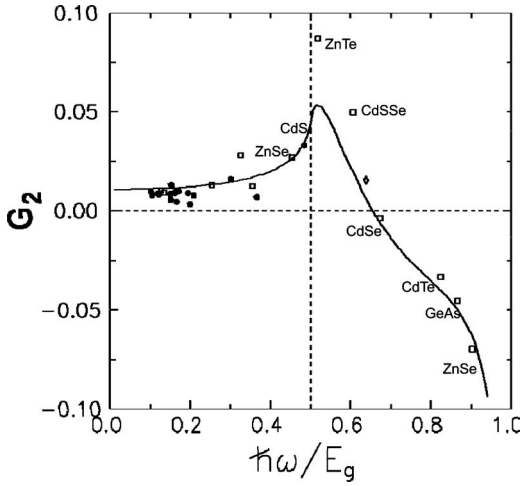

Spectral dependence of the function G_2 ($\propto n_2$) for $0 < \hbar\omega/E_{gap} < 1$ along with measured data for a few semiconductors [125].

ement. One potential approach (still unproved) is to make use of low-dimensional semiconductors. Confinement in one or more dimensions of the conduction band electrons can change the nonlinear optical response of a semiconductor in a number of ways. This includes confinement structures that are of the order of and smaller than the exciton Bohr radius in either one (quantum well), two (quantum wire), or all three (QD) spatial dimensions [99,102]. In each of these structures an excited electron is confined by the dimensions of the structure, and its behavior can be significantly altered from that of a bulk semiconductor of the same material [99,102].

As discussed previously, the transition matrix elements are a product of the density of electron states (N_e) times the integral over the spatial overlap of the electron wave functions in the valence and conduction bands. The overlap integral referred to above depends on the details of the confined structure, and it can ac-

Figure 45

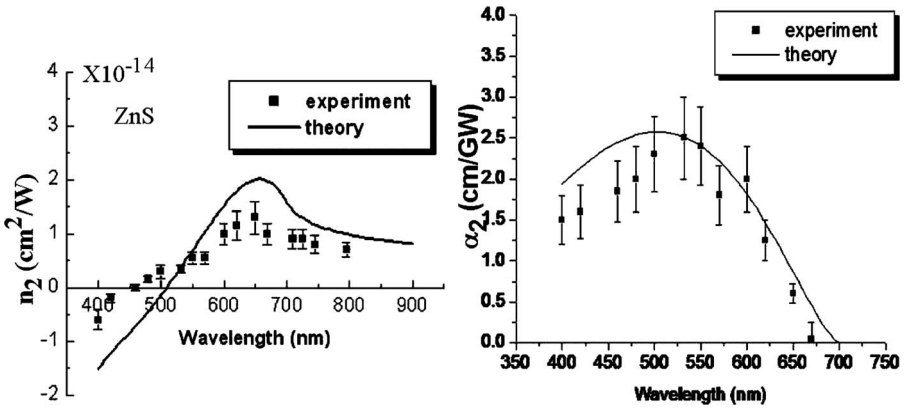

Wavelength dispersion of n_2 in ZnS (left) and 2PA spectrum (right) [127].

Figure 46

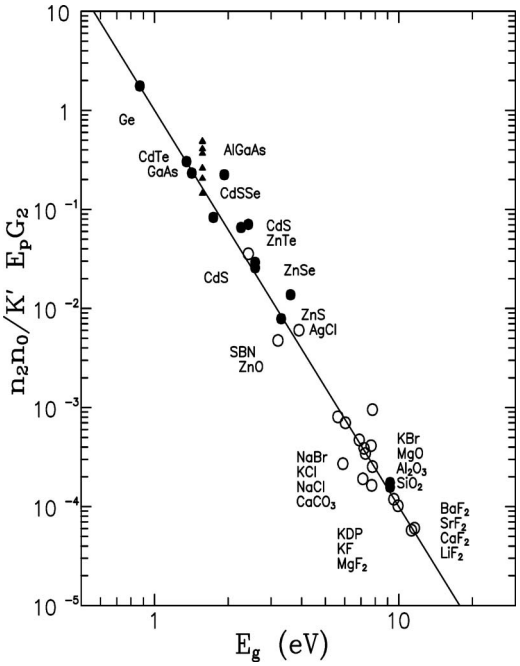

Log-log plot of the scaled dispersion function G_2 showing the E_g^{-1} dependence of n_2 [125].

tually be enhanced (or reduced) relative to the bulk case. For interband transitions between the valence and the conduction band(s), the oscillator strength μ_{cv} depends on

$$\mu_{cv} \propto \int_V \psi_v^*(\vec{r},\vec{k})(\vec{E}\cdot\vec{p})\psi_c(\vec{r},\vec{k})dr^3, \tag{4.28}$$

where $\vec{p}$ is the electron momentum operator, $\psi_v(\vec{r},\vec{k})$ and $\psi_c(\vec{r},\vec{k})$ are the electron wave functions in the valence and conduction bands, respectively, and the allowed wave vectors $\vec{k}$ depend on the dimensionality. For the *confined* states we can write

$$\psi(\vec{r},\vec{k}) = \sum c_k \phi(\vec{k},\vec{r}) \cong \phi(0,\vec{r}) \sum c_k e^{i\vec{k}\cdot\vec{r}} = \phi(0,\vec{r})F(\vec{r}), \tag{4.29}$$

where the function $F(\vec{r})$ is traditionally called the envelope function while $\phi(0,r)$ is the Bloch wave function at $\vec{k}=0$. As a result Eq. (4.28) can be expanded as

$$\int_V \phi_{v0}^* F_v^*(\vec{E}\cdot\vec{p})F_c dr^3 + \int_V F_v^* F_c \phi_{v0}^*(\vec{E}\cdot\vec{p})\phi_{c0} dr^3. \tag{4.30}$$

The first integral vanishes owing to the orthogonality between the valence and the conduction band Bloch wave function, while the other terms are slowly varying over any one unit cell. These terms can therefore be pulled out of the integral to give

$$\int_V F_v^* F_c \phi_{v0}^* (\vec{E}\cdot\vec{p})\phi_{c0} dr^3 \cong \sum [F_v^* F_c] \int_V \phi_{v0}^* (\vec{E}\cdot\vec{p})\phi_{c0} dr^3, \qquad (4.31)$$

where the sum is over unit cells in which $F_v^* F_c$ is slowly varying so that

$$\sum [F_v^* F_c] = \int_V F_v^* F_c dr^3. \qquad (4.32)$$

As a result the oscillator strength of the transition is determined by the integral $\int_V F_v^* F_c dr^3$, which is the overlap of the envelope functions and is either zero or nonzero depending on the parity of F_v^* and F_c.

In a similar way we can examine the *intraband oscillator strength of the transition between two states in the conduction band*. This is particularly important, since some two-photon transitions of interest will likely involve both a band-to-band transition and an intersubband transition. In this case we have

$$\int_V \Psi_{cj}^* (\vec{E}\cdot\vec{p})\Psi_{ci} dr^3 \qquad (4.33)$$

where i and j represent two different states in the conduction band. This can be expanded to

$$\int_V \phi_{cj0}^* \phi_{ci0} F_{cj}^* (\vec{E}\cdot\vec{p}) F_{ci} dr^3 + \int_V F_{cj}^* F_{ci} \phi_{cj0}^* (\vec{E}\cdot\vec{p})\phi_{ci0} dr^3. \qquad (4.34)$$

Here again we can examine both of these integrals over unit cells, and in this case the first integral is nonzero and the second is zero if we take them as Block wave functions. The first integral can again be zero or nonzero depending on the parity of F_{ej}^* and F_{ei}. However, one must consider that the $(\vec{E}\cdot\vec{p})$ operator will change the parity of F_{ei}.

The changes in the electron density of states in going from a bulk semiconductor (electron motion allowed in full three dimensions, k_x, k_y and k_z) to quantum wells (electron motion allowed in two dimensions, k_y and k_z), to quantum wires (electron motion restricted to one dimension, k_z) and finally to QDs in which the electron is completely confined (zero dimensions) are illustrated in Fig. 47 [102]. As the dimensionality is decreased, the electron density becomes progressively more localized in energy. In fact, in zero dimensions (for QDs), the resulting discrete energy spectrum resembles that found in molecular systems.

The interest in dimensionally reduced semiconductors for nonlinear optics has been limited primarily to quantum wells and QDs [102]. The reason is simply that these structures can be fabricated in a number of different ways. High-quality quantum wires have proved to be difficult to fabricate, and the main driver for their development has been quantum wire lasers [130].

While the physics of electron confinement from one to three dimensions on nanoscales is a fascinating and current subject, here we will focus on the nonlinear optical properties of such structures. Quantum wells have become a mature technology, and indeed nominal enhancement of resonant nonlinear optical properties has been reported. For type II–VI semiconductor crystallites imbedded in glass matrices (QDs) it is not clear whether significant enhancement occurs [131], although there has been a report of large enhancement for III–V nanocrystals in glass [132]. The magnitude of enhancement experimentally possible in GaAs QDs is still unresolved although progress has been made on iden-

Figure 47

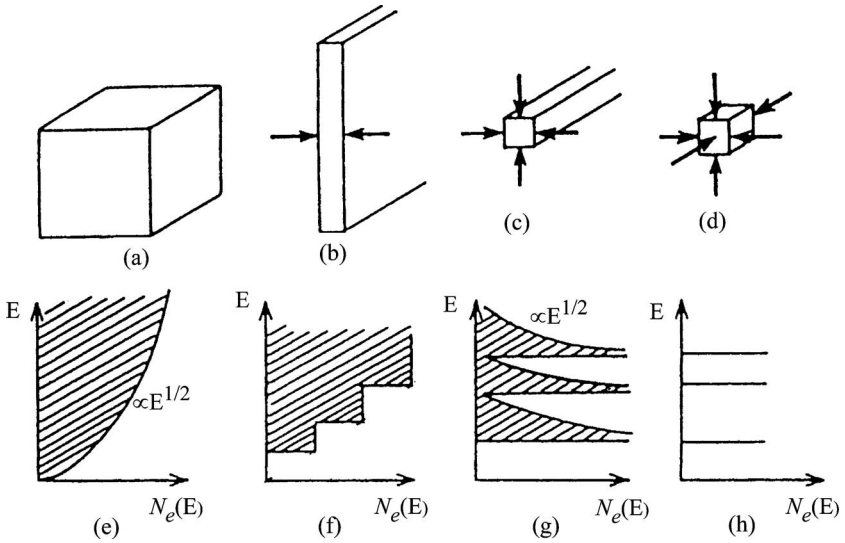

(a) No confinement in electron motion in conduction band (3D bulk sample). (b) Electron confinement in 1D (2D quantum wells). (c) Confinement in 2D (1D quantum wires). (d) 3D confinement (0D QDs). (e)–(h) Electron energy E versus density of states $N_e(E)$ for (e) 3D, (f) 2D, (g) 1D and (h) 0D semiconductors [102].

tifying fabrication conditions which yield the desired geometries of the dot structures, etc. where materials research, especially in the GaAs system, is still at the frontiers of the field.

4.3a. Quantum Wells

Quantum well structures have been fabricated in a surprisingly large number of materials, $Al_xGa_{1-x}As/GaAs$, In_xGa_{1-x} $As/GaAs$, InGaAsP/InP, and $GaN/Al_xGa_{1-x}N$, to name but a few [133–135]. However, the onus for nonlinear optics has been on AlGaAs/GaAs structures for a number of important reasons. First, this material system is widely used in the optics industry for making lasers and detectors, as well as modulators of various kinds. Second, the molecular beam epitaxy (MBE) fabrication technology is very highly advanced, and the proliferation of MBE machines throughout the world has resulted in easy availability of high-quality samples. Third, on the physics side, not only is there an excellent lattice match for the composite structures, which reduces the internal strain, the reduced electron mass is also very small, leading to large nonlinearities. Hence here we focus on this material system. Shown in Fig. 48 (top) is a typical quantum well structure composed of alternating AlGaAs and GaAs layers deposited by MBE [136]. As indicated in Fig. 48 (bottom) periodic modulation of the bandgap results, with the bandgap energy of GaAs being lower than that of AlGaAs. As a result, the lowest energy conduction band electrons are confined to the GaAs regions in allowed discrete energy states whose location and number depend on the detailed composition of the $Al_xGa_{1-x}As$. The electron wave functions are essentially sinusoidal across the GaAs layers and exponentially decaying in the AlGaAs layers. The general parity conditions discussed above require that states of the same symmetry in the valence and conduction bands be connected by transitions, i.e., the even symmetry states (e.g., cosinelike

wave functions) and the odd symmetry states. (When there is significant overlap of the wave functions between next-nearest-neighbor GaAs layers, the structure is called a "superlattice"). The resulting calculated absorption spectrum consists of a series of steps with transitions to confined energy levels E_m occurring from the valence band when the photon energy $\hbar\omega \geq E_m$ occurs as indicated in Fig. 49(b), until $\hbar\omega \geq E_{gap\ AlGaAs}$, at which point it becomes a smooth continuum of the kind associated with bulk semiconductor samples; see Fig. 49 [102]. Associated with each bound electronic state is an exciton level that produces discrete peaks in the absorption spectrum lying below the photon energy associated with that bound state.

The observed absorption spectra of quantum wells agree with these predictions, see Fig. 50 [136]. As expected, the onset of the absorption of bulk GaAs occurs at a lower photon energy than the quantum well. Furthermore the quantum well exciton features even at room temperature are better defined (narrower) than in the bulk sample. In addition they show new features not discussed above that require a more sophisticated treatment of the valence electrons than that allowed in a two-band model. Most specifically, the excitons associated with the light hole and heavy hole valence bands produce two separate peaks in the absorption spectrum.

The early definitive experimental work on the nonlinear properties of multiple quantum wells (MQWs), which showed enhanced nonlinear properties due to electron confinement and hence galvanized the field, is shown in Fig. 51 and reported in Table 13 [137]. This work focused on the nonlinear index change due to saturation of the exciton level. The intensity-dependent change in the exciton absorption coefficient was measured around resonance in a series of MQWs of different thickness, and the Kramers–Kronig relations were used to evaluate the corresponding index change. Both the maximum index change and the bandgap energy increase with decreasing well width were found. A very important feature of these results is that for a given MQW, the index change is sublinear in the incident intensity; i.e., an effective n_2 is not a useful concept similar to the results found in bulk semiconductors and discussed above. Enhancements of a factor of ~3 occur in the maximum refractive index change per excited electron in going

Figure 48

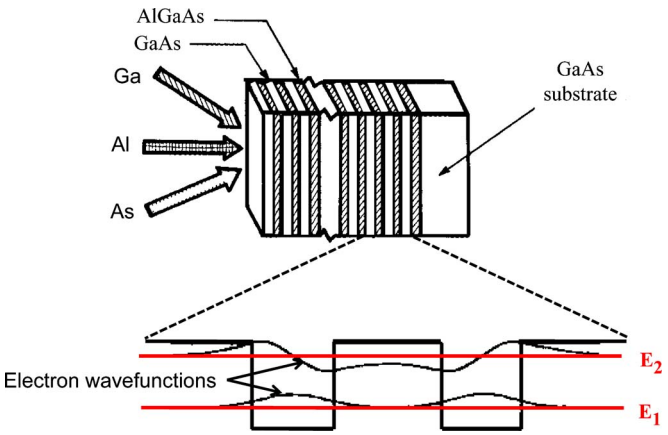

(a) Typical MBE-deposited GaAs–AlGaAs quantum well. (b) Example of energy levels and wave functions associated with electrons confined to the AlGaAs regions [136].

Figure 49

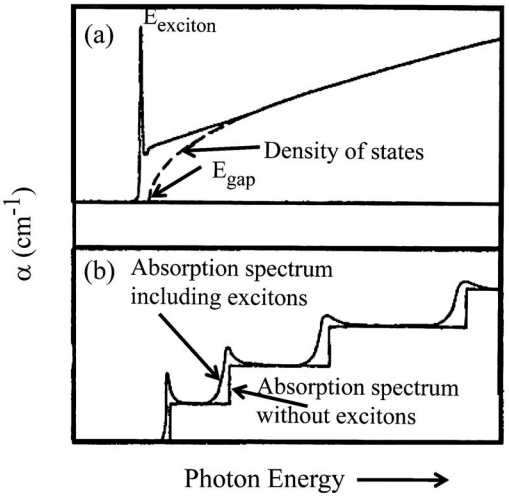

(a) Idealized absorption spectrum for bulk GaAs including the exciton. (b) Idealized absorption spectrum of an AlGaAs–GaAs quantum well [102].

from bulk GaAs to relatively small GaAs MQWs [137]. Because the absorption is different for each data point in Fig. 51, it is more useful (see Fig. 52) to discuss the index change per electron raised from the valence to conduction bands. However, this calculation also shows about a factor of 3 maximum enhancement for the MQWs. That is, the σ_r we used for describing bulk materials is enhanced.

Subsequent experiments on GaAs/AlAs quantum wells at frequencies around half the bandgap also showed enhancements of a factor of 2–3 in n_2 [138]. In yet another set of experiments, the nonlinearities of InGaAs/InAlGaAs quantum wells were measured near their bandgap. The resonant excitation and saturation of the exciton line in the 1.48–1.55 μm spectral range gave a value of n_2 of 6×10^{-10} cm^2/W or

Figure 50

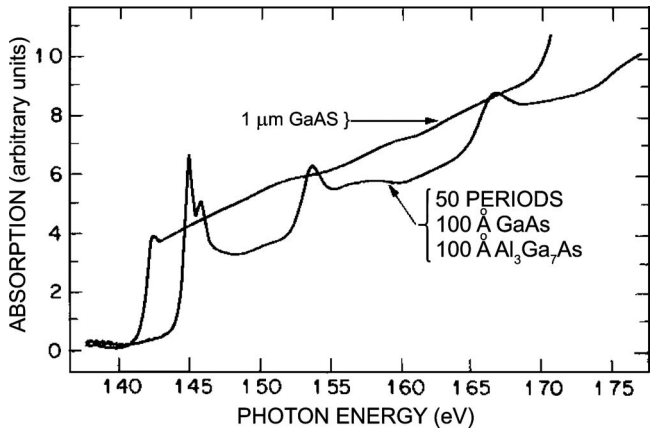

Measured room temperature absorption spectrum of a 1 μm GaAs platelet and of a 50 period quantum well of comparable thickness. Note that the net thickness of the quantum well sample is one half of the bulk sample [136].

Figure 51

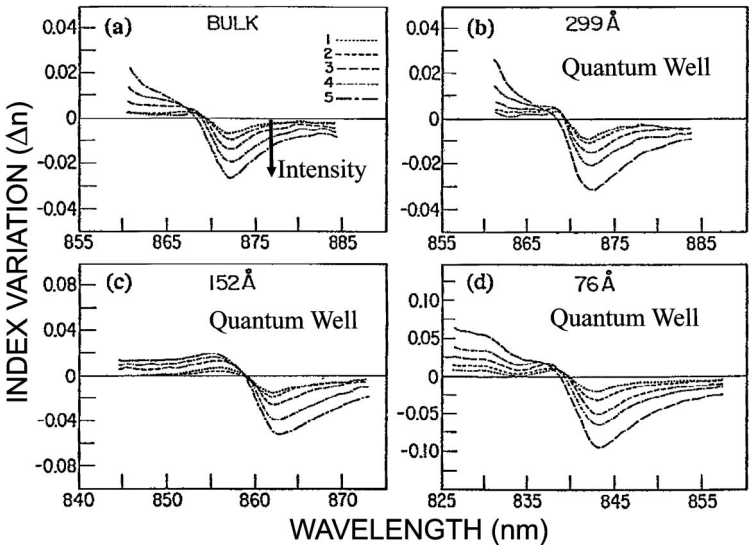

Refractive index change calculated by using the Kramers–Kronig relation on measured absorption coefficients for a variety of different quantum well widths at five incident power levels 0.67, 1.27, 2.65, 5.4, and 7 KW cm^2. Here $n_{2,\text{eff}}(\text{max}) \sim 1.5 \times 10^{-6}$ cm^2 W [137].

an index change of 6×10^{-4} for intensities in the 100 MW/cm^2 range [139]. However, unfortunately no comments were made on enhancements relative to bulk media [139]. Finally, large enhancements were reported for GaAs/AlGaAs quantum wells measured with 532 nm radiation, although no indication is given of the bulk values used for comparison at that wavelength [140]. The net conclusion is that modest enhancements of a factor of 2–3 have been measured.

4.3b. Quantum Dots

In fact, by reducing the size in all three dimensions, forming what is called a QD, the material properties exhibit the largest changes relative to the bulk semiconductor. The reason for this is that each atom in a bulk material sees its neighbors as replicas of itself. Hence very few atoms are at the edge or interface surface of the material, so that the material parameters or response of the material to an external stimulus is basically determined by the atoms in the bulk. Thus in bulk media the surface atoms can almost always be neglected, even though their environment or bonding to their neighbors is very different.

Table 13. Measurements of Nonlinear Refraction Coefficient n_2 and Absorption in Various MQWs

Material	λ_{bandgap} (nm)	n_2 (cm^2/W)	α_{NL} (cm/GW)	λ (nm)
GaAs/AlGaAs [137]	~840–870	$\sim 1.5 \times 10^{-6}$	6	816
GaAs/AlAs [138]	~740	5.5×10^{-13}	4	1545
InGaAs/InAlGaAs [139]	~1600	6.0×10^{-10}	6.6×10^4	1500
GaAs/AlGaAs [140]		6.5×10^{-11}	6.5×10^5	532

Figure 52

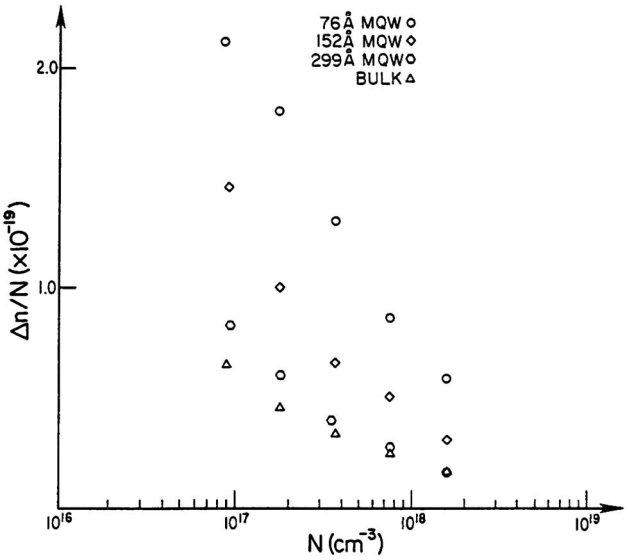

Maximum change in refractive index per carrier concentration versus the carrier concentration [137].

On the other hand, for a nanosize structure like a QD the situation is dramatically different [102]. In this case all of the atoms are influenced by the fact that the structure has a surface even though the nanostructure may be a cube of 100 atoms on a side or composed of a million atoms. The consequence of the effect of the surface atoms and small volumes is that the energy level structure of the material is dramatically changed. Since the optical properties of a material depend intimately on its electronic structure, all of the material properties become dependent on size. This result implies that the nonlinear optical coefficients at a specific wavelength can be tuned by changing QD dimensions.

In many ways QDs made by MBE have features that resemble those of molecules such as discrete optical transitions. However, it is not at all obvious that the change in behavior due to a decrease in size will in practice always enhance nonlinear optical parameters as opposed to decreasing their nonlinear efficiencies.

The simplest approximation is to assume spherically symmetric crystallites and a two-band model. (Assuming ellipsoids has had only a minor effect on theoretical results [141,142]. For example, the conduction band wave function $F_c(\vec{r})$ can be expressed in terms of the product of spherical Bessel functions of order ℓ, $j_\ell[\beta_{\ell p}(r/r_0)]$, where r_0 is the crystallite radius and $\beta_{\ell p}$ is its pth zero and spherical harmonics $Y_\ell^m(\theta,\varphi)$, so that [131]

$$F_c(\vec{r}) = B_{\ell p} j_\ell[\beta_{\ell p}(r/r_0)] Y_\ell^m(\theta,\varphi), \tag{4.35}$$

where $B_{\ell p}$ is a normalization constant. The valence band wave function $F_h(\vec{r})$ has a similar form. Taking the zero of energy at the top of the valence band, the energy levels for the conduction electrons occur at

$$E_{\ell p}^c = E_{\text{gap}} + \frac{\hbar^2 \beta_{\ell p}^2}{2 m_c r_0^2}, \tag{4.36a}$$

with successive levels $1s$ ($\ell=0$, $p=1$), $1p$ ($\ell=1$, $p=1$), etc. and for the valence band

$$E^{h}_{\ell' p'} = \frac{\hbar^2 \beta^2_{\ell' p'}}{2 m_h r_0^2}. \tag{4.36b}$$

The valence and conduction band energy levels are shown schematically in Fig. 53. Since $\mu_{cv} \propto \int_V F_v^* F_c dr^3$, the selection rules are $\delta_{\ell\ell'}$, $\delta_{nn'}$, $\delta_{mm'}$; so allowed transitions (in this model) can occur only between similar symmetry states in the valence and conduction bands. In addition, there is a correction to the energies due to the interaction between the hole and electron pair; so the resonance frequency for a transition is given by

$$\hbar\omega_{\ell p} = E_g + \frac{\hbar^2 \beta^2_{\ell p}}{2 m_h r_0^2} + \frac{\hbar^2 \beta^2_{\ell p}}{2 m_e r_0^2} - b\frac{e^2}{\varepsilon_r r_0}, \tag{4.37c}$$

where b is a numerical factor equal to 1.8 for $ps \rightarrow ps$ transitions.

Note that a different notation is frequently used when electron spin and spin–orbit coupling is included [131]. The valence band(s) arises from p orbitals, which in the simplest case are sixfold degenerate (i.e., p_x, p_y, and p_z with two possible spin states each). Normally spin–orbit coupling lifts the degeneracy and results in a fourfold degenerate $pP_{3/2}$ valence band level and a twofold degenerate $pP_{1/2}$ level. The complication arises because of the coupling between the atomic angular momentum **J** and the angular momentum **L** associated with the envelope functions. As explained in detail in [131], for the lowest energy levels, even symmetry states involving $\ell=0$ and $\ell=2$ are denoted $pS_{3/2}$ (in the valence band and pS_e in the conduction band) and the lowest odd symmetry energy levels are $pP_{3/2}$ for $\ell=1$ and $\ell=3$, etc. It is this notation that is frequently used to describe transitions in QDs.

Glasses doped with II–VI semiconductor crystallites: Semiconductor crystallites doped into various glasses have been known for many decades as absorp-

Figure 53

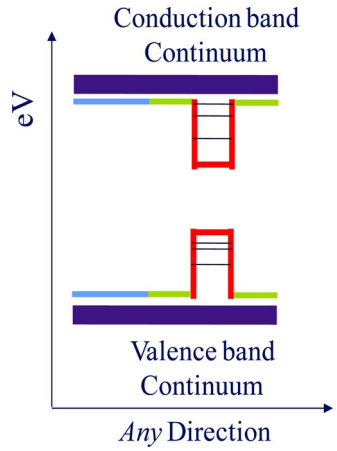

Schematic representation of the energy spectrum of the valence and conduction bands for a QD.

tion edge filters produced commercially by companies such as Schott and Corning. By varying the crystallite size down to nanometer dimensions, the absorption edge can be tuned over >100 nm, a well-known feature of QDs in general. Early degenerate four-wave mixing experiments near resonance by Jain and Lind stimulated interest in the nonlinear optics community in these systems [143]. The most common semiconductor constituents have been the II–VI compounds CdS, CdSe, and CdTe (reviewed in [131]).

A consensus on the nonlinear properties of these semiconductor doped glasses has been slow to emerge in the literature because of the complexity of these systems. Much of the work has been summarized in the excellent review article by Banfi *et al.* [131]. Three mechanisms for exciting the semiconductor electrons out of the valence band have been identified. First there is the usual absorption of a photon to move an electron from the valence to conduction band as discussed above. The narrow luminescence peak associated with this process has a relaxation (recombination) time of nanoseconds. Second, there are trapping states due to bonds dangling from the glass or semiconductor or both at the interface with the glass. This process leads to a broad fluorescence peak with relaxation times of microseconds. The broad distribution is indicative of a broad spectrum of trap states. Third, photodarkening of the glass, which depends on the integrated optical flux, also occurs. This effect is believed to be due to the ejection of electrons out of the semiconductor into the glass disordered matrix where they are trapped. This darkening, which is strongly sample dependent, can be eliminated by heating the sample [144]. The contributions of these processes to the net nonlinearity can have different signs and different relaxation times, depending on the particular system under consideration. Furthermore, these processes are coupled. For example, in a darkened sample the recombination time goes from nanoseconds to picoseconds [145,146].

Whether quantum size effects are relevant depends on the ratio of the crystallite radius r_0 to the exciton Bohr radius a_B, i.e., $R = r_0/a_B$. For example, a_B is 3.2, 5.6 and 7.4 nm for CdS, CdSe, and CdTe respectively [131]. For $R < \sim 3$, significant quantum size effects have been found to appear. See, for example, the complex absorption spectrum measured in CdSe-doped glasses shown in Fig. 54 [147]. Many different transitions with widely differing transition strengths between localized states are shown theoretically to contribute and their relative contribution depends strongly on the crystal size.

The situation with respect to the nonlinear properties has been complicated by a number of factors [131]. For example, there is always a distribution in the crystallite sizes resulting from the fabrication methods used, which, given the strong dependence of the electronic states and transition dipole moments between them on size as illustrated in Fig. 54, tends to smooth out the optical response [131]. This affects primarily the resonant response. Unless specifically measured, the average size of the crystallites and their density is estimated to at best an accuracy of $\pm 10\%$. Still another complicating factor is the fact that the crystallite composition, for example in CdSSe glasses, is *not* the same as that of the starting material [148]. Furthermore, free-carrier absorption is an important contribution to the effective 2PA when measured with picosecond and longer pulses, and the two effects were infrequently separated from one another experimentally [131]. In summary, the detailed properties of the samples and their contributing physics were in many cases not sufficiently well defined.

The resonant intensity-dependent index and absorption change was measured,

Figure 54

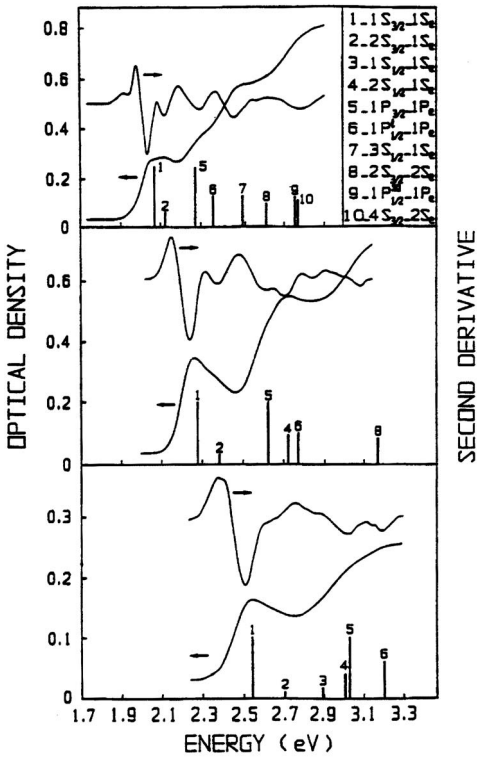

Low-temperature absorption spectra and their second derivative for three CdSe-doped glasses with mean crystal radii of 3.8, 2.6, and 2.1 nm, from top to bottom. The calculated contributing transitions are shown as stick spectra and are identified in the inset [141,142].

for example, in a CdSSe-doped glass with average crystallite size of 11 nm, at the boundary between quantum confinement and bulk sample behavior [149]. The experimental results for the index change are shown in Fig. 55 for a crystallite concentration of $\sim 10^{-3}$. The index change reported was $\sim 10^{-5}$, in reasonable agreement with the values both predicted from the partly phenomenological semiconductor plasma theory based on bulk semiconductor parameters and by applying the Kramers–Kronig relations to the observed absorption change [149].

Banfi and coworkers have carried out extensive measurements on the nonresonant properties of II–VI doped glasses, accompanied by complete characterization of relevant sample properties [131]. The key definitive results summarized in the excellent review paper by these authors are shown in Figs. 56–58 [131]. Both femtosecond and picoseconds pulses at different frequencies were used on both bulk samples and a series of nanocrystallites with crystal radii varying over 4.8–14.0 nm for CdTe and 5.2–13.5 nm for $CdS_{0.9}Se_{0.1}$. To within a factor of 2 (which is comparable with the overall experimental uncertainty), no significant variation in $\mathrm{Imag}[\chi^{(3)}](\propto \alpha_2)$ versus crystallite size was found for all the cases and wavelengths studied, and the values were essentially equal to the bulk sample value, i.e., no enhancement was observed; see Fig. 56. Given that varying the crystal radius varies the semiconductor bandgap, the authors also tested whether the nonresonant nonlinearity of quantum confined samples followed the trends predicted for bulk samples discussed in Subsection 4.2, specifically the functions $F(\omega)$ and $G(\omega)$ in

Figure 55

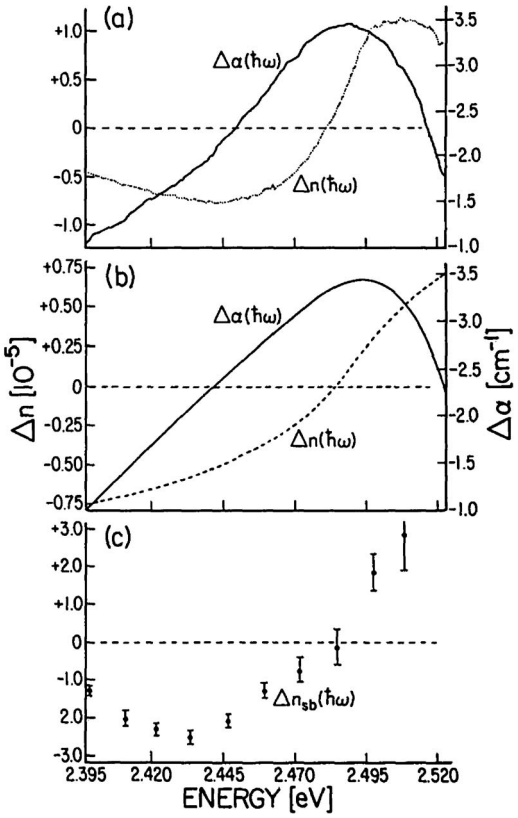

Absorptive changes and corresponding dispersive index changes. (a) Experimental results: $\Delta\alpha=\alpha(N=10^{18}\ \mathrm{cm}^{-3})-\alpha(N=0)$. (b) Theoretical results, $\Delta\alpha=\alpha\mathrm{p}(\mathrm{I}=3\ \mathrm{MW/cm}^2)-\Delta\alpha(\mathrm{I}=200\ \mathrm{kW/cm}^2)$. (c) Measured dispersive index changes, Δn_{sb}, using single-beam interferometry [149].

Eqs. (4.20) and (4.4). The results in Figs. 57 and 58 show agreement with the bulk semiconductor results to within a factor of 2. The key conclusion from these detailed studies is that quantum size effects have at most a factor of 2 effect on the nonresonant nonlinearities for the values of R investigated!

Another approach rooted in chemistry is to form semiconductor crystallites in colloidal suspensions via chemical reactions. Recently additional 2PA experiments were reported on small II–VI crystallites made this way, also over a broad range of frequencies [150]. The crystallite sizes for CdTe ($r_0=3.2, 6.6$ nm) and CdSe ($r_0=1.9, 2.1, 2.2, 2.4$ nm) were smaller than those discussed above in the doped glasses studied by Banfi *et al.* [131]. An example of these results is shown in Fig. 59. Two cases were studied, the degenerate 2PA case, i.e., when two photons of the same frequency were absorbed, and the nondegenerate case, when the input photons had different frequencies. Note the oscillatory behavior observed in α_2, which is now evident for these smaller crystallites, versus frequency due to quantum confinement. It was found that including band mixing in the theory gave a significant improvement to their agreement between theory and experiment, although the agreement was less satisfactory for the smallest crystallites, probably because the effects of the split-off band were not included in the Kane k-p theory. The experimental results showed that the volume fraction normalized 2PA cross section actu-

Figure 56

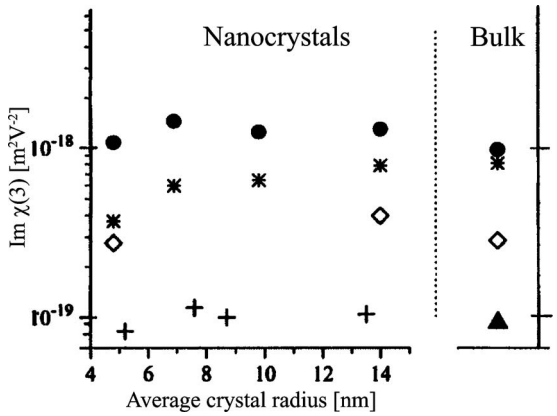

Measured $\mathrm{Im}(\chi^{(3)})$ versus crystallite radius r_0 and for a bulk crystal at wavelengths of 1.2 μm (●), 1.4 μm (∗) and 1.58 μm (◇) for CdTe and at 0.79 μm (+) for $CdS_{0.9}Se_{0.1}$ nanocrystals and bulk CdS [131].

ally *decreased* with decreasing crystallite radius for $R = r_0/a_B < 1$. This decrease is small and agrees with the expectation for the small reduction in density of available states as the dot size decreases. It would be expected that these results would be applicable to other hosts and is consistent with the results of Banfi *et al.* for glasses [131].

Unfortunately, the anticipated enhancements of optical nonlinearities were not

Figure 57

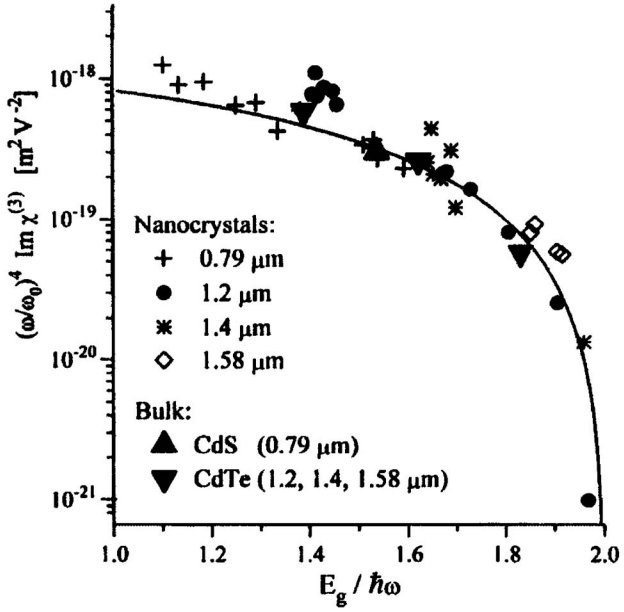

Plot of the scaled quantity $(\omega/\omega_0)^4\mathrm{Im}(\chi^{(3)})$ for bulk CdS and CdTe crystals as well as CdTe and $CdS_{0.9}Se_{0.1}$ nanocrystals with the radii shown in Fig. 56. The solid curve is a fit to Eq. (4.20) [131].

realized for glasses doped with II–VI semiconductors. Furthermore, these doped glasses were found to be unsuitable for a range of nonlinear integrated optics applications involving all-optical switching devices because of the semiconductor properties of the II–VIs involved. Namely, these bulk materials have a large effective electron mass, which produces an unfavorable trade-off between index change and absorption and the index change saturates at a small value [151,152].

There has been limited work performed on QDs in other materials systems: the results are summarized in Table 14 In a study of III–V semiconductors using pump–probe Z-scan studies of GaAs nanocrystals grown in porous glass, the nonlinear coefficient reported is 1.3×10^{-11} cm^2/W. The bound electronic nonlinear refraction in the quantum confined sample was found to be enhanced by a factor of 30 relative to that of the bulk crystal [132]. This is the only example of large enhancements reported in GaAs nanocrystals.

The other QD system in Table 14 involves a complicated sample structure. The Mn:ZnSe samples consist of a MnSe core, $Zn_{1-x}Mn_xSe$ diffusion region, and an outer ZnSe layer. The authors found the nonlinearity to decrease with decreasing QD diameter.

It would appear that the variation in results from different experiments indicates that more careful experiments are needed.

Prospects for GaAs QDs: However, based on the enhancement obtained from the previously discussed MQW work, it is possible that the GaAs system could yield still better results for QDs. On the other hand, based on the II–VI QDs just discussed, predicting enhancements can be a dangerous business. Controlled growth of 0D QDs in the GaAs system has only been achieved in the past decade or so; so there are expectations for new nonlinear optics measurements to test the enhancement hypothesis in this technologically important material system.

The Stranski–Krastanov (SK) MBE growth mode is the preferred method for

Figure 58

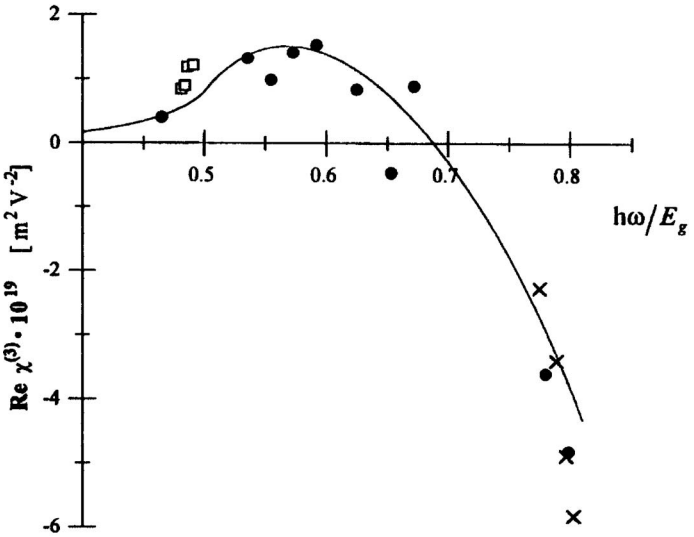

Plot of Re($\chi^{(3)}$) versus $\hbar\omega/E_{gap}$ for commercial semiconductor doped glasses (●), $CdS_{0.9}S_{0.1}$ series glasses (□) and CdTe series glasses (×). The solid curve is the best fit to Eq. (4.26) [131].

Figure 59

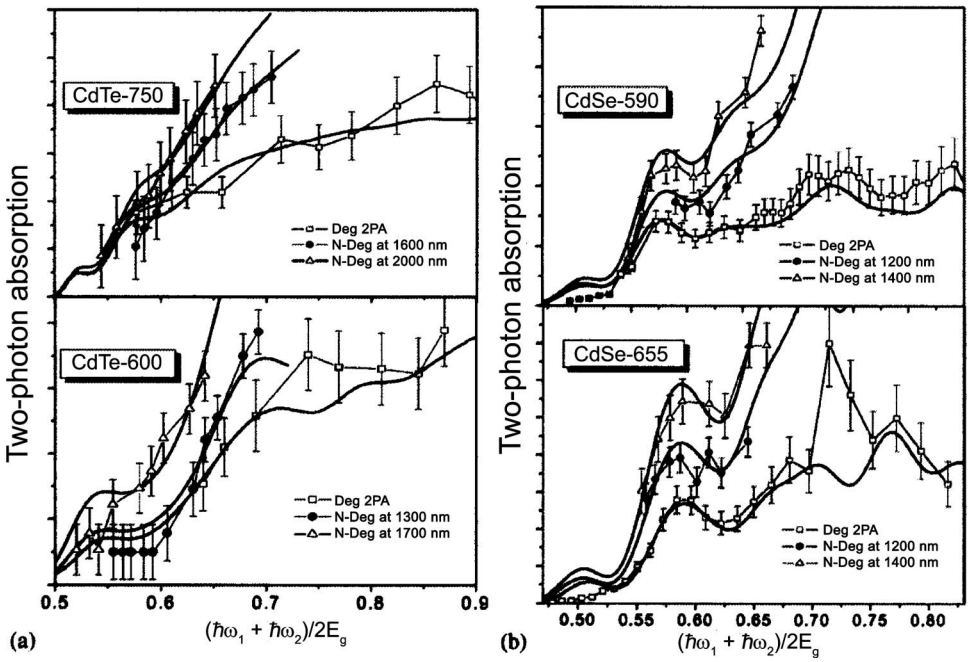

Degenerate and nondegenerate 2PA spectra for two CdTe doped glasses with crystallite radii of 6.6 nm (CdTe-750) and 3.2 nm (CdTe-600) and for two CdSe doped glasses with crystallite radii of 2.4 nm (CdSe-590) and 2.1 nm (CdSe-600) [150].

growing GaAs QDs and capping them with higher bandgap material [154,155]. For this growth mode the deposited material has a slightly larger lattice constant than the substrate. For example, in this approach a material such as InAs is deposited on a substrate like GaAs or AlAs. InAs has a lattice constant that is about 7% larger than that of GaAs or AlAs; so the small lattice mismatch introduces strain. During SK growth, the first few layers of InAs, typically 1.6 monolayers, forms a pseudomorphic 2D layer, called the "wetting layer" [Fig. 60(a)]. After this critical thickness, however, 2D growth is no longer energetically favorable, and the energy reduction in strain more than compensates for the increase in surface energy as the 2D islands organize or self-assemble [156] into 3D islands [Fig. 60(b)].

Under typical growth conditions the buried QDs are observed to be well aligned but significantly nonuniform in size, shape, and position [157–159]. As shown in Fig. 61 the QD structures are composed of different shapes. While there has been significant progress in improving the homogeneity of both morphology and positioning of QDs, achieving control to better than 10% remains a considerable

Table 14. Nonlinearities Reported in Various QD Systems

Material	n_2	α_{NL}	λ (nm)
Mn:ZnSe [153]	1.4×10^{-14} cm^2/W	8.4 cm/GW	800
GaAs in porous vicor glass [132]	1.3×10^{-11} cm^2/W	80 cm/GW	1064

Figure 60

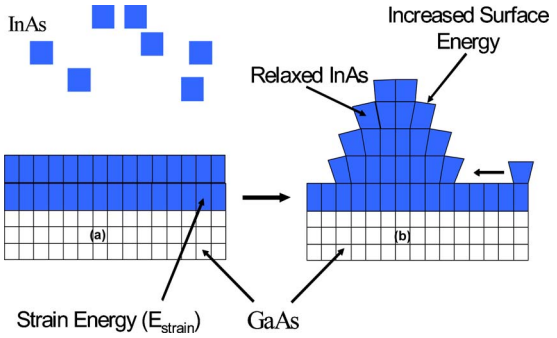

Strain driven Stranski–Krastanov formation of a QD.

challenge. For the SK growth, typical densities are 10^{10}–10^{12} cm^{-2}, although much smaller densities are possible with care [160]. Meanwhile typical SK QD diameters [161] are from 10 to 30 nm. Depending on the growth conditions, as shown in Fig. 62, QDs can grow randomly spaced or in regular rows. Such regularity raises the possibility of a cooperative QD response.

Figure 61

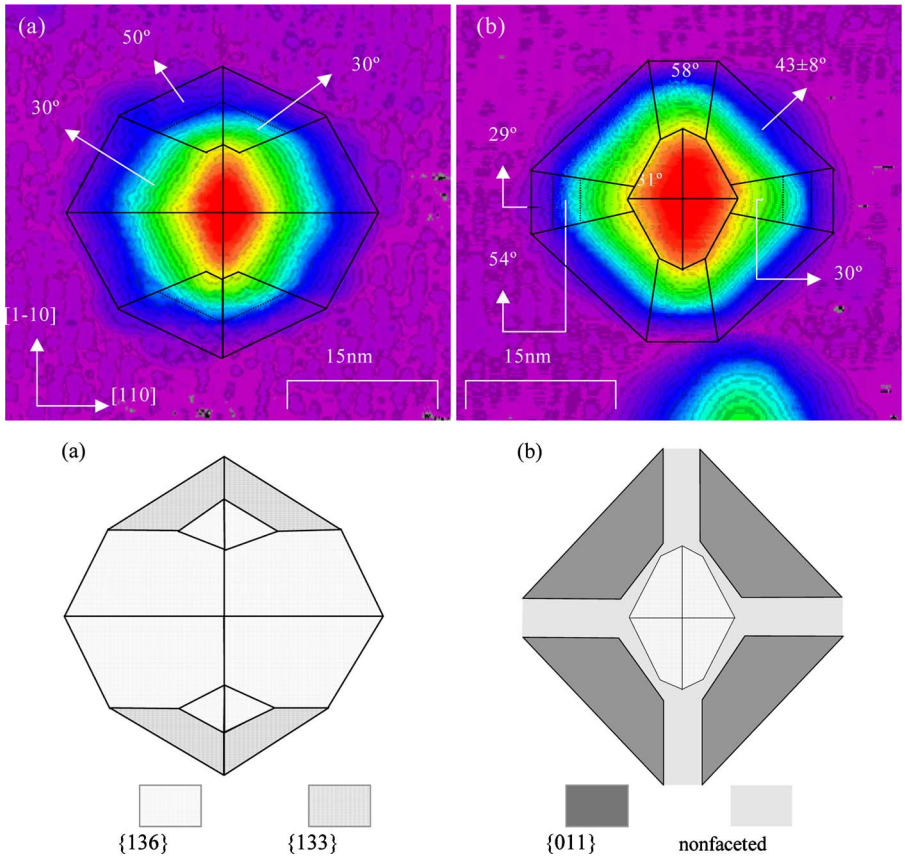

Scanning tunneling microscope image of the structure for two different QD shapes observed.

Figure 62

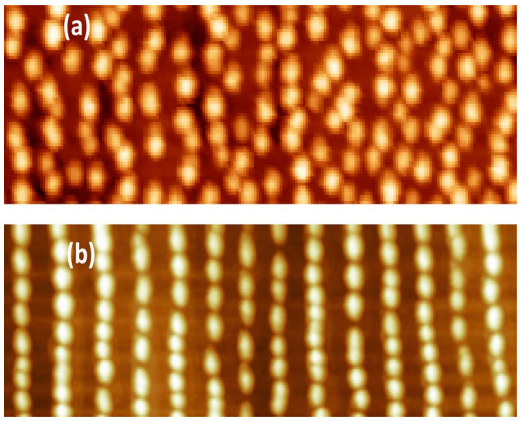

(a) One layer of QDs that are randomly distributed; (b) several layers of QDs that are influenced by the vertical stacking to form a vertical and lateral alignment that results in a large lateral separation between QDs.

A very different approach to producing GaAs QDs is based on colloidal growth [162–165]. Colloidal QDs are synthesized in a beaker from precursor compounds dissolved in solution. The synthesis is based on a three-component system composed of precursors, organic surfactants, and solvents. When the solution is heated to a sufficiently high temperature, the precursors chemically transform into monomers. Once the concentration of monomers reaches a supersaturated solution the nanocrystal self-assembled growth begins and is stabilized by a layer of surfactants attached to their surface. The typical size of a colloidal QD is smaller than their MBE counterpart and is about 2–8 nm in diameter. The smaller size therefore results in high densities of about 10^{14} cm^{-2}. The application of colloidal QDs to the broad field of nonlinear optics may be larger than the possibilities for MBE nanostructures because of their significantly lower fabrication cost. However, even colloidal QDs suffer from poor uniformity of size with an inhomogeneity that is typically also of the order of 10%.

4.3c. Summary for Quantum Confinement Structures

For both quantum wells and QDs it is clear that the expectation of a dramatically large enhancement in the nonlinear optical coefficients has not been clearly and consistently demonstrated, and one can ask why? Basically the reason is that estimates of the potential enhancement are complicated and that all of the experimental conditions, material preparation factors, and competing physics are difficult to control.

A brief summary of the more important issues is given next. For example, we might expect the enhancement due to confinement to first increase with decreasing size owing to the increase in the overlap of the wave functions, but at some point we might expect a decrease with decreasing size as the overlap weakens as the lowest energy state moves near the top of the well. Furthermore, the comparison between low-dimensional and bulk material is again difficult because of linewidth and fill factor issues that can significantly lower the effective enhancement. Another issue of importance is that low-dimensional structures have a high density of surface states that are localized at the interface between the semi-

conductor's well and barrier. That the optical excitation to these states is stronger than in the bulk and second-harmonic generation at an interface is one good example. Obviously, the nonlinear behavior of low-dimensional structures could have significantly larger interface issues. Yet another possibility for an observed enhanced nonlinear behavior could be the differences in the nonradiative lifetime. The discrete nature of the energy levels in a low-dimensional structure presents the potential of a longer nonradiative lifetime, a larger excited state population, and a narrower spectral linewidth. On the other hand, surface and interface states can have the opposite effect, shortening the nonradiative lifetime, and must also be considered.

All of these issues, and most likely some that we did not recognize, play a role in the nonlinear interaction between light and low-dimensional structures. Many of the early investigations of the enhancement due to confinement have not yet paid careful attention to many of these issues. In many ways, the question of nonlinear optical effects in confined structures begs for more comparison between theory and carefully designed experiments in order to single out different issues and develop a clear understanding of the effects of decreasing the dimensions of nonlinear optical materials in order to take advantage and optimize the potential enhancement and therefore engineer more efficient nonlinear optical materials.

5. Nuclear (Vibrational) Contributions to n_2

When light couples via electric dipole interaction to other (than electronic) normal modes in matter, there is an intensity-dependent change in the refractive index [166]. Coupling to vibrational modes that modulate the molecular polarizability can give rise to significant contributions via $n_{2,\mathrm{nuc}}$ (10%–20% in glasses). The formulation given below is for the cw case, normally valid for pulse widths greater than $1-10$ ps and has as its starting point a single vibrating molecule.

It is well known that an isolated molecule containing N atoms can typically have $3N-6$ vibrational degrees of freedom. Some are dipole active, i.e., they modulate the permanent dipole moment, and others are Raman active, i.e., they modulate the molecule's polarizability [167]. Dipole active modes are observed in the linear absorption spectrum, whereas Raman active modes participate in nonlinear optical interactions such as Raman scattering and stimulated Raman scattering. In condensed matter these rules can be broken, and weak Raman active modes can appear in the linear absorption spectrum and vice versa.

Since this effect is rarely found in textbooks, we give a more detailed discussion than in previous sections. The polarizability for a molecule can be written as [167,168]

$$\bar{\alpha}_{\ell m} = \left[\bar{\alpha}^{L}_{\ell m} + \sum_{\beta} \bar{q}^{\beta}_{n} \left. \frac{\partial \bar{\alpha}^{\beta}_{\ell mn}}{\partial \bar{q}^{\beta}_{n}} \right|_{\bar{q}^{\beta}_{n}=0} \right]. \tag{5.1}$$

The key material parameter is the nonlinear polarizability tensor $\partial \bar{\alpha}^{\beta}_{\ell mn} / \partial \bar{q}^{\beta}_{n}$, which characterizes the coupling between the light and the Raman active vibrational modes. In Eq. (5.1), the summation over β is taken over all of the Raman active vibrational modes, which have a vibrational amplitude $\bar{\vec{q}}^{(\beta)}$. For a single cw incident field $E_{\ell}(\vec{r},t)$ of frequency ω, a nonlinear polarization parallel to the incident field [for $n_{2\|,\mathrm{nuc}}(-\omega;\omega)$] is induced in the molecule of the form

$$\bar{p}_\ell^{\mathrm{NL}} = \sum_\beta \bar{q}_n^\beta \left.\frac{\partial \bar{\alpha}_{\ell\ell n}^\beta}{\partial \bar{q}_n^\beta}\right|_{\bar{q}_n^\beta=0} [f^{(1)}]^2 E_\ell, \tag{5.2}$$

which includes the local field correction $f^{(1)}$. The potential energy associated with this interaction is given by

$$\bar{V}_{\mathrm{int}} \propto -\int \bar{p}_\ell^{\mathrm{NL}} dE_\ell = -\frac{1}{2}\sum_\beta \bar{q}_n^\beta \left.\frac{\partial \bar{\alpha}_{\ell\ell n}^\beta}{\partial \bar{q}_n^\beta}\right|_{\bar{q}_n^\beta=0} [f^{(1)}]^2 E_\ell E_\ell. \tag{5.3}$$

From classical mechanics, there is an all-optical force $\vec{\bar{F}}^\beta$ that induces the vibration in the βth mode (approximated as a simple harmonic oscillator) in the molecule given by

$$\bar{F}_n^\beta = -\frac{\partial}{\partial \bar{q}_n^\beta} V_{\mathrm{int}} = \frac{1}{2} \left.\frac{\partial \bar{\alpha}_{\ell\ell n}}{\partial \bar{q}_n^\beta}\right|_{\bar{q}_n^\beta=0} [f^{(1)}]^2 E_\ell E_\ell = \bar{m}_\beta [\ddot{\bar{q}}_n^\beta + \bar{\Gamma}_\beta \dot{\bar{q}}_n^\beta + \bar{\Omega}_\beta^2 \bar{q}_n^\beta], \tag{5.4}$$

where $\bar{m}_\beta$ is the effective mass associated with the vibration and $\bar{\Gamma}_\beta^{-1}$ is the optical phonon lifetime [168]. Note that the field product contains frequencies at 2ω and 0, which drive the vibrations at $\Omega=0$ and $\Omega=2\omega$. Here $\bar{\Omega}_\beta$ is the normal mode (natural) vibration frequency versus Ω, which is the frequency at which $\bar{q}_n^\beta$ is driven by the mixing of the optical fields. The response due to 2ω clearly depends on the wavelength of the incident light. In the subsequent discussion we focus on the dc term, although the harmonic term will progressively contribute more to the process as the light frequency is decreased toward the vibrational frequency. Substituting the solution to Eq. (5.4) into (5.2) gives, in the molecule's frame of reference,

$$\bar{p}_\ell^{\mathrm{NL}}(\vec{r},t) = \sum_\beta \frac{1}{8\bar{m}_\beta \bar{\Omega}_\beta^2} \left[\left.\frac{\partial \bar{\alpha}_{\ell\ell n}^\beta}{\partial \bar{q}_n^\beta}\right|_{\bar{q}_n^\beta=0} \right]^2 [f^{(1)}]^4 |\mathcal{E}_\ell(\omega)|^2 \mathcal{E}_\ell(\omega) e^{i(\vec{k}\cdot\vec{r}-\omega t)} + \mathrm{c.c.} \tag{5.5}$$

Inserting into the slowly varying phase and amplitude approximation gives

$$\Rightarrow n_{2\parallel,\mathrm{nuc}}(-\omega;\omega) = \sum_\beta \frac{N}{4n_\ell^2(\omega)\bar{m}_\beta \varepsilon_0^2 c \bar{\Omega}_\beta^2} \left[\left.\frac{\partial \bar{\alpha}_{\ell\ell n}^\beta}{\partial \bar{q}_n^\beta}\right|_{\bar{q}_n^\beta=0} \right]^2 [f^{(1)}]^4. \tag{5.6}$$

Similar considerations give

$$n_{2\perp,\mathrm{nuc}}(-\omega;\omega) = \sum_\beta \frac{N}{4n_\ell(\omega)n_m(\omega)\varepsilon_0^2 \bar{m}_\beta c \bar{\Omega}_\beta^2} \left[\left.\frac{\partial \bar{\alpha}_{\ell mn}^\beta}{\partial \bar{q}_n^\beta}\right|_{\bar{q}_n^\beta=0} \right]^2 [f_\ell^{(1)} f_m^{(1)}]^2. \tag{5.7}$$

Most of the interest in $n_{2,\mathrm{nuc}}$ has been for glasses that have small Kerr nonlinearities, especially in the case of fused silica. The principal problem in evaluating $n_{2,\mathrm{nuc}}$ has been the lack of information about the molecular Raman polarizability tensor and the fact that disorder etc. in the glassy state leads to continuous rather than discrete Raman spectra. There is, however, a wealth of Raman scattering spectra that

arise from thermally excited vibrations in a medium. For a single molecule, the x-polarized Raman spectrum in the limit $k_B T \gg \hbar\bar{\Omega}_\beta$ (typically room temperature) is given by

$$\frac{I_\parallel(\omega_s)}{\Delta\Omega I(\omega_p)} = \sum_\beta \frac{\omega_s^4}{8c^4(4\pi)^2\varepsilon_0^2}\left\langle \left| \frac{\partial\bar{\alpha}_{\ell\ell n}^\beta}{\partial\bar{q}_n^\beta}\bigg|_{\bar{q}_n^\beta=0} \right|^2 \right\rangle \frac{k_B T}{\bar{m}_\beta\bar{\Omega}_\beta^2} \times\left\{ \frac{\bar{\Gamma}_\beta/2\pi}{(\omega_s-\omega_p+\bar{\Omega}_\beta)^2+\bar{\Gamma}_\beta^2} + \frac{\bar{\Gamma}_\beta/2\pi}{(\omega_s-\omega_p-\bar{\Omega}_\beta)^2+\bar{\Gamma}_\beta^2} \right\}, \quad (5.8)$$

which contains the same Raman tensor as $n_{2\parallel,\mathrm{nuc}}$ [168]. Here $\Delta\Omega$ is the standard notation for the solid angle subtended at the detector in spontaneous Raman scattering and is not related to the sound wave frequency.

The glass disorder can be described by a distribution of phonon frequencies $f(\bar{\Omega}_\beta-\bar{\Omega}_{\beta 0})$. Comparing the single-molecule Raman spectra (and Raman gain) data with the Raman spectra of the glasses shows that for the spectral width $\Delta\bar{\Omega}_\beta$ of $f(\bar{\Omega}_\beta-\bar{\Omega}_{\beta 0})$ with the approximation $\Delta\bar{\Omega}_\beta \gg \bar{\Gamma}_\beta$, the Lorenzian functions can be written as $\delta(\omega_s-\omega_p\pm\bar{\Omega}_\beta)$. Integrating over the distribution $f(\bar{\Omega}_\beta-\bar{\Omega}_{\beta 0})$ and eliminating the Raman polarizability gives

$$n_{2\parallel,\mathrm{nuc}}(-\omega;\omega) \cong \frac{c^3(4\pi)^2}{n^2(\omega)\omega^4 k_B T}\frac{\int_0^\infty I_\parallel(\omega_s)d(\omega-\omega_s)}{\Delta\Omega I(\omega)}. \quad (5.9)$$

In this equation $\int_0^\infty I_\parallel(\omega_s)d(\omega_p-\omega_s)$ is the absolute value of the integrated spontaneous Raman spectrum for the Stokes side over the solid angle $\Delta\Omega$, a relatively easy measurement.

The OKE technique referred to in Table 15 consists of the excitation of a total index change with an intense femtosecond pulse and then use of a second femtosecond pulse to probe the index change [169,171]. A typical result is shown in Fig. 63(a). The ringing corresponds to the vibrational response when the ultrashort pulse of duration Δt excites the vibration as a δ-function impulse, i.e., $\Delta t\Omega_\beta \ll 1$. Detailed modeling shows that after about ~10 ps the measured $n_{2,\mathrm{eff}} = n_{2,/\mathrm{Kerr}} + n_{2,\mathrm{nuc}}$; see Fig. 63(b) [83].

Data also exist for $n_{2,\mathrm{nuc}}$ in media other than glasses. The noninstantaneous response of liquid CS_2 has been measured by a number of authors (for example [83,172]). Careful analysis of experimental data led to the following results mea-

Table 15. Fractional Contribution Measured of $n_{2,\mathrm{nuc}}$ to the total n_2 for a Few Glasses

Glass	Wavelength (nm)	Nuclear Fraction (%)	Method
Fused silica (SiO_2) [166]	Visible	~15–18	Raman
87%GeS_2-13%Ga_2S_3 [169]	825	13±5	35 fs OKE
64%PbO-14%Bi_2O_3-7%B_2O_3-15%SiO_2 [169]	825	12±5	35 fs OKE
0%–50%GeO_2 in GeO_2-SiO_2 [170]	800	13–18	18 fs SRTBC[a]
20%Nb_2O_5-80%TeO_2 [171]	800	20	100 fs OKE

[a]SRTBC-spectrally resolved two beam coupling.

Figure 63

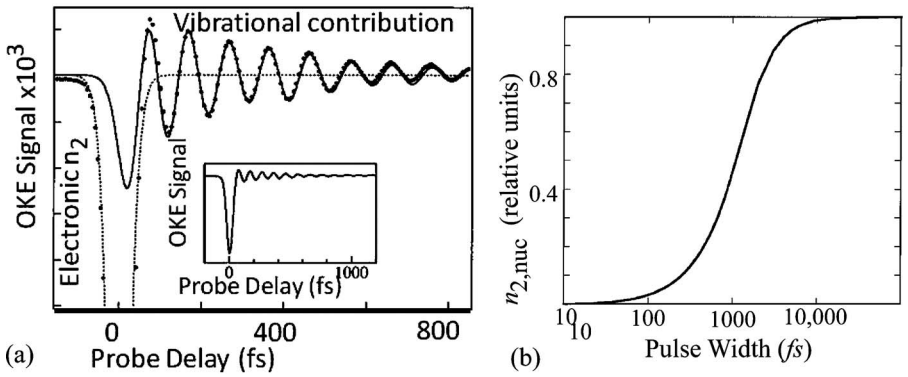

(a) Time-resolved (function of probe delay) closed aperture Z scan at fixed z with ~35 fs pulses of a Ge–Ga–S glass. The relative change in transmittance $\delta T/T$ of the probe beam was recorded. Filled circles, experimental data; solid curve, nuclear contribution calculated from the Raman spectra; dotted curve, electronic contribution. The total experimental signal is shown in the inset [169]. (b) Calculated contribution of $n_{2,\mathrm{nuc}}$ in fused silica versus pulse width [83].

sured with 100 fs pulses [83]: contributions of electronic n_2, 19%, sub-pulse-width response; vibrational 64%, decay time ~170 fs; and rotational 17%, decay time 880 fs. We discuss the rotational contribution, $n_{2,\mathrm{rot}}$, in Section 6.

6. Molecules with Anisotropic Polarizabilities

Changes in the orientation of molecules due to applied fields provide an important contribution to the intensity-dependent refractive index in states of matter in which reorientation of anisotropic molecules can occur. The required anisotropy is in the linear molecular polarizability, and the states of matter composed of such molecules are liquids and liquid crystals [173].

There are two principal mechanisms. An incident field induces anisotropic dipoles in molecules, and the interaction between these individual dipoles and the applied field leads to a torque by which the molecules tend to reorient parallel to the incident field direction. Some net molecular realignment of the molecule's largest polarizability axis results in a net increase in the bulk refractive index parallel to the applied field and a decrease in the direction orthogonal to it. In liquid crystals, this reorientation is a collective phenomenon. Finite temperature, which tends to homogenize the alignment because of thermal fluctuations in the orientation, limits the net alignment. The characteristic response times are the reorientation times allowed by the viscosity.

The second mechanism is limited to liquid crystals. There are strong intermolecular forces that lead to net molecular alignment over microscopic, mesoscopic, and/or macroscopic volumes. These aligned regions can be realigned by applied fields, as described above, but usually very slowly relative to the single-molecule case. More important is the absorption of the incident light, which results in increasing liquid crystal temperature and a weakening of the intermo-

lecular forces relative to thermal fluctuations. Decreasing alignment leads to progressively more spatially uniform refractive index and large index changes with temperature.

6.1. Single-Molecule Reorientation of Anisotropic Molecules

Analysis of molecules with 3D molecular anisotropy involves Euler angles and straightforward but cumbersome mathematics. Instead of discussing the most general case, we illustrate this with the simpler case of a linear molecule such as CS_2 with symmetry in the polarizability orthogonal to the linear axis [2]. The geometry of interest is illustrated in Fig. 64(a). The incident field in the laboratory frame of reference is assumed to lie along the x axis,

$$\vec{E}(\vec{r},t) = \hat{e}_x \mathrm{E}_0(\omega)\cos(\vec{k}\cdot\vec{r} - \omega t),$$

and the polarizability tensor in the molecule's frame of reference is given by

$$\vec{\vec{\alpha}} = \begin{array}{|c|c|c|}\hline \bar{\alpha}_{\parallel} & 0 & 0 \\ \hline 0 & \bar{\alpha}_{\perp} & 0 \\ \hline 0 & 0 & \bar{\alpha}_{\perp} \\ \hline \end{array}$$

with $\alpha_{\parallel} > \alpha_{\perp}$. The local field at the molecule is given by

$$\vec{\mathrm{E}}_{\mathrm{loc}} = [\hat{e}_{\bar{x}} \cos\theta_a - \hat{e}_{\bar{y}} \sin\theta_a \cos\phi_a + \hat{e}_{\bar{z}} \sin\theta_a \sin\phi_a] f^{(1)} \mathrm{E}_0(\omega)\cos(\omega t),$$

$$f^{(1)} = \frac{\varepsilon_r(\omega) + 2}{3}, \tag{6.1}$$

and the dipole moment induced in the ath molecule is given by

Figure 64

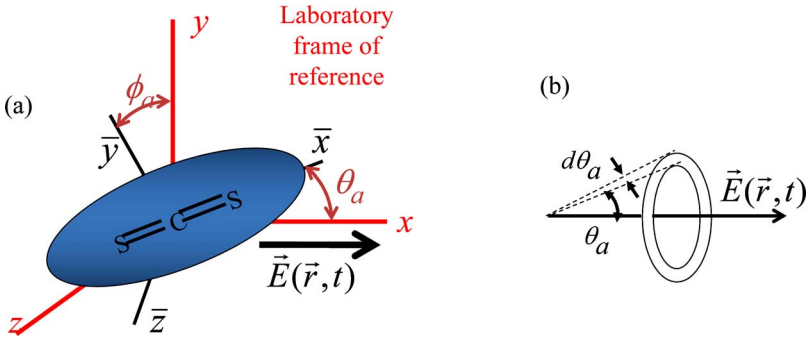

(a) Orientation coordinates of a liquid CS_2 molecule when an optical field is along the x axis in the laboratory frame of reference (x,y,z). The molecular frame of reference is defined by $(\bar{x},\bar{y},\bar{z})$. (b) Solid-angle element with circular symmetry.

$$\vec{\vec{p}}_a(\vec{r},t) = \vec{\vec{\alpha}} \cdot \vec{\mathrm{E}}_{\mathrm{loc}} = [\hat{e}_{\tilde{x}}\bar{\alpha}_{\parallel}\cos\theta_a - \hat{e}_{\tilde{y}}\bar{\alpha}_{\perp}\sin\theta_a\cos\phi_a + \hat{e}_{\tilde{z}}\bar{\alpha}_{\perp}\sin\theta_a\sin\phi_a] \times [f^{(1)}]^2\mathrm{E}_0(\omega)\cos(\omega t). \tag{6.2}$$

The polarization P_x induced along the laboratory frame's x axis is given by

$$\mathrm{P}_x = N\langle \hat{e}_x \cdot \vec{\vec{p}}_a \rangle = N[\bar{\alpha}_{\perp} + (\bar{\alpha}_{\parallel} - \bar{\alpha}_{\perp})\langle\cos^2\theta_a\rangle][f^{(1)}]^2\mathrm{E}_0(\omega), \tag{6.3}$$

in which $\langle\ \rangle$ denotes the average over all possible molecular orientations, i.e., over θ_a. Because of the molecular symmetry, the average is taken over rings with effective area elements $\sin\theta_a\, d\theta_a$ (i.e., $-d\cos\theta_a$), see Fig. 64(b). The probability $\Pr(\theta_a)$ of finding a molecular axis ($\alpha_{\parallel}$) in a cone at angle θ_a to the x axis (field direction), with a cone width $-d\cos\theta_a$, is

$$\Pr(\theta_a) \propto d\cos\theta_a \times \exp - \left[\frac{\text{Ordering potential energy}}{\text{Disordering energy}}\right],$$

normalized to $\int_1^0 \Pr(\theta_a) = 1$. The ordering is due to the potential energy of the induced electric dipole in the applied field,

$$\mathrm{V}_{\mathrm{int}} = -\frac{1}{2}\vec{\vec{p}}_a \cdot \vec{E}_{\mathrm{loc}} = -\frac{1}{2}[\bar{\alpha}_{\parallel}\cos^2\theta_a + \bar{\alpha}_{\perp}\sin^2\theta_a][f_{\mathrm{or}}^{(1)}]^2\mathrm{E}_0^2(\omega)\overline{\cos^2(\omega t)}, \tag{6.4}$$

where $\overline{\cos^2(\omega t)}$ is the time average of $\cos^2(\omega t)$, i.e., $\frac{1}{2}$. The disorder is due to thermal fluctuations of energy $k_{\mathrm{B}}T$. Thus

$$\Pr(\theta_a) = \frac{\exp\left\{\left[-\dfrac{\bar{\alpha}_{\perp}\mathrm{E}_0^2(\omega)}{4k_{\mathrm{B}}T} + \dfrac{(\bar{\alpha}_{\parallel} - \bar{\alpha}_{\perp})\cos^2\theta_a\mathrm{E}_0^2(\omega)}{4k_{\mathrm{B}}T}\right][f^{(1)}]^2\right\} d\cos\theta_a}{\displaystyle\int_1^0 \exp\left\{\left[-\frac{\bar{\alpha}_{\perp}\mathrm{E}_0^2(\omega)}{4k_{\mathrm{B}}T} + \frac{(\bar{\alpha}_{\parallel} - \bar{\alpha}_{\perp})\cos^2\theta_a\mathrm{E}_0^2(\omega)}{4k_{\mathrm{B}}T}\right][f^{(1)}]^2\right\} d\cos\theta_a}, \tag{6.5}$$

and therefore

$$\langle\cos^2\theta_a\rangle = \frac{\displaystyle\int_1^0 \cos^2\theta_a \exp\left(\frac{(\bar{\alpha}_{\parallel} - \bar{\alpha}_{\perp})\cos^2\theta_a}{4k_{\mathrm{B}}T}[f^{(1)}]^2\mathrm{E}_0^2(\omega)\right) d\cos\theta_a}{\displaystyle\int_1^0 \exp\left(\frac{(\bar{\alpha}_{\parallel} - \bar{\alpha}_{\perp})\cos^2\theta_a}{4k_{\mathrm{B}}T}[f^{(1)}]^2\mathrm{E}_0^2(\omega)\right) d\cos\theta_a}. \tag{6.6}$$

Assuming that the net reorientation is small and therefore that quantities of the form e^x can be expanded as $1+x$, after some algebra

$$\mathrm{P}_x = N\left\{\bar{\bar{\alpha}}f^{(1)} + \frac{(\bar{\alpha}_{\parallel} - \bar{\alpha}_{\perp})^2\mathrm{E}_0^2(\omega)}{45k_{\mathrm{B}}T}[f^{(1)}]^2[f^{(1)}]^2\right\}\mathrm{E}_0(\omega), \tag{6.7}$$

in which $\bar{\bar{\alpha}}$ is the isotropic polarizability due to completely randomly oriented molecules before a strong optical field is turned on. The nonlinear contribution

can now be written as an effective intensity-dependent refractive index coefficient $n_{2,\mathrm{or}}$ as

$$n_{2\parallel,\mathrm{or}}(-\omega;\omega)=\frac{N}{n_x^2\varepsilon_0^2 c}\frac{(\bar{\alpha}_\parallel-\bar{\alpha}_\perp)^2}{45k_\mathrm{B}T}[[f^{(1)}]^{2(1)}]^4. \tag{6.8}$$

It is easy to calculate the effect of the strong field on the index with polarization along y and z axes,

$$n_{2\perp,\mathrm{or}}(-\omega;\omega)=-\frac{N}{n_x^2\varepsilon_0^2 c}\frac{(\bar{\alpha}_\parallel-\bar{\alpha}_\perp)^2}{90k_\mathrm{B}T}[[f^{(1)}]^{2(1)}]^4. \tag{6.9}$$

Note that in principle all of the molecules can be aligned by a sufficiently strong optical field; see Fig. 65. In practice, other phenomena such as damage and ionization limit the effect to small net angle changes. For the 3D case where $\bar{\alpha}_{xx}\neq\bar{\alpha}_{yy}\neq\bar{\alpha}_{zz}$,

$$n_{2\parallel,\mathrm{or}}(-\omega;\omega)=\frac{N}{n_x^2\varepsilon_0^2 c}\frac{[[f^{(1)}]^{2(1)}]^4}{45k_\mathrm{B}T}\{[\bar{\alpha}_{xx}^2+\bar{\alpha}_{yy}^2+\bar{\alpha}_{zz}^2]-[\bar{\alpha}_{xx}\bar{\alpha}_{zz}+\bar{\alpha}_{xx}\bar{\alpha}_{yy}+\bar{\alpha}_{yy}\bar{\alpha}_{zz}]\}. \tag{6.10}$$

The turn-on and turn-off times of this effective nonlinearity depend strongly on the local viscosity and the temperature. The simplest equation that describes the time dynamics is

$$\Delta\dot{\theta}+\frac{\Delta\theta}{\bar{\tau}_D}=\text{torque}=-\frac{\partial}{\partial\theta}V_\mathrm{int}=-\frac{1}{4}[\bar{\alpha}_\parallel-\bar{\alpha}_\perp]\langle\sin(2\theta_a)\rangle|\mathrm{E}_\mathrm{loc}(\omega,t)|^2$$

with $\bar{\tau}_D=\mathrm{C}\eta/k_\mathrm{B}T$ and viscosity η; the numerical factor C depends on the details of the molecular shape. The classic example is liquid carbon disulfide, the case just discussed theoretically. Here there are many contributions [83,172]. Decay times ranging from 900 fs to a few picoseconds have been reported (for example, [83,172,174]). The magnitude was $n_{2,\mathrm{Kerr}}\cong n_{2,\mathrm{or}}\cong 1-5\times10^{-14}$ cm^2/W for this case. Typically, the larger the molecule, the longer the decay time; for example, ~30 ps was measured for nitrobenzene [174].

6.2. Liquid Crystals

The nonlinear optics of liquid crystals is in some ways closely related to the previous case. Strong intermolecular forces between liquid molecules in the liquid

Figure 65

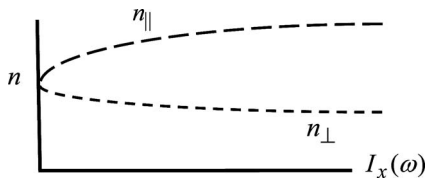

Variation with input light intensity of the refractive index parallel ($n_\parallel$) and perpendicular ($n_\perp$) to the applied field.

Figure 66

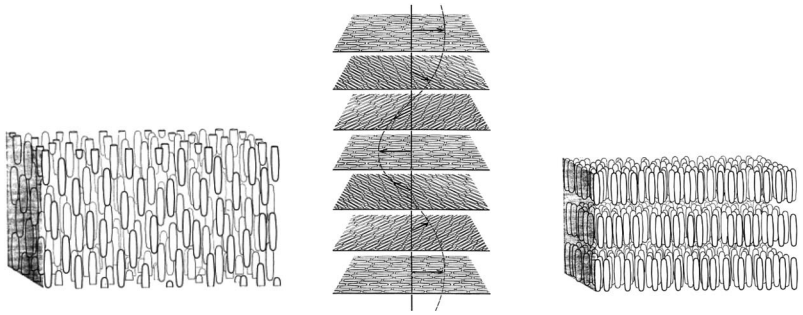

Examples of molecules and their alignment in nematic, cholosteric, and smectic liquid crystals [173].

state can lead to a unique form of matter in which molecular clusters exist, aligned along a direction in space (the "director"). It is this alignment that leads to the name liquid "crystal." There are many families of liquid crystals; see Fig. 66 [173]. Most of the molecules can be considered to have ellipsoidal shapes as shown in Fig. 67(a). The structure of one of the most commonly used and extensively studied molecules, 5CB, is shown in Fig. 67(b). Examples of R and R′ are C_nH_{2n+1}, $C_nH_{2n+1}O$, and nitro and cyano (e.g., 5CB) groups. A single molecular structure can take on different liquid crystal ordering as temperature or the side groups are changed. For example, nCB is not a liquid crystal for $n \leq 4$, and it is nematic for $n = 5-7$ and then smectic for larger n. Although some molecules may exhibit a permanent dipole moment, the net alignment in the liquid state averages the dipole moment to zero over optical wavelengths. Note that the alignment is not perfect and is described by a scalar order parameter $S = 0.5[\langle 3\cos^2\theta - 1]\rangle$, where θ is the angle between the molecular long axis (typically along $\alpha_{\|}$), and the average over all molecules of the direction of $\alpha_{\|}$, $\hat{n}$, is called the "director."

We focus on nematic liquid crystals in which the preponderance of experiments in nonlinear optics have been performed and in which there are multiple mecha-

Figure 67

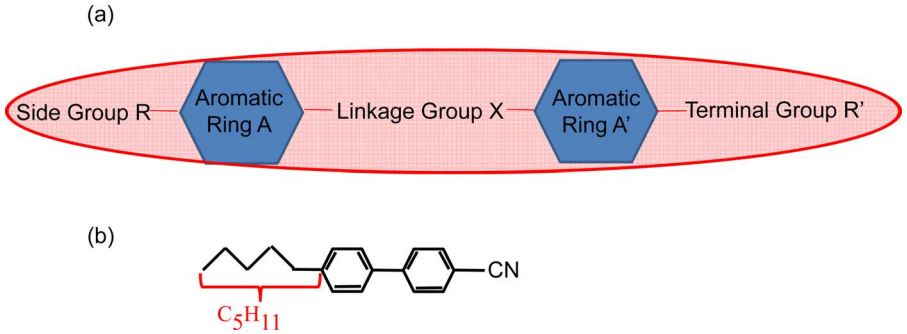

(a) Schematic of a typical liquid crystal molecule. (b) The chemical structure of a 5CB liquid crystal molecule [173].

nisms that give rise to n_2 [173]. In bulk form these materials, when oriented, exhibit a uniaxial refractive index distribution if the molecules have approximate or exact cylindrical symmetry. At properly prepared single boundaries, or between two plates with prepared surfaces, it is possible to anchor the orientation of the molecules for some distance away from the boundary. There are two possible directions for $\hat{n}$, parallel to (planar) or orthogonal to (homeotropic) to the boundary, shown in Fig. 68. For all intents and purposes, these aligned nematic cells behave as uniaxial crystals characterized by refractive indices $n_{\parallel}=(\varepsilon_{\parallel})^{1/2}$ and $n_{\perp}=(\varepsilon_{\perp})^{1/2}$, i.e., with a birefringence $\Delta n=n_{\parallel}-n_{\perp}$. As the temperature is raised, a second-order phase transition to an isotropic liquid occurs, and order is lost. In the transition region, the correlation distance over which orientational order exists decreases, resulting in a decreasing order parameter, and the birefringence approaches vanishing value.

As in all other molecular systems, a laser will induce in nematic liquid crystals changes in the populations of the electronic energy states, resulting in nonlinear polarizations of various orders. These so-called electronic nonlinearities of liquid crystals are typical of organic molecules. Except for some effects associated with the ordered arrangement of the molecules, the magnitudes of the refractive index coefficients n_2 are the same order of magnitude as other organic molecules discussed above. On the other hand, laser-induced density, temperature, order parameter, and director axis orientation in nematic liquid crystals are responsible for some of the largest optical nonlinearities discovered to date.

6.2a. Orientational Optical Nonlinearities of Nematic Liquid Crystals

Isotropic phase: Just above the nematic-isotropic transition temperature T_{NI}, short-range molecular correlation still persists, and laser-induced orientation of these highly polarizable molecules exhibits critical pretransitional behavior. These critical phenomena are described by the Landau–deGennes theory of second-order phase transition [175]. The free energy per unit volume is of the form

$$F = F_0 + \frac{1}{2}AQ_{ij}Q_{ji} - \frac{1}{4}\chi_{ij}E_i^*E_j, \tag{6.11a}$$

Figure 68

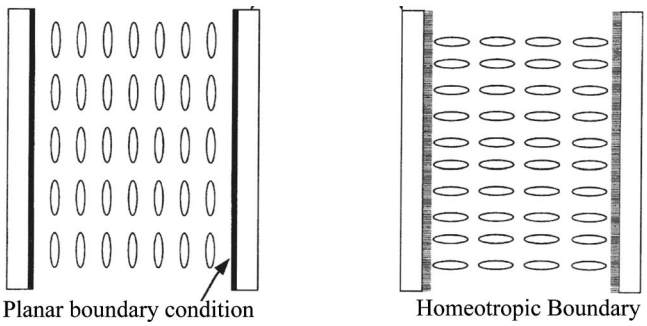

Two nematic liquid crystal molecular alignments obtained between two glass plates with different surface treatments [173].

$$A = a(T - T^*), \tag{6.11b}$$

where Q_{ij} is a general-order parameter tensor a and T^* ($\sim T_{\mathrm{NI}}$, nematic-isotropic phase transition temperature) are constants, and E denotes the applied optical field. For an x-polarized laser, for example, the total optically induced polarization P_x consists of a linear and a nonlinear term:

$$P_x = \left(\varepsilon_0 \bar{\chi} + \varepsilon_0 \frac{2}{3} \Delta\chi Q\right) E_x = P_x^L + P_x^{NL}. \tag{6.12}$$

$P_x^L = \varepsilon_0 \bar{\chi} E$ is the linear polarization, $\bar{\chi}$ is the linear susceptibility, and the nonlinear polarization is given by

$$P_x^{\mathrm{NL}} = \frac{2}{3} \varepsilon_0 \Delta\chi Q E. \tag{6.13}$$

From Eqs. (6.11), the dynamical equation for Q_{ij} becomes

$$\eta \frac{\partial Q_{ij}}{\partial t} + A Q_{ij} = f_{ij}, \tag{6.14}$$

$$f_{ij} = \frac{1}{6} \Delta\chi \left(E_i^* E_j - \frac{1}{3} |E|^2 \delta_{ij} \right). \tag{6.15}$$

Here η is the viscosity coefficient in the isotropic phase.

The solution for Q_{ij} is

$$Q_{ij}(t) = \int_{-\infty}^{t} \left[\frac{f_{ij}(t')}{\eta} e^{-(t-t')/\tau} \right] dt', \tag{6.16a}$$

$$\tau = \frac{\eta}{A} = \frac{\eta}{a(T - T^*)}. \tag{6.16b}$$

Here τ is the relaxation time constant associated with the viscosity.

For a linearly polarized ($i=j$) square pulse of duration τ_p, $f_{ij} = f_{ii} = 1/9 \Delta\chi E^2$, we have

$$Q_{ii} = \tau \Delta\chi E^2 (1 - e^{-\tau/\tau_p})/9\eta. \tag{6.17}$$

From Eqs. (6.16a) and (6.16b), note that as the temperature approaches $T^* (\sim T_c)$, both the response time and the optical nonlinearity (which is proportional to Q_{jj}) diverge as $(T - T^*)^{-1}$, as reported in previous studies of the optically induced Kerr effect and optical wavefront conjugation [176,177]. Typical magnitudes of $\chi^{(3)}$ for orientational optical nonlinearities in the isotropic phase are of the order of 10^{-12} esu at temperatures far from T_{NI}, and $\sim 10^{-10}$ esu within a few degrees of T_{NI}.

Nematic phase—purely optically induced director axis reorientation nonlinearities: In the nematic phase, the free energies associated with splay, twist, and bend deformations in a nematic liquid crystal (shown in Fig. 69) are of the forms

$$\text{splay}, \quad f_1 = \frac{1}{2} K_1 (\nabla \cdot \hat{n})^2; \tag{6.18a}$$

$$\text{twist}, \quad f_2 = \frac{1}{2} K_2 (\hat{n} \cdot \nabla \times \hat{n})^2; \tag{6.18b}$$

$$\text{bend}, \quad f_3 = \frac{1}{2} K_3 (\hat{n} \times \nabla \times \hat{n})^2. \tag{6.18c}$$

The optical dipole-field interaction is given by

$$F_{\text{op}} = -\frac{1}{4\pi} \int \mathbf{D} \cdot d\mathbf{E} = -\frac{\varepsilon_\perp}{8\pi} E^2 - \frac{\Delta\varepsilon \langle (\hat{n} \cdot \mathbf{E})^2 \rangle}{8\pi}. \tag{6.19}$$

The angle brackets denote a time average. Field-induced reorientation of the director axis arises as a result of the total system's tendency to assume a new configuration with a new minimum in the free energy. For such processes, the first term on the RHS of Eq. (6.19) is not involved, whereas the second term shows that the director axis will align with the optical field polarization as, in general, the optical dielectric anisotropy $\Delta\varepsilon$ for nematic liquid crystals is greater than zero.

Consider the interaction geometry depicted in Fig. 70. A linearly polarized laser in the form of a plane wave is obliquely incident on a homeotropically aligned nematic liquid crystal with the propagation wave vector **K** making an angle ($\beta + \theta$) with the director axis. If the reorientation angle θ is small, then only one elastic constant K_1 (for splay distortion) is involved. A minimization of the total free energy of the system yields a torque balance equation:

$$K_1 \frac{d^2\theta}{dz^2} + \frac{\Delta\varepsilon \langle E_{\text{op}}^2 \rangle}{8\pi} \sin 2(\beta + \theta) = 0. \tag{6.20}$$

In the small θ approximation, this becomes

$$2\xi^2 \frac{d^2\theta}{dz^2} + (2 \cos 2\beta)\theta + \sin 2\beta = 0, \tag{6.21}$$

where $\xi^2 = 4\pi K_1 / [\Delta\varepsilon \langle E^2_{\text{op}} \rangle]$.

Figure 69

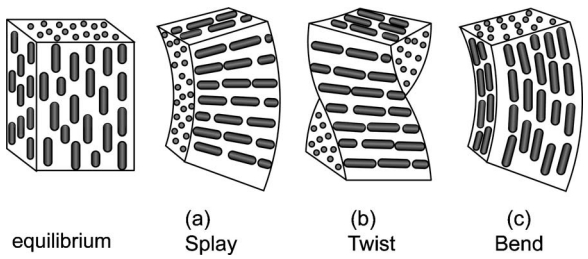

(a) Splay, (b) twist, and (c) bend distortions that occur in liquid crystals [173].

Figure 70

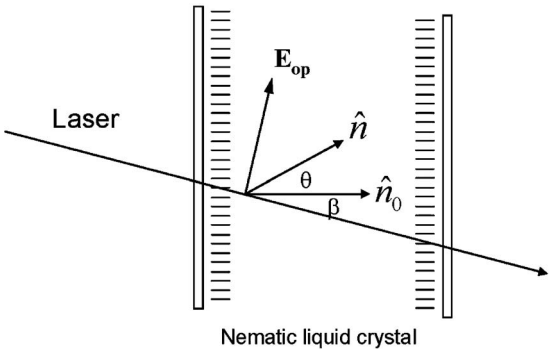

Geometry for the interaction of a linearly polarized (extraordinary ray) laser beam with a homeotropically aligned nematic liquid crystal film. $\hat{n}_0$ and $\hat{n}$ are the directors before and after the application of the optical field [173].

Using the so-called hard-boundary condition, i.e., ($\theta=0$ at $z=0$ and at $z=d$), the solution of Eq. (6.21) is

$$\theta = \frac{1}{4\xi^2}\sin 2\beta(dz - z^2). \tag{6.22}$$

As a result of this reorientation, the incident laser (an extraordinary wave) experiences a z-dependent refractive index change given by

$$\Delta n(z) = n_e(\beta + \theta) - n_e(\beta), \tag{6.23}$$

where $n_e(\beta+\theta)$ is the extraordinary ray index given by

$$n_e(\beta + \theta) = \frac{n_{\parallel} n_{\perp}}{[n_{\parallel}^2 \cos^2(\beta + \theta) + n_{\perp}^2 \sin^2(\beta + \theta)]^{1/2}}. \tag{6.24}$$

For small θ, the change in the local refractive index $\Delta n(z)$ is of the from $\Delta n(z) = n_{2,\mathrm{lc}}(z)I$ where $I=\frac{1}{2}\varepsilon_0 nc\mathrm{E}_{\mathrm{op}}^2$ and $\alpha_2(z)$ (defined here as the local nonlinearity, not the 2PA coefficient) is given by

$$\alpha_2(z) = \frac{(\Delta\varepsilon)^2 \sin^2(2\beta)}{4Kc}(dz - z^2). \tag{6.25}$$

For the oblique incidence geometry, the interaction length is $d/\cos\theta$, and thus the equivalent refractive index coefficient $n_{2,\mathrm{lc}}$ obtained by integrating and averaging the local value $\alpha_2(z)$ over the interaction length is given by

$$n_{2,\mathrm{lc}} = \frac{[\Delta\varepsilon \sin(2\beta)d]^2}{24K_1 c \cos^2(\beta)}. \tag{6.26}$$

Using typical values of $d=100\ \mu$m, $\Delta\varepsilon \sim 0.6$, $K_1=10^{-6}$ dyne, $\beta=45°$, and noting that in cgs units a factor of 4×10^7 needs to be accounted for in converting ergs/(s cm^2) and W/cm^2 to the unit for the intensity I, we have

$$n_{2,\mathrm{lc}} \sim 8 \times 10^{-3}\ \mathrm{cm}^2/\mathrm{W}. \tag{6.27}$$

For more general cases in which splay, twist, and bend distortions are all included, the laser-induced director axis reorientation is described by an equation of the form

$$(K_1 \sin^2\theta' + K_3 \cos^2\theta')\frac{d^2\theta}{dz^2} - (K_3 - K_1)\sin\theta'\cos\theta'\left(\frac{d\theta}{dz}\right)^2 + \frac{\Delta\varepsilon}{16\pi}[\sin 2\theta'(|E_x|^2 - |E_y|^2) + \cos 2\theta'(E_x E_z^* + E_x^* E_z)] = 0. \tag{6.28}$$

In the case of an input laser beam of finite beam size, mutual torques exerted by molecules situated within and outside the laser beam will also be involved, giving rise to extra terms that depend on radial derivatives of θ, $\mathrm{d}\theta/\mathrm{dr}$; the resulting reorientation profile is a nonlocal function with respect to the applied field [178,179]. Such nonlocal nonlinearities are particularly important in nonlinear optical processes involving the focused laser beam's transverse intensity dependence, such as self-focusing, defocusing and soliton formation [180–183].

The dynamics of molecular reorientation by an optical field is described by balancing the optical molecular and the viscous torques. For the interaction geometry given in Fig. 70, the resulting equation is of the form

$$\gamma\frac{\partial\theta}{\partial t} = K\frac{\partial^2\theta}{\partial z^2} + \frac{\Delta\varepsilon\langle E_{\mathrm{op}}^2\rangle}{8\pi}\sin(2\beta + 2\theta). \tag{6.29}$$

If E_{op}^2 is a plane wave, and for the usual case of $\theta \ll 1$, we may write $\theta(t,z) = \theta(t)\sin(\pi z/d)$, and Eq. (6.29) yields

$$\dot{\theta} = -\frac{K\pi^2}{\gamma d^2}\theta + \frac{\Delta\varepsilon\langle E_{\mathrm{op}}^2\rangle}{8\pi\gamma}\sin 2\beta + \theta\frac{\Delta\varepsilon\langle E_{\mathrm{op}}^2\rangle}{4\pi\gamma}\cos 2\beta, \tag{6.30a}$$

or

$$\dot{\theta} = -\frac{1}{\tau_r}\theta + a + b\theta. \tag{6.30b}$$

Here $a = \Delta\varepsilon\langle E_{\mathrm{op}}^2\rangle\sin(2\beta)/8\pi\gamma$, $b = \Delta\varepsilon\langle E_{op}^2\rangle\sin(2\beta)/4\pi\gamma$, and τ_r is the relaxation time constant for reorientation of the director axis:

$$\tau_r = \gamma d^2/K_1\pi^2. \tag{6.30c}$$

Again, for a typical cell with cell thickness $d \sim 10\ \mu$m, $\gamma = 0.1\ P$, and $K_1 = 10^{-6}$ dyne, $\tau_r \approx 10$ ms. It is important to note here that the relaxation time constant in a highly correlated molecular system such as a nematic liquid crystal is strongly dependent on the interaction geometry as well as the intensity distribution of the incident light. In a two-wave mixing geometry involving a sinusoidal optical intensity grating, for example, the mutual torques exerted by molecules situated in the optical intensity maxima and minima will give rise to a dependence on the grating constant as well as the cell thickness. The corresponding relaxation time constant becomes

$$\tau_r = \frac{\gamma}{K}\left(\frac{1}{\frac{\pi^2}{d^2} + q^2}\right), \tag{6.31}$$

where $\Lambda = 2\pi/q$ is the grating constant.

Using a thinner cell with less viscous liquid crystals, the response time can be reduced further to ~1 ms; i.e., the upper limit to the useful optical modulation rate is ~1 KHz. In recent years, with the development of nematic liquid crystals with low viscosity and high birefringence, tens of kilohertz modulation rates can be achieved, making nematic liquid crystals candidate materials for image processing and display applications.

Although the relaxation dynamics is in the millisecond regime, the switching onset dynamics can be much faster, since the laser-induced reorientation process is governed mainly by the intensity, in the limit where the optical torque exerted by an intense laser on the director axis is much larger than the elastic torque, i.e.,

$$\left|\frac{\Delta\langle E_{\text{op}}^2\rangle}{8\pi}\right| \sin(2\beta + 2\theta) \gg \left|K_1 \frac{\partial^2\theta}{\partial z^2}\right|. \tag{6.32}$$

Equations (6.30) then become

$$\dot{\theta} = a + b\theta \rightarrow \theta(t) = \frac{a}{b}(e^{bt} - 1). \tag{6.33}$$

Note that if the laser intensity is sufficiently large such that $a\tau_p \cong \Delta\varepsilon E_{\text{op}}^2 \tau_p/\gamma$, it is possible to induce a significant reorientation $\theta(\tau_p)$ in a time as short as nanoseconds. Such an ultrafast response of the director axis deformation in nematic as well as smectic liquid crystals has been demonstrated in early studies by Khoo and co-workers, using nanosecond laser pulses, and by Eichler and others, using picosecond lasers [184–186].

6.2b. Giant Orientational Optical Nonlinearities in Doped Nematic Liquid Crystals

By introducing photosensitive dye or molecular dopants to mediate, facilitate, and enhance the reorientation process, studies have demonstrated that the optical nonlinearities $n_{2,\text{lc}}$ can be made even orders of magnitude larger, ranging from 10^{-3} to 10^3 cm^2/W [187–193].

One of the mechanisms is mediated by the photoexcited dye molecular dopants. The excited dye molecules exert intermolecular torques $\tau_{\text{mol}} \sim A\tau_{\text{op}}$ on the liquid crystal molecules that could be stronger than the optical torque τ_{op}, i.e., A can be as large as 100 or more, and it can be positive or negative. In Methyl-Red-doped nematic liquid crystals, $n_{2,\text{lc}}$ can be much larger than 1 cm^2/W [187,188]. Studies of Methyl-Red-doped nematic liquid crystals also show that the nonlinearities can be modulated by an applied ac electric field by changing the frequency; a low-frequency (e.g., 300 Hz) ac field will enhance the reorientation nonlinearity, whereas a high-frequency (30 kHz) ac field will quench the reorientation and turn off the optical nonlinearity, pointing to the possibility of dual-frequency switching–modulation applications [194,195].

In some nematic liquid crystals doped with azo compounds, for example azobenzenes, studies have shown that the trans-cis configuration changes in the excited azo-dopant are also an effective mechanism for creating large optical nonlinearities [196–198]. In these materials, the ground state azo dye molecules are in the trans configuration that is oblong in shape, and they conform to the alignment of the director axis. When photoexcited to the bent cis configuration, they disturb the nematic axis alignment and cause disorder, i.e., induce a negative change in the order parameter ($-\Delta S$), resulting in a change in the birefringence; cf. Fig. 71. Such trans-cis isomerization can happen quite rapidly (in nanoseconds), and so the resulting index birefringence changes can be effected very rapidly.

6.2c. Field-Assisted Photorefractivity in Nematic Liquid Crystals

Another mechanism that gives rise to extraordinarily large optical nonlinearities in nematic liquid crystal is photorefractivity [199–201]. Under the combined action of an optical and a dc bias field, the process of photocharge production and creation of space-charge fields that result in a refractive index change is analogous to the photorefractive (PR) effect occurring in electro-optically active polymers and inorganic crystals as discussed in Section 7, but with an important difference. In inorganic photorefractive crystals, such as $BaTiO_3$, the induced index change Δn is *linearly* related to the total electric field E—the so-called Pockels cell effect. On the other hand, nematic liquid crystals possess centrosymmetry ($+\hat{n}$ is equivalent to $-\hat{n}$), and the field-induced refractive-index change is quadratic in the total electric field, i.e., $\Delta n = n_2 E^2$—the Kerr effect. As we will see presently, such a quadratic dependence actually allows the mixing of the applied dc field with the space-charge field for enhanced director-axis reorientation effects [199–202,194,203].

For a typical wave mixing interaction (see Fig. 72) a spatially periodic (sinusoidal) incident optical intensity distribution $I_{op} = I_0 \sin(q\xi)$ acting on the photocharge-producing impurities or dopants such as dyes, C60, and carbon nanotubes in the nematic liquid crystals generates a PR-like space-charge field E_{ph} of the form [199]

Figure 71

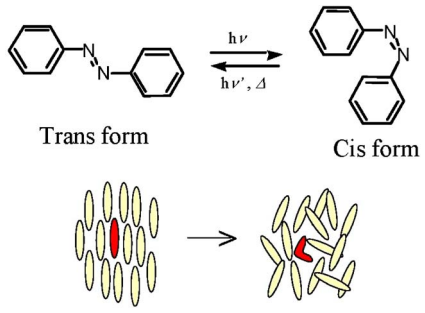

Schematic depiction of the trans-cis configuration changes experienced by an azo molecule when photoexcited, and their effect in lowering the order parameter of an aligned nematic liquid crystal [196–198].

$$E_{\mathrm{ph}} = E_{\mathrm{ph}}^{(0)} \cos(q\xi) = \left[\frac{mk_{\mathrm{B}}T}{2e} qv \frac{\sigma - \sigma_d}{\sigma} \right] \cos(q\xi), \tag{6.34}$$

where m is the optical depth of modulation factor, k_{B} is again Boltzmann's constant, and σ is the conductivity under illumination. Furthermore, σ_d is dark state conductivity, and $\nu = (D^+ - D^-)/(D^+ + D^-)$, where D^+ and D^- are the diffusion constants for positive and negative ions, respectively, and $q = 2\pi/\Lambda$ is again the grating wave vector, with Λ the grating period.

In nematic liquid crystals, the action of the applied dc field on the director axis reorientation generates two other forms of space-charge fields in conjunction with the conductivity and dielectric anisotropies. For an interaction geometry as depicted in Fig. 72, these space-charge fields are of the form [200,201,204]

$$E_{\Delta\sigma} = -\frac{[(\sigma_{\parallel} - \sigma_{\perp})\sin\theta\cos\theta]}{\sigma_{\parallel}\sin^2\theta + \sigma_{\perp}\cos^2\theta} E_{\mathrm{dc}}, \quad E_{\Delta\varepsilon} = -\frac{[(\varepsilon_{\parallel} - \varepsilon_{\perp})\sin\theta\cos\theta]}{\varepsilon_{\parallel}\sin^2\theta + \varepsilon_{\perp}\cos^2\theta} E_{\mathrm{dc}} \tag{6.35}$$

or, for small θ,

$$E_{\Delta\sigma} \approx -\frac{\Delta\sigma}{\sigma_{\perp}} \theta E_{\mathrm{dc}}; \quad E_{\Delta\varepsilon} \approx -\frac{\Delta\varepsilon}{\varepsilon_{\perp}} \theta E_{\mathrm{dc}}. \tag{6.36}$$

The total electric field in coordinate form then becomes

Figure 72

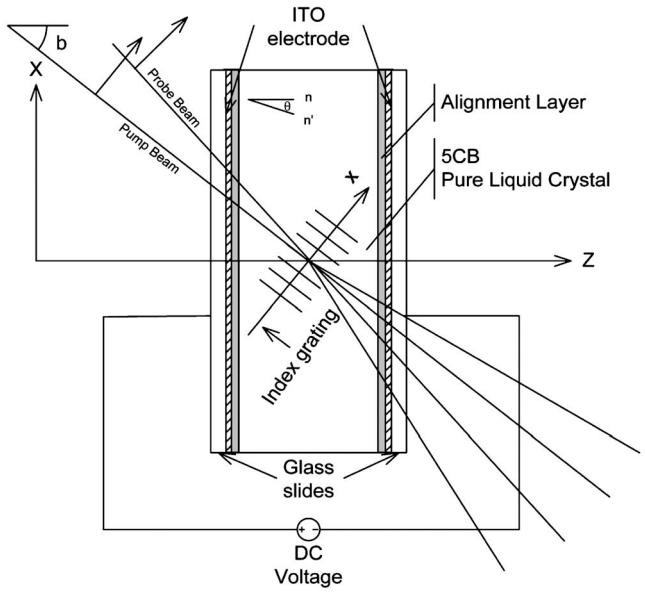

Typical experimental setup involving two linearly polarized coherent beams that are overlapped at an oblique incident angle on an aligned liquid crystal cell. Transparent conducting electrode coated windows allow application of a small dc voltage [199].

$$E_{\text{total}} = \left[-\left(\frac{\Delta\sigma}{\sigma_\perp} + \frac{\Delta\varepsilon}{\varepsilon_\perp}\right) E_{\text{dc}}\theta\cos\beta - E_{\text{ph}}\cos\beta, \quad 0, \right.$$

$$\left. E_{\text{dc}} - \left(\frac{\Delta\sigma}{\sigma_\perp} + \frac{\Delta\varepsilon}{\varepsilon_\perp}\right) E_{\text{dc}}\theta\sin\beta - E_{\text{ph}}\sin\beta \right]$$

$$= [-(E_\Delta \cdot \theta + E_{\text{ph}})\cos\beta, \quad 0, \quad E_{\text{dc}} - (E_\Delta \cdot \theta + E_{\text{ph}})\sin\beta], \tag{6.37}$$

where $E_\Delta = (\Delta\sigma/\sigma_\perp + \Delta\varepsilon/\varepsilon_\perp)E_{\text{dc}}$.

Accordingly, the total free energy of the system becomes

$$F = \frac{k}{2}\{[\vec{\nabla}\cdot n(\vec{r})]^2 + [\vec{\nabla}\times n(\vec{r})]^2\} - \frac{\Delta\varepsilon}{8\pi}[\vec{E}\cdot n(\vec{r})]^2 - \frac{\Delta\varepsilon_{\text{op}}}{8\pi}[\vec{E}_{\text{op}}\cdot n(\vec{r})]^2. \tag{6.38}$$

Here $\Delta\varepsilon$ is the dc field anisotropy and $\Delta\varepsilon_{\text{op}}$ is the optical dielectric anisotropy. Writing $\hat{n} = (\sin\theta, 0, \cos\theta)$, and minimizing the free energy with respect to the reorientation angle θ yields the Euler–Lagrange equation for θ:

$$k\frac{d^2\theta}{dz^2} + k\frac{d^2\theta}{d\xi^2} + \frac{\Delta\varepsilon}{4\pi}[E_\Delta E_z\cos(\beta)\cdot\theta + E_z E_{\text{ph}}\cos(\beta)] + \frac{\Delta\varepsilon\cdot E_{\text{op}}^2}{8\pi}[\sin(2\beta) + 2\cos(2\beta)\cdot\theta] = 0. \tag{6.39}$$

Assuming that a hard boundary condition exists, a solution for θ is of the form

$$\theta = \theta_0 \sin\left(\frac{\pi z}{d}\right)\cos(q\xi). \tag{6.40}$$

Equation (6.39) then yields the familiar solution for the reorientation: θ_0 is nonvanishing only when the applied dc field is above a threshold:

$$\theta_0 = \frac{\frac{1}{2}\frac{\Delta\varepsilon_{\text{op}}}{\Delta\varepsilon}E_{\text{op}}^2\cdot\sin(2\beta) + E_{\text{ph}}^{(0)}E_{\text{dc}}\cos(\beta)}{\left[E_\Delta E_{\text{dc}}\cos(\beta) + \frac{\Delta\varepsilon_{\text{op}}}{\Delta\varepsilon}E_{\text{op}}^2\cos(2\beta)\right] - E_F^2\left[1 + \left(\frac{qd}{\pi}\right)^2\right]}, \tag{6.41a}$$

$$E_{dc} \geq E_F\left[\frac{[1 + (qd/\pi)^2] - (\Delta\varepsilon_{\text{op}}/\Delta\varepsilon)(E_{\text{op}}/E_F)^2\cos(2\beta)}{\left(\frac{\Delta\sigma}{\sigma_\perp} + \frac{\Delta\varepsilon}{\varepsilon_\perp}\right)\cdot\cos\beta}\right]^{1/2}. \tag{6.41b}$$

For 5CB, for example, $K \sim 10^{-11}$ N, the ac field difference in the dielectric constant $\Delta\varepsilon \sim 11$ ($\varepsilon_\parallel \sim 16$, $\varepsilon_\perp \sim 5$) and $\Delta\sigma/\sigma_\perp \sim 0.5$. For a typical wave mixing geometrical and optical parameters ($qd \sim 2\pi$, and the internal angle $\beta = 22.5^\circ$), $E_f d = V_F \sim 1$ V, $\alpha \sim 1.5$, and $V_{\text{th}} = \alpha V_F \sim 1.5$ V.

Experimental measurements have shown that in typical doped nematic liquid crystals, E_{ph} is estimated to be just a few volts per centimeter, but in conjunction with a E_{dc} of a few volts per micrometer, the second term in the numerator $E_{ph}E_{dc}$ is over 10000 $(V/cm)^2$ and is generally much larger than the optical contribution responsible for the first term in the numerator of (6.41a) for the milliwatt-power lasers typically used in these studies [201]. In other words, the occurrence of PR optical nonlinearities in nematic liquid crystals is due mainly to the applied dc field acting in concert with the optically induced space-charge field, and its (n_2) magnitude depends critically on the dc bias field strength. Figure 73 reproduces the typical observed self-diffraction as a function of the applied dc voltage, clearly showing the threshold effect as well as the enhanced response from photocharge-producing dopants such as carbon nanotubes. In this particular study, the nonlinear index coefficients n_2 obtained were 1.3×10^{-3} cm^2/W for the undoped sample and 0.8 cm^2/W for the single-wall carbon nanotube doped nematic liquid crystal. Other studies using a variety of other photocharge-producing dopants have also obtained large n_2 in this range.

Note that the $E_{dc}E_{ph}$ term $[\sim\cos(q\xi)]$ is $\pi/2$ phase shifted from the induced optical intensity grating $I_{opt}^2 \propto \sin^2(q\xi)$, similar to that found in inorganic PR crystals discussed below. The $\pi/2$ phase shift gives rise to strong two-beam coupling effects; cf. Fig. 74.

6.2d. Optical Nonlinearities Associated with Order Parameter Changes, and Thermal and Density Effects

In addition to director axis reorientation, there are several other mechanisms that lead to changes in the refractive indices of the liquid crystal under the action of an optical field. These include laser-induced molecular internal temperature change dT, electrostrictive density changes $d\rho^T$ and $d\rho^e$, and order parameter changes dS, for a fixed initial director axis arrangement. The total index change Δn can therefore be written as

Figure 73

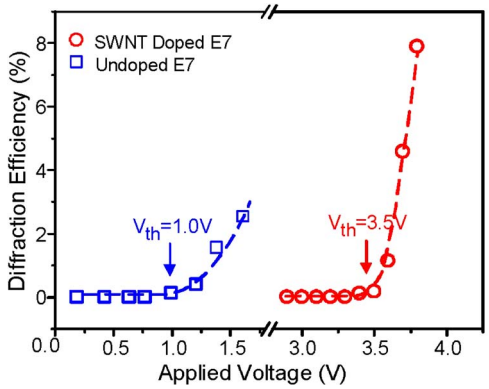

Dependency of first-order diffraction efficiencies on the applied dc voltage in undoped (squares) and single-wall carbon-nanotube -doped (circles) nematic liquid crystals. Sample thickness $d=25$ μm; grating constant $\Lambda=23$ μm; wave-mixing angle 2°; $\beta=22.5°$. The incident optical intensities are 200 and 2 mW/cm^2 for the undoped and doped samples, respectively [201].

$$\Delta n = \left(\frac{\partial n}{\partial T}\right)_{\rho} dT + \left(\frac{\partial n}{\partial \rho}\right)_{T} d\rho^{T} + \left(\frac{\partial n}{\partial \rho}\right)_{T} d\rho^{e} + \left(\frac{\partial n}{\partial S}\right)_{T,\rho} dS. \qquad (6.42)$$

The first term on the RHS of Eq. (6.42), $(\partial n/\partial T)_{\rho} dT$, can be caused by a very short-pulse laser that modifies the spectral dependence of the molecular absorption and emission process [205,206]. This term is usually quite small and is not affected significantly by the ordering or molecular correlations present in the liquid crystalline phase. The second term on the RHS comes from a laser-induced overall rise in temperature and the resulting changes in the density. The third term on the RHS is due to the electrostrictive effect in nonabsorbing materials, i.e., the tendency of a material to move toward a region of high field strength. The contribution unique to nematic liquid crystalline systems is the last term, which is influenced by order parameter changes. This mechanism is the dominant one as a result of the critical dependence of the nematic's extraordinary and ordinary refractive indices $n_{\parallel}=(\varepsilon_{\parallel})^{1/2}$ and $n_{\perp}=(\varepsilon_{\perp})^{1/2}$ on the order parameter S (see Fig. 75), i.e.,

$$n_{\parallel} = n_{\parallel}(\rho, S), \quad n_{\perp} = n_{\perp}(\rho, S). \qquad (6.43)$$

Figure 74

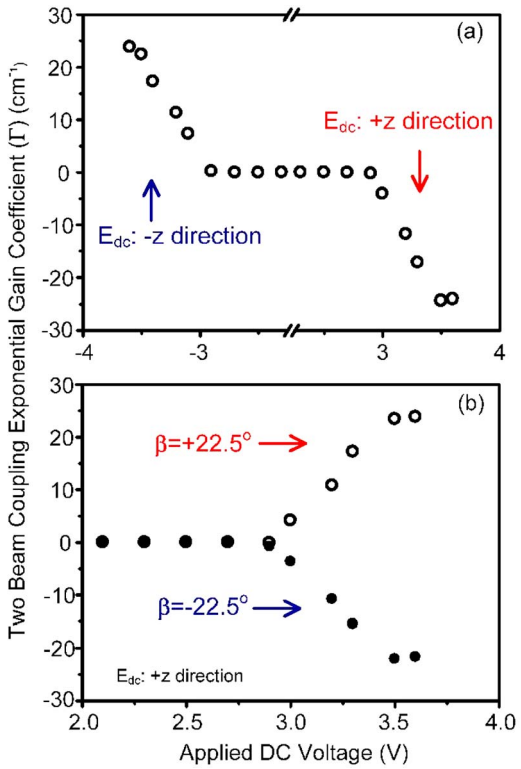

Two-beam coupling exponential gain coefficients as a function of (a) the direction and (b) magnitude of the applied dc bias field obtained with the carbon-nanotube-doped nematic liquid crystals. Sample thickness $d=25\ \mu$m; grating constant $\Lambda=23\ \mu$m; wave-mixing angle 2°; $\beta=\pm 22.5°$. The incident optical intensity used is 2 mW/cm^2. Note that the direction of beam coupling is dependent on the applied bias field direction as well as the orientation (β) of the director axis [201].

Several mechanisms can be employed to change the order parameter. In Subsection 6.2b, we briefly discussed trans-cis isomerism of optically excited azo dopants as an effective means of causing order parameter changes. Owing to the order parameter's critical dependence on the temperature (see Fig. 75), a more frequently investigated mechanism is laser-induced temperature and order parameter modification. The corresponding induced temperature index gradients are of the form [207,173]

$$\frac{dn_{\|}}{dT} = \frac{1}{n_{\|}}\left(C_1\frac{d\rho}{dT} + \frac{2}{3}C_2 S\frac{d\rho}{dT} + \frac{2}{3}C_2\rho\frac{dS}{dT}\right), \tag{6.44a}$$

$$\frac{dn_{\perp}}{dT} = \frac{1}{n_{\perp}}\left(C_1\frac{d\rho}{dT} - \frac{1}{3}C_2 S\frac{d\rho}{dT} - \frac{1}{3}C_2\rho\frac{dS}{dT}\right), \tag{6.44b}$$

where C_1 and C_2 are nematic liquid crystal parameters [207].

Estimating the nonlinear index coefficients associated with these thermal-density-order parameter effects can be a very complex exercise, since the interaction geometries are in general multidimensional and the laser-induced temperature and density changes are strongly coupled by the hydrodynamical equations [205,206]

$$-\frac{\partial^2}{\partial t^2}(\Delta\rho) + v^2\nabla^2(\Delta\rho) + v^2\beta_T\rho_0\nabla^2(\Delta T) + \frac{\eta}{\rho_0}\frac{\partial}{\partial t}\nabla^2(\Delta\rho) = \frac{\gamma^e}{8\pi}\nabla^2(E^2), \tag{6.45a}$$

$$\rho_0 C_v\frac{\partial}{\partial t}(\Delta T) - \lambda_T\nabla^2(\Delta T) - \frac{(C_p - C_v)}{\beta_T}\frac{\partial}{\partial t}(\Delta\rho) = \frac{u}{\tau} = \frac{\alpha nc}{4\pi}E^2. \tag{6.45b}$$

Here ρ_0 is the unperturbed density of the liquid crystal, C_p and C_v the specific heats, λ_T the thermal conductivity, v the speed of sound, γ^e the electrostrictive

Figure 75

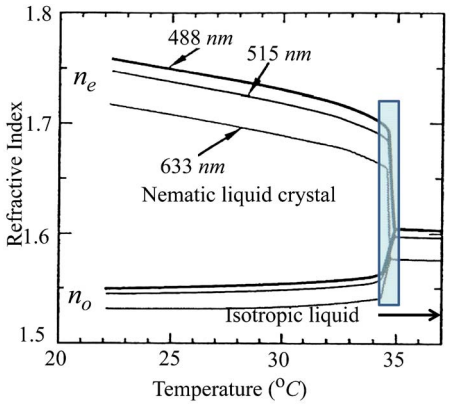

Temperature dependence of the extraordinary and ordinary refractive indices of aligned nematic liquid crystals for three visible wavelengths. The nematic liquid transition region is defined by the pale blue shaded region [173].

coefficient $[\gamma^e=\rho_0(\rho\varepsilon/\partial\rho)_T]$, β_T the coefficient of volume expansion, and η a viscosity coefficient. Equation (6.45a) describes the effects of thermal expansion and electrostriction on the density change, whereas (6.45b) describes the photoabsorption and the resulting temperature rise and heat diffusion process.

These coupled equations for the laser-induced temperature and density distributions $\Delta T(z)$ and $\Delta\rho(z)$ will then have to be incorporated into the equation describing the order parameter S of the system. Following the Landau–deGennes theory, the free energy density of the system with a temperature distribution $T(z)$ and order parameter $S(z)$ is given by [208]

$$f=a(T(z)-T^*)S(z)^2+bS(z)^3+cS(z)^4+L\left(\frac{dS(z)}{dz}\right)^2-g_1S_1-g_2S_2. \tag{6.46}$$

In this expression, a, T^*, b, c, and L are thermodynamic parameters, g_1 and g_2 are the surface potentials per unit volume, and S_1 and S_2 are the surface order parameters. For a typical nematic liquid crystal such as 5CB, $b=-5.3\times10^5$ J/m^3, $c=9.8\times10^5$ J/m^3, $T^*=307.14$ K, and $L=4.5\times10^{-12}$ J m^{-1} [208]. At equilibrium, $S(z)$ is determined by minimization of the free energy equation:

$$\frac{\partial f}{\partial S}-\frac{d}{dz}\left(\frac{\partial f}{\partial(\partial S/\partial z)}\right)=0 \tag{6.47}$$

with the boundary conditions

$$-\left(\frac{\partial f}{\partial(\partial S/\partial z)}\right)_1+\frac{\partial f_{S_1}}{\partial S_1}=0,\quad \left(\frac{\partial f}{\partial(\partial S/\partial z)}\right)_2+\frac{\partial f_{S_2}}{\partial S_2}=0. \tag{6.48}$$

Thermal and density effects induced by short intense laser pulses: To render the problem tractable, most experimental and theoretical studies have adopted interaction geometries that reduce the dimensions and complexities of the problem [209–211]. One example is wave mixing involving a spatially periodic, plane-wave, optical field, i.e., a 1D optical grating intensity distribution of the form $E^2=2E_0{}^2\cos qy$, where $\mathbf{q}=\mathbf{k}_1-\mathbf{k}_2$ is the grating wave vector. Correspondingly, $\Delta\rho$ and ΔT are of the form $\Delta\rho=\rho(t)\cos(\vec{q}\cdot\vec{y})$ and $\Delta T=T(t)\cos(\vec{q}\cdot\vec{y})$, where $\rho(t)$ and $T(t)$ are the density and temperature grating amplitudes.

Consider the transient case involving intense laser pulses. For simplicity in illustration, we assume a flat-top square pulse of duration τ_p. For $0<t<\tau_p$, Eqs. (6.45) can be solved to yield the following temperature and density grating amplitudes [209,210]:

$$T(t)=\left[\frac{\alpha cnE_0{}^2}{4\pi\rho_0C_v\Gamma_R}\right](1-\exp(-\Gamma_Rt)), \tag{6.49}$$

$$\rho(t)=\left[\frac{\gamma^eE_0{}^2}{4\pi v^2}\right](1-\exp(-\Gamma_Bt)\cos\Omega t)-\left[\frac{\beta_T\alpha cnE_0{}^2}{4\pi C_v\Gamma_R}\right](1-\exp(-\Gamma_Rt)). \tag{6.50}$$

The density change $\rho(t)=\rho^e(t)+\rho^T(t)$ as given in Eq. (6.50) has two distinct components:

$$\rho^e(t) = \frac{\gamma^e {E_0}^2}{4\pi\nu^2}(1 - \exp(-\Gamma_B t)\cos\Omega t), \tag{6.51a}$$

$$\rho^T(t) = \frac{-\beta_T \alpha c n {E_0}^2}{4\pi C_v \Gamma_R}(1 - \exp(-\Gamma_R t)). \tag{6.51b}$$

The propagating component of $\rho^e(t)$ arises from the electrostrictive effect and is proportional to γ^e; it is characterized by the Brillouin relaxation constant (acoustic decay time) $\tau_B = {\Gamma_B}^{-1} = 2\rho_0/\eta q^2$ and frequency $\Omega = \sqrt{q^2\nu^2 - {\Gamma_B}^2}$. The ρ^e component gives rise to a spectrum of propagating acoustic waves. The other component, $\rho^T(t)$, is the thermoelastic contribution (proportional to β^T) caused by thermal heating and is characterized by the thermal time constant $\tau_R = {\Gamma_R}^{-1} = \rho_0 C_v/\lambda_T q^2$; it is a diffusive effect. In liquid crystals $n \sim 1.5$, $\eta = 7 \times 10^{-2}$ kg m^{-1} s^{-1}, $v = 1540$ m s^{-1}, $\rho_0 = 10^3$ kg m^{-3}, and $\lambda_T/\rho_0 C_v = 0.79 \times 10^{-7}$ m^2/s [173]. For a grating period of 20 μm, $\tau_R \approx 100$ μs and $\tau_B \approx 200$ ns [207].

In the steady state when $\tau_p \gg \tau_B$, τ_R, the density contributions are generally vanishingly small, while the temperature contribution builds up to a maximum value and produces an index change Δn_T given by

$$\Delta n_T = \frac{\alpha c n E_0^2}{4\pi\rho_0 C_v \Gamma_R}\frac{\partial n}{\partial T} = n_2^{\mathrm{SS}}(T) I_{\mathrm{op}}. \tag{6.52}$$

This allows us to define a steady-state nonlinear index coefficient

$$n_2^{\mathrm{SS}}(T) = \frac{\alpha}{\rho_0 C_v \Gamma_R}\left(\frac{\partial n}{\partial T}\right). \tag{6.53}$$

Recalling that $\Gamma_R = Dq^2$, Eq. (6.53) becomes

$$n_2^{\mathrm{SS}}(T) = \frac{\alpha}{\rho_0 C_v D q^2}\left(\frac{\partial n}{\partial T}\right). \tag{6.54}$$

Using typical liquid crystalline parameters, $\rho \sim 1$ g/cm^3, $C_p \approx C_v \approx 2$ J/g/K, $D \approx 2 \times 10^{-3}$ cm^2/s, $\alpha \sim 100$ cm^{-1}, $dn/dT \approx 10^{-3}$ K^{-1} and a grating period $\Lambda = 2\pi/q = 20$ μm, we get

$$n_2^{\mathrm{SS}}(T) \approx \frac{100}{4\pi} \times \frac{(20 \times 10^{-4})^2}{1 \times 2 \times 2 \times 10^{-3}} \times 10^{-3} \approx 2.5 \times 10^{-6}\ \mathrm{cm^2/W}. \tag{6.55}$$

Near the nematic-isotropic transition temperature, the magnitude of dn/dT [especially d$n_\parallel$/dT], can be as high as 10^{-2} K^{-1} (cf. Fig. 75), and the nonlinear index coefficients $n_{2,\mathrm{lc}}$ can be as large as 10^{-4} cm^2/W. These rough estimates are actually in good order-of-magnitude agreement with experimental observations.

7. Photorefractive Nonlinearities

The PR effect is known to occur in electro-optic photoconductive materials. It essentially arises from the space-charge field set up by the diffusion and or transport of photogenerated charge carriers that in turn modifies the index of refrac-

tion through the Pockels effect [212–223]. In this respect, the refractive index of a medium can change through photorefraction as a result of optical beam illumination. This process was first observed by Ashkin and colleagues in 1966, and its very origin remained for several years a subject of discussion [224]. Today it is widely accepted that the kinetic model first suggested by the Kiev group [225,226] can adequately describe the physics of photorefraction. Irrespective of the details behind the actual mechanisms involved, all types of PR effects share common characteristics. In all cases the induced refractive index (which can be significant) can vary anywhere from nonlocal to local and is typically characterized by a finite or relatively slow response time. In addition these effects can be observed at low optical intensities and can persist in the dark over long periods, unless erased with uniform illumination. This effect can be observed in many types of materials and over a broad wavelength range—from the visible to long wavelengths etc. [212–217].

A PR material involves both acceptor and donor impurities with energy levels lying between the conduction and the valence band. These levels and physical mechanisms behind the PR effect are schematically depicted in Fig. 76. In this arrangement, an optical beam photoexcites carriers from donor centers, which in turn diffuse or move through the conduction band. Charge recombination also takes place via acceptors. The space-charge field established during this process can then electro-optically alter the refractive index [225].

In the presence of a static electric field $\vec{E}$, the refractive index changes in these materials are determined by how the electro-optic effect modifies the impermeability tensor [215], e.g.,

$$\Delta \eta_{ij} = \Delta\left(\frac{1}{n^2}\right)_{ij} = r_{ijk}E_k + s_{ijkm}E_kE_m. \tag{7.1}$$

In Eq. (7.1) r_{ijk} and s_{ijkm} represent linear and quadratic electro-optic coefficients, respectively. Typically, PR index changes are driven by linear Pockels effects. In this case, the 27 elements of the rank 3 tensor r_{ijk} can be contracted, i.e.,

Figure 76

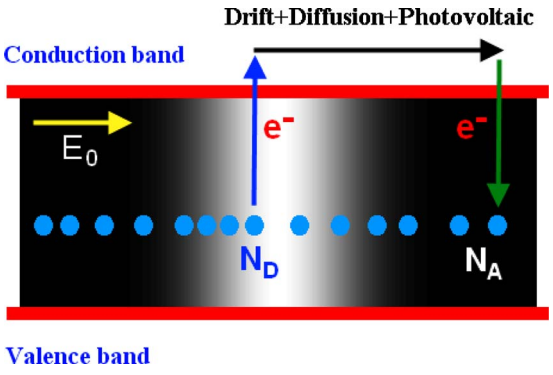

Sample of a typical PR material showing donor and acceptor impurity states in the gap between the valence and conduction bands, the raising of an electron via light absorption from a donor state into the conduction band, electron transport due to drift and diffusion effects, and the subsequent trapping of the electron in an acceptor state.

$$\Delta\left(\frac{1}{n^2}\right)_l = r_{lm}E_m. \tag{7.2}$$

The dynamics of electron photogeneration and recombination together with those of diffusion and transport are governed by the Kukhtarev–Vinetskii model [225,226]. As indicated in Fig. 76, the PR material contains donor impurities with density N_D, out of which N_D^+ are ionized. The density of acceptor atoms is also taken to be N_A. Under dark conditions charge neutrality requires that $\langle N_D^+\rangle = N_A$ [219]. Of course the nonionized portion of the donor impurities are candidates for electron photogeneration. From these arguments it follows that the rate equation for the donor density is given by

$$\frac{\partial N_D^+}{\partial t} = \hat{s}(I + I_d)(N_D - N_D^+) - \gamma_R N_e N_D^+. \tag{7.3}$$

In Eq. (7.3), N_e is the electron density in the conduction band and γ_R is the carrier recombination rate; $\hat{s}$ is the photoexcitation cross section and is related to the absorption cross section α_1 via $\hat{s} = \alpha_1/h\nu$. I is the externally imposed optical intensity, and I_d is the so-called dark intensity that phenomenologically accounts (through the product $\hat{s}I_d$) for the rate of thermally generated electrons. The continuity equation also demands that

$$\frac{\partial}{\partial t}(N_D^+ - N_e) + \frac{1}{e}\nabla \cdot \vec{J} = 0, \tag{7.4}$$

where $e = |e|$ represents the electron charge. In the absence of any photovoltaic contributions (to be considered in Subsection 7.3), the current density can in general include both a diffusion and a drift component, that is,

$$\vec{J} = eN_e\mu\vec{E} + k_B T\mu\,\nabla N_e. \tag{7.5}$$

In Eq. (7.5) μ is the electron mobility and is related to the carrier diffusion constant $D = k_B T\mu/e$. The first term in Eq. (7.5) describes drift transport resulting from the presence of an electric field component $\vec{E}$, while the second (associated with the thermal energy $k_B T$) accounts for diffusion effects. The total electric field $\vec{E}$ is the sum of the external bias field and that established from the generated space charge. Finally, Gauss's law dictates that

$$\vec{\nabla} \cdot (\varepsilon\vec{E}) = e(N_D^+ - N_e - N_A) \tag{7.6}$$

where $\varepsilon = \varepsilon_0\varepsilon_r$ is the static permittivity of the material. The set of Eqs. (7.3)–(7.6) completely describes the PR effect. Once the total space-charge field $\vec{E}$ is known, then Eq. (7.2) can be used to analyze any index changes resulting from an optical illumination I. Of importance is also the relative order of the densities involved, e.g., $N_D \gg N_A \gg N_e$ [212–219]. Models accounting for bipolar transport (holes and electrons) can also be developed along similar lines [227,228].

7.1. Diffusion Nonlinearity

In the absence of any external bias ($E_0 = 0$), the PR effect is dominated by the diffusion process [225]. The way the diffusion mechanism affects optical wave

propagation is primarily nonlocal, and as a result it leads to an energy exchange between plane wave components [214,215]. The manifestation of diffusion effects can vary considerably depending on the nature of optical illumination. For example two-wave mixing is possible if the illumination is periodic (if it is the outcome of two interfering plane waves), while for finite optical beams beam fanning and self-bending can take place [212–214]. For these reasons these two cases will be dealt with separately.

7.1a. Diffusion-Induced Two-Wave Mixing

Let us consider two monochromatic plane waves (of the same color) interfering in a PR crystal. The total electric field associated with these two waves is written in the form $\vec{E}_T = E_1\hat{e}_1 \exp[i(\omega t - \vec{k}_1\cdot\vec{r})] + E_2\hat{e}_2 \exp[i(\omega t - \vec{k}_2\cdot\vec{r})]$, and hence the resulting total optical intensity or illumination is given by $I_T = I_0 + [I_1 \exp(-i\vec{K}\cdot\vec{r}) + \text{c.c.}]$. In the last expression $I_0 = |E_1|^2 + |E_2|^2$ represents the constant intensity background of the total intensity, while $I_1 = \hat{e}_1\cdot\hat{e}_2 E_1 E_2^*$ is the amplitude of the periodic component of this interference pattern. The grating wave vector is defined as $\vec{K} = \vec{k}_1 - \vec{k}_2$ and is related to the spatial period Λ of the interference via $K = 2\pi/\Lambda$. In principle this problem cannot be treated analytically. Yet approximate solutions can be obtained under steady-state conditions ($\partial/\partial t = 0$) by using perturbation methods, provided that the periodic component is small, i.e., $I_1 \ll I_0$. In this regard, to first order, all the unknown quantities in Eqs. (7.3)–(7.6) are written as $x = x_0 + [x_1 \exp(-i\vec{K}\cdot\vec{r}) + \text{c.c.}]$ [215,219]. After some algebra, direct substitution into Eqs. (7.3)–(7.6) leads to the following result concerning the space-charge field:

$$E_{1\text{sc}} = -i\frac{K\dfrac{k_B T}{e}}{1 + \dfrac{K^2}{k_D^2}}\frac{I_1}{I_0}. \tag{7.7}$$

In Eq. (7.7), $k_D = e\sqrt{N_A/(\varepsilon k_B T)}$ represents the Debye wave number, which in turn determines the Debye screening radius $L_D = 2\pi/k_D$ [215]. Some of the features of Eq. (7.7) merit further discussion. To begin with, the imaginary factor i appearing in the numerator of Eq. (7.7) clearly suggests that the space-charge field $E_{1\text{sc}}$ (and hence the resulting index grating) is $\pi/2$ out of phase with respect to the light periodic pattern inducing it. Thus PR diffusion effects are nonlocal. This field is proportional to the depth of modulation I_1/I_0 and to the thermal potential $k_B T/e$. Finally, the amplitude of $E_{1\text{sc}}$ reaches a maximum when $K = k_D$. Analysis also indicates that the time required for this space-charge field to form is directly related to the dielectric relaxation time $\tau_d = \varepsilon/\sigma = \varepsilon/e\mu N_{eo}$ [214].

To better appreciate two-wave mixing effects we consider the coherent interaction of two plane waves propagating at angles $\pm\theta$ with respect to the z axis. For demonstration purposes we assume that the periodic pattern forms along the x axis, e.g., $\vec{K} = \vec{k}_1 - \vec{k}_2 = K\hat{x}$. In this case the grating vector is related to the wave vectors via $K = 2k_0 n_0 \sin\theta$, where n_0 is the effective refractive index of the crystal. The index perturbation induced by the periodic part of the illumination pattern can be obtained from Eq. (7.2). For typical arrangements this index change can be written in the form $\Delta n = -n_0^3 r_{\text{eff}} E_{\text{sc}}/2$ [215,219], where r_{eff} is an effective electro-optic

coefficient that depends on the electro-optic tensor and the orientation of the space-charge field with respect to the crystal's axes. Thus the refractive index in the PR crystal is given by

$$n = n_0 + \frac{1}{2}\left[n_1 \exp(-i\varphi)\frac{I_1}{I_0}\exp(-iKx) + \text{c.c.} \right], \tag{7.8}$$

where

$$n_1 \exp(-i\varphi) = n_0^3 r_{\text{eff}} \frac{iK\dfrac{k_B T}{e}}{1 + \dfrac{K^2}{k_D^2}}. \tag{7.9}$$

From Eq. (7.9) it is again obvious that the index grating is indeed $\pi/2$ out of phase with respect to the periodic intensity pattern resulting from the interference of these two plane waves, in agreement with the previous discussion. By substituting this latter expression into the Helmholtz equation and by retaining synchronous terms [217–219], one obtains the following coupled evolution equations for the slowly varying field amplitudes $E_1(z), E_2(z)$:

$$\begin{aligned} i\frac{dE_1}{dz} &= -\frac{\pi n_1}{\lambda \cos\theta}\exp(-i\varphi)\hat{e}_1\cdot\hat{e}_2\frac{|E_2|^2}{|E_1|^2+|E_2|^2}E_1, \\ i\frac{dE_2}{dz} &= -\frac{\pi n_1}{\lambda \cos\theta}\exp(i\varphi)\hat{e}_1\cdot\hat{e}_2\frac{|E_1|^2}{|E_1|^2+|E_2|^2}E_2, \end{aligned} \tag{7.10}$$

where in deriving Eqs. (7.10) we have omitted any loss effects. These latter equations describe the two-wave mixing process and together with Eq. (7.9) can be written in a simpler version:

$$\begin{aligned} \frac{dE_1}{dz} &= -\frac{g}{2}\frac{|E_2|^2}{|E_1|^2+|E_2|^2}E_1 \\ \frac{dE_2}{dz} &= \frac{g}{2}\frac{|E_1|^2}{|E_1|^2+|E_2|^2}E_2, \end{aligned} \tag{7.11}$$

where the gain g is given by

$$g = \frac{2\pi}{\lambda\cos\theta}\hat{e}_1\cdot\hat{e}_2 n_0^3 r_{\text{eff}}\frac{K(k_B T/e)}{1+(K^2/k_D^2)}. \tag{7.12}$$

As expected, in the absence of any losses the overall power in the system is conserved, e.g., $|E_1|^2+|E_2|^2=\text{const}$ [215]. Moreover, from Eqs. (7.11) it is evident that the signal field E_2 gains energy at the expense of the pump field E_1. In the limit where the signal is weak compared with the pump ($|E_2| \ll |E_1|$), one readily finds that the signal intensity will experience amplification according to $I_2 = I_{20}\exp(gz)$. It is also apparent from Eq. (7.12) that the two-wave mixing gain attains a maximum at a specific angle of interaction $\theta_{\max}$, i.e., when $K = k_D = 2k_0 n_0 \sin\theta_{\max}$, in which case $g_{\max} = (\pi n_0^3 r_{\text{eff}} k_B T k_D \hat{e}_1\cdot\hat{e}_2)/(e\lambda\cos\theta)$. To appreciate these effects, let us consider the following values corresponding to typical PR materials under standard tempera-

ture conditions: $n_0=2.3$, $r_{\text{eff}}=250$ pm/V, $\varepsilon_r=800$, $N_A=2\times10^{22}$ m^{-3}, $\lambda=0.5$ μm. For this case we find that $\theta_{\max}\approx4^\circ$ and $g_{\max}\approx20$ cm^{-1}. Other arrangements, such as contra-directional two-wave mixing as well as four-wave mixing configurations, can be similarly analyzed [215,220,221].

7.1b. Diffusion Effects on Beam Propagation

The nonlocal character of the diffusion PR process also affects in a crucial manner the propagation of optical beams. One such effect is beam fanning [212–221]. Fanning is a direct outcome of the diffusion nonlinearity, and as its name implies it leads to asymmetric fanning and self-bending of a single beam [229]. It typically arises from scattered light from the beam itself when it encounters inhomogeneities and impurities in the PR crystal. The scattered light components are then amplified by all the plane-waves composing the beam via two-wave mixing. The end result is the amplification of spatial scattering noise and the subsequent deterioration of the optical beam. This energy transfer has been investigated in several works using multiple-wave mixing approaches [229,230].

Another possibility is a two-wave mixing energy exchange between all the spectral components composing an optical beam. This is a deterministic effect and can be observed only if beam-fanning is carefully eliminated in the experimental arrangement. To examine this latter mechanism, one has to first obtain the diffusion-induced space-charge field [231]. Given that under no external bias the current density is zero, the diffusion-induced space-charge field can be determined from Eq. (7.5), e.g., $\vec{E}_{\text{sc}}=-(k_{\text{B}}T/e)(\nabla N_e/N_e)$. In addition, since $N_e\propto I+I_d$, we find that

$$\vec{E}_{\text{sc}}=-\frac{k_{\text{B}}T}{e}\frac{\nabla I}{I+I_d}. \tag{7.13}$$

To see how the diffusion nonlinearity will affect a beam, let us consider a Gaussian beam propagating along z. The space charge in Eq. (7.13) is assumed to vary only in the x coordinate. In this case, the electric optical field amplitude E of this wavefront will evolve according to

$$i\frac{\partial E}{\partial z}+\frac{1}{2k}\frac{\partial^2 E}{\partial x^2}+\frac{k_0}{2}n_0^3 r_{\text{eff}}\frac{k_{\text{B}}T}{e}\left(\frac{\partial(|E|^2)/\partial x}{1+|E|^2}\right)E=0, \tag{7.14}$$

where in Eq. (7.14) the electric field has been normalized with respect to the dark intensity level. This problem can be solved in closed form under high-illumination conditions ($|E|^2\gg1$) provided that beam is initially Gaussian, i.e., $E(z=0,x)=A\exp[-x^2/(2w_0^2)]$. In this case analysis shows that the Gaussian beam regularly diffracts, while its center self-bends during propagation [232] by an amount x_d that is given by

$$x_d=\frac{k_0^2 w_0^2 n_0^4 r_{\text{eff}} k_{\text{B}}T}{2e}[2\xi\tan^{-1}\xi-\ln(1+\xi^2)], \tag{7.15}$$

where $\xi=z/kw_0^2$. For the same parameters used in Subsection 7.1a, one finds that a Gaussian beam with an initial spot size of $w_0=4$ μm is expected to self-deflect by a distance of $x_d=5.7$ μm after a distance of 10 diffraction lengths ($\xi=10$). This effect is schematically depicted in Fig. 77. Intuitively the beam deflection can be ex-

Figure 77

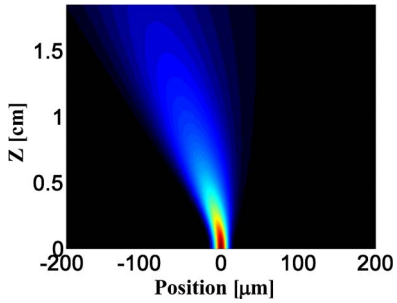

Light spreading on propagation due to diffraction and self-bending in a PR medium due to the nonlocality of the optical response.

plained by considering the spatial profile of the space-charge field and consequently of the index distribution. If the optical beam is Gaussian-like then resulting space-charge field E_{sc} is almost linearly varying across the beam, and as a result the induced index prism leads to self-bending.

7.2. Screening Photorefractive Nonlinearity

When a PR material is strongly biased another type of nonlinearity manifests itself: the screening nonlinearity [233–235]. As we will see, this nonlinearity is primarily local in nature, and in the same PR system it can lead to both self-focusing and defocusing conditions depending on the polarity of the external bias. The strength of the screening mechanism can be substantial, and it can respond at very low optical power levels. This type of nonlinearity has been extensively investigated in conjunction with optical soliton effects, self-focusing, and instability phenomena, and most recently in the exploration of nonlinear optically induced lattices to mention a few topics [236].

7.2a. Physical Origins of the Screening Photorefractive Nonlinearity

To understand the origin of the screening nonlinearity, we consider Eqs. (7.3)–(7.6) under steady-state conditions, assuming for simplicity that the space-charge field is established in only one direction (in this case x). By keeping in mind the inequalities $N_D \gg N_A \gg N_e$ associated with the densities, from Eqs. (7.3) and (7.6) one can show that [233,234]

$$N_D^+ = N_A\left(1+\frac{\varepsilon}{eN_A}\frac{\partial E_{sc}}{\partial x}\right), \tag{7.16}$$

$$N_e = \frac{\hat{s}(N_D-N_A)}{\gamma_R N_A}(I+I_d)\left(1+\frac{\varepsilon}{eN_A}\frac{\partial E_{sc}}{\partial x}\right)^{-1}. \tag{7.17}$$

At this point, let us also assume that the power density $I(x,z)$ of the optical beam attains asymptotically a constant value I_∞ at $x \to \pm\infty$. This constant I_∞ can be finite or zero depending on the experimental arrangement used. In these regions of constant illumination, the space-charge field is also independent of x, i.e.,

$E_{sc}(x \to \pm\infty, z) = E_0$. If the spatial extent of the optical wave is much less than the x width W of the PR crystal, then under a constant voltage bias V, E_0 is approximately $E_0 = V/W$. On the other hand, if W is comparable with the wave's width, then this approximation breaks down. In this case the intensity profile of the optical beam has to be taken into account in order to estimate the appropriate correction factors [234]. From Eq. (7.17) the free-electron density N_{e0} in these regions is given by

$$N_{e0} = \frac{\hat{s}(N_D - N_A)}{\gamma_R N_A}(I_\infty + I_d). \tag{7.18}$$

Under steady-state conditions, Eq. (7.4) implies that $\nabla \cdot \vec{J} = 0$. Hence in 1D configurations the current density should, as expected, be constant everywhere, i.e., J=constant. Therefore $N_{e0}E_0 = N_e E_{sc} + (k_B T/e)\partial N_e/\partial x$ or

$$E_{sc} = \frac{N_{e0}E_0}{N_e} - \frac{k_B T}{e}\frac{1}{N_e}\frac{\partial N_e}{\partial x}. \tag{7.19}$$

Substitution of Eq. (7.17) into Eq. (7.19) gives the final expression for the space-charge field:

$$E_{sc} = E_0\frac{(I_\infty + I_d)}{(I + I_d)}\left(1 + \frac{\varepsilon}{eN_A}\frac{\partial E_{sc}}{\partial x}\right) - \frac{k_B T}{e}\frac{(\partial I/\partial x)}{(I + I_d)} + \frac{k_B T}{e}\frac{\varepsilon}{eN_A}\left(1 + \frac{\varepsilon}{eN_A}\frac{\partial E_{sc}}{\partial x}\right)^{-1}\frac{\partial^2 E_{sc}}{\partial x^2}. \tag{7.20}$$

Under strong bias conditions the drift component dominates the transport process, and thus any diffusion effects can be neglected [terms associated with $k_B T/e$ in Eq. (7.20)]. In addition, for relatively broad beams in typical PR media the term $(\varepsilon/eN_A)\partial E_{Sc}/\partial x \ll 1$, and as result Eq. (7.20) can be expressed in a simpler form, i.e., [233,234],

$$E_{sc} = E_0\frac{(I_\infty + I_d)}{(I + I_d)}. \tag{7.21}$$

It is interesting to note that one could have arrived at this same relation by considering an intensity-dependent conductivity $\sigma(I)$ and only drift transport provided that J=constant. In other words, Eq. (7.21) results if we assume that the conductivity varies with intensity according to $\sigma = \sigma_d(I + I_d)/I_d$, where σ_d is the dark conductivity of the PR material [235]. Under constant voltage bias V we also expect that

$$V = -\int_{-W/2}^{W/2} E_{sc}\,dx. \tag{7.22}$$

The index changes in the PR medium can now be estimated from Eq. (7.2). In typical arrangements this is given by [233–235]

$$\Delta n = -\frac{n_0^3}{2} r_{eff} E_{sc} = -\frac{n_0^3}{2} r_{eff} E_0\left(\frac{I_\infty + I_d}{I + I_d}\right). \tag{7.23}$$

It is important to emphasize that in many experiments the so-called dark-intensity level I_d is artificially elevated by externally illuminating the crystal, either from the top or along the other input polarization. Such an elevation not only

speeds up the PR time response but also allows better controllability in experimental setups.

To get an appreciation of the index changes expected in this regime, let us assume a Gaussian-like beam traversing a biased PR material ($I_\infty=0$). If we let $n_0=2.3$, $r_{\text{eff}}=250$ pm/V, and if the external bias strength is $E_0=2$ kV/cm, then for a Gaussian having a peak intensity 10 times higher than I_d, we find that the index change between the center and the far tails of the beam is approximately $\Delta n \approx 3 \times 10^{-4}$. This level of index change is more than enough to enable a host of nonlinear self-action effects. The index change corresponding to this case is plotted in Fig. 78(a). As the figure indicates, for $E_0>0$ the refractive index is higher at the beam center (in essence the PR effect lowers the index at the tails), and as a result this PR system behaves in a self-focusing fashion. On the other hand, if $E_0=-2$ kV/cm, e.g., if the polarity of the external bias is reversed, the index profile is inverted. In this latter case, the index at the center of the beam attains a minimum, and thus in this regime the PR medium is defocusing [Fig. 78(b)]. What is interesting is that the same crystal can be either self-focusing or defocusing depending on the polarity of the external bias. In other words the sign of the screening nonlinearity can be tuned at will. Equation (7.23) also indicates that the screening nonlinearity has a saturable Kerr-like nonlinear response. This issue is of importance to the stability of 2D self-trapped beams.

In two transverse dimensions the problem becomes more complicated because of the space-charge field boundary conditions. In many occasions these effects can be understood by only considering the drift component and by assuming again that $\sigma=\sigma_d(I+I_d)/I_d$. Given that $\vec{E}_{\text{sc}}=-\nabla V$ and $\nabla\cdot(\sigma\vec{E}_{\text{sc}})=0$, the following equation for the potential is derived [214]:

$$\nabla^2 V+\frac{\nabla I}{I+I_d}\cdot\nabla V=0. \tag{7.24}$$

In general this latter equation must solved numerically during propagation subject to appropriate mixed boundary conditions for the potential function V. An analytic solution can be obtained when the optical beam is cylindrical, e.g., $I=I_0\,\text{circ}(r/a)$ for $r<a$ and zero elsewhere (diffraction effects are neglected here). In this case the conductivity of the PR medium is $\sigma_b=\sigma_d(I_0+I_d)/I_d$ for $r<a$ and $\sigma_b=\sigma_d$ for $r>a$. The space-charge electric field associated with this latter arrangement

Figure 78

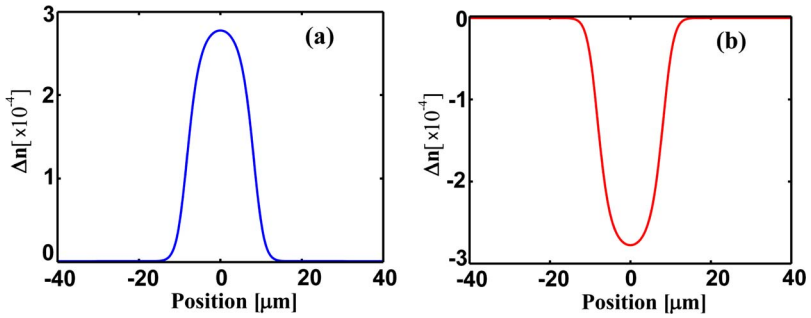

Refractive index change produced by a 1D optical beam with intensity $10I_d$ in a PR crystal for (a) a self-focusing and (b) self-defocusing nonlinearity.

can be obtained by using standard methods from electrostatics. To do so we assume that the electric field away from the high-conductivity rod ($r<a$) is E_0. More specifically, in polar coordinates (r,ϑ), E_{sc} is given by [237]

$$\vec{E}_{sc}=\begin{cases}\dfrac{2E_0\hat{x}}{2+(I_0/I_d)} & r<a\\[2ex] E_0\hat{x}+a^2E_0\left[\dfrac{I_0}{I_0+2I_d}\right]\left[\dfrac{\cos(2\vartheta)}{r^2}\hat{x}+\dfrac{\sin(2\vartheta)}{r^2}\hat{y}\right] & r>a\end{cases}, \tag{7.25}$$

The index profile corresponding to this cylindrical optical beam can be determined from Eq. (7.2). This index distribution is shown in Fig. 79. In general the index change is azimuthally asymmetric, and this is a characteristic of the screening nonlinearity. Similar results can be obtained for other classes of optical beams, e.g., Gaussian.

Typical values associated with screening nonlinearities as obtained in typical PR crystals are listed in Table 16.

7.2b. Self-Trapped Beams—Screening Photorefractive Solitons

The possibility of optical PR solitons was first suggested in 1992 [238]. Nonlinear optical wave propagation under the action of screening PR effects can be considered by starting from the Helmholtz equation. By writing the optical electric field in the form $E=\Phi(x,z)\exp(ikz)$ and by assuming a slowly varying envelope $\Phi(x,z)$, we find that [233,234]

$$i\frac{\partial\Phi}{\partial z}+\frac{1}{2k}\frac{\partial^2\Phi}{\partial x^2}-k_0\frac{n_0^3}{2}r_{\text{eff}}E_0\left(\frac{I_\infty+I_d}{I+I_d}\right)\Phi=0. \tag{7.26}$$

This equation can be more conveniently studied in normalized units and coordinates, i.e., if $\xi=z/kx_0^2$, $s=x/x_0$, $\Phi=(2\eta_0I_d/n_0)^{1/2}U$, in which case one obtains

$$i\frac{\partial U}{\partial\xi}+\frac{1}{2}\frac{\partial^2U}{\partial s^2}-\beta\left(\frac{1+\rho}{1+|U|^2}\right)U=0. \tag{7.27}$$

In Eq. (7.27), $\rho=I_\infty/I_d$ is an intensity ratio and $\beta=(k_0x_0)^2(n_0^4r_{\text{eff}}/2)E_0$ is the strength of the screening PR nonlinearity. For singular bright beams that tend to zero at $x\to\pm\infty$, $\rho=0$ in Eq. (7.27). The bright self-trapped states or solitons of Eq. (7.27)

Figure 79

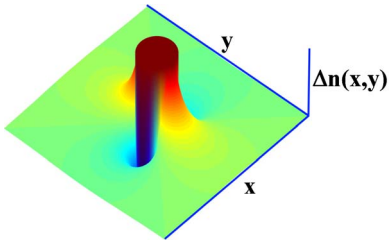

Index change induced in a PR medium by a 2D cylindrical beam.

Table 16. PR Materials Used for Screening Nonlinearities and Their Relevant Material Properties

Material	Dopant	λ (μm)	$n^3 r_{\text{eff}}$ (pm/V)	τ_{diel} (s)[a]	$\Delta n_{\max}$	E_{dc} (KV/cm)
$Sr_{0.75}Ba_{0.25}Nb_2O_6$	Ce	0.4–0.6	17390	0.1–1.0	0.005	3
$Sr_{0.6}Ba_{0.4}Nb_2O_6$	Ce	0.4–0.6	3000	0.1–1.0	0.0014	3
$BaTiO_3$	Fe	0.4–0.9	21,500	0.1–1.0	0.005	2.5
InP	Fe	0.9–1.3	52	10^{-6}–10^{-4}	5×10^{-5} [b]	8

[a] At an intensity of 1 W/cm^2.
[b] With enhancement can go to 5×10^{-4}.

can be obtained by assuming that their field profile is given by $U = r^{1/2} y(s) \exp(i\nu\xi)$, where r is the ratio of the soliton's peak intensity to the dark intensity I_d. In this case we find that [233,234],

$$\frac{d^2y}{ds^2} - 2\nu y - 2\beta \frac{y}{1+ry^2} = 0. \tag{7.28}$$

This last differential equation can be integrated further provided that $\nu = -(\beta/r)\ln(1+r)$, e.g.,

$$\left(\frac{dy}{ds}\right)^2 = (2\beta/r)[\ln(1+ry^2) - y^2 \ln(1+r)], \tag{7.29}$$

from which the soliton field profile $y(s)$ can be uniquely determined. These solutions are possible only for $\beta > 0$ or $E_0 > 0$, that is, under self-focusing conditions [236]. The intensity distribution corresponding to a soliton in SBN:60 with $n_0 = 2.3$, $r_{\text{eff}} = 225$ pm/V, at a bias of $E_0 = 2$ kV/cm, at $\lambda = 0.5$ μm is shown in Fig. 80. Similarly, dark as well as gray soliton solutions can be identified under defocusing nonlinear conditions [234,235].

7.3. Photovoltaic Nonlinearity

Photovoltaic, or photogalvanic. effects are known to occur in noncentrosymmetric crystals such as, for example, $LiNbO_3$, $BaTiO_3$, and $KNbO_3$ [212–220]. This

Figure 80

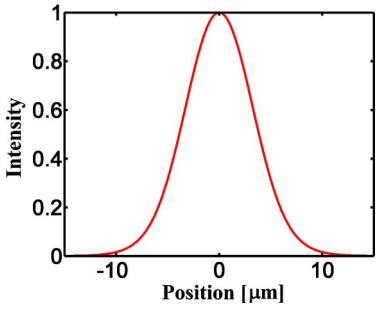

Intensity distribution corresponding to a bright spatial soliton in SBN:60.

mechanism results from the asymmetric excitation of carriers and essentially gives rise to a current density [214]. This is because carriers are photoexcited from impurity centers with a momentum preferentially oriented along the c axis. From these considerations, the current density associated with the photovoltaic effect is proportional to the number of available donors, the optical intensity I, and the photoexcitation cross section $\hat{s}$, i.e.,

$$J_{\mathrm{PV}} = e\hat{s}(N_D - N_D^+)L_{\mathrm{PV}}I. \tag{7.30}$$

In Eq. (7.30) L_{PV} is a characteristic length associated with this photogalvanic transport anisotropy—for example, in $LiNbO_3$, L_{PV} is approximately 5 Å. More formally, the photovoltaic part in the current density can be expressed as

$$\vec{J}_{\mathrm{PV}} = \beta_{ijk}E_jE_k, \tag{7.31}$$

where β_{ijk} represents a third-rank tensor. By adding the photovoltaic component of Eq. (7.30) to the total current density passing through a PR material, one obtains

$$\vec{J} = en\mu\vec{E} + k_{\mathrm{B}}T\mu\,\nabla N_e + \kappa_{\mathrm{eff}}\hat{s}(N_D - N_D^+)I\hat{c}, \tag{7.32}$$

where κ_{eff} is the photovoltaic constant and $\hat{c}$ is a unit vector along the c axis of the crystal. For example, under open circuit conditions ($\vec{J}=0$) and provided that diffusion effects can be neglected in Eq. (7.32) we find that $E_{\mathrm{sc}}=-\kappa_{\mathrm{eff}}\hat{s}(N_D - N_D^+)I/(eN_e\mu)$. Given that normally $N_D^+ \approx N_A$ and that $N_e=\hat{s}(N_D-N_A)(I+I_d)/\gamma_R N_A$, from Eq. (7.17) we find the photovoltaic space-charge field in a PR medium [239,240]:

$$E_{\mathrm{sc}} = -E_P\frac{I}{I+I_d}. \tag{7.33}$$

In Eq. (7.33) $E_P=\kappa_{\mathrm{eff}}\gamma_R N_A/(e\mu)$ represents the photovoltaic field constant, which is typically of the order of 10^4–10^7 V/m. Index changes resulting from the photogalvanic space-charge field can then be obtained from $\Delta n=-n_0^3 r_{\mathrm{eff}}E_{\mathrm{sc}}/2$, e.g., [239]

$$\Delta n = \frac{n_0^3 r_{\mathrm{eff}}E_P}{2}\frac{I}{I+I_d}. \tag{7.34}$$

As in the case of the screening process, the photovoltaic nonlinearity is also saturable. In addition, in most photovoltaic PR media, the coefficient $r_{\mathrm{eff}}E_P$ is negative, and thus this saturable nonlinearity is of the defocusing type. For this reason dark photovoltaic solitons have been regularly observed in Fe-doped $LiNbO_3$ crystals [240] (see Table 17). On the other hand, by tuning the background illumination, a transition from defocusing to self-focusing can occur in $LiNbO_3$ by exploiting the anisotropy of the photovoltaic tensor. Self-focusing photogalvanic self-action effects were also observed in KNSBN $[(K_xNa_{1-x})_{2A-2}(Sr_yBa_{1-y})_{2-A}Nb_2O_6]$[236]. For example, in $LiNbO_3$, a crystal characterized by a large photovoltaic constant, if we as-

Table 17. Typical Parameters Associated with Fe-Doped $LiNbO_3$

r_{33} (pm/V)	$\Delta n_{\max}$	At Intensity	τ_{response}
30	0.001	~W/cm^2	~minutes

sume that $n_0=2.2$, $r_{\text{eff}}=30$ pm/V, and $E_P \approx 10^6$ V/m, then for $I \gg I_d$ we find that $\Delta n \cong 1.6\times 10^{-4}$. The photovoltaic nonlinearity can be obtained under open and closed circuit conditions and in conjunction and or competition with the screening nonlinearity [236].

7.4. Photorefractive Nonlinearities Due to dc Kerr Effects

Nonlinear self-action PR effects are also possible in centrosymmetric media as a result of the dc Kerr effect [214,215]. In this case, the index change is obtained from the quadratic electro-optic tensor s_{ijkm} [in Eq. (7.1)] as discussed in the introduction to Section 7. Such crystals include, for example, potassium tantalate niobate (KTN) and potassium lithium tantalate niobate (KLTN) [241,242]. For example, KLTN has a perovskite structure, and in its highest symmetry phase it is cubic. In this cubic phase the material's PR properties are described by the quadratic electro-optic effect. The index change in this system because of the dc Kerr effect is given by [242]

$$\Delta n = -\frac{n_0^3}{2} g_{\text{eff}} P^2, \tag{7.35}$$

where the induced dc low-frequency polarization P is assumed to vary linearly with the electric field E, that is,

$$P = \varepsilon_0(\varepsilon_r - 1)E. \tag{7.36}$$

In the above equations, g_{eff} is the effective quadratic electro-optic coefficient of the PR material and ε_r stands for the static relative permittivity. From the latter relations, the expected index change is [243,244]

$$\Delta n = -\frac{n_0^3 g_{\text{eff}} \varepsilon_0^2 (\varepsilon_r - 1)^2}{2} E_{\text{sc}}^2. \tag{7.37}$$

If, for example, such a PR material is externally biased, then the maximum index change is expected to be approximately $\Delta n_{\max} \approx n_0^3 (g_{\text{eff}}/2)\varepsilon_0^2(\varepsilon_r - 1)^2 E_0^2$, where again as in the screening case $E_0 = V/W$. For example, for a KLTN crystal, where $\varepsilon_r \approx 8000$, $n_0 = 2.2$, and $g_{\text{eff}} = 0.12$ m^4 C^{-2}, and for an applied external bias field of $E_0 = 2$ kV/cm, we find that $\Delta n_{\max} \approx 1.3\times 10^{-4}$.

8. Electrostrictive Effect

"Electrostriction is a property of all electrical nonconductors, or dielectrics, that manifests itself as a relatively slight change of shape, or mechanical deformation, under the application of an *electric field*. Reversal of the electric field does not reverse the direction of the deformation." [245] Like the Kerr nonlinearity, electrostriction is a universal mechanism that occurs in all materials. This is also true for an optical field, with the difference that in this case the compression is proportional to the time average of the square of the optical field. This field-induced stress leads to an increase in the material density. Since the number density of atoms or molecules also increases, there is an increase in the electromagnetic energy density and an increase in the refractive index. Thus $n_{2,\text{el}} > 0$.

For an optical field polarized along the x direction, the material displacement $\vec{u}$ due to the compression creates an elastic strain in the direction of the applied strong field, $S_{xx}=\partial u_x/\partial x$. For a detailed discussion of stresses and strains, see the book by B. A. Auld [246]. This leads via the elasto-optic effect to a nonlinear polarization of the form

$$P_i^{\mathrm{NL}}(\vec{r},t) = -\varepsilon_0 n_i^2 n_j^2 p_{ijxx} S_{xx} E_j(\vec{r},t), \tag{8.1}$$

in which the $p_{ijk\ell}$ is the elasto-optic tensor (also known as the acousto-optic tensor) [167]. For $n_{2\parallel,\mathrm{el}}(-\omega;\omega)$, $i=j=x$ is appropriate (coefficient p_{11} in Voigt notation) and for $n_{2\perp,\mathrm{el}}(-\omega;\omega)$, $i=j=y$ (p_{21} in Voigt notation) for the case of an additional, weak ("probe") y-polarized beam.

For an unclamped medium, the work done in compressing the medium (ΔU) is equal to the increase in electromagnetic energy density (ΔW). The work done is

$$\Delta W = \mathrm{p_{st}}\frac{\Delta V}{V} = -\mathrm{p_{st}}\frac{\Delta\rho}{\rho}, \tag{8.2}$$

where $\mathrm{p_{st}}$ is the effective pressure exerted by the electromagnetic field on the medium and the change in electromagnetic energy is

$$\Delta U = \overline{\Delta\left(\frac{1}{2}\varepsilon_0\varepsilon_{r,x}[\mathrm{E_0}\cos(kz-\omega t)]^2\right)} = \varepsilon_0\frac{\mathrm{E_0^2}}{4}\frac{\partial\varepsilon_{r,x}}{\partial\rho}\Delta\rho. \tag{8.3}$$

Setting $\Delta U=\Delta W$, noting that $\Delta\rho=[\partial\rho/\partial \mathrm{p_{st}}]\mathrm{p_{st}}$, and defining $K=[(1/\rho)\times(\partial\rho/\partial \mathrm{p_{st}})]^{-1}$ as the bulk modulus for pure compressive forces (i.e., only $S_{11}\neq 0$, which corresponds to a plane wave field polarized along the x axis), gives

$$S_{11} = \frac{\Delta\rho}{\rho} = \frac{\varepsilon_0\rho}{4K}\mathrm{E_0^2}\frac{\partial\varepsilon_{r,x}}{\partial\rho} = -\frac{\varepsilon_0 n_x^4 p_{11}\mathrm{E_0^2}}{4K}. \tag{8.4}$$

For an isotropic material, $K=(c_{11}+2c_{12})/3$, whereas for anisotropic materials K depends on the crystal symmetry, propagation direction, etc. Substituting this equation for S_{11} into $P_x^{\mathrm{NL}}(\vec{r},t)$ finally gives $n_{2\parallel,\mathrm{el}}$ in terms of the electrostrictive constant γ_{el} (defined below) as

$$n_{2\parallel,el}(-\omega;\omega) = \frac{n_x^6 p_{11}^2}{4Kc} = \frac{\gamma_{\mathrm{el}}}{4Kc}. \tag{8.5}$$

It is straightforward to show that

$$n_{2\perp,el}(-\omega;\omega) = \frac{n_x^3 n_y^3 p_{11} p_{12}}{4Kc}. \tag{8.6}$$

Values for $n_{2\parallel,\mathrm{el}}$ are given in Table 18 for a number of materials. In general, the softer the material, the larger is the nonlinearity. Elasto-optic data can be found in [247,248].

Turn-on and turn-off times are a complex issue. Turning an optical beam on or off involves inducing compressive forces in the medium. They lead to the generation of a spectrum of acoustic waves. The acoustic decay time $\tau_s(\Omega_s)\propto\Omega_s^{-2}$, and the details of beam shape, sample boundaries, etc., influence the acoustic spectrum generated, which includes both compressional and shear waves for a

Figure 81

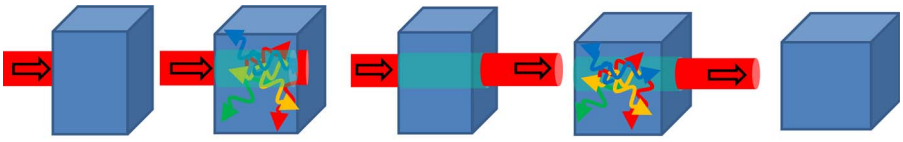

Sequence of events that occur when an intense light beam enters and exits a dielectric medium. (a) Light at entrance facet to medium. (b) Sound waves are generated by the material contraction induced by the entering beam. (c) Steady-state compression exists in the medium as long as the light is present. (d) The tail end of the beam exits the medium, releasing the compression and generating sound waves. (e) The medium has relaxed to its initial state.

finite-sized beam. In Fig. 81 is shown the sequence of events that occurs. Figure 81(a) shows the sample before the optical beam enters it. As the beam enters the sample, material compression occurs accompanied by the generation of sound waves in all directions; see Fig. 81(b). Beam turn-off is again accompanied by acoustic phonon generation; see Fig. 81(d). In an infinite medium, the *shortest* turn-on and turn-off times are given by the acoustic transit time across the optical beam (beam diameter) $/v_S$, with $v_S \sim 1$ μm/s, giving microsecond–nanosecond times. Therefore, the shorter the optical pulse, the smaller the value of $n_{2\|,\mathrm{el}}$, since it takes an acoustic transit time to establish this nonlinearity.

The electrostrictive contribution to n_2 has typically amounted to a tens of percent contribution to the Kerr effect in various solids and a somewhat larger contribution in liquids because of their low velocity of sound. The spurious effects that it causes have led to important features including spurious optical signals in fused silica glass fibers, since they have such a small native $n_{2,\mathrm{Kerr}}$ [249–251]. Another example is the effect of electrostriction in relatively tight focusing geometries for microsecond–nanosecond pulses in liquid CS_2 found experimentally and numerically in optical limiting studies [252,253]. Contributions as large as 30% have been seen. In materials where there is also some absorption, these effects can be combined with or masked by thermally driven acoustic waves, which have behaviors similar to those discussed in the next section.

Table 18. Values of $n_{2\|,\mathrm{el}}$

Material	Polarization λ (μm)	Elasto-optic Coefficeint	K (10^{10} m^2/N)	n	$n_{2\|,\mathrm{el}}$ (cm^2/W)
Fused silica	(0.63)	$p_{11}=0.12$	3.69	1.46	0.4×10^{-16}
GaAs	[110] (1.15)	$p=\sim0.14$	~7.6	3.37	1.6×10^{-15}
MgO	[100] (0.59)	$p_{11}=0.08$	~15.3	1.74	1.0×10^{-17}
Al_2O_3	[001] (0.63)	$p_{33}=0.20$	~27.0	1.76	3.7×10^{-17}
Polystyrene	(0.63)	$p_{11}=0.31$	0.54	1.59	2.4×10^{-15}
Acetone		$p_{11}=0.35$	0.080	1.36	8.5×10^{-15}
Methanol		$p_{11}=0.32$	0.083	1.33	5.7×10^{-15}

9. Thermo-optic Effect

Although conceptually simple, the index change produced by light absorption is a very complex problem in general [252–254]. Absorption leads to a temperature change δT, which in turn also leads to a change in local density. A change in density leads to the generation of sound waves, which effectively relieve the stresses induced by the density changes. Both δT and $\delta\rho$ lead to changes in refractive index as discussed in Section 6, i.e.,

$$\delta n = \left(\frac{\partial n}{\partial \rho}\right)_T \delta\rho + \left(\frac{\partial n}{\partial T}\right)_\rho \delta T. \tag{9.1}$$

The resulting temperature change is given by the thermal diffusion equation

$$\rho C_p \frac{\partial(\delta T)}{\partial t} - \kappa\nabla^2(\delta T) = Q = \alpha_1 I, \tag{9.2}$$

where Q is the absorbed power per unit volume per unit time. To a first approximation, the temperature change is the dominant contribution to the thermal nonlinearity.

What makes this problem difficult is the calculation of the steady-state temperature and hence index distribution. On short times scales of single femtosecond, picosecond, and nanosecond pulses, the initial thermally induced index distribution mirrors that of the incident optical beam. However, for mode-locked lasers as well as for cw excitation, the effects are cumulative over microsecond time scales. At this point the size, shape, and thermal boundary conditions of the sample become important in establishing the steady-state index change—and these vary from sample to sample, by geometry, etc.

Optical experiments involve spatially finite beams. Transients due to sound waves occur over the time it takes an acoustic wave to traverse the optical beam, similar to electrostriction. The velocity of sound is $1-4\ \mu\text{m/ns}$. Hence for the usual cases of $0.1-1$ mm beams, acoustic transient effects can be ignored for optical pulses $1\ \mu$s long, and shorter. Furthermore, since the effect on index of density changes is usually much smaller than temperature changes, density changes in the first approximation are neglected.

It is useful to find some simple approach to estimating how large $n_{2,\text{th}}$ is for the thermo-optic effect. We start by rewriting Eq. (9.2) as

$$\rho C_p \frac{\partial \delta T}{\partial t} - \kappa\nabla^2 T = Q = \alpha_1 I, \qquad \rho C_p\left[\frac{\partial \delta T}{\partial t} - \frac{\kappa\nabla^2}{\rho C_p}\delta T\right] = \alpha_1 I \tag{9.3}$$

and note that the term $\kappa\nabla^2/\rho C_p$ has the units of time. The $\nabla^2\delta T$ term indicates that any characteristic time will depend on the beam shape, an unwelcome complication. It is useful to assume a Gaussian intensity distribution given by

$$I(\vec{r},t) = I_0(z)\exp[-r^2/w_0^2 - t^2/\tau_{\text{opt}}^2], \tag{9.4}$$

where $I_0(z)$ is the on-axis distribution (along the z axis), which decays exponentially with distance z due to absorption. Assuming further that the pulse width τ_{opt} is much shorter than the thermal diffusion time τ_{th}, the maximum temperature distribution is given by the pulse energy absorbed with the spatial temperature dis-

tribution given by the Gaussian beam distribution. The maximum temperature change across the beam $\delta T_{\max}(\vec{r})$ is given by

$$\delta T_{\max}(\vec{r}) = \frac{\alpha_1}{\rho C_p} I(r) \int_{-\infty}^{\infty} e^{-t^2/\tau_{\text{opt}}^2} dt = \sqrt{\pi}\tau_{\text{opt}} \frac{\alpha_1}{\rho C_p} I(\vec{r}). \tag{9.5}$$

Note that in

$$\nabla^2[\delta T_{\max}(r)] = \left[\frac{1}{r}\frac{\partial}{\partial r} + \frac{\partial^2}{\partial r^2}\right] \delta T_{\max}(r) = -\frac{4}{w_0^2}\left\{1 - \frac{r^2}{w_0^2}\right\} \delta T_{\max}(r) \tag{9.6}$$

the largest δT occurs between $r=0$ and $r=w_0$. This equation can be simplified by neglecting the r^2/w_0^2 term, which means that the any solution will be at best approximate. However, this makes it possible to estimate the time evolution of δT and the turn-off time subsequent to removing the optical field from

$$\frac{\partial \delta T_{\max}(\vec{r},t)}{\partial t} = -\frac{4\kappa}{w_0^2 \rho C_p} T_{\max}(\vec{r},t) \Rightarrow \delta T_{\max}(\vec{r},t) = \delta T_{\max}(0,t) e^{-t/\tau_{\text{th}}}, \tag{9.7}$$

where $\tau_{\text{th}} = w_0^2 \rho C_p / 4\kappa$. Note that τ_{th} is not just a material constant! It depends on sample and beam geometry, heat sinking, beam size, etc. A sampling of τ_{th} for a variety of materials ($w_0 = 0.1$ mm) is listed in Table 19. Note that

1. There is a strong dependence on the beam size, i.e., w_0^2.
2. Excluding metals, the τ_{th} varies by about 2 orders of magnitude for a wide range of materials.
3. Because they contain the same atoms, mostly carbon and hydrogen, τ_{th} in the organic solvents varies by less than an order of magnitude.

An effective nonlinearity $n_{2,\text{th}}$ can be estimated as follows:

$$\delta n_{\max}(\vec{r}) = \left[\frac{\partial n}{\partial T}\right] \delta T_{\max}(\vec{r}) = \sqrt{\pi}\left[\frac{\partial n}{\partial T}\right] \tau_{\text{opt}} \frac{\alpha_1}{\rho C_p} I(\vec{r}) \Rightarrow n_{2,\text{th}} \cong \sqrt{\pi}\left[\frac{\partial n}{\partial T}\right] \tau_{\text{opt}} \frac{\alpha_1}{\rho C_p}.$$

For a pulse with a Gaussian shape with $\tau_{\text{th}} \gg \tau_{\text{opt}}$ it is the pulse energy ΔE_{pulse} rather than the intensity that is important and

$$\delta n_{\max} = \frac{2^{3/2}}{\pi w_0^2}\left[\frac{\partial n}{\partial T}\right] \frac{\alpha_1}{\rho C_p} \Delta E_{\text{pulse}}. \tag{9.8}$$

As an example, consider GaAs:

Table 19. τ_{th} for a Variety of Materials

Material	GaAs	Al_2O_3	NaCl	ZnO	Acetone	C_6H_6	Methanol
k (W/cm °C)	0.55	0.024	0.065	0.30	0.0019	0.0016	0.0020
C_p (joules/g/°C)	0.33	0.75	0.85	0.83	2.2	1.7	2.4
ρ (g/cm^3)	5.32	3.98	2.2	5.5	0.79	0.90	0.80
τ_{th} (ms)	0.080	3.1	0.72	0.39	45	24	20
$dn/dT \times 10^{-4}$ (/°C)	1.6–2.7	0.13	0.25	0.1	−5.6	−6.2	−4.0

$$\alpha = 1\ \text{cm}^{-1} \text{ and } \Delta t = 1\ \mu\text{s} \Rightarrow n_{2,\text{th}} = 3 \times 10^{-10}\ \text{cm}^2/\text{W}\ \text{(much bigger than Kerr effect)},$$

$$\alpha = 1\ \text{cm}^{-1} \text{ and } \Delta t = 1\ \text{ns} \Rightarrow n_{2,\text{th}} = 3 \times 10^{-13}\ \text{cm}^2/\text{W}\ \text{(comparable with Kerr effect)}$$

$$\alpha = 1\ \text{cm}^{-1} \text{ and } \Delta t = 1\ \text{ps} \Rightarrow n_{2,\text{th}} = 3 \times 10^{-16}\ \text{cm}^2/\text{W}\ \text{(negligible)}.$$

For high repetition rates (mode-locked lasers), the key question is the energy accumulation over all the pulses within the time window τ_{th}. For example, a mode-locked laser operating with 1 ps pulses at a repetition rate of 100 MHz accumulates energy from 10^3 pulses over τ_{th}, giving a cumulative $n_{2,\text{th}} = -1.2 \times 10^{-12}\ \text{cm}^2/\text{W}$, larger than the Kerr nonlinearity!

10. Cascading Nonlinearity

There are two ways in which a second-order nonlinearity can contribute to an effective $n_{2,\text{cas}}$. In the first, called "local cascading," a third-order susceptibility is obtained as the product of the molecular second-order susceptibilities $\beta^{(2)}(-2\omega;\omega,\omega)\beta^{(2)}(-\omega;2\omega,-\omega)$ and $\beta^{(2)}(-0;\omega,-\omega)\beta^{(2)}(-\omega;\omega,0)$. The light–matter interaction occurs at the molecular level, and there is no propagation of a 2ω signal. The second is also proportional to the product between second-order nonlinearities $[\chi^{(2)}(-2\omega;\omega,\omega)\chi^{(2)}(-\omega;2\omega,-\omega)]$ but does involve the generation of a second-harmonic beam that exchanges energy with the fundamental on propagation. This can be called "nonlocal cascading."

10.1. Local Cascading

Local cascading refers to a pair of two-step processes, each involving the product of two optical fields at a noncentrosymmetric molecule. A nonlinear, local polarization is generated at the sum or difference frequency via the molecular second-order susceptibility $\beta^{(2)}_{ijk}(-[\omega_1 \pm \omega_2];\omega_1,\pm\omega_2)$. The local field generated at $\omega_1 \pm \omega_2$ then mixes with the fields at ω_1 and ω_2 via $\beta^{(2)}_{ijk}(-\omega_1;\omega_1 \pm \omega_2, \mp\omega_2)$ and $\beta^{(2)}_{ijk}(\mp\omega_2;\omega_1 \pm \omega_2,-\omega_1)$, respectively, to give *new* polarization fields at ω_1 and $\pm\omega_2$, respectively. The particular case of interest here, i.e., the contribution to $n_{2\|,\text{cascl}}(-\omega;\omega)$, i.e., a single input field, involves the two-step processes $\omega+\omega \rightarrow 2\omega$ (second-harmonic generation) and $2\omega-\omega \rightarrow \omega$ (difference frequency generation), and the two-step process $\omega-\omega \rightarrow 0$ (dc rectification) and $0+\omega \rightarrow \omega$ (sum frequency generation).

A straightforward approach to such a cascading process is to assume that an optically excited electron in an anharmonic potential leads to material polarizations at the frequencies ω, 0, 2ω, etc. The *total* displacement of the electron from equilibrium $\vec{\vec{q}}$ obeys a nonlinear driven simple harmonic oscillator equation of the form

$$\ddot{\bar{q}}_i + \bar{\Gamma}_i \dot{\bar{q}}_i + \bar{\omega}_i^2 \bar{q}_i = -\frac{e}{\bar{m}} E_i - \frac{\bar{k}_{ijk}}{\bar{m}} \bar{q}_j \bar{q}_k - \frac{\bar{k}_{ijk\ell}}{\bar{m}} \bar{q}_j \bar{q}_k \bar{q}_\ell, \tag{10.1}$$

where $\bar{k}_{ijk}$ and $\bar{k}_{ijk\ell}$ are nonlinear force constants that can be related directly to measured second- and third-order susceptibilities $\chi^{(2)}_{ijk}(-[\omega_p+\omega_q];\omega_p,\omega_q) \propto N\beta^{(2)}_{ijk}(-[\omega_p+\omega_q];\omega_p,\omega_q)$ and $\chi^{(3)}_{ijkl}(-[\omega_p+\omega_q+\omega_r];\omega_p,\omega_q,\omega_r) \propto N\gamma^{(3)}_{ijkl}(-[\omega_p+\omega_q+\omega_r];\omega_p,\omega_q,\omega_r)$, respectively. The parameter $\bar{\omega}_i$ is a resonance frequency associated with a transition from the ground state to an excited state, and ultimately a summation over all of the excited states will be required. $\bar{\Gamma}_i$ is a phenomenological damping term related to the lifetime of the excited state. For cascading, the discussion is limited solely to $\bar{k}_{ijk}$. The inclusion of $\bar{k}_{ijk\ell}$ would lead directly to the third-order Kerr nonlinearity in this model.

For a single incident field of frequency ω, $\vec{\bar{q}}$ is the total electron displacement, which has components at multiples of ω due to the nonlinearity, i.e.,

$$\bar{q}_i = \bar{q}_i(0) + \bar{q}_i(\omega) + \bar{q}'_i(\omega) + \bar{q}_i(2\omega) + \bar{q}_i(3\omega) + \ \ldots\ . \tag{10.2}$$

Note that the displacement at ω has been separated into the displacement associated with the linear polarization, $\bar{q}_i(\omega)$, and $\bar{q}'_i(\omega)$ due to the nonlinear interactions, which also produce a nonlinear polarization at ω. Since local nonlinear optical interactions at the molecule level are normally very small,

$$\bar{q}_i(\omega) \gg \bar{q}_i(2\omega), \bar{q}'_i(\omega), \bar{q}_i(0), \bar{q}_i(3\omega), \text{ etc.} \tag{10.3}$$

Hence the linear optics solution for $\bar{q}_i(\omega)$ can be substituted to produce the nonlinear term $\bar{q}_i(\omega)\bar{q}_i(\omega)$ driving the linear equations for $\bar{q}_i(0)$ and $\bar{q}_i(2\omega)$. In turn, products of those solutions with $\bar{q}_i(\omega)$, i.e., $\bar{q}_i(2\omega)\bar{q}_j(\omega)$ and $\bar{q}_i(0)\bar{q}_j(\omega)$, are used to generate nonlinear terms for obtaining solutions for $\bar{q}'_i(\omega)$ (via $2\omega-\omega$ and $0+\omega$) and $\bar{q}_i(3\omega)$ (which is not of interest here). This procedure results in

$$\bar{q}'_i(\omega) = -\frac{1}{2}\left\{ \frac{e^3}{2\bar{m}^5} \bar{k}_{ijm}\bar{k}_{mk\ell}\left[\frac{\mathrm{E}^*_j(\omega)\mathrm{E}_k(\omega)\mathrm{E}_\ell(\omega)}{D_i(\omega)D^*_j(\omega)D_m(2\omega)D_k(\omega)D_\ell(\omega)} + \frac{\mathrm{E}_j(\omega)\mathrm{E}^*_k(\omega)\mathrm{E}_\ell(\omega)}{D_i(\omega)D_j(\omega)D_m(0)D^*_k(\omega)D_\ell(\omega)} \right] \right\} e^{i(kz-\omega t)} + \text{c.c.}, \tag{10.4}$$

where $D_i(\omega) = \bar{\omega}_i^2 - \omega^2 - i\Gamma_i\omega$. Clearly the first term is the result from the second-harmonic pathway and the second from dc rectification. Defining in the usual way the nonlinear polarization as $P^{\mathrm{NL}}_i(\omega) = -eN\bar{q}'_i(\omega)$, straightforward algebra results in

$$n_{2,\mathrm{casl}} = \frac{1}{4n_i^2\varepsilon_0 c}\chi^{(3)}_{\Re,\mathrm{casl},ijk\ell}(-\omega;\omega,-\omega,\omega) = \frac{1}{4n_i^2 c}\frac{\bar{m}}{2\bar{e}^2 N}[D_m(2\omega)\chi^{(2)}_{mk\ell} \times(-2\omega;\omega,\omega)\chi^{(2)}_{ijm}(-\omega;-\omega,2\omega) + D_m(0)\chi^{(2)}_{mjk}(0;\omega,-\omega)\chi^{(2)}_{i\ell m}(-\omega;\omega,0)]. \tag{10.5}$$

It is useful to estimate the order of magnitude of $n_{2,\mathrm{casl}}$ for $LiNbO_3$ at nonresonant wavelengths with $N = 1.89\times10^{28}$ mol/m^3, $\rho = 4.64$ g/cm^3, $\chi^{(3)}_{zzz} = 56$ pm/V:

$$n_{2,\mathrm{casl}} \cong \frac{\bar{m}D(0)}{4n^2ce^2N}[\chi^{(2)}_{zzz}]^2 \cong 5\times 10^{-16}\ \mathrm{cm}^2/\mathrm{W},$$

which is negligible in this case. Consider also another example, the nonlinear organic DSTMS (4-*N*,*N*-dimethylamino-4-*N*-methyl-stilbazolium 2,4,6-trimethylbenzenesulfonate), which has the following properties: $\chi^{(2)}=424$ pm/V, $N=1.8\times 10^{27}$ molecules/m^3, $n=2.45$, $\mathrm{D}(0)\sim\pi\times 10^{15}$ rad/s, which yield $n_{2,\mathrm{casl}}\cong 5\times 10^{-14}$ cm^2/W, certainly not negligible [255].

Since this is a local effect, occurring at the molecular level, the turn-on and turn-off times are essentially instantaneous.

10.2. Nonlocal Cascading

This process in second-order nonlinear materials was identified in the early days of nonlinear optics by Ostrovskii but was overlooked until future experiments brought it back to light [256,257]. This process does *not* lead to a change in the refractive index of a material, but does result in a nonlinear phase-shift between interacting beams coupled via a second-order nonlinear process. This nonlinear phase shift depends in a complicated way on the intensities of the interacting beams, and it accumulates with distance so that it does mimic the effects of an intensity-dependent refractive index coefficient [258–262].

The interest here is in a single incident beam $[\mathrm{E}_i(\omega),\ \omega,\ k_i(\omega)]$ that experiences an effective nonlinearity $n_{2,\mathrm{casnl}}$. In a noncentrosymmetric medium, this fundamental beam can generate a second-harmonic either by birefringence phase matching $[\mathrm{E}_j(2\omega),\ 2\omega,\ k_j(2\omega);\ \Delta k=2k_i(\omega)-k_j(2\omega)=0]$ or quasi-phase-matching (QPM) $\mathrm{E}_i(2\omega), 2\omega, k_i(2\omega);\ \Delta k=2k_i(\omega)-k_i(2\omega)+\kappa=0$ where $\kappa=2\pi/\Lambda$ and Λ is the QPM period]. Away from the phase match, i.e., $\Delta k\neq 0$, the fundamental and harmonic waves travel at different phase velocities. That is, if $\Delta k>0$, the harmonic beam travels faster than the fundamental and vice versa for $\Delta k<0$; so the relative phase be-

Figure 82

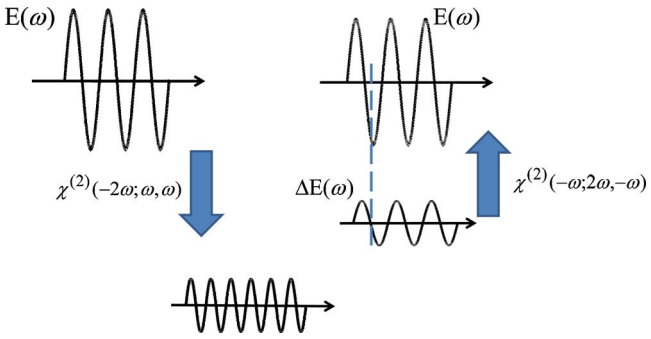

Schematic representation of the second-harmonic process that leads off-phase match to a nonlinear phase shift in the fundamental. When some harmonic is generated by upconversion, it travels at a different phase velocity than the fundamental. The harmonic is downconverted back to the fundamental frequency with a phase shift proportional to the product of the phase velocity mismatch and the coherence length. Thus the reconstituted fundamental experiences a net phase shift [258].

tween the two beams changes with propagation distance. As the energy oscillates between the fundamental and the harmonic, relative phase information is transferred also, and this is the basis of the nonlinear phase shift.

Consider the fundamental beam incident on a second-order crystal. As indicated in Fig. 82, the second harmonic is generated via $\chi^{(2)}(-2\omega;\omega,\omega)$, and it propagates some distance (typically the coherence length) before it converts back to the fundamental via $\chi^{(2)}(-\omega;2\omega,-\omega)$. It recombines partially out of phase with the incident fundamental because of the difference in phase velocities. The incremental phase shift at a given point depends on the interactions that occur earlier in the sample and hence is nonlocal. Furthermore, the higher the fundamental input intensity, the larger the conversion to the harmonic, and hence the larger the relative phase shift imparted by the recombining fundamental. This makes the process nonlinear.

The equations satisfied by the fundamental and harmonic are the standard ones associated with second-harmonic generation [field notation in Eq. (2.1)], for example, for type 1 phase matching:

$$\omega+\omega\rightarrow 2\omega, \qquad \frac{d}{dz}\mathcal{E}(z,2\omega)=i\frac{2\omega}{n(2\omega)c}\chi^{(2)}_{\text{eff}}(-2\omega;\omega,\omega)\mathcal{E}^2(\omega)e^{i\Delta kz};$$

$$2\omega-\omega\rightarrow \omega, \qquad \frac{d}{dz}\mathcal{E}(z,\omega)=i\frac{2\omega}{n(\omega)c}\chi^{(2)}_{\text{eff}}(-\omega;2\omega,-\omega)\mathcal{E}(2\omega)\mathcal{E}^*(\omega)e^{-i\Delta kz};$$

$$\zeta_1=\frac{2k_{\text{vac}}(\omega)}{n(\omega)}\chi^{(2)}_{\text{eff}}(-\omega;2\omega,-\omega); \quad \zeta_2=\frac{2k_{\text{vac}}(\omega)}{n(2\omega)}\chi^{(2)}_{\text{eff}}(-2\omega;\omega,\omega); \quad (10.6)$$

in which $\chi^{(2)}_{\text{eff}}=\hat{e}^*_i(2\omega)\chi^{(2)}_{ijj}(-2\omega;\omega,\omega)\hat{e}_j(\omega)\hat{e}_j(\omega)$, where $\hat{e}_j(\omega)$ denotes the field unit vectors. Numerical solutions for the fundamental's nonlinear phase shift, fundamental intensity versus distance, and nonlinear phase shift with input intensity are shown in Figs. 83 and 84 [262]. The increase in the nonlinear phase shift in the fun-

Figure 83

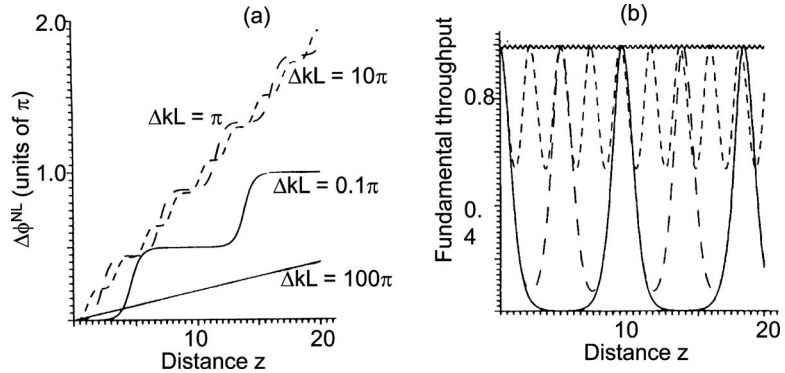

(a) Calculated cw nonlinear phase shift $\Delta\phi^{\text{NL}}$ experienced by the fundamental with distance for different values of phase mismatch ΔkL. (b) Corresponding fraction of light in the fundamental beam, also as a function of propagation distance [258].

Figure 84

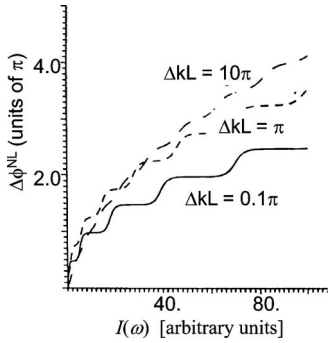

Variation with the incident fundamental intensity of the nonlinear phase shift $\Delta\phi^{\mathrm{NL}}$ for various phase mismatches ΔkL [258].

damental, $\Delta\phi^{\mathrm{NL}}(\omega)$, occurs in steps with the step size increasing with increasing $\ell_{\mathrm{coh}}=\pi/|\Delta k|$ with a maximum step size of $\pi/2$, Fig. 83(a). Also, as shown in Figs. 83(a) and 85, there is a maximum nonlinear phase shift with distance that occurs at $|\Delta kL|\cong 1.6\pi$. Note that for large phase mismatch, the conversion to the harmonic is small, $\Delta\phi^{\mathrm{NL}}(\omega)$ grows quasi-linearly with distance, and a definition for $n_{2,\mathrm{casnl}}$ would be useful. Finally, note that the steps in phase shift occur as the harmonic converts back to the fundamental, in keeping with the simple model in Fig. 82. Note, however, that there is a local phase shift of $\pi/2$ for fundamental-to-harmonic and another $\pi/2$ for harmonic-to-fundamental conversion; so the nonlinear phase shift due to backconversion of the harmonic to the fundamental exists on the background of a π phase shift. The growth of $\Delta\phi^{\mathrm{NL}}(\omega)$ with input intensity is initially linear in

Figure 85

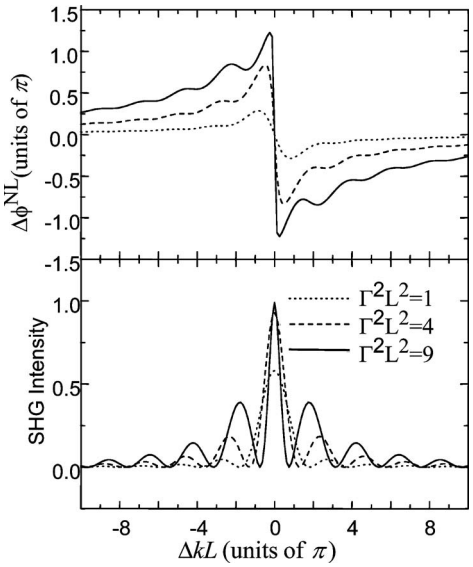

Variation with phase mismatch ΔkL of (a) the nonlinear phase shift $\Delta\phi^{\mathrm{NL}}$ and the second-harmonic intensity for various values of the normalized nonlinearity. Here $\Gamma=\omega d_{\mathrm{eff}}^{(2)}|E_0|/c\sqrt{n_\omega n_{2\omega}}$ [258].

intensity but does saturate at very high intensities as shown in Figs. 84 and 85, since the second harmonic departs from $\mathrm{sinc}^2(\Delta kL/2)$ under those conditions [263]. Finally, from Fig. 83(b), it is clear that the sample length has to be chosen so that the fundamental is fully recovered to its input value in order to maintain high net fundamental throughput. As always when looking at nonlinear phase shifts there is the associated nonlinear loss, which here is the loss of the fundamental. For low conversion this loss mimics 2PA; i.e., two photons go the second harmonic as opposed to heat in the real 2PA case.

As suggested in Fig. 84, for large ΔkL, i.e., small harmonic conversion, or small input irradiance, i.e., again small depletion, it is possible to obtain a simple formula for $n_{2,\mathrm{casnl}}$. First, the harmonic generation equation is solved for negligible depletion of the fundamental, and the solution is inserted into the equation for fundamental regeneration. This gives

$$\begin{aligned}&\frac{d}{dz}\mathcal{E}(z,\omega)=i\frac{\zeta_1\zeta_2}{\Delta k}[1-e^{i\Delta kz}]|\mathcal{E}(\omega)|^2\mathcal{E}(\omega)\\ \Rightarrow&\frac{d}{dz}\mathcal{E}(z,\omega)=\frac{\zeta_1\zeta_2}{\Delta k}\{\sin(\Delta kz)+i[1-\cos(\Delta kz)]\}|\mathcal{E}(\omega)|^2\mathcal{E}(\omega).\end{aligned} \tag{10.7}$$

To find a simple definition for the effective $n_{2,\mathrm{nlcas}}$ coefficient in the negligible fundamental depletion regime, one can simply compare the imaginary part of Eq. (10.7) at some point z with the Kerr formulas $d\mathcal{E}(z,\omega)/dz=ik_{\mathrm{vac}}n_{2,\mathrm{Kerr}}I(\omega)\mathcal{E}(z,\omega)$. This procedure yields

$$n_{2,\mathrm{nlcas}}=\frac{4\omega[d_{\mathrm{eff}}^{(2)}]^2}{c^2\varepsilon_0 n^2(\omega)n(2\omega)\Delta k}\sin^2\left(\frac{\Delta kz}{2}\right), \tag{10.8}$$

in which L is the sample length. Of course, this definition gives a comparison of a local $\chi^{(3)}$ nonlinearity to the nonlocal cascading. A different comparison can be made by integrating both third-order and cascaded second-order equations over the sample length prior to defining an effective n_2 (or effective α_2), which includes the effects of copropagating fundamental and second-harmonic beams [264]. Note that in the final version we use $d_{ijj}^{(2)}(-2\omega;\omega,\omega)=2\chi_{ijj}^{(2)}(-2\omega;\omega,\omega)$, since it is the material constant $d_{iJ}^{(2)}$ that is commonly tabulated for second-order interactions. For fundamental input intensities consistent with negligible fundamental depletion, the accumulated nonlinear phase shift $\Delta\phi^{\mathrm{NL}}$ at the end of a sample of length L is given by

$$\Delta\phi^{\mathrm{NL}}=\int_0^L k_{\mathrm{vac}}n_{2,\mathrm{nlcas}}dzI(\omega)=\frac{2\omega^2[d_{\mathrm{eff}}^{(2)}]^2}{c^2\varepsilon_0 n^2(\omega)n(2\omega)\Delta k}L\{1-\mathrm{sinc}[\Delta kL]\}I(\omega). \tag{10.9}$$

There are a number of interesting properties exhibited by the cascading nonlinearity. For example, for $\Delta kL\to\infty$, $\Delta\phi^{\mathrm{NL}}$ is proportional to L, similar to the Kerr case. Furthermore, the sign of the effective nonlinearity $n_{2,\mathrm{nlcas}}$ depends on the wave-vector mismatch: it is positive for $\Delta k>0$ and changes sign when the wave vector mismatch condition is tuned through $\Delta k=0$; i.e., the nonlinearity can be changed from self-focusing to self-defocusing.

$\chi^{(2)}$ interactions are parametric processes, i.e., they conserve energy. This follows immediately from the real part of Eq. (10.7), which describes the periodic

exchange of energy between the fundamental and the harmonic and can be written in the negligible fundamental depletion limit as

$$\frac{d}{dz}I(\omega) = -\frac{4[d_{\text{eff}}^{(2)}]^2 k_{\text{vac}}^2(\omega)}{n(2\omega)n^2(\omega)\varepsilon_0 c\Delta k}\sin(\Delta kz)I^2(z,\omega). \tag{10.10}$$

The small loss of the fundamental at $z=L$ due to the generation of the second harmonic is obtained from

$$\int_0^L \frac{dI(z,\omega)}{I^2(z,\omega} = -\frac{4[d_{\text{eff}}^{(2)}]^2 k_{\text{vac}}^2(\omega)}{n(2\omega)n^2(\omega)\varepsilon_0 c\Delta k}\int_0^L \sin\,(\Delta kz))dz; \tag{10.11}$$

so the normalized fundamental transmission coefficient for the sample is given by

$$T = 1 - \frac{I(0,\omega) - I(L,\omega)}{I(0,\omega)} \cong 1 - \frac{2[d_{\text{eff}}^{(2)}]^2 k_{\text{vac}}^2(\omega)}{n(2\omega)n^2(\omega)\varepsilon_0 c}L^2 I(0,\omega)\text{sinc}^2\left(\frac{\Delta kL}{2}\right). \tag{10.12}$$

This formula is reminiscent of the 2PA process that accompanies the Kerr nonlinearity near a two-photon resonance, but of course there is no absorptive loss in this process and only a "loss" of the fundamental to the harmonic.

Experiments have confirmed the theoretical predictions for this cascading process. A Z-scan experiment measures the nonlinear phase shift experienced by a beam passing through a sample and hence works for the cascading nonlinearity as well. Results are shown in Fig. 86 for the phase shift experienced when second-harmonic generation is tuned through the phase-match condition in a KTP ($KTiOPO_4$) sample [265]. The small differences between experiment and numerical solutions to the theory are probably because the calculations were done for cw plane waves, whereas only approximate corrections were applied to the results of the experiments, which involved pulses and finite beams. However, it is perhaps surprising that results of experiments performed in a limit of strong second-harmonic conversion bear a strong resemblance to Eqs. (10.9) and (10.12), which were derived in the negligible fundamental depletion limit. Nonlocal cascading also leads to the spectral broadening normally associated with self-phase-modulation [266]. Furthermore, all-optical switching based on cascading has also been obtained for a number of device configurations and found to be in excellent agreement with theory [258].

Clearly this nonlinearity will exist in all second-order materials. We illustrate this with the example at $\lambda = 1\ \mu$m of QPM $LiNbO_3$, which is phase matchable, and the organic crystal DSTMS, which is not phase matchable and has a coherence length of only 3.6 μm but a very large nonlinearity $d_{11} = 214$ pm/V [255]. For $L = 1$ cm, $n_{2,\text{casnl}}$ is calculated to be 2×10^{-12} cm^2/W and 3.6×10^{-13} cm^2/W for QPM $LiNbO_3$ (assuming $|\Delta kL| \sim 1.6\pi$) and DSTMS at $\lambda_{\text{vac}} = 1\ \mu$m [255]. The conclusion is obvious, namely, that the material must either be phase matchable or the second-order nonlinearity huge, or preferably both, for this mechanism to be important! Furthermore, this effect saturates, and hence these analytical results are valid *only* for small intensities.

The turn-on and turn-off times are given by the transit time for light to cross the sample.

Figure 86

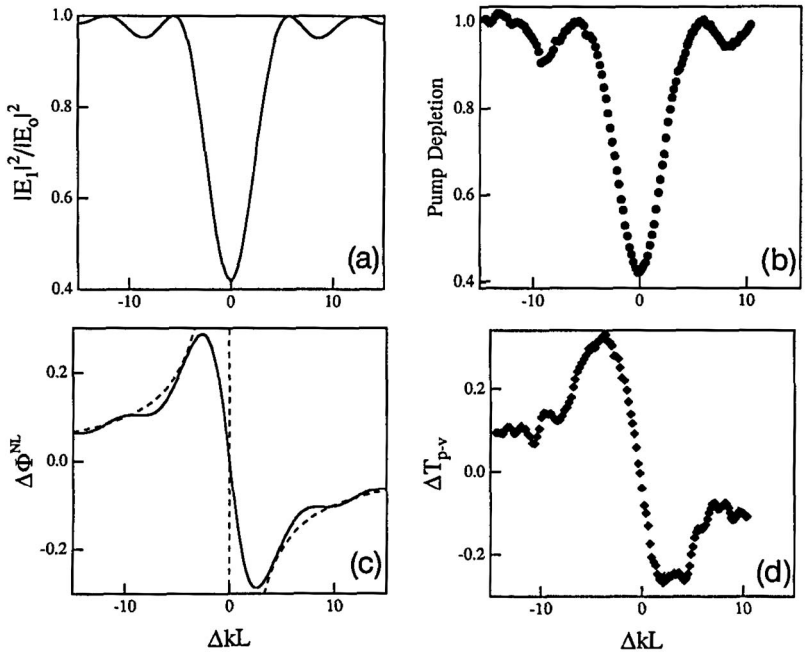

Theory and experiment for the nonlocal cascading nonlinearity in KTP near its phase-matching condition for second-harmonic generation as measured by Z scan. (a) Theory and (b) experiment for effective two-photon loss from the harmonic to the fundamental. (c) Theory and (d) experiment for the nonlinear phase shift [265].

11. Conclusions

The phenomena discussed here lead to a large spectrum of possibilities for the magnitude and speed of an intensity-dependent change in the refractive index and absorption. The salient question is, what material (or material system) is the optimum? A panel was convened in 1986 to discuss just this question, and its report was published as a paper [267]. There it was concluded that to within a couple of orders of magnitude, the product ($n_2 \times$ response time) is a constant. Twenty years later, this conclusion is still valid for nonlinearities ranging over 16 orders of magnitude!

Also pointed out in that series of papers is that the details of an application dictate which material system is most appropriate. For example, for all-optical switching that requires picosecond response times, it is usually necessary to accumulate a nonlinear phase shift of about π in a nonlinear medium to get sufficient interference between two beams to perform a switching operation. This seems to imply that one simply needs to make the nonlinear medium long enough (L) or the intensity (I) high enough to get π, since $\Delta\phi^{NL}=n_2IL$. However, linear and nonlinear loss or even fabrication technology will limit the practical sample length, especially since high throughput is also an important criterion. Furthermore, the Kerr relation $\Delta n=n_2I$ is only a low-intensity approximation, and there is an upper limit to Δn due to either saturation or material damage. These considerations have led to the definition of two figures of merit $W=2\Delta n_{max}(I)/\lambda_{vac}\alpha_1>1$

and $T=\lambda_{vac}\alpha_2(I)/n_2(I)<1$, where α_2 is the 2PA coefficient, that need to be satisfied [268]. The material that best satisfies these conditions and allows nonlinear phase shifts of $>100\pi$ is fused silica at 1550 nm in fiber form because of its very low loss and beam confinement, which arrests beam spreading on propagation and maintains high intensities for kilometer distances. The lesson here is that materials should be operated in their nonresonant regime, because there the ultrafast Kerr nonlinearity is a constant and the loss, linear and nonlinear, is very small. Note however, that even in fibers, if the operating wavelength is extended into the region in which absorption occurs due to vibrations, the figures of merit can be violated; so in general specific materials are useful only over specific wavelength ranges. This is a strong argument for continuing intensive research into the spectral dependence of nonlinear coefficients over broad wavelength ranges.

While most of this paper has looked at nonlinear refraction, it is impossible to fully describe these phenomena without also mentioning the nonlinear absorption processes that lead to these effects. Just as linear absorption leads to refraction via causality and Kramers–Kronig relations, similar connections can be made with nonlinear processes, as the example of the bound electronic n_2 resulting from a combination of Raman, ac Stark, and 2PA effects. Every change in index can be attributed to an absorption process occurring at some frequency even if widely separated.

For applications that do not require fast response times (longer than microseconds), PR and liquid crystal media are ideal. They can have nonlinearities >1 cm^2/W and are ideal as media for exploring new phenomena. In fact, in most of these cases it is the integrated energy rather than the intensity that is the key parameter. Furthermore, the changes in refractive index may not be reversible. For example, turning off the index change may require illuminating the medium with radiation of a different wavelength. This is the case for the huge nonlinearities that rely on trans-cis isomerization of organic molecules.

Thermally related nonlinearities are also very large and easily accessible with low-power cw lasers. But bear in mind that a temperature change generated locally diffuses with time, and the final steady state is determined by a sample's geometry, thermal conductivity, and thermal boundary conditions. Hence the results of an experiment may not be reproducible from sample to sample.

The nuclear contribution due to vibrational modes and electrostriction are normally relatively small effects. We note, however, that they do lead to large stimulated effects such as stimulated Raman and Brillouin scattering under appropriate conditions [1,2].

One of the most common consequences of an intensity-dependent refractive index on all time scales is the self-focusing or self-defocusing of high-intensity optical beams with finite cross section. The beam itself creates an effective lens in the medium as a direct consequence of $\Delta n(I)$. On propagation this can lead to fascinating effects in high-intensity nonlinear optics and ultimately damage (see [269] for recent reviews). When the nonlinear effect approximately cancels out dispersion or diffraction, this can result in beams with fascinating properties, which do not spread in time or space, as solitons or solitary waves or both, better known as optical bullets [270].

In addition, we note that the intensity-dependent refractive index can have an effect on second-order nonlinear interactions such as second-harmonic generation and optical parameteric oscillators, whose efficiency is based on phase matching

that requires finding conditions to make some index difference vanish. For example, in birefringent crystal media, both the intensity-dependent refractive index coefficients and dn/dT depend on the optical polarization. Hence changing the incident intensity can detune the phase-matching condition in frequency conversion devices.

Additional ramifications of an intensity-dependent refractive index and nonlinear absorption can be found in standard textbooks [1,2].

References

1. Y. R. Shen, *The Principles of Nonlinear Optics* (Wiley-Interscience, 1984).
2. R. W. Boyd, *Nonlinear Optics* (Academic, 1992).
3. B. J. Orr and J. F. Ward, "Perturbation theory of the non-linear optical polarization of an isolated system," Mol. Phys. **20**, 513–526 (1971).
4. M. G. Kuzyk, "Fundamental limits on third-order molecular susceptibilities," Opt. Lett. **16**, 1183–1185 (2000).
5. M. Yoshizawa, Y. Hattori, and T. Kobayashi, "Nonlinear optical susceptibilities of epitaxially grown polydiacetylene measured by femtosecond time-resolved spectroscopy," Phys. Rev. B **47**, 3882–3889 (1993).
6. R. Adair, L. L. Chase, and R. A. Payne, "Nonlinear refractive index of optical crystals," Phys. Rev. B **39**, 3337–3350 (1989).
7. L. Chase and E. W. Van Stryland, in *Handbook of Laser Science and Technology, Supplement 2: Optical Materials*, M. Weber, ed. (CRC Press, 1995), Sect. 8, pp 269–366.
8. R. DeSalvo, A. Said, D. Hagan, and E. Van Stryland, "Infrared to ultraviolet measurements of two-photon absorption and n_2 in wide bandgap solids," IEEE J. Quantum Electron. **32**, 1324–1333 (1996).
9. J. Wang, M. Sheik-Bahae, A. A. Said, D. J. Hagan, and E. W. Van Stryland, "Time-resolved Z-scan measurements of optical nonlinearities," J. Opt. Soc. Am. B **11**, 1009–1017 (1994).
10. A. A. Said, M. Sheik-Bahae, D. J. Hagan, T. H. Wei, J. Wang, J. Young, and E. W. Van Stryland, "Determination of bound-electronic and free-carrier nonlinearities in ZnSe, GaAs, CdTe, and ZnTe," J. Opt. Soc. Am. B **9**, 405–414 (1992).
11. D. W. Hall, M. A. Newhouse, N. F. Borrelli, W. H. Dumbaugh, and D. L. Weidman, "Nonlinear optical susceptibilities of high-index glasses," Appl. Phys. Lett. **54**, 1293–1295 (1989).
12. For example, D. S. Chemla and J. Zyss, eds., *Nonlinear Optical Properties of Organic Molecules and Crystals*, Quantum Electronics—Principles and Applications, P. F. Liao and P. Kelley, eds. (Academic, 1987), Vols. 1 and 2.
13. A. J. Heeger, "Nobel Lecture: Semiconducting and metallic polymers: the fourth generation of polymeric materials," Rev. Mod. Phys. **73**, 681–700 (2001).
14. C. Sauteret, J. P. Hermann, R. Frey, F. Pradere, J. Ducuing, R. H. Baughman, and R. R. Chance, "Optical nonlinearities in one-dimensional-conjugated polymer crystals," Phys. Rev. Lett. **36**, 956 (1976).
15. R. R. Chance and G. N. Patel, "Solid-state polymerization of a diacetylene crystal: thermal, ultraviolet, and γ-ray polymerization of 2,4-hexadiyne-1,6-diol *bis*-(*p*-toluene sulfonate)," J. Polym. Sci., Part B: Polym. Phys. **16**, 859–881 (1978).
16. M. Sinclair, D. Moses, K. Agaki, and A. J. Heeger, "Anisotropy of the third-

order nonlinear-optical susceptibility in a degenerate-ground-state conjugated polymer: *trans*-$(CH)_x$," Phys. Rev. B **38**, 10724–10733 (1988).
17. W.-S. Fann, S. Benson, J. M. J. Madey, S. Etemad, G. L. Baker, and A. J. Heeger, "Spectrum of $\chi^{(3)}(-3\omega;\omega,\omega,\omega)$ in polyacetylene: an application of free-electron laser in nonlinear optical spectroscopy," Phys. Rev. Lett. **62**, 1492–1495 (1989).
18. P. C. M. McWilliams, G. W. Hayden, and Z. G. Soos, "Theory of even-parity state and two-photon spectra of conjugated polymers," Phys. Rev. B **43**, 9777–9791 (1991).
19. W. E. Torruellas, K. B. Rochford, R. Zanoni, S. Aramaki, and G. I. Stegeman, "The cubic susceptibility dispersion of poly(4-BCMU) thin films: third harmonic generation and two-photon-absorption measurements," Opt. Commun. **82**, 94–100 (1991).
20. B. Lawrence, W. Torruellas, M. Cha, G. I. Stegeman, J. Meth, S. Etemad, and G. Baker, "Identification and role of two-photon excited states in a π-conjugated polymer," Phys. Rev. Lett. **73**, 597–600 (1994).
21. W. E. Torruellas, B. L. Lawrence, G. I. Stegeman, and G. Baker, "Two-photon saturation in the bandgap of a molecular quantum wire," Opt. Lett. **21**, 1777–1779 (1996).
22. S. Polyakov, F. Yoshino, M. Liu, and G. Stegeman, "Nonlinear refraction and multiphoton absorption in polydiacetylenes from 1200 to 2200 nm," Phys. Rev. B **69**, 115421 (2004).
23. D. Mukhopadhyay and Z. G. Soos, "Nonlinear optical and electroabsorption spectra of polydiacetylene crystals and films," J. Chem. Phys. **104**, 1600–1610 (1996).
24. R. K. Meyer, R. E. Benner, Z. V. Vardeny, M. Liess, M. Ozaki, K. Yoshino, Y. Ding, and T. Barton, "Two photon absorption spectra of luminescent conducting polymers," Synth. Met. **84**, 549–550 (1997).
25. L. De Boni, L. S. Corrêa, D. T. Balogh, R. M. Faria, S. C. Zilio, L. Misoguti, and C. R. Mendonça, "MEH-PPV chloroform solution degenerated two photon absorption spectrum," proceedings of Encontro Nacional de Física da Matéria Condensada XXVI (ENFMC XXVI), Ann. Opt. **5**, 1–3 (2003).
26. A. Samoc, M. Samoc, M. Woodruff, and B. Luther-Davies, "Tuning the properties of poly(*p*-phenylenevinylene) for use in all-optical switching," Opt. Lett. **20**, 1241–3 (1995).
27. E.g., Z. Iqbalt, N. S. Murthyt, Y. P. Khannat, J. S. Szobotai, R. A. Dalterio, and F. J. Owens, "The mechanism of the solid-state phase transitions in the polydiacetylene, poly-4BCMU: thermal, x-ray diffraction and Raman scattering studies," J. Phys. C **20** 4283–4295 (1987).
28. W. Krug, E. Miao, M. Derstine, and J. Valera, "Optical absorption and scattering losses of PTS and poly(4-BCMU) thin-film waveguides in the near infrared," J. Opt. Soc. Am. B **6**, 726–732 (1989).
29. Reviewed in A. Bahtiar, K. Koynov, A. Kibrom, T. Ahn, and Chr. Bubeck, "Multiphoton spectroscopy of polymers for all-optical switching," Proc. SPIE **6330**, 63300C (2006).
30. G. Wegner, "Recent progress in the chemistry and physics of poly(diacetylenes)," in *Molecular Metals: Proceedings of the NATO Conference on Molecular Metals*, W. E. Hatfield, ed. (Springer, 1979) p. 209.
31. Z. G. Soos, P. C. M. McWilliams, and G. W. Hayden, "Coulomb correlations and two-photon spectra of conjugated polymers," Chem. Phys. Lett. **171**, 14–18 (1990).
32. Reviewed in T. Kobayashi, "Ultrafast relaxation in conjugated polymers

with large optical nonlinearity," Synth. Met. **49–50**, 565–581 (1992).
33. G. M. Carter, Y. J. Chen, and S. K. Tripathy, "Intensity dependent index of refraction in organic materials," Opt. Eng. **24**, 609–612 (1985).
34. J. Bolger, T. G. Harvey, W. Ji, A. K. Kar, S. Molyneux, B. S. Wherrett, D. Bloor, and P. Norman, "Near-resonant third-order optical nonlinearities in *p*-toluene sulfonate polydiacetylene," J. Opt. Soc. Am. B **9**, 1552–1557 (1992).
35. P. A. Gass, I. Abram, R. Raj, and M. Schott, "The nonlinear optical spectrum of polydiacetylene in the near infrared," J. Chem. Phys. **100**, 88–97 (1994).
36. A. K. Bhowmik and M. Thakur, "Self-phase modulation in polydiacetylene single crystal measured at 720–1064 nm," Opt. Lett. **26**, 902–904 (2001).
37. B. L. Lawrence, M. Cha, W. E. Torruellas, G. I. Stegeman, S. Etemad, and G. Baker, "Measurement of the nonlinear refractive index and two photon absorption coefficient of PTS at 1064 nm," Appl. Phys. Lett. **64**, 2773–2775 (1994).
38. R. Quintero-Torres and M. Thakur, "Measurement of the nonlinear refractive index of polydiacetylene using Michelson interferometry and z-scan," J. Appl. Phys. **85**, 401–403 (1999).
39. J. A. DeAro, U. Lemmer, D. Moses, and S. K. Buratto, "Nanoscale optical microscopy of conjugated polymer films," Synth. Met. **101**, 300–301 (1999).
40. C. H. Lee, J. Y. Park, Y. W. Park, D. Moses, A. J. Heeger, T. Noguchid, and T. Ohnishid, "Polarization dependence of the photoconductivity of stretch-oriented poly(*p*-phenylenevinylene) films," Synth. Met. **101**, 444–445 (1999).
41. M. Samoc, A. Samoc, and B. Luther-Davies, "Two-photon and one-photon resonant third-order nonlinear optical properties of π-conjugated polymers," Synth. Met. **109**, 79–83 (2000).
42. M. Samoc, A. Samoc, B. Luther-Davies, and M. Woodruff, "The concept of guiding light with light and negative third-order optical nonlinearities of organics," J. Opt. A, Pure Appl. Opt. **5**, 681–687 (1996).
43. M. Samoc, A. Samoc, B. Luther-Davies, Z. Bao, L. Yu, B. Hsieh, and U. Scherf, "Femtosecond Z-scan and degenerate four-wave mixing measurements of real and imaginary parts of the third-order nonlinearity of soluble conjugated polymers," J. Opt. Soc. Am. B **15**, 817–825 (1998).
44. K. Rochford, R. Zanoni, G. I. Stegeman, W. Krug, E. Miao, and M. W. Beranek, "Measurement of nonlinear refractive index and transmission in polydiacetylene waveguides at 1.319 pm," Appl. Phys. Lett. **58**, 13–15 (1991).
45. M. Samoc, A. Samoc, B. Luther-Davies, J. Swiatkiewicz, C. Q. Jin, and J. W. White, "Real and imaginary components of the third-order nonlinearity of polyaniline dodecylbenzenesulfonic salt," Opt. Lett. **20**, 2478–2480 (1995).
46. R. Rangel-Rojo, S. Yamada, H. Matsuda, H. Kasai, H. Nakanishi, A. K. Kar, and B. S. Wherrett, "Spectrally resolved third-order nonlinearities in polydiacetylene microcrystals: influence of particle size," J. Opt. Soc. Am. B **15**, 2937–2945 (1998).
47. X. Chen, G. Zou, Y. Deng, and Q. Zhang, "Synthesis and nonlinear optical properties of nanometer-size silver-coated polydiacetylene composite vesicles," Nanotechnology **19**, 195703 (2008).
48. K. D. Belfield, K. J. Schafer, W. Mourad, and B. A. Reinhardt, "Synthesis of

new two-photon absorbing fluorene derivatives via Cu-mediated Ullmann condensations," J. Org. Chem. **65**, 4475–4481 (2000).
49. M. Yamashita, S. Kikuma, Y. Yamaoka, H. Murakami, R. Morita, and H. Shigekawa, "Nonresonant femtosecond second hyperpolarizabilities of intramolecular charge-transfer molecules with great excited- and ground-state dipole-moment differences," Appl. Phys. Lett. **75**, 28–30 (1999).
50. For example, S. R. Marder, S. W. Perry, G. Bourhill, C. B. Gorman, B. G. Tiemann, and K. Mansour, "Relation between bond-length alternation and second electronic hyperpolarizability of conjugated organic molecules," Science **261**, 186–189 (1993); Chr. B. Gorman and S. R. Marder, "An investigation of the interrelationships between linear and nonlinear polarizabilities and bond-length alternation in conjugated organic molecules," **90**, 11297–11301 (1993).
51. D. Lu, G. Chen, J. W. Perry, and W. A. Goddard III, "Valence-bond charge-transfer model for nonlinear optical properties of charge-transfer organic molecules," J. Am. Chem. Soc. **116**, 10679–10685 (1994).
52. Reviewed in S. Barlow and S. R. Marder, "Nonlinear optical properties of organic materials," in *Functional Organic Materials: Syntheses, Strategies and Applications*, T. J. J. Muller and U. H. F. Bunz, eds. (Wiley, 2007), Chap. 11.
53. Reviewed in J. M. Hales and J. W. Perry, "Organic and polymeric 3rd-order nonlinear optical materials and device applications," in *Introduction to Organic Electronic and Optoelectronic Materials and Devices*, S.-S. Sun and L. Dalton, eds. (CRC Press, 2008), Chap. 17.
54. See, for example, R. M. de Ridder, A. Driessen, E. Rikkers, P. V. Lambeck, and M. B. J. Diemeer, "Design and fabrication of electro-optic polymer modulators and switches," Opt. Mater. **12**, 205–214 (1999).
55. D. L. Wise, *Electrical and Optical Polymer Systems* (CRC Press, 1998).
56. G. I. Stegeman, A. Galvan-Gonzales, M. Canva, R. Twieg, T. C. Kowalczyk, X. Q. Zhang, H. S. Lackritz, S. Marder, S. Thayumanavan, K. P. Chan, A. K.-Y. Jen, and X. Wu, "Photodegradation of various electro-optic polymer families," Nonlinear Opt. **25**, 57–66 (2000).
57. M. B. Marques, G. Assanto, G. I. Stegeman, G. R. Mohlmann, E. W. P. Erdhuisen, and W. H. G. Horsthuis, "Intensity dependent refractive index of novel polymer materials: measurements by nonlinear grating coupling," Appl. Phys. Lett. **58**, 2613–2615 (1991).
58. M. J. Goodwin, C. Edge, C. Trundle, and I. Bennion, "Intensity-dependent birefringence in nonlinear organic polymer waveguides," J. Opt. Soc. Am. B **5**, 419–424 (1988).
59. H. Kanbara, H. Kobayashi, and T. Kaino, "Highly efficient ultrafast optical Kerr shutters with the use of organic nonlinear materials," J. Opt. Soc. Am. B **11**, 2216–2223 (1994).
60. S. Ohira, I. Rudra, K. Schmidt, S. Barlow, S. J. Chung, Q. Zhang, J. Matichuk, S. R. Marder, and J.-L. Bredas, "Electronic and vibronic contributions to two-photon absorption in donor-acceptor-donor squaraine chromophores," Chem.-Eur. J. **14**, 11082–11091 (2008).
61. K. S. Mathis, M. G. Kuzyk, C. W. Dirk, A. Tan, S. Martinez, and G. Gampos, "Mechanisms of the nonlinear optical properties of squaraine dyes in poly(methyl methacrylate) polymer," J. Opt. Soc. Am. B **15**, 871–883 (1998).
62. D. W. Garvey, Q. Li, M. G. Kuzyk, C. W. Dirk, and S. Martinez, "Sagnac interferometric intensity-dependent refractive-index measurements of poly-

mer optical fiber," Opt. Lett. **21**, 104–106 (1996).
63. M. G. Kuzyk, U. C. Paek, and C. W. Dirk, "Guest-host polymer fibers for nonlinear optics," Appl. Phys. Lett. **59**, 902–904 (1991).
64. S.-J. Chung, S. Zheng, T. Odani, L. Beverina, J. Fu, L. A. Padilha, A. Biesso, J. M. Hales, X. Zhan, K. Schmidt, A. Ye, E. Zojer, S. Barlow, D. J. Hagan, E. W. Van Stryland, Y. Yi, Z. Shuai, G. A. Pagani, J.-L. Bredas, J. W. Perry, and S. R. Marder, "Extended squaraine dyes with large two-photon absorption cross-sections," J. Am. Chem. Soc. **128**, 14444–14445 (2006).
65. J. M. Hales, S. Zheng, S. Barlow, S. R. Marder, and J. W. Perry, "Bisdioxaborine polymethines with large third-order nonlinearities for all-optical signal processing," J. Am. Chem. Soc. **128**, 11362–11363 (2008).
66. H. Ma and A. K.-Y. Jen, "Functional dendrimers for nonlinear optics," Adv. Mater. **13**, 1201–1205 (2001).
67. M. Samoc, A. Samoc, B. Luther-Davies, M. G. Humphrey, and M. P. Cifuentes, "Nonlinear absorption: materials and mechanisms," in *Proceedings of the Symposium on Photonics Technologies for 7th Framework Program Wroclaw 12-14 October 2006* (2006) 230–233 .
68. S. J. Chung, K. S. Kim, T. C. Lin, G. S. He, J. Swiatkiewicz, and P. N. Prasad, "Cooperative enhancement of two-photon absorption in multi-branched structures," J. Phys. Chem. B **103**, 10741–10745 (1999).
69. O. Varnavski, A. Leanov, L. Liu, J. Takacs, and T. Goodson, "Large nonlinear refraction and higher order nonlinear optical effects in a novel organic dendrimer," J. Phys. Chem. B **104**, 179–188 (2000).
70. For example, W. Jones, ed., *Organic Molecular Solids: Properties and Applications* (CRC Press 1997).
71. For example, H. S. Nalwa and S. Miyata, eds., *Nonlinear Optics of Organic Molecules and Polymers* (CRC Press, 1997).
72. E. W. Van Stryland, M. Sheik-Bahae, A. A. Said, and D. J. Hagan, "Characterization of nonlinear optical absorption and refraction," Prog. Cryst. Growth Charact. Mater. **27**, 279–311 (1993).
73. T. H. Wei, D. J. Hagan, M. J. Sence, E. W. Van Stryland, J. W. Perry, and D. R. Coulter, "Direct measurements of nonlinear absorption and refraction in solutions of phthalocyanines," Appl. Phys. B **54**, 46–51 (1992).
74. For example, J. Worlock, "Two-photon spectroscopy," in *Laser Handbook*, F. T. Arecchi and E. O. Schulz-Dubois, eds. (North Holland,1972), Vol. 2, pp. 1323–1369.
75. W. Blau, H. Byrne, W. M. Dennis, and J. M. Kelly, "Reverse saturable absorption in tetraphenylporphyrins," Opt. Commun. **56**, 25–29 (1986).
76. T. Xia, D. Hagan, A. Dogariu, A. Said, and E. Van Stryland, "Optimization of optical limiting devices based on excited-state absorption," Appl. Opt. **36**, 4110–4122 (1997).
77. C. Giuliano and L. Hess, "Nonlinear absorption of light: optical saturation of electronic transitions in organic molecules with high intensity laser radiation," IEEE J. Quantum Electron. **3**, 358–367 (1967).
78. O. V. Przhonska, J. Lim, D. Hagan, and E. Van Stryland, "Nonlinear light absorption of polymethine dyes in liquid and solid media," J. Opt. Soc. Am. B **15**, 802–809 (1998).
79. R. Lepkowicz, A. Kobyakov, D. J. Hagan, and E. W. Van Stryland, "Picosecond optical limiting in reverse saturable absorbers: a theoretical and experimental study," J. Opt. Soc. Am. B **19**, 94–101 2002.
80. J. H. Lim, O. V. Przhonska, S. Khodja, S. Yang, T. S. Ross, D. J. Hagan, E. W. Van Stryland, M. V. Bondar, and Y. L. Slominsky, "Polymethine and

squarylium molecules with large excited-state absorption," Chem. Phys. **245**, 79–97 (1999).
81. Answers.com, http://www.answers.com/topic/glass.
82. Discussed in G. P. Agrawal, *Nonlinear Fiber Optics*, 3rd ed., Optics and Photonics Series, P. L. Kelley, I. P. Kaminow, and G. P. Agrawal, eds. (Academic, 2001).
83. S. Santran, L. Canioni, L. Sarge, Th. Cardinal, and E. Fargin, "Precise and absolute measurements of the complex third-order optical susceptibility," J. Opt. Soc. Am. B **21**, 2180–2190 (2004).
84. Th. Cardinal, E. Fargin, J. J. Videau, L. Canioni, B. Busquet, V. Rodriguez, M. Couzi, P. Thomas, and L. Petit, "Interaction laser dans les verres et processus optique non linéaires," Verre (Paris) **13**, 16–25 (2007).
85. R. Adair, L. L. Chase, and S. A. Payne, "Nonlinear refractive-index measurements of glasses using three-wave frequency mixing," J. Opt. Soc. Am. B **4**, 875–881 (1987).
86. S. R. Friberg and P. W. Smith, "Nonlinear optical glasses for ultrafast optical switches," IEEE J. Quantum Electron. **QE-23**, 2089–2094 (1987).
87. M. A. Newhouse, D. L. Weidman, and D. W. Hall, "Enhanced-nonlinearity single-mode lead silicate optical fiber," Opt. Lett. **15**, 1185–1187 (1990).
88. J. E. Aber, M. C. Newstein, and B. A. Garetz, "Femtosecond optical Kerr effect measurements in silicate glasses," J. Opt. Soc. Am. B **17**, 120–127 (2000).
89. T. Cardinal, E. Fargin, G. Le Flem, and S. Leboiteux, "Correlations between structural properties of $Nb_2-O_5-NaPO_3-Na_2B_40_7$ glasses and non-linear optical activities," J. Non-Cryst. Solids **222**, 228–234 (1997).
90. J. C. Sabadel, P. Armand, D. Cachau-Herreillat, P. Baldeck, O. Doclot, A. Ibanez, and E. Philippot, "Structural and nonlinear optical characterizations of tellurium oxide-based glasses: $TeO_2-BaO-TiO_2$," J. Solid State Chem. **132**, 411–419 (1997).
91. B. Jeansannetas, S. Blanchandin, P. Thomas, P. Marchet, J. C. Champarnaud-Mesjard, T. Merle-MeHjean, B. Frit, V. Nazabal, E. Fargin, G. Le Flem, M. O. Martin, B. Bousquet, L. Canioni, S. Le Boiteux, P. Segonds, and L. Sarger, "Glass structure and optical nonlinearities in thallium(I) tellurium(IV) oxide glasses," J. Solid State Chem. **146**, 329–335 (1999).
92. M. Asobe, "Nonlinear optical properties of chalcogenide glass fibers and their application to all-optical switching," Opt. Fiber Technol. **3**, 142–148 (1997).
93. G. Lenz, J. Zimmermann, T. Katsufuji, M. E. Lines, H. Y. Hwang, S. Spalter, R. E. Slusher, S. W. Cheong, J. S. Sanghera, and I. D. Aggarwal, "Large Kerr effect in bulk Se-based chalcogenide glasses," Opt. Lett. **25**, 254–256 (2000).
94. J. Requejo-Isidro, A. K. Mairaj, V. Pruneri, D. W. Hewak, M. C. Netti and J. J. Baumberg, "Self refractive non-linearities in chalcogenide based glasses," J. Non-Cryst. Solids **317**, 241–246 (2000).
95. F. Smektala, C. Quemard, V. Couderc, and A. Barthelemy, "Non-linear optical properties of chalcogenide glasses measured by Z-scan," J. Non-Cryst. Solids **274**, 232–237 (2000).
96. J. M. Harbold, F. Ömer Ilday, F. W. Wise, and B. G. Aitken, "Highly nonlinear Ge–As–Se and Ge–As–S–Se glasses for all-optical switching," IEEE Photon. Technol. Lett. **14**, 822–824 (2002).
97. H. C. Nguyen, K. Finsterbusch, D. J. Moss, and B. J. Eggleton, "Dispersion

in nonlinear figure of merit of As_2Se_3 chalcogenide fibre," Electron. Lett. **42**, 571–572 (2006).
98. N. L. Boling, A. J. Glass, and A. Owyoung, "Emperical relations for predicting nonlinear refractive index changes in optical solids," IEEE J. Quantum Electron. **QE-14**, 601–608 (1978).
99. H. Haug and S. W. Koch, *Quantum Theory of the Optical and Electronic Properties of Semiconductors* (World Scientific, 1990).
100. M. Sheik-Bahae, "Optical nonlinearities in the transparency region of bulk semiconductors," in *Nonlinear Optics in Semiconductors I*, E. Garmire and A. Kost, eds. (Academic, 1999), Chap. 4, pp 257–318.
101. Cl. Klingshirn, *Semiconductor Optics* (Springer-Verlag, 2001).
102. A. D. Yoffe, "Low-dimensional systems: quantum size effects and electronic properties of semiconductor microcrystallites (zero-dimensional systems) and some quasi-two-dimensional systems," Adv. Phys. **51**, 799–890 (2002).
103. Reviewed by A. Othonos, "Probing ultrafast carrier and phonon dynamics in semiconductors," J. Appl. Phys. **83**, 1789–1830 (1998).
104. Reviewed by J. Mørk, M. L. Nielsen, and T. W. Berg, "The dynamics of semiconductor optical amplifier: modeling and applications," Opt. Photonics News **14**(7), 42–48 (July 2003).
105. Reviewed in R. J. Manning, A. D. Ellis, A. J. Poustie, and K. J. Blow, "Semiconductor laser amplifiers for ultrafast all-optical signal processing," J. Opt. Soc. Am. B **14**, 3204–3216 (1997).
106. J. Mørk and A. Mecozzi, "Theory of the ultrafast optical response of active semiconductor waveguides," J. Opt. Soc. Am. B **13**, 1803–1815 (1996).
107. P. LiKamWa, A. Miller, J. S. Roberts, and P. N. Robson, "130 ps recovery of all-optical switching in a GaAs multiquantum well directional coupler," Appl. Phys. Lett. **58**, 2055–2057 (1991).
108. Y. H. Lee, A. Chavez-Pirson, S. W. Koch, H. M. Gibbs, S. H. Park, J. Morhange, A. Jeffery, N. Peyghambarian, L. Banyai, A. C. Gossard, and W. Wiegmann, "Room-temperature optical nonlinearities in GaAs," Phys. Rev. Lett. **57**, 2446–2449 (1986).
109. L. Banyai and S. W. Koch, "A simple theory for the effects of plasma screening on the optical spectra of highly excited semiconductors," Z. Phys. B **63**, 283–291 (1986).
110. A. G. Aronov, D. E. Pikus, and D. Shekhter, "Quantum theory of free-electron dielectric constant in semiconductors," Sov. Phys. Solid State **10**, 645–647 (1968).
111. D. H. Auston, S. McAffee, C. V. Shank, E. P. Ippen, and O. Teschke, "Picosecond spectroscopy of semiconductors," Solid-State Electron. **21**, 147–150 (1978).
112. D. A. B. Miller, C. T. Seaton, M. E. Prise, and S. D. Smith, "Band-gap resonant nonlinear refraction in III–V semiconductors," Phys. Rev. Lett. **47**, 197–200 (1981).
113. B. S. Wherrett, A. C. Walker, and F. P. Tooley, "Nonlinear refraction for cw optical bistability," in *Optical Nonlinearities and Instabilities in Semiconductors*, H. Haug, ed. (Academic, 1988), p. 239.
114. T. S. Moss, "Theory of intensity dependence of refractive index," Phys. Status Solidi B **101**, 555–561 (1980).
115. E. O. Kane, "Band structure of narrow gap semiconductors," in *Narrow Gap Semiconductors Physics and Applications*, Vol. 133 of Lecture Notes in Physics, W. Zawadski, ed. (Springer Verlag, 1980), pp. 13–31.

116. J. W. Kurnick and J. M. Powell, "Optical absorption in pure single crystal InSb at 298° and 78° K," Phys. Rev. **116**, 597–604 (1959).
117. H. P. Li, C. H. Kam, Y. L. Lam, W. Ji, "Optical nonlinearities and photoexcited carrier lifetime in CdS at 532 nm," Opt. Commun. **190**, 351–356 (2001).
118. X. J. Zhang, W. Ji, and S. H. Tang, "Determination of optical nonlinearities and carrier lifetime in ZnO," J. Opt. Soc. Am. B **14**, 1951–1955 (1997).
119. V. Dubikovskiy, D. J. Hagan, and E. W. Van Stryland, "Large nonlinear refraction in InSb at 10 μm and the effects of Auger recombination," J. Opt. Soc. Am. B **25**, 223–235 (2008). Note: a range of values is given, since here Boltzmann statistics do not hold and the cross section becomes density dependent.
120. T. Boggess, S. Moss, I. Boyd, and A. Smirl, "Nonlinear-optical energy regulation by nonlinear refraction and absorption in silicon," Opt. Lett. **9**, 291–293 (1984).
121. N. Peyghamberian and S. W. Koch, "Semiconductor nonlinear properties," in *Nonlinear Photonics*, H. M. Gibbs, G. Khitrova, and N. Peyghamberian, eds., Vol. 30 of Springer Series in Electronics and Photonics, D. H. Auson, W. Engl, and T. Sugnao, eds. (Springer-Verlag, 1990), Chap. 2, pp 7–60.
122. M. Sheik-Bahae and E. W. Van Stryland, "Ultrafast nonlinearities in semiconductor laser amplifiers," Phys. Rev. B **50**, 171–178 (1994).
123. D. C. Hutchings, M. Sheik-Bahae, D. J. Hagan, and E. W. Van Stryland, "Kramers–Krönig relations in nonlinear optics," Opt. Quantum Electron. **24**, 1–30 (1992).
124. D. C. Hutchings and E. W. Van Stryland, "Nondegenerate two-photon absorption in zinc-blende semiconductors," J. Opt. Soc. Am. B **9**, 2065–2074 (1992).
125. M. Sheik-Bahae, D. C. Hutchings, D. J. Hagan, and E. W. Van Stryland, "Dispersion of bound electronic nonlinear refraction in solids," IEEE J. Quantum Electron. **QE-27**, 1296–1309 (1991).
126. B. S. Wherrett, "Scaling rules for multiphoton interband absorption in semiconductors," J. Opt. Soc. Am. B **1**, 67–72 (1984).
127. M. Balu, L. Padilha, D. J. Hagan, E. W. Van Stryland, S. Yao, K. Belfield, S. Zheng, S. Barlow, and S. Marder, "Broadband Z-scan characterization using a high-spectral-irradiance, high-quality supercontinuum," J. Opt. Soc. Am. B **25**, 159–165 (2008).
128. G. I. Stegeman, A. Villeneuve, J. Kang, J. S. Aitchison, C. N. Ironside, K. Al-hemyari, C. C. Yang, C.-H. Lin, H.-H. Lin, G. T. Kennedy, R. S. Grant, and W. Sibbett, "AlGaAs below half bandgap: the silicon of nonlinear optical materials," Int. J. Nonlinear Opt. Phys. **3**, 347–371 (1994).
129. E. Dulkeith, Y. A. Vlasov, X. Chen, N. C. Panoiu, and R. M. Osgood, Jr., "Self-phase-modulation in submicron silicon-on insulator photonic wires," Opt. Express **14**, 5324–5334 (2006).
130. M. Higashiwaki, S. Shimomura, S. Hiyamizu, and S. Ikawa, "Self-organized GaAs quantum-wire lasers grown on B-oriented GaAs substrates by molecular beam epitaxy," Appl. Phys. Lett. **74**, 780–782 (1999).
131. G. P. Banfi, V. Degiorgio, and D. Ricard, "Nonlinear optical properties of semiconductor nanocrystals," Adv. Phys. **47**, 447–510 (1998).
132. M. D. Dvorak, B. L. Justus and A. D. Berry, "Pump/probe Z-scan studies of GaAs nanocrystals grown in porous glass," Opt. Commun. **116**, 149–152 (1995).
133. R. Dingle, W. Wiegmann, and C. H. Henry, "Quantum states of confined

carriers in very thin $Al_xGa_{1-x}As-GaAs-Al_xGa_{1-x}As$ heterostructures," Phys. Rev. Lett. **33**, 827–830 (1974).
134. For example, C. Y. Liu and S. Yuan, "InGaAs/GaAs quantum well circular ring lasers fabricated by laser direct writing and pulsed anodic oxidation," J. Cryst. Growth **268**, 364–368 (2004).
135. For example, H. M. Ng, C. Gmachl, S. N. G. Chu, and A. Y. Cho, "Molecular beam epitaxy of $GaN/Al_xGa_{1-x}N$ superlattices for 1.52–4.2 μm intersubband transitions," J. Cryst. Growth **220**, 432–438 (2000).
136. For example, reviewed in S. Schmitt-Rink, D. S. Chemla, and D. A. B. Miller, "Linear and nonlinear optical properties of semiconductor quantum wells," Adv. Phys. **38**, 89–188 (1989).
137. S. H. Park, J. F. Morhange, A. D. Jefferey, R. A. Morgan, A. Chavez-Pirson, H. M. Gibbs, S. W. Koch, N. Peyghamberian, M. Derstine, A. C. Gossard, J. H. English, and W. Weigmann, "Measurements of room-temperature, band-gap-resonant optical nonlinearities of GaAs/AlGaAs multiple quantum wells and bulk GaAs," Appl. Phys. Lett. **52**, 1201–1203 (1988).
138. S. J. Wagner, J. Meier, A. S. Helmy, J. S. Aitchison, M. Sorel, and D. C. Hutchings, "Polarization-dependent nonlinear refraction and two-photon absorption in GaAs/AlAs superlattice waveguides below the half-bandgap," J. Opt. Soc. Am. B **24**, 1557–1563 (2007).
139. L. Brzozowskia, E. H. Sargent, A. Spring Thorpe and M. Extavour, "Direct measurements of large near-band edge nonlinear index change from 1.48 to 1.55 μm in InGaAs/InAlGaAs multiquantum wells," Appl. Phys. Lett. **82**, 4429–4431 (2003).
140. R. Liu, Y. Shu, G. Zhang, J. Sun, X. Xing, B. Pi, J. Yao, Z. Wang, and J. Xu, "Study of nonlinear absorption in GaAs/AlGaAs multiple quantum wells using the reflection Z-scan," Opt. Quantum Electron. **39**, 1207–1214 (2007).
141. A. L. Efros and A. V. Rodina, "Confined excitons, trions and biexcitons in semiconductor microcrystals," Solid State Commun. **72**, 645–649 (1989).
142. A. L. Efros and A. V. Rodina, "Band-edge absorption and luminescence of nonspherical nanometer-size crystals," Phys. Rev. B **47**, 10005–10007 (1993).
143. R. K. Jain and R. C. Lind, "Degenerate four-wave mixing in semiconductor-doped glasses," J. Opt. Soc. Am. **73**, 647–653 (1983).
144. P. Horan and W. Blau, "Photodarkening effect and the optical nonlinearity in a quantum-confined, semiconductor-doped glass," J. Opt. Soc. Am. B **7**, 304–308 (1990).
145. S. S. Yao, C. Karaguleff, A. Gabel, R. Fortenberry, C. T. Seaton, and G. I. Stegeman, "Ultrafast carrier and nonlinear grating lifetimes of optical filter glass," Appl. Phys. Lett. **46**, 801–802 (1985).
146. M. Ghanassi, M. C. Schanne-Klein, F. Hache, A. I. Ekimov, D. Ricard, and Chr. Flytzanis, "Time-resolved measurements of carrier recombination in experimental semiconductor-doped glasses: confirmation of the role of Auger recombination," Appl. Phys. Lett. **62**, 78–80 (1993).
147. A. I. Ekimov, F. Hache, M. C. Schanne-Klein, D. Ricard, Chr. Flytzanis, I. A. Kudryavtsev, T. V. Yazeva, A. V. Rodina, and Al. L. Efros, "Absorption and intensity-dependent photoluminescence measurements on CdSe quantum dots: assignment of the first electronic transitions," J. Opt. Soc. Am. B **10**, 100–107 (1993).
148. N. F. Borrelli, D. W. Hall, H. J. Holland, and D. W. Smith, "Quantum con-

finement effects of semiconductor crystallites in glass," J. Appl. Phys. **61**, 5399–5409 (1987).
149. G. R. Olbright, N. Peyghambarian, S. W. Koch, and L. Banyai, "Optical nonlinearities of glasses doped with semiconductor microcrystallites," Opt. Lett. **12**, 413–415 (1987).
150. L. A. Padilha, J. Fu, D. J. Hagan, E. W. Van Stryland, C. L. Cesar, L. C. Barbosa, C. H. B. Cruz, D. Buso, and A. Martucci, "Frequency degenerate and nondegenerate two-photon absorption spectra of semiconductor quantum dots," Phys. Rev. B **75**, 075325 (2007).
151. E. M. Wright, S. W. Koch, J. E. Ehrlich, C. T. Seaton, and G. I. Stegeman, "Semiconductor figure of merit for nonlinear directional couplers," Appl. Phys. Lett. **52**, 2127–2129 (1988).
152. N. Finlayson, W. C. Banyai, C. T. Seaton, G. I. Stegeman, M. O'Neill, T. J. Cullen, and C. N. Ironside, "Optical nonlinearities in CdS_xSe_{1-x}-doped glass waveguides," J. Opt. Soc. Am. B **6**, 675–684 (1989).
153. C. Gan, M. Xiao, D. Battaglia, N. Pradhan, and X. Peng, "Size dependence of nonlinear optical absorption and refraction of Mn-doped ZnSe nanocrystals," Appl. Phys. Lett. **91**, 201103 (2007).
154. Z. Yin, X. Tang, J. Zhao, and S. Deny, "Effects of growth conditions on InAs quantum dot formation by metal-organic chemical vapor deposition using tertiarybutylarsine in pure N_2 ambient," J. Appl. Phys. **99**, 124306 (2006).
155. M. Tetsuya, M. Tomoyuki, and K. Fumio, "Topological characteristics of InAs quantum dot with GaInAs cover using Sb surfactant," Appl. Phys. Lett. **88**, 183109 (2006).
156. S. C. Lee, L. R. Dawson, K. J. Malloy, and S. R. Brueck, "Molecular-beam epitaxial growth of one-dimensional rows of InAs quantum dots on nanoscale-patterned GaAs," Appl. Phys. Lett. **79**, 2630–2632 (2001).
157. C. Cornet, A. Schliwa, J. Even, F. Doré, C. Celebi, A. Létoublon, E. Macé, C. Paranthoën, A. Simon, P. M. Koenraad, N. Bertru, D. Bimberg, and S. Loualiche, "Electronic and optical properties of InAs/InP quantum dots on InP(100) and InP(311)*B* substrates: theory and experiment," Phys. Rev. B **74**, 035312 (2006).
158. J. D. Bauer, D. Schuh, E. Uccelli, R. Schulz, A. Kress, F. Hofbauer, J. J. Finley, and G. Abstreiter, "Long-range ordered self-assembled InAs quantum dots epitaxially grown on (110) GaAs," Appl. Phys. Lett. **85**, 4750–4752 (2004).
159. X. Wang, Z. M. Wang, B. Liang, G. J. Salamo, and C.-K. Shih, "Direct spectroscopic evidence for the formation of one-dimensional wetting wires during the growth of InGaAs/GaAs quantum dot chains," Nano Lett. **6**, 1847–1851 (2006).
160. P. Ballet, J. B. Smathers, and G. J. Salamo, "*In-situ* observation of InAs self-organized islands on AlAs surfaces," Appl. Phys. Lett. **75**, 337–339 (1999).
161. P. Ballet, J. B. Smathers, H. Yang, C. L. Workman, and G. J. Salamo, "Control of size and density of InAs/(Al,Ga)As self-organized islands," J. Appl. Phys. **90**, 481–487 (2001).
162. X. Peng, "Mechanisms of shape control and evolution of nanocrystals," Adv. Mater. **15**, 459–463 (2003).
163. W. W. Yu, Y. A. Wang, and X. Peng, "Formation and stability of size-, shape-, and structure-controlled CdTe nanocrystals: ligand effects on monomers and nanocrystals," Chem. Mater. 4300–4308 (2003).

164. J. Jack Li, Y. A. Wang, W. Guo, J. C. Keay, T. D. Mishima, M. B. Johnson, and X. Peng, "Large-scale synthesis of nearly monodisperse CdSe/CdS core/shell nanocrystals using air-stable reagents via successive ion layer adsorption and reaction," J. Am. Chem. Soc. **125**, 12567–12575 (2003).
165. X. Wang, L. Qu, J. Zhang, X. Peng, and M. Xiao, "Surface-related emission in highly luminescent CdSe quantum dots," Nano Lett. **3**, 1103–1106 (2003).
166. R. Hellwarth, J. Cherlow, and T.-T. Yang, "Origin and frequency dependence of nonlinear optical susceptibilities of glasses," Phys. Rev. B **1**, 964–967 (1975).
167. F. A. Hopf and G. I. Stegeman, *Applied Classical Electrodynamics, Vol 1: Linear Optics*, Wiley Series in Pure and Applied Physics, S. S. Ballard and J. W. Goodman, eds. (Wiley, 1985).
168. F. A. Hopf and G. I. Stegeman, *Applied Classical Electrodynamics, Vol 2: Nonlinear Optics*, Wiley Series in Pure and Applied Physics, S. S. Ballard and J. W. Goodman, eds. (Wiley, 1985).
169. I. Kang, S. Smolorz, T. Krauss, F. Wise, B. G. Aitken, and N. F. Borrelli, "Time-domain observation of nuclear contributions to the optical nonlinearities of glasses," Phys. Rev. B **54**, R12641–R12644 (1996).
170. S. Smolorz, F. Wise, and N. F. Borrelli, "Measurement of the nonlinear optical response of optical fiber materials by use of spectrally resolved two-beam coupling," Opt. Lett. **24**, 1103–1105 (1999).
171. S. Montant, A. Le Calvez, E. Freysz, and A. Ducasse, "Time-domain separation of nuclear and electronic contributions to the third-order nonlinearity in glasses," J. Opt. Soc. Am. B **15**, 2802–2807 (1998).
172. D. McMorrow, W. T. Lotshaw, and G. A. Kenney-Wallace, "Femtosecond optical Kerr studies on the origin of the nonlinear response in simple liquids," IEEE J. Quantum Electron. **24**, 443–454 (1988).
173. I. C. Khoo, "Nonlinear optics of liquid crystalline materials," Phys. Rep. **471**, 221–267 (2009).
174. M. A. Duguay and J. W. Hansen, "An ultrafast light gate," Appl. Phys. Lett. **15**, 192–194 (1969).
175. P. G. de Gennes, *The Physics of Liquid Crystals* (Clarendon, 1974).
176. G. K. L. Wong and Y. R. Shen, "Study of pretransitional behavior of laser-field-induced molecular alignment in isotropic nematic substances," Phys. Rev. A **10**, 1277–1284 (1974).
177. D. Fekete, J. Au Yeung, and A. Yariv, "Phase conjugate reflection by degenerate four wave mixing in a nematic crystal in the isotropic phase," Opt. Lett. **5**, 51–53 (1980).
178. I. C. Khoo, T. H. Liu, and P. Y. Yan, "Nonlocal radial dependence of laser-induced molecular reorientation in a nematic liquid crystal: theory and experiment," J. Opt. Soc. Am. B **4**, 115–120 (1987).
179. E. Brasselet, A. Lherbier, and L. J. Dube, "Transverse nonlocal effects in optical reorientation of nematic liquid crystals," J. Opt. Soc. Am. B **23**, 36–44 (2006).
180. I. C. Khoo, G. Finn, R. R. Michael, and T. H. Liu, "Passive optical self-limiter using laser induced axially symmetric and asymmetric transverse self-phase modulations in a liquid crystal film," Opt. Lett. **11**, 227–229 (1986).
181. I. C. Khoo, J. Y. Hou, T. H. Liu, P. Y. Yan, R. R. Michael, and G. M. Finn, "Transverse self-phase modulation and bistability in the transmission of a laser beam through a nonlinear thin film," J. Opt. Soc. Am. B **4**, 886–891

(1987).
182. C. Conti, M. Peccianti, and G. Assanto, "Observation of optical spatial solitons in a highly nonlocal medium," Phys. Rev. Lett. **92**, 113902 (2004).
183. G. Demeter and D. O. Krimer, "Light-induced dynamics in nematic liquid crystals—a fascinating world of complex nonlinear phenomena," Phys. Rep. **448**, 133–162 (2007).
184. I. C. Khoo and R. Normandin, "Nanosecond laser-induced transient and erasable permanent grating diffractions and ultrasonic waves in a nematic film," Appl. Phys. **55**, 1416–1418 (1984).
185. I. C. Khoo, R. R. Michael, and P. Y. Yan, "Theory and experiment on optically induced nematics axis reorientation and nonlinear effects in the nanosecond regime," IEEE J. Quantum Electron. **QE-23**, 267–272 (1987).
186. H. J. Eichler and R. Macdonald, "Flow alignment and inertial effects in picosecond laser-induced reorientation phenomena of nematic liquid crystals," Phys. Rev. Lett. **67**, 2666–2669 (1991).
187. I. C. Khoo, S. Slussarenko, B. D. Guenther, and W. V. Wood, "Optically induced space charge fields, dc voltage, and extraordinarily large nonlinearity in dye-doped nematic liquid crystals," Opt. Lett. **23**, 253–255 (1998).
188. L. Lucchetti, M. Di Fabrizio, O. Francescangeli, and F. Simoni, "Colossal optical nolinearity in dye-doped liquid crystals," Opt. Commun. **233**, 417–424 (2004).
189. W. M. Gibbons, P. J. Shannon, S.-T. Sun, and B. J. Swetlin, "Surface-mediated alignment of nematic liquid crystals with polarized laser light," Nature **351**, 49–50 (1991).
190. I. C. Khoo, H. Li, and Y. Liang, "Optically induced extraordinarily large negative orientational nonlinearity in dye-doped-liquid crystal," IEEE J. Quantum Electron. **29**, 1444–1447 (1993).
191. H. Li, Y. Liang, and I. C. Khoo, "Transient laser induced orthogonal director axis reorientation in dye-doped liquid crystal," Mol. Cryst. Liq. Cryst. **251**, 85–92 (1994).
192. I. Jánossy and L. Szabados, "Optical reorientation of nematic liquid crystals in the presence of photoisomerization," Phys. Rev. E 4598–4604 (1998).
193. T. V. Truong, L. Xu, and Y. R. Shen, "Dynamics of the guest–host orientational interaction in dye-doped liquid-crystalline materials," Phys. Rev. E **72**, 051709 (2005).
194. I. C. Khoo, M. Y. Shih, M. V. Wood, B. T. Guenther, P. H. Chen, F. Simoni, S. S. Slussarenko, O. Francescangeli, and L. Lucchetti, "Dye-doped photorefractive liquid crystals for dynamic and storage holographic grating formation and spatial light modulation," Proc. IEEE **87**, 1987–1911 (1999).
195. M. Kaczmarek, M. Y. Shih, R. S. Cudney, and I. C. Khoo, "Electrically tunable, optically induced dynamic and permanent gratings in dye-doped liquid crystals," IEEE J. Quantum Electron. **38**, 451–457 (2002).
196. I. C. Khoo, P. H. Chen, M. Y. Shih, A. Shishido, and S. Slussarenko, "Supra optical nonlinearities (SON) of methyl-red and azobenzene liquid crystal-doped nematic liquid crystals," Mol. Cryst. Liq. Cryst. **358**, 1–13 (2001).
197. A. T. Shishido, O. Tsutsumi, A. Kanazawa, T. Shiono, T. Ikeda, and N. Tamai, "Rapid optical switching by means of photoinduced change in refractive index of azobenzene liquid crystals detected by reflection-mode

analysis," J. Am. Chem. Soc. **119**, 7791–7796 (1997), and references therein.
198. Y. L. Yu and T. Ikeda, "Alignment modulation of azobenzene-containing liquid crystal systems by photochemical reactions," J. Photochem. Photobiol. C **5**, 247–265 (2004).
199. E. V. Rudenko and A. V. Sukhov, "Optically induced spatial charge separation in a nematic and the resultant orientational nonlinearity," JETP **78**, 875–882 (1994).
200. I. C. Khoo, H. Li, and Y. Liang, "Observation of orientational photorefractive effects in nematic liquid crystals," Opt. Lett. **19**, 1723–1725 (1994).
201. I. C. Khoo, "Orientational photorefractive effects in nematic liquid crystal film," IEEE J. Quantum Electron. **32**, 525–534 (1996).
202. G. P. Wiederrecht, B. A. Yoon, and M. R. Wasielewski, "High photorefractive gain in nematic liquid crystals doped with electron-donor and acceptor molecules," Science **270**, 1794–1797 (1995).
203. I. C. Khoo, K. Chen, and Y. Z. Williams, "Orientational photorefractive effect in undoped and CdSe nano-rods doped nematic liquid crystal—bulk and interface contributions," IEEE J. Sel. Top. Quantum Electron. **12**, 443–450 (2006).
204. W. Helfrich, "Conduction-induced alignment of nematic liquid crystals: basic model and stability consideration," J. Chem. Phys. **51**, 4092–4105 (1969).
205. M. E. Mack, "Stimulated thermal light scattering in the picosecond regime," Phys. Rev. Lett. **22**, 13–15 (1969).
206. H. J. Eichler, P. Gunter, and D. N. Pohl, *Laser Induced Dynamic Grating* (Springer-Verlag, 1986).
207. I. C. Khoo and R. Normandin, "The mechanism and dynamics of transient thermal grating diffraction in nematic liquid crystal films," IEEE J. Quantum Electron. **21**, 329–335 (1985).
208. See, for example, P. Sheng, "Boundary-layer phase transition in nematic liquid crystals," Phys. Rev. A **26**, 1610–1617 (1982).
209. I. C. Khoo, R. G. Lindquist, R. R. Michael, R. J. Mansfield, and P. Lopresti, "Dynamics of picosecond laser induced density, temperature and flow-reorientation effects in the mesophases of liquid crystals," J. Appl. Phys. **69**, 3853–3859 (1991).
210. I. C. Khoo, J. Y. Hou, G. L. Din, Y. L. He, and D. F. Shi, "Laser induced thermal, orientational and density nonlinear optical effects in nematic liquid crystals," Phys. Rev. A **42**, 1001–1004 (1990).
211. I. C. Khoo, J. H. Park, and J. D. Liou, "Theory and experimental studies of all-optical transmission switching in a twist-alignment dye-doped nematic liquid crystal," J. Opt. Soc. Am. B **25**, 1931–1937 (2008).
212. P. Günter and J.-P. Huignard, eds., *Photorefractive Materials and Their Applications I: Basic Effects* (Springer-Verlag, 1988).
213. P. Günter and J.-P. Huignard, eds., *Photorefractive Materials and Their Applications II: Survey of Applications* (Springer-Verlag, 1988).
214. P. Günter and J.-P. Huignard, eds., *Photorefractive Materials and Their Applications 1: Basic Effects* (Springer-Verlag, 2006).
215. P. Yeh, *Introduction to Photorefractive Nonlinear Optics* (Wiley, 1993).
216. M. P. Petrov, S. I. Stepanov, and A. V. Khomenko, in *Photorefractive Crystals in Coherent Optical Systems*, Vol. 59 of Series in Optical Sciences (Springer-Verlag, 1991).
217. J. Frejlich, *Photorefractive Materials: Fundamental Concepts, Holo-*

graphic Recording, and Materials Characterization (Wiley-Interscience, 2006).
218. Papers in *Selected Papers on Photorefractive Materials*, Vol. MS86 of SPIE Milestone Series, F. M. Davidson, ed. (SPIE, 1994).
219. A. Yariv, *Optical Electronics*, 4th ed. (Saunders College Publishing/ Harcourt Brace, 1991).
220. B. Ya. Zel'dovich, N. F. Pilipetsky, and V. V. Shkunov, *Principles of Phase Conjugation* (Springer-Verlag, 1985).
221. J. Feinberg, "Photorefractive nonlinear optics," Phys. Today **41**(10), 46–52 (1988).
222. G. C. Valley and M. B. Klein, "Optimal properties of photorefractive materials for optical data processing," Opt. Eng. **22**, 704–711 (1983).
223. J. Feinberg, D. Heiman, A. R. Tanguay, Jr., and R. W. Hellwarth, "Photorefractive effects and light-induced charge migration in barium titanate," J. Appl. Phys. **51**, 1297–1305 (1980).
224. A. Ashkin, G. D. Boyd, J. M. Dziedzic, R. G. Smith, A. A. Ballman, J. J. Levinstein, and K. Nassau, "Optically-induced refractive index inhomogeneities in $LiNbO_3$ and $LiTaO_3$," Appl. Phys. Lett. **9**, 72–74 (1966).
225. N. Kukhtarev, V. B. Markov, S. G. Odulov, M. S. Soskin, and V. L. Vinetskii, "Holographic storage in electrooptic crystals. I. Steady state," Ferroelectrics **22**, 949–960 (1979).
226. V. O. Vinetskii and N. V. Kukhtarev, "Theory of the conductivity induced by recording holographic gratings in nonmetallic crystals," Sov. Phys. Solid State **16**, 2414–2415 (1975).
227. G. C. Valley, "Simultaneous electron/hole transport in photorefractive materials," J. Appl. Phys. **59**, 3363–3366 (1986).
228. G. Picoli, P. Gravey, C. Ozkul, and V. Vieux, "Theory of two-wave mixing gain enhancement in photorefractive InP:Fe: a new mechanism of resonance," J. Appl. Phys. **66** 3798–3813 (1989).
229. M. Segev, Y. Ophir, and B. Fischer, "Nonlinear multi two wave mixing and the fanning process in photorefractive media," Opt. Commun. **77**, 265–274 (1990).
230. A. A. Zozulya, M. Saffman, and D. Z. Anderson, "Propagation of light beams in photorefractive media," Phys. Rev. Lett. **73**, 818–821 (1994).
231. O. V. Lyubomudrov and V. V. Shkunov, "Self-bending specklons in photorefractive crystals," J. Opt. Soc. Am. B **11**, 1403–1408 (1994).
232. D. N. Christodoulides and M. I. Carvalho, "Compression, self-bending, and collapse of Gaussian beams in photorefractive crystals," Opt. Lett. **19**, 1714–1716 (1994).
233. M. Segev, G. C. Valley, B. Crosignani, P. D. Porto, and A. Yariv, "Steady-state spatial screening solitons in photorefractive materials with external applied field," Phys. Rev. Lett. **73**, 3211–3214 (1994).
234. D. N. Christodoulides and M. I. Carvalho, "Bright, dark, and gray spatial soliton states in photorefractive media," J. Opt. Soc. Am. B **12**, 1628–1633 (1995).
235. M. Segev, M. Shih, and G. C. Valley, "Photorefractive screening solitons of high and low intensity," J. Opt. Soc. Am. B **13**, 706–718 (1996).
236. E. DelRe, M. Segev, D. Christodoulides, B. Crosignani, and G. Salamo, "Photorefractive solitons," in [214], Chap. 11.
237. G. F. Calvo, F. Agulló-López, and M. Carrascosa, "Transition from local to nonlocal photorefractive nonlinearity on increasing spatial dimensionality," Opt. Commun. **233**, 439–444 (2004).

238. M. Segev, B. Crosignani, A. Yariv, and B. Fischer, "Spatial solitons in photorefractive media," Phys. Rev. Lett. **68**, 923–926 (1992).
239. G. C. Valley, M. Segev, B. Crosignani, A. Yariv, M. M. Fejer, and M. Bashaw, "Dark and bright photovoltaic spatial solitons," Phys. Rev. A **50**, R4457–R4460 (1994).
240. M. Taya, M. C. Bashaw, M. M. Fejer, M. Segev, and G. C. Valley, "Observation of dark photovoltaic spatial solitons," Phys. Rev. A **52**, 3095–3100 (1995).
241. A. Agranat, V. Leyva, and A. Yariv, "Voltage-controlled photorefractive effect in paraelectric $KTa_{1-x}Nb_xO_3:Cu,V$," Opt. Lett. **14**, 1017–1019 (1989).
242. A. Agranat, R. Hofmeister, and A. Yariv, "Characterization of a new photorefractive material: $K_{1-y}L_yT_{1-x}N_x$," Opt. Lett. **17**, 713–715 (1992).
243. M. Segev and A. J. Agranat, "Spatial solitons in centrosymmetric photorefractive media," Opt. Lett. **22**, 1299–1301 (1997).
244. E. DelRe, B. Crosignani, M. Tamburrini, M. Segev, M. Mitchell, E. Refaeli, and A. J. Agranat, "One-dimensional steady-state photorefractive spatial solitons in centrosymmetric paraelectric potassium lithium tantalate niobate," Opt. Lett. **23**, 421–423 (1998).
245. "Electrostriction," *Encyclopaedia Britannica*, http://www.britannica.com/EBchecked/topic/184067/electrostriction.
246. B. A. Auld, *Acoustic Fields and Waves in Solids* (Wiley, 1973).
247. R. J. D. Miller, R. Casalegno, K. A. Nelson, and M. D. Fayer, "Laser-induced ultrasonics: a dynamic holographic approach to the measurement of weak absorptions, optoelastic constants and acoustic attenuation," Chem. Phys. **72**, 371–9 (1982).
248. D. A. Pinnow, "Elastooptical materials," in *Handbook of Lasers with Selected Data on Optical Technology*, R. J. Pressley, ed. (CRC Press, 1971), Chap. 17.
249. E. L. Buckland and R. W. Boyd, "Electrostrictive contribution to the intensity-dependent refractive index of optical fiber," Opt. Lett. **21**, 1117–1119 (1996).
250. E. L. Buckland and R. W. Boyd, "Measurement of the frequency response of the electrostrictive nonlinearity in optical fiber," Opt. Lett. **22**, 676–678 (1997).
251. A. Fellega, A. Melloni, and M. Martinelli, "Measurement of the frequency response induced by electrostriction in optical fibers," Opt. Lett. **22**, 1615–1617 (1997).
252. D. I. Kovsh, D. J. Hagan, and E. W. Van Stryland, "Numerical modeling of thermal refraction in liquids in the transient regime," Opt. Express **4**, 315–327 (1999).
253. D. I. Kovsh, S. Yang, D. J. Hagan, and E. W. Van Stryland, "Nonlinear optical beam propagation for optical limiting," Appl. Opt. **38**, 5168–5180 (1999).
254. M. Sheik-Bahae, A. A. Said, D. J. Hagan, M. J. Soileau, and E. W. Van Stryland, "Nonlinear refraction and optical limiting in thick media," Opt. Eng **30**, 1228–1235 (1991).
255. L. Mutter, F. D. J. Brunner, Zh. Yang, M. Jazbinšek, and P. Günter, "Linear and nonlinear optical properties of the organic crystal DSTMS," J. Opt. Soc. Am. B. **24**, 2556–2561 (2007).
256. L. A. Ostrovskii, "Self-action of light in crystals," JETP Lett. **5**, 272–275 (1967).

257. G. R. Meredith, "Second-order cascading in third-order nonlinear optical processes," J. Chem. Phys. **77**, 5863–5871 (1982).
258. Reviewed in G. I. Stegeman, D. J. Hagan, and L. Torner, "$\chi^{(2)}$ cascading phenomena and their applications to all-optical signal processing, mode-locking, pulse compression and solitons," Opt. Quantum Electron. **28**, 1691–1740 (1996).
259. R. C. Eckardt and J. Reintjes, "Phase matching limitations of high efficiency second harmonic generation," IEEE J. Quantum Electron. **20**, 1178–1187 (1984).
260. A. Kobyakov, U. Peschel, R. Muschall, G. Assanto, V. P. Torchigin, and F. Lederer, "Analytical approach to all-optical modulation by cascading," Opt. Lett. **20**, 1686–1688 (1995).
261. A. Kobyakov, U. Peschel, and F. Lederer, "Vectorial type-II interaction in cascaded quadratic nonlinearities—an analytical approach," Opt. Commun. **124**, 184–94 (1996).
262. G. I. Stegeman, M. Sheik-Bahae, E. W. Van Stryland, and G. Assanto, "Large nonlinear phase shifts in second-order nonlinear-optical processes," Opt. Lett. **18**, 13–15 (1993).
263. K. R. Parameswaran, J. R. Kurtz, R. V. Roussev, and M. M. Fejer, "Observation of 99% pump depletion in single-pass second-harmonic generation in a periodically poled lithium niobate waveguide," Opt. Lett. **27**, 43–45 (2002).
264. E. W. Van Stryland, "Third-order and cascaded nonlinearities," in *Laser Sources and Applications*, A. Miller and D. M. Finlayson, eds., Scottish Graduate Series (CRC Press and Taylor & Francis, 1997), pp 15–62 (1996).
265. R. J. DeSalvo, D. J. Hagan, M. Sheik-Bahae, G. Stegeman, H. Vanherzeele, and E. W. Van Stryland, "Self-focusing and defocusing by cascaded second order effects in KTP," Opt. Lett. **17**, 28–30 (1991).
266. M. L. Sundheimer, Ch. Bosshard, E. W. VanStryland, G. I. Stegeman, and J. D. Bierlein, "Large nonlinear phase modulation in quasi-phase-matched KTP waveguides due to cascaded second-order processes," Opt. Lett. **18**, 1397–9 (1993).
267. Series of articles published by multiple authors under the general title "Research on nonlinear optical materials: an assessment," Appl. Opt. **26**, 211–234 (1987).
268. G. I. Stegeman, "Material figures of merit and implications to all-optical switching," Proc. SPIE, **1852**, 75–89 (1993).
269. Many articles in *Self-Focusing: Past and Present*, R. W. Boyd, S. G. Lukishova and Y. R. Shen, eds. (Springer Science, 2009).
270. S. Trillo and W. Torruellas, eds., *Spatial Solitons* (Springer-Verlag, 2001).

Demetri N. Christodoulides received his Ph.D. degree in Electrical Engineering from Johns Hopkins University in 1986. From 1986 to 1987 he was a Post-doctoral Fellow with Bell Communications Research. From 1987 to 2002, he was with the Department of Electrical Engineering at Lehigh University, and in 2002 he joined the College of Optics and Photonics/CREOL at the University of Central Florida. His research interests are mainly in the areas of nonlinear optics, nonlinear fiber optics, light-wave technology, and quantum

electronics. He is the author or coauthor of more than 200 scientific publications. His most significant contributions include the prediction and observation of Bragg, vector, and discrete (lattice) solitons. In the past, he served as a Topical Editor for the *IEEE Journal of Quantum Electronics* and the *Journal of the Optical Society of America B*. He has chaired or served on several conferences and conference committees. Prof. Christodoulides is a Fellow of the American Physical Society and of the Optical Society of America.

I. C. Khoo received the Ph.D. degree in Physics from the University of Rochester in 1976. He joined Penn State in 1984 and currently holds the W. E. Leonhard Chair Professorship in the Electrical Engineering Department. He is the author or coauthor of more than 500 scientific publications [~210 journal and proceedings papers and 290 conference presentations]. His research interests are centered on novel electro-optical and nonlinear optical materials such as liquid crystals, nonlinear multiphoton absorbing liquids, nanoparticulates, and metamaterials, and on the studies of various nonlinear optical processes and their applications in advanced optoelectronic platforms and systems. He is the author or coauthor of several books and book chapters, including *Liquid Crystals* (2nd ed., Wiley, 2007) and *Optics and Nonlinear Optics of Liquid Crystals* (World Scientific, 1995). He is a Fellow of the Optical Society of America, IEEE and the UK Institute of Physics and currently chairs the National Academy of Science—U.S. Advisory Committee/International Commission for Optics, and serves as a Vice President in the International Commission for Optics.

Gregory J. Salamo holds the Basore Chair in Nanotechnology and Innovation. He received the Ph.D. in physics from City University of New York in 1973, where he also worked as an intern student at Bell Laboratories in Murray Hill, New Jersey, from 1968 to 1973. His postdoctoral work was at the Institute of Optics of University of Rochester in New York from 1973 to 1975. He joined the faculty of the University of Arkansas in January of 1975, where he is now Distinguished Professor of Physics and the Basore Professor in Nanotechnology and Innovation. He has carried out research in the areas of optical spatial solitons, quantum optics, and the optical properties of semiconductors. His research is currently focused on growing III–V semiconductors and ferroelectrics by using molecular beam epitaxy, scanning tunneling microscopy, and transmission electron microscopy. He is Director of a National Science Foundation (NSF) Materials Research Science and Engineering Center on the Physics of Semiconductor Nanostructures and Director of the Arkansas Institute for Nanoscale Material Science and Engineering. He has published more than 200 papers in referred journals, has given numerous contributed and invited talks, has contributed several book chapters, and is editor of the Springer Lecture Notes in Nanoscience. He also pursues the development of interdisciplinary research and education through the establishment of a new MS/Ph.D. degree program in Micro Electronics–Photonics, which is now the home of 60 graduate students and

which provides greater career opportunities for students and faculty in the sciences. He has also started new laboratory courses in Laser Physics, Quantum Optics, Nonlinear Optics, Optic Communications, Optical Properties of Solids, and Nanoscale Fabrication and Imaging, each with separate NSF Awards. He is the principal investigator for an NSF educational laboratory in nanotechnology, a GK-12 NSF Graduate Student Fellowship program, a NSF partnership for Innovation program for spin-off small business, an NSF collaborative grant with Texas Instruments, and a Hughes Grant for an Undergraduate Research Center in Nanoscience. He is a Fellow of the Optical Society of America and won the UA Baum Award for Teaching, the most prestigious UA award made to one faculty member each year. He was also the 2009 Case Arkansas Professor of the Year. His total research awards amount to more than $40M dollars.

George Stegeman was born in 1942 in Edinburgh Scotland of Polish parents. The family immigrated to Canada in 1949. He and his wife Ann married in 1969 and they have three adult children, two boys and a girl. He received his education in Toronto Canada, graduating from Engineering Physics from the University of Toronto in 1965. He received his Ph.D. in Physics at the University of Toronto in 1969. After he was appointed to the faculty there in 1970, he progressed through the ranks to Professor in 1980. In 1980 he moved to the Optical Sciences Center of the University of Arizona. Since 1990 he has been the Cobb Family Chair in the College of Optics and Photonics/CREOL at the University of Central Florida. He retired in 2009 and is Professor Emeritus in the college of Optics and Photonics, University Central Florida. Currently he is teaching Nonlinear Optics at various institutions and preparing a textbook on this subject. He has served as Topical Editor (1992–1996) and as Editor-in-Chief for the *Journal of the Optical Society of America B* (2000–2006), as North American Editor of *Journal of Optical and Quantum Electronics* (1997–2000), and is currently the editor of Physics Reports for the field of optics. He has been a member of Editorial Boards of *Wave Electronics* (1979–1983), *Applied Physics Letters*, and the *Journal of Applied Physics* (1987–1989), *Optics Communications* (1986–2000), *Optics Letters* (1989–1993), the *Journal of Optical Materials* (1991–1992), the *Journal of Nonlinear Optics* (1991 to the present), and the International Advisory Board, *Journal of the Korean Optical Society of Korea* (2000-2009). He has chaired or cochaired numerous conferences, including the Annual Meeting of OSA, QELS, Nonlinear Optics, and Nonlinear Integrated Optics.

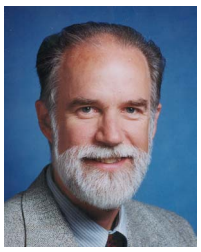

Eric W. Van Stryland is a Professor of Optics and Past Dean of CREOL and FPCE, College of Optics and Photonics, University of Central Florida. He received a Ph.D. in Physics in 1976 from the University of Arizona, Optical Sciences Center, where he worked on optical coherent transients and photon counting statistics. He worked in the areas of femtosecond pulse production, multiphoton absorption in solids, and laser-induced damage at the University of Southern California. He joined the University of North Texas in l978, helping to form the Center for Applied Quantum Electronics. In l987 he joined the newly

formed CREOL (Center for Research and Education in Optics and Lasers) at the University of Central Florida. NSF has funded him for the past 30 years. His current research interests are in the characterization of the nonlinear optical properties of materials and their temporal response as well as the applications of these nonlinear materials properties for optical switching, etc. He helped develop the Z-scan and also established the methodology for applying Kramers–Kronig relations to ultrafast nonlinearities and helped develop the field of cascaded second-order effects. He is a fellow of the OSA, a former member of their Board, a senior member of the Laser Institute of America and a former board member, a Fellow of SPIE and IEEE and a member of the APS, SPIE, and MRS. He also served as a Topical Editor for *Optics Letters*. He was elected Vice President of the OSA, which led to becoming President in 2006. He graduated 27 Ph.D.'s, published ~300 papers, and is on the ISI "highly cited" list. In 2003 he was awarded the highest honor UCF bestows, the Pegasus Award. He was Director of the School of Optics/CREOL from July 1999 to May of 2004. With the elevation of the School to a College, he became its first Dean. In addition, Governor Bush established the Florida Photonics Center of Excellence (FPCE) in 2003 and he was Director of that Center along with CREOL until he retired as dean in January 2009.